Dissertation

Development of fibre-optic transmission systems with UV diode lasers and high stability single-mode waveguides

A thesis submitted by

Cornell Peter Gonschior

for the degree of
Doctor of Philosophy

at
City University London
School of Engineering & Mathematical Sciences
Measurement and Instrumentation

London, April 2013

Table of Contents

List of tables

List of figures

Acknowledgements

During the course of this work seemingly unsurmountable obstacles were encountered. Without the optimism, encouragement and expertise of Prof. Karl-Friedrich Klein this work would not have been possible. He provided a starting point and the environment for this research. He gave me the opportunity to present and discuss this work all over the world and to learn from experts face to face. I am deeply indebted to him for all his advise, whatever sphere of life it would concern, and his sincere friendship.

I want to thank Prof. Tong Sun and Prof. Ken T. V. Grattan for the possibility to do a doctorate at the City University London. Their advise and contribution during visits at City as well as their thorough revisions of papers and documents were very valuable to me. The collaboration with Prof. Georg Hillrichs from the HS Merseburg and the team from the Fraunhofer Institute for Mechanics and Materials (IWM) in Halle was most fruitful and pointed me in the right directions. When visiting the IPHT in Jena I highly appreciated the engaging discussions with Dr. Johannes Kirchhof, Dr. Sonja Unger and Anka Schwuchow.

One of the biggest helpers during the experimental work and for discussion of results was Jan Heimann. I thank him for his deep insights and never-ending humour even in the harshest of times. For her preparedness and for providing her expertise in the use of the scanning electron microscope, I am grateful to Elke Landrock-Bill.

As contributors on the supplier side, I want to thank Sönke Baumann and Doreen Heyse for the use of equipment and facilities at Omicron-Laserage Lasersysteme GmbH as well as their time for remote damage experiments. In addition, I am thankful towards Prof. Georg Kuka from Fiberware GmbH and Dr. Andy Gillooly from Fibercore Ltd. for providing commercial as well as developmental fibre samples.

I am very grateful for the long-term encouragement from my family and friends, who always believed in me. And thank you, Julia, for your patience, understanding and love, that I can only hope to return one day to the same extent as I receive it.

Copyright declaration

Abstract

Fibre-coupled 405 nm diode laser systems are rarely used with fibre output powers higher than 50 mW. A rapid degradation of these systems has been known for several years. Meanwhile, the typical power of single-mode diode lasers around 400 nm is in the order of 100 to 300 mW, leading to single-mode fibre core power densities in the 1 MW/cm² range. This is three orders of magnitude below the established threshold for optical damage. Nevertheless, in the major investigations undertaken in this work, periodic surface structures have been observed on the end surfaces of synthetic silica fibres when they are exposed to long-term irradiation with light from 405 nm continuous-wave diode lasers. The growth of these laser-induced periodic surface structures (LIPSS) on the proximal fibre end surfaces is responsible for the power degradation. They exhibit multiple bends, break-ups and bifurcations, unlike interference patterns but rather like the effect caused by short-pulsed laser irradiation on wide band-gap dielectrics. Detailed investigations have allowed the conclusion to be drawn that the key parameters contributing to the generation of the LIPSS are power density, surface roughness, polarisation direction and the presence of ultraviolet defect centres.

The spectral damage behaviour of differently treated and doped fibre types was investigated by 405 nm laser irradiation. All fibres showed a strong generation and transformation of various defect centres due to the irradiation. It was concluded that a multi-photon process is responsible for the induced defect centres. A two-step absorption at the singlet-triplet transition of the ODC(II) is proposed and consistent with models from literature. This absorption could generate excitons which in turn transform precursors into defect centres. An efficient transformation or bleaching of ODC(II) into E'_{γ} centres supports this proposal.

After the discovery of the LIPSS on the launching end surfaces of single-mode fibres, different measures were investigated to mitigate the effect, the most effective being a spliced and cleaved short piece of launch-fibre. As a preparation for future higher power laser diodes, the launch-fibre was made from a very low solarisation multi-mode fibre. When the launch-fibre is used on the launching end, the transmission of the fibre is highly stabilised. However, the growth of a LIPSS on the distal end is stimulated, due to a constantly high power density. The beam quality of the emitted beam was reduced and this degradation was characterised. Subsequently, simulations showed the negative impact of the LIPSS on the beam quality. In addition, this provided an opportunity for creating a small accessible laboratory at the distal fibre end. Samples were taken after different periods of irradiation to investigate the evolution of the LIPSS at the same damaging power density. In order to prevent this damage, silica end-caps were used on the distal fibre ends. Assemblies with launch-fibre and end-cap performed with high stability over a period of two month of constant irradiation with the 405 nm single-mode laser.

Symbols and abbreviations

AFM	atomic force microscopy
AS	all-silica
ASE	amplified spontaneous emission
BC	boundary conditions
CC	cleaved and clamped
CFC	cleaved, flame-polished and clamped
CP	clamped and polished
CVD	chemical vapour deposition
CW	continuous-wave
DUV	deep ultraviolet
EDX	energy dispersive x-ray spectroscopy
FBG	fibre Bragg grating
FIB	focused ion beam
FM	fundamental mode
FMF	few-mode fibre
FUT	fibre under test
FWHM	full width half maximum
GP	glued and polished
HOM	higher-order mode
HR-TEM	high resolution transmission electron microscopy
HSFL	high spatial frequency LIPSS
IAS	imaging and alignment system
IVD	inside vapour deposition
IVPO	inside vapour phase oxidation
laser	light amplification by stimulated emission of radiation
LDM	laser diode module
LIPSS	laser-induced periodic surface structure
LMA	large mode area
LMF	low-mode fibre
LSFL	low spatial frequency LIPSS
MCVD	modified chemical vapour deposition
MFD	mode-field diameter
MMF	multi-mode fibre
MML	multi-mode laser
NA	numerical aperture
NBOHC	non-bridging oxygen hole centre
Nd:YAG	neodymium-doped yttrium aluminium garnet

NIR	near infrared
NUV	near ultraviolet
ODC	oxygen deficiency centre
OSA	optical spectrum analyser
OVD	outside vapour deposition
PANDA	polarisation-maintaining and absorption-loss-reducing
PCF	photonic crystal fibre
PCVD	plasma-activated chemical vapour deposition
PM	power meter
PM	polarisation-maintaining
PML	perfectly matched layers
POL	peroxy linkage
POR	peroxy radical
QW	quantum well
SEM	scanning electron microscope
SMF	single-mode fibre
SML	single-mode laser
SSR	spot size ratio
TEM	transmission electron microscope
THG	third-harmonic generation
ToF-SIMS	time-of-flight secondary ion mass spectroscopy
UV	ultraviolet
VAD	vapour-phase axial deposition
VIS	visible light

a-Si	amorphous Silicone
Al	Aluminium
ArF	Argon fluoride
As	Arsenic
Ca	Calcium
Cl	Chlorine
D	Deuterium
F	Fluorine
Ga	Gallium
Ge	Germanium
H	Hydrogen
He	Helium
In	Indium
KrF	Krypton fluoride

N	Nitrogen
O	Oxygen
P	Phosphorous
Pt	Platinum
Sb	Antimony
Si	Silicone
SiO_2	Silica

A	fibre core area
a	fibre core radius
A_{eff}	effective mode area
c	speed of light
d	thickness
E	energy
E	electrical field amplitude
f	focal length
h	Planck's constant
I_{core}	mean power density in fibre core
I_{peak}	peak power density of Gaussian beam
I_{spot}	mean power density in laser spot
k_0	vacuum wavenumber
k_B	Boltzmann's constant
l	length
L	loss
M^2	beam quality factor
N	density of states
n	refractive index
n_{cl}	refractive index in fibre cladding
n_{co}	refractive index in fibre core
P	UV defect precursor
P	power
R	radius of curvature
s	spot size
S_0	singlet ground state
S_1	singlet excited state
T	temperature
t	time
T_1	triplet excited state
V	normalised frequency

w	beam width
w_0	(beam) spot size
z	position
z_R	Rayleigh length
α	linear attenuation coefficient
α_a	acceptance angle
β	non-linear attenuation coefficient
Δr	lateral misalignment
η	coupling efficiency
θ	angular misalignment
θ_c	critical angle
θ_{ff}	far-field angle
Λ	periodicity
λ_0	vacuum wavelength
λ_n	wavelength wavelength in medium with refractive index n
ν	frequency
ρ	material density

1 Introduction

1.1 Abstract

This introduction to the thesis gives the background and context of this work, as well as an overview of the issues of fibre-coupled diode laser systems in the near ultraviolet. The aims and objectives of this work are presented and the structure and design of the thesis are introduced at the end of this chapter, providing an outline of the undertaken work.

1.2 Background and context of this work

Due to the development of continuous-wave (CW) and pulsed semiconductor lasers with high power, there is an increasing demand for single-mode fibres (SMF) with long-term stability. For wavelengths in the visible range (VIS) above 450 nm, the damage threshold at the end surfaces is the main issue restricting the lifetime. On the other hand, additional damaging mechanisms can be expected for shorter wavelengths. The coupling efficiency is another parameter that is important in the whole wavelength range. It is extremely low due to the small core diameter, if broadband light sources or LEDs with near-field diameters in the order of approximately 500 µm are used. Therefore, violet and near ultraviolet (NUV) lasers are the best candidates for light sources in fibre-optic systems with these SMFs. Although the output power is in the order of several milliwatts, the intensity in the small fibre core is significantly high, in the order of MW/cm^2. Thus, UV damage has to be taken into account, even in the wavelength region above 300 nm.

It was reported that SMF deployed with NUV CW diode lasers degraded rapidly. With the lifetime improvement in the area of NUV diode lasers the output power of the lasers increased simultaneously by orders of magnitude in the last decade. In meantime, single-mode laser diodes with power levels of 300 mW are available in commercial products. This increase cannot be handled by regular SMF deployed with the diode lasers at the moment. Severe fibre damage was reported to the laser manufacturers, which rendered the fibre useless. However, this damage was not precisely reproducible and the damage period varied from one day to several weeks [Baumann2008].

There are several effects that can be expected to affect the transmission of the fibre. High intensity levels at both fibre end surfaces could generate depositions by reaction of light with the surrounding atmosphere. Due to higher power density in the small diameter cores deep ultraviolet (DUV) damage by two-photon absorption could be an issue. The latter would not degrade the linear transmission at the laser wavelength significantly at a low intensity, because the induced loss should appear below 300 nm. Two-photon absorption is reversible, which means if the intensity is reduced two-photon absorption decreases. However, UV damage induced by two-photon absorption is not reversible. If

other non-linear effects appeared, the power at the laser wavelength would be decreased. If extremely high power densities occur, mechanical damage could be generated at the fibre end surface and also inside the fibre, for example due to focussing effects. In addition to lens-shaped surfaces, self-focusing at higher intensities because of the Kerr effect can occur.

New applications in the UV require lower spot sizes or better beam qualities than available until a few years ago. Therefore, a SMF for delivery of UV light is a candidate for these requirements. However, single-mode lasers are necessary for an excellent power coupling. Currently, only NUV or violet laser diodes are commercially available. If those are combined with SMF, this is of great interest for new applications in the medical, lithography and sensor field. These combinations are generally used to either improve the beam quality of the laser by filtering the fundamental mode with the fibre or to maintain the good beam quality of the laser and obtain more flexibility in a system design. Furthermore, the separation of light source and application is possible, which is interesting for applications in harsh environments or where temperature steps over several hundred degrees occur.

NUV laser light is being used for soft tissue treatment for several years now [Guffey2006, Kirshenbaum2011]. In the first applications the light was delivered directly from the laser, but for *in vivo* treatment more flexibility and low bending radii were needed. Multi-mode fibre (MMF) could be used to achieve a high output power coupled from multi-mode lasers. If fibre bundles were used, the power could be increased additionally. But the power density on the treated tissue would not rise proportionally, because of the larger spot. A better and faster tissue ablation could be achieved with a Gaussian beam profile coming from a SMF. Higher beam quality and higher intensity from a small single-mode core produce power densities in the order of kW/cm² in a focus spot smaller than 100 µm [Kato2008, Lee2010].

NUV single-mode systems are also being used in confocal microscopy for exciting fluorescent dies and autofluorescence of materials. In lithography they are used for wafer inspection and high-definition DVD mastering [Baumann2008]. The use in photo lithography ranges from lab-on-a-chip production and creating masks for edging to digital holography [Scharnweber2011].

1.3 Aims and objectives of this work

The work is aimed at improving the stability of fibre-coupled diode laser systems in the NUV. In particular, a focus is set on a laser wavelength of 405 nm. A base for future research in the area of UV-VIS single-mode fibre-coupled laser systems should also be established. To achieve these goals the major objectives of the work were set as follows:

- The implementation of spectral measurements of small core fibres (< 5 µm) in the UV region down to 200 nm, including characterisation of specific fibre parameters.
- The implementation of a fibre damage system using high-power 405 nm CW diode lasers.
- The study of fibre bulk damage in differently doped and treated core materials.
- The study of the degradation of 405 nm single-mode fibre-coupled laser systems, additionally using polarisation-maintaining fibre.
- The study of surface modifications on proximal and distal fibre end surfaces using external measurement techniques.
- Determining the main factors of degradation of different fibre systems to derive and test a system with higher stability.
- Giving a recommendation for a system with higher stability and for transferring the results to other laser wavelengths (CW: 488 nm; pulsed: 266 nm, 355 nm, 515 nm).
- Achieving a conclusion of the work and the discussion of the possibilities of extending the work towards future directions.
- Reporting the results obtained at various stages of the research, in various international conferences and journals.

1.4 Structure and design of the thesis

This thesis is divided into self-containing chapters. Each chapter represents a specific area of research and reports on the achievement of the aforementioned aims and objectives.

The first chapter introduces the issues of fibre-coupled NUV diode laser systems, to show the importance of improving these systems. The aims and objectives of this work are brought forward and the structure and design of the thesis is outlined.

In Chapter 2 background information on UV fibre-optic systems from literature is given. The light-guiding mechanisms in silica-based fibres are explained. Different fibre types currently used in science and technology are presented, from multi-mode and single-mode fibres, with and without polarisation-maintenance, as well as photonic crystal fibres. The case of transmitting laser light, especially at higher power densities, is discussed and issues of coupling efficiency and beam quality are addressed. At the end of this chapter the production of optical fibre is explained.

Chapter 3 deals with the basics of laser and fibre material interaction in the NUV. The design of the used laser diodes is presented in more detail and the effects of high power

densities on the silica material are explained. The effects are split into bulk and surface effects.

The setup of a damage measurement system using 405 nm laser diode modules is presented in Chapter 4. This setup was used together with a DUV spectral measurement setup for small core fibres to look at spectral loss effects of the NUV laser irradiation in the DUV in silica fibres. The main experiments were long-term irradiation tests of different fibre types. The major effect in these long-term tests was a surface effect, which was studied with multi-mode and single-mode 405 nm diode lasers. The influence of the fibre surface preparation on the damage behaviour was studied subsequently. An extensive discussion of this effect concludes the chapter.

The setup with the multi-mode laser was further used for short-term irradiation of experimental low-mode fibres (LMF) with differently treated and doped cores. These experiments are presented in Chapter 5. The generation and modification of defect centres were investigated time-dependently with the DUV spectral measurement setup. The results of this research are compared to experimental results and defect models from literature.

The mitigation of the surface effect based on the results from Chapter 4 and 5 is discussed in Chapter 6. Several parameters can be adjusted to improve the long-term stability of the fibre-coupled laser systems. The implemented system at 405 nm is presented, which offers high stability for long-term use. The characteristic performance values are given and set in comparison to the systems available before this work started.

Finally, Chapter 7 concludes the realised work and gives an outlook on how to continue and improve on this work from an applications point of view.

1.5 Summary

The background and context of this work was presented in this chapter. An overview of the issues of fibre-coupled diode laser systems in the NUV was given and the aims and objectives of this work brought forward. The structure and design of the thesis are introduced to provide an outline of the work undertaken.

2 Background of fibre-optic systems

2.1 Abstract

This chapter provides a short introduction into the light-guiding and coupling mechanisms of optical fibres. Afterwards linear and non-linear losses in a fibre are discussed. As it is important for some of the later chapters the production process of silica fibre is presented in the last section.

2.2 Light-guiding and coupling mechanisms in optical fibres

A step index fibre, depicted in Figure 2-1, with a refractive index n_{co} in the core larger than the refractive index n_{cl} in the cladding, can be fully characterised using the normalised frequency or V number [Gloge1971, Senior1992, Mitschke2005]:

$$V = k_0 \cdot a \cdot \mathrm{NA} \tag{2-1},$$

with the vacuum wavenumber $k_0 = \frac{2 \cdot \pi}{\lambda_0}$ (2-2),

and the numerical aperture $\mathrm{NA} = \sqrt{n_{co}^2 - n_{cl}^2}$ (2-3),

where a is the fibre core radius and λ_0 the vacuum wavelength.

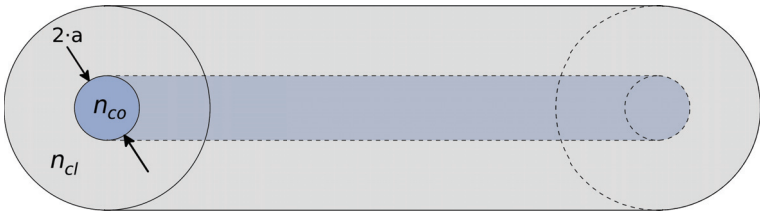

Figure 2-1: Schematic of a step-index fibre.

The V number determines the number of modes that can be excited in the step index fibre for a specific wavelength. In the range from 0 to 2.405 only the fundamental mode can propagate in the step index fibre. Thus fibres with $V \leq 2.405$ are called single-mode fibres (SMF) and V = 2.405 determines the cut-off wavelength λ_{CO} as follows:

$$\lambda_{CO} = \frac{2 \cdot \pi}{2.405} \cdot a \cdot \mathrm{NA} \tag{2-4}.$$

For V > 2.405 multiple modes can propagate in the fibres, which are then called multi-mode fibres (MMF). They can be further distinguished as few-mode fibres (FMF) and low-mode fibres (LMF). Just below the cut-off wavelength only a few modes (< 10) can propagate or due to the small fibre core the number of modes is low (< 100).

In a SMF the fundamental mode can propagate in two orthogonal polarisation directions. If linearly polarised light is launched into a SMF, then the polarisation can get partially coupled to the other polarisation mode due to stochastic imperfections along the fibre. Bending the SMF can also change the polarisation direction at the output end. To guide linearly polarised light more strongly polarisation-maintaining (PM) fibres have to be used. These fibres introduce a strong birefringence to reduce the influence of the small stochastic effects [Emslie2007]. This can happen by using an elliptical core or cladding design (form birefringence) or by introducing stress elements symmetrically around the core (stress birefringence).

A SMF does not necessarily have to be a step-index fibre. In so-called microstructured or photonic crystal fibre (PCF) the light is confined in the core by modified total internal reflection or by the photonic band gap effect [Knight1996, Kirchhof2004]. A lattice of holes is arranged in a mostly hexagonal shape around a core of solid material or of air (air core fibre). The holes either reduce the average refractive index for wavelengths in the order of the hole sizes, which leads to modified total internal reflection, or a periodic arrangement of holes confines the light according to the photonic band gap effect.

Ray theory is used to describe the excitation and propagation of light in MMF. The light is confined by total internal reflection below a critical angle θ_c. Using Snell's law the critical angle inside the MMF is defined by the following equation [Senior1992]:

$$\cos(\theta_c) = \frac{n_{cl}}{n_{co}} \tag{2-5}.$$

This equation also shows that the refractive index of the core n_{co} needs to be higher than the refractive index of the cladding n_{cl} for total internal reflection to take place. Extending this equation to the end surface of a MMF in air, the maximum acceptance angle α_a can be used to determine the numerical aperture of the fibre as follows:

$$\mathrm{NA} = \sin(\alpha_a) = \sqrt{n_{co}^2 - n_{cl}^2} \tag{2-6}.$$

The ray theory is not applicable for SMF, instead the Gaussian beam theory needs to be used and is employed for all further calculations. The electric field of a laser beam or the fundamental mode of a SMF can be simplified described as a Gaussian distribution along its radius r. The intensity of the beam or mode is the square of the electrical field.

$$E = E_0 \cdot e^{-\left(\frac{r}{w(z)}\right)^2} \tag{2-7}$$

$$I = I_0 \cdot e^{-2\cdot\left(\frac{r}{w(z)}\right)^2} \tag{2-8},$$

with $I \sim E^2$.

Here $w(z)$ is the mode-field radius along the propagation axis z at which the field amplitude drops to 1/e or the intensity drops to $1/e^2$ in radial direction. In the waist of a focussed laser beam ($z = 0$) or along a homogeneous SMF the mode-field radius is called the spot size w_0. However, instead of the spot size the mode-field diameter (MFD) is often mentioned. The spot size w_0 is constant in the SMF and approximated by [Marcuse1977]:

$$\frac{w_0}{a} = 0.65 + 1.619 \cdot V^{-1.5} + 2.879 \cdot V^{-6} \qquad (2\text{-}9).$$

For a SMF w_0 is 10 to 20 % larger than the fibre core radius a. The mode-field radius of an unguided Gaussian beam in air from a laser or at the end of a SMF changes according to:

$$w(z) = w_0 \cdot \sqrt{\left(\frac{z}{z_R}\right)^2 + 1} \qquad (2\text{-}10),$$

with $z_R = \frac{\pi \cdot w_0^2}{\lambda}$ (2-11).

The Rayleigh length z_R is the distance from the focus at which the beam radius increases by factor √2. Examples for the focus of a laser beam and a laser beam focused into a SMF are shown in Figure 2-2.

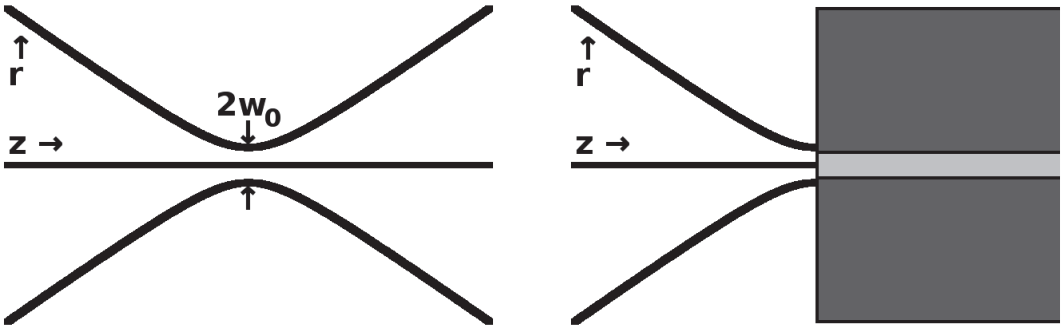

Figure 2-2: On the left, there is an example for focussing a laser beam. The part beyond the beam waist can be replaced by a SMF, as is shown on the right, to illustrate the excitation of a SMF by a laser beam.

The power coupling efficiency of two mode fields, for example from a focused laser beam into a SMF, can be calculated using an overlap integral [Brinkmeyer2002]:

$$\eta \simeq \frac{\left|\iint E_T \cdot E_R^* \partial r \partial \varphi\right|^2}{\iint |E_T|^2 \partial r \partial \varphi \cdot \iint |E_R|^2 \partial r \partial \varphi} \qquad (2\text{-}12)$$

Here E_T is the electrical field of the transmitting fibre or laser spot and E_R the electrical field of the fundamental mode in the receiving fibre. This equation was solved by Nemoto and co-workers [Nemoto1979] for loss in SMF splices and can be applied for a single-

mode laser coupling into SMF. From the simplified equations the following efficiency can be evolved:

$$\eta = \left[\frac{2\cdot s_1\cdot s_2}{s_1^2+s_2^2}\cdot\exp\left(-\frac{\Delta r^2+(k_0\cdot s_1\cdot s_2\cdot\sin\theta)^2}{2\cdot(s_1^2+s_2^2)}\right)\right]^2 \tag{2-13}$$

Here s is the spot size of each mode field, for example s_1 for transmitting fibre and s_2 for receiving fibre, Δr is the lateral misalignment, k_0 is the wavenumber and θ is the angular misalignment. It is important to mention that the parameter s used by Nemoto is defined as the mode field radius in the beam waist (or in the near field of the fibre) at which the intensity falls to 1/e. This is an old definition, but it can be adjusted easily using the following relation:

$$s = \frac{w_0}{\sqrt{2}} \tag{2-14}$$

The resulting equation for the efficiency using modern spot size definition is:

$$\eta = \left(\frac{2\cdot w_{0,1}\cdot w_{0,2}}{w_{0,1}^2+w_{0,2}^2}\right)^2\cdot\exp\left(-\frac{2\cdot\Delta r^2+\frac{1}{2}\cdot(k_0\cdot w_{0,1}\cdot w_{0,2}\cdot\sin\theta)^2}{w_{0,1}^2+w_{0,2}^2}\right) \tag{2-15}$$

The prefactor did not change compared to Formula 2-13. It determines the loss for a spot size mismatch and only depends on the spot size ratio (SSR) which did not change. This loss is also not dependent on the propagation direction.

In the exponential term the lateral and angular misalignment determine the loss. Only the loss by angular misalignment depends on the wavelength, where as the loss by spot size mismatch or lateral offset is wavelength independent. This influence is caused by the fixed relation of wavelength and spot size to the numerical aperture or far-field angle of the SMF. As given by the diffraction limit for a Gaussian-shaped beam:

$$\theta_{ff} = \frac{\lambda}{\pi\cdot w_0} \tag{2-16}$$

To simulate the losses it is best to analyse the misalignments by themselves while neglecting the others. The resulting equations for the losses are:

a) SSR mismatch ($\Delta r = 0$ and $\theta = 0$)

$$L_{SSR} = -10\cdot\log\left[\left(\frac{2\cdot w_{0,1}\cdot w_{0,2}}{w_{0,1}^2+w_{0,2}^2}\right)^2\right] = 20\cdot\log\left(\frac{w_{0,1}^2+w_{0,2}^2}{2\cdot w_{0,1}\cdot w_{0,2}}\right) \tag{2-17}$$

b) lateral misalignment ($w_{0,1} = w_{0,2} = w_0$ and $\theta = 0$)

$$L_{lat} = 10 \cdot \log\left[\exp\left(-\frac{2 \cdot \Delta r^2}{w_{0,1}^2 + w_{0,2}^2}\right)\right] \approx 4.343 \cdot \left(\frac{\Delta r}{w_0}\right)^2 \tag{2-18}$$

c) angular misalignment ($w_{0,1} = w_{0,2} = w_0$ and $\Delta r = 0$)

$$L_{angle} = 10 \cdot \log\left[\exp\left(-\frac{(k_0 \cdot w_{0,1} \cdot w_{0,2} \cdot \sin\theta)^2}{2 \cdot (w_{0,1}^2 + w_{0,2}^2)}\right)\right] \approx 4.343 \cdot \left(\frac{\pi}{\lambda} \cdot w_0 \cdot \sin\theta\right)^2 \tag{2-19}$$

The lateral offset is not a problem when aligning a focused beam to a fibre end surface, because the maximum is easily found by adjustment. But the spot size ratio is more or less fixed. In addition an angular misalignment is also possible if beam and fibre are not on the same optical axis. In Figures 2-3 and 2-4 the results of loss simulations are shown. A SSR of 1.6 gives a coupling loss of 1 dB. A coupling loss of 3 dB is reached if a laser beam with a beam waist diameter of 5 µm should be coupled into a SMF with 2.2 µm mode field diameter (MFD).

For easier coupling with a larger laser spot and reduced intensity inside the fibre, fibres known as large mode area (LMA) fibres can be used. A drawback of this concept is the increased sensitivity to angular misalignment, because the numerical aperture of the fibre is extremely reduced to keep the V number below 2.405. In Figure 2-4 it is shown that an increase from a spot size of 1.1 µm to 3.5 µm increases the loss in dB by a factor

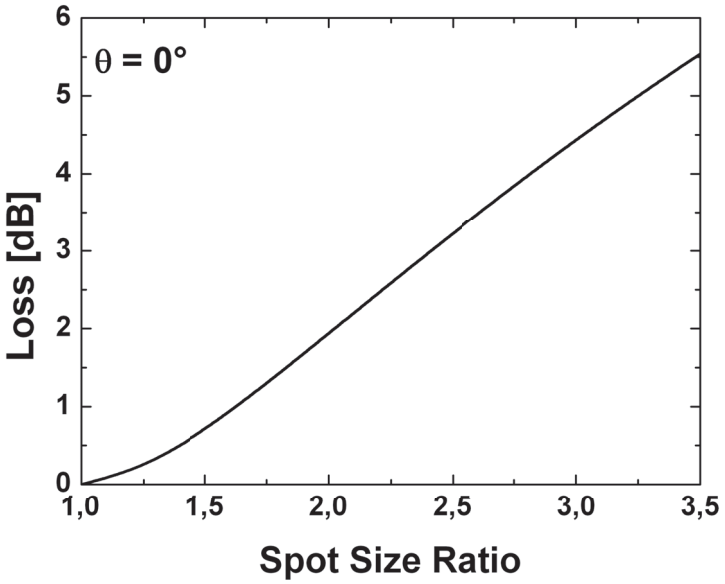

Figure 2-3: Coupling loss over SSR according to equation 2-17.

of 10 for a fixed input angle θ. This behaviour was already experimentally shown for the visible spectral range [Gambling1978].

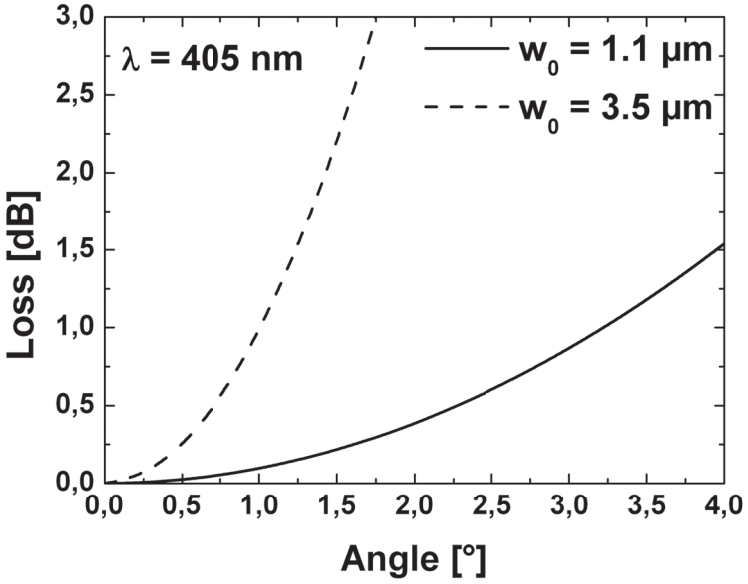

Figure 2-4: Coupling loss at 405 nm over angular misalignment for two different spot sizes according to equation 2-19.

Since there is no diffraction limited beam, the beam of a SMF or of a laser shows some difference to a Gaussian beam. This difference is described by the M² factor, which increases the diffraction limit [Sun2012]. The actual beam spot size $w_{0,s}$ in the focus can then be calculated by far-field approximation:

$$w_{0,s} = \frac{\lambda_n \cdot f}{\pi \cdot w_{0,l}} \cdot M^2 \qquad (2\text{-}20).$$

Here f is the focal length of the imaging system and $w_{0,l}$ the beam radius of the collimated laser beam at the input of the focusing lens. For calculations with Formula 2-10 the Rayleigh length z_R has to be divided by M². If the M² factor is larger than unity, the focusing possibilities are impaired. The M² factor of a SMF is 1.07 and therefore well suited for maintaining a high beam quality. In some cases, the fundamental mode of a laser has a higher M², compared to a SMF. Then, the SMF acts as a M² filter and improves the beam quality.

2.3 Linear and non-linear losses in light-guiding fibres

The spectral attenuation between 500 nm and 1600 nm of a light-guiding fibre is characterised predominantly by Rayleigh scattering:

$$\alpha_{Rayleigh} \sim \frac{1}{\lambda^4} \quad (2\text{-}21).$$

Below this range the attenuation increases significantly because of ultraviolet (UV) absorption due to electron transitions between valence and conduction band as well as energy levels in the band gap by contamination and generated defects. Above 1600 nm

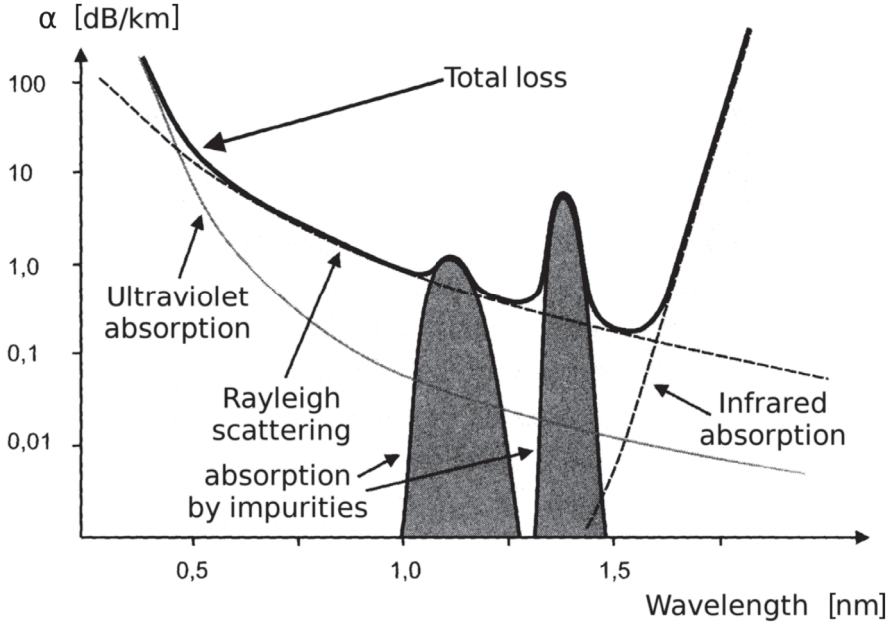

Figure 2-5: Typical spectral attenuation of a SMF with Ge doped core. According to [Mitschke2005].

near infra-red (NIR) absorption due to molecule vibrations is dominant, with a maximum at 10 µm wavelength [Heitmann2004]. Figure 2-5 gives an overview for Germanium doped SMF. Due to the Ge doping the UV absorption is already prominent at 500 nm. Additionally, hydroxyl (OH) absorption bands are shown. The harmonics of the OH resonance at 2730 nm are responsible for attenuation peaks at 1390 nm, 1240 nm and 950 nm [Agrawal2007].

For the wavelength range below 400 nm the total loss L_t in dB of a fibre is a sum of several effects given by the following equation:

$$L_t(\lambda) = 2 \cdot L_{Fresnel} + L_{fibre}(\lambda) + L_{defects}(\lambda) \quad (2\text{-}22),$$

where $L_{Fresnel}$ is the Fresnel loss, L_{fibre} is the intrinsic loss along the fibre and $L_{defects}$ are UV induced losses due to defect generation. The Fresnel loss for both end surfaces is fixed to about 0.36 dB when using silica glass:

$$L_{Fresnel} = -10 \cdot \log\left[1 - \left(\frac{n_{SiO_2} - n_{air}}{n_{SiO_2} + n_{air}}\right)^2\right] \approx 0.177 \text{ dB} \quad (2\text{-}23).$$

with $n_{SiO2} \approx 1.5$ and $n_{air} \approx 1$.

The UV induced losses only need to be taken into account if they are close to the laser wavelength, as it is known from ArF excimer lasers at 193 nm [Klein1996a]. Given by the spectral attenuation, the maximum value of these losses varies. However, they can anneal quickly without UV irradiation.

The intrinsic fibre loss is defined as:

$$L_{fibre} = 10 \cdot \log\left(\frac{I(0^+)}{I(l^-)}\right) \quad (2\text{-}24)$$

Here l is the length of the fibre and $I(0^+)$ and $I(l^-)$ are the intensities in the fibre, behind the input ($z = 0^+$) and before the output ($z = l^-$) surfaces, respectively. For a defect-free fibre the change of the intensity along the propagation axis z inside the fibre can be described by a differential equation, taking the non-linearities in attenuation into account [Taylor1988, Brimacombe1989, Karlitschek1995, Klein1996a]:

$$-\frac{dI}{dz} = \alpha(\lambda) \cdot I + \beta(\lambda) \cdot I^2 \quad (2\text{-}25)$$

The linear attenuation coefficient α(λ) in cm^{-1} is the basic attenuation in pure silica and is determined by Rayleigh scattering and the intrinsic UV absorption bands of silica. It can be transferred into $\alpha_{dB}(\lambda)$ in dB/m. The wavelength dependent behaviour is presented in [Fabian1993, Klein1996b]. The non-linear coefficient β(λ) describes the intensity dependent two-photon absorption for high intensities, for example for pulsed lasers. Typical values for both coefficients are given in [Taylor1988, Brimacombe1989, Karlitschek1995, Klein1997a]. By integrating Formula 2-25 the intrinsic loss L_{fibre} in a fibre with length l can be calculated, if the initial intensity $I(0^+)$ is known:

$$L_{fibre} = 10 \cdot \log\left(\frac{I(0^+)}{I(l^-)}\right) = 10 \cdot \log\left[\left(1 + I(0^+) \cdot \frac{\beta}{\alpha}\right) \cdot e^{+\alpha \cdot l} - I(0^+) \cdot \frac{\beta}{\alpha}\right] \quad (2\text{-}26)$$

Figure 2-6 shows loss L_{fibre} over intensity $I(0^+)$ qualitatively. Two MMF with different length of 1 m and 10 m are simulated at a wavelength of 405 nm. Values of $\alpha = 8.3 \cdot 10^{-5}$ cm^{-1} (0.04 dB/m) and $\beta = 5.7 \cdot 10^{-10}$ cm/MW were extrapolated from values at shorter wavelength and used for the simulations. At low intensities the loss increases mainly with the fibre length, because two-photon absorption can be neglected. At higher intensities non-linear losses increase significantly. The threshold for this process depends on the interaction length for non-linear losses as well. It is important to note that at a certain point within the increasing loss slope the surface damage threshold of silica is exceeded. Additionally, α and β themselves depend on the intensity in the fibre [Koehler2003, Muehlig2005]. Therefore, different values need to be applied for lower and higher intensities. However, at 405 nm no two-photon absorption should be expected below power densities of 1 GW/cm² for moderate fibre lengths.

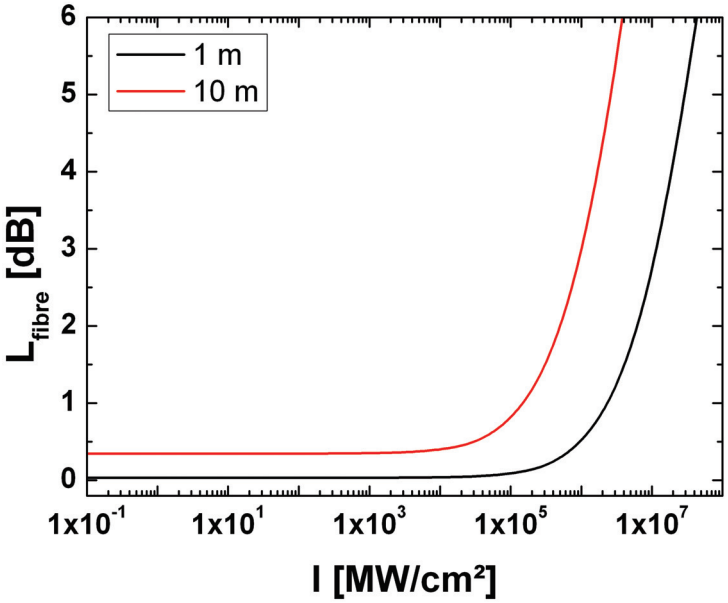

Figure 2-6: Example for non-linear fibre loss of a MMF at 405 nm with different fibre length ($\alpha = 8.3 \cdot 10^{-5}$ cm^{-1} and $\beta = 5.7 \cdot 10^{-10}$ cm/MW).

2.4 Manufacturing of preforms and light-guiding fibres

For the manufacturing of light-guiding fibre the production of high-quality preforms is most important. Generally the fibre drawing can either maintain or degrade the material properties provided by a preform and not improve them. The fibres used in this work are synthetic silica fibres, basically consisting of SiO_2 in an amorphous structure. Compounds

with Silicone are very abundant in the Earth's crust and mostly found as sand or granite. When heated liquid silica is being cooled below its softening point of ~1600 °C it can either crystallise, if crystallisation seeds are present, or form a supercooled liquid with a high viscosity. Further cooling quenches the supercooled liquid and it converts into a glass at a glass transition temperature of ~1100°C. The actual temperature at which the transition or quenching happens is called the fictive temperature, which also depends on the cooling rate [Kemeter2002].

Synthetic silica preform production uses chemical vapour deposition (CVD) processes, which are also called flame hydrolysis. For this purpose a liquid silicone halide, for example $SiCl_4$ is needed. If the liquid $SiCl_4$ is vaporised, mixed with oxygen (O_2) and heated to a reaction temperature higher than 1300°C, then SiO_2 particles will be formed with Cl_2 as chemical by-product. These spherical silica particles, also called soot particles, are amorphous and have a diameter of about 100 nm. An example of a cluster of soot particles is shown in Figure 2-7. They form a porous and opaque solid, which builds up layer by layer to yield in a soot preform [Li1985, Kemeter2002]. The CVD process uses a gas stream together with a H_2O_2 burner, leading to a soot reaction and a SiO_2 deposition. This process easily allows the doping of the deposited silica. In addition to $SiCl_4$, vaporised forms of $GeCl_4$, $POCl_3$ or $C_2F_3Cl_3$ can be added to the gas stream, for Germanium, Phosphorous or Fluorine doping, respectively. For the difference in refractive index between core and cladding of a light-guiding fibre, either the index of the core can be raised by Ge or P doping or the index of the cladding can be depressed by F doping.

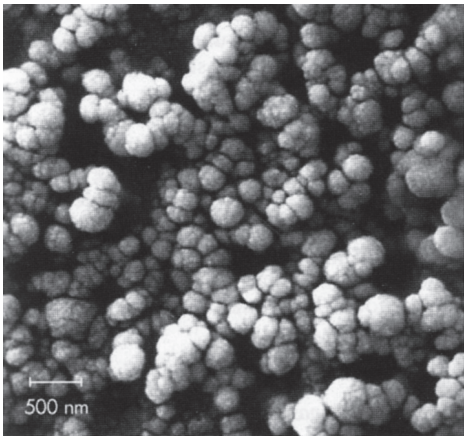

Figure 2-7: Scanning electron microscope (SEM) image of silica soot. The silica microspheres of about 100 nm diameter stick together easily and consist of smaller spheres themselves [Kemeter2002].

The CVD methods for the actual manufacturing of the preform are distinguished as the outside vapour deposition (OVD) and the inside vapour deposition (IVD). The OVD process is performed radially on a target rod, which allows for easy layer doping, or it is per-

formed axially, called the vapour-phase axial deposition (VAD) process [Li1985]. The latter allows for a continuously grown preform, but needs very precise control of the burner flame for an exact doping procedure. When the soot preform is received it can be dried in a Cl_2 and He atmosphere at 1000°C. Afterwards it needs to be consolidated in a He atmosphere at ~1400°C in a furnace, which results in a perfectly transparent glass blank. The main IVD process is called modified chemical vapour deposition (MCVD). The gases for the hydrolysis are being streamed through a silica tube rotating on a lathe. The glass tube is then heated along its axis by a moving H_2O_2 burner and soot is deposited as well as consolidated on the inner wall. By controlling the composition of the reaction gases a different doping of up to ten layers is possible [Kemeter2002]. Due to the direct consolidation a drying of deposited soot is not possible and a complex drying of the preform needs to be performed [Li1985]. An alternative form is the plasma-activated CVD (PCVD). Instead of a burner a microwave resonator generates a plasma inside the rotating tube and particles are directly consolidated on the inner wall. Several thousand thin layers are possible. However, for both IVD processes a final hole in the centre of the tube remains, which is closed by collapsing the rotating preform at ~2000°C. For doped cores this results in a characteristic dip of the dopant concentration in the centre due to sublimation of the doping species.

The manufacture of a polarisation-maintaining single-mode fibre using stress-birefringence depends on the desired structure. A bow-tie design is achieved by modifying the MCVD process towards an inside vapour phase oxidation (IVPO) process, which etches away opposite sides of boron doped layers [Emslie2007]. The final collapsed preform exhibits bow-tie shaped stress members. For a PANDA design (Polarisation-maintaining AND Absorption-loss-reducing) holes need to be drilled symmetrically around the core by use of ultra-sonic boring. The stress inducing elements, mostly boron doped silica rods, are then inserted into the holes [Li1985]. For all fibre types it is possible to reduce the amount of deposited material and achieve a desired core-cladding ratio by jacketing the preform. This means that the preform is put into a silica tube of appropriate diameter and then drawn into fibre. The production of preforms for and the fibre drawing of photonic crystal fibre is different from that for all-silica fibre and not discussed in detail here. Nevertheless, plenty of information can be found in literature [Knight1996, Birks1997, Knight1998, Cregan1999, Kirchhof2004].

Finally, the preform is stretched or drawn into a fibre on a drawing tower as depicted in Figure 2-8. The preform is inserted and further on fed into a furnace with a temperature of about 2000°C. A drop of molten glass falls from the preform and draws the fibre behind. The drop is used to feed the fibre through the setup and then cut off. The fibre is pulled with a capstan and spooled on a drum. The temperature of the furnace is con-

trolled in a range where neither defects are induced by too high temperature nor the viscose material is strained. The drawing and the feeding velocity are appropriately controlled to maintain the quantity of fed and drawn material. The diameter of the fibre is measured at several steps inside the setup to control the drawing velocity and thereby the desired diameter. The fibre is coated with a polymer for mechanical protection. This applied coating can be for example an acrylate or a polyimide, while the former is cured by UV light, the latter is thermally cured [Polymicro2011]. A proof test at the end of the line assures the mechanical strength of the drawn fibre. A slow cooling of the fibre is obtained by using towers as high as 10 m and enclosing the fibre in certain sections with metal tubing, which is flushed with inert gases [Kemeter2002].

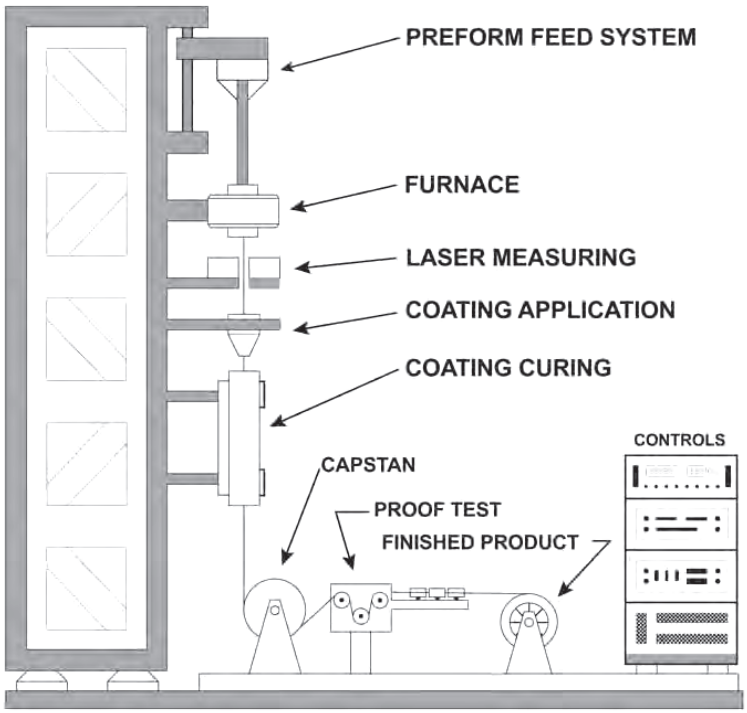

Figure 2-8: Schematic of a drawing tower [Polymicro2011].

2.5 Summary

After the introduction of the light-guiding and coupling characteristics of optical fibres, their linear and non-linear losses were addressed. The importance and the extent of these effects at 405 nm were discussed. The presentation of different preform production methods showed the possibilities for fibre manufacturers to influence and improve their products.

3 Interaction of laser light and silica fibres

3.1 Abstract

Generally the impact of long-wavelength visible (VIS) or near infrared (NIR) light on the properties of silica materials is only seen for short-pulsed high-peak-power laser systems. The InGaN diode at 405 nm (3 eV), introduced as the main light source for the damage measurements on silica fibres in this chapter, offers a comparably low power and continuous wave (CW) operation. The interaction of deep ultraviolet (DUV) broadband and laser light sources on silica bulk material leading to material modifications is presented. Most of these effects are also seen in silica fibres. The last section discusses surface effects seen from laser irradiation and the damage generated on the optical surfaces.

3.2 InGaN diode laser

A physical system of particles like atoms, ions or molecules described by quantum mechanics can only have distinct eigenstates and a certain energy level is ascribed to every eigenstate. The occupancy of these levels follows a Boltzmann distribution for positive temperature T [Kneubuehl1999], which is very important:

$$\frac{N_2}{N_1} \propto \exp\left(-\frac{E_2 - E_1}{k_B \cdot T}\right) \qquad (3\text{-}1),$$

with Boltzmann's constant $k_B \approx 1.38 \cdot 10^{-23}$ J/K.

In a two-level system with E_1 and E_2 ($E_2 > E_1$) in thermal equilibrium the density of particles in excited states N_2 at E_2 is lower than the density of states N_1 at E_1 ($N_1 > N_2$). According to Einstein there are three possible interaction processes of a two-level system with electromagnetic radiation: spontaneous emission, induced absorption and stimulated emission [Kneubuehl1999, Eichler2002]. In spontaneous emission the decay of an excited particle from E_2 to ground level E_1 can be correlated to the emission of a photon at wavelength λ_0:

$$E_2 - E_1 = h \cdot \nu = \frac{h \cdot c_0}{\lambda_0} \qquad (3\text{-}2),$$

with frequency ν, Planck's constant $h \approx 6.626 \cdot 10^{-34}$ J·s and speed of light c_0 in vacuum.

For the spontaneous emission the phase, direction and polarisation of the photon is stochastic, therefore it is incoherent radiation. Induced absorption describes the process when a photon with energy $h \cdot \nu = E_2 - E_1$ excites a particle from ground level E_1 into the higher level E_2. A reversal of this is the stimulated emission. When the decay of a particle is influenced by electromagnetic radiation the emitted photon with energy $h \cdot \nu$ has the

same phase, direction and polarisation as the stimulating radiation. Thus the stimulated emission as well as the induced absorption are coherent processes. Solving the rate equations of the three processes for a system in thermal equilibrium permeated by a electromagnetic field shows that absorption dominates and weakens the incident radiation [Kneubuehl1999, Eichler2002].

The conditions for an amplification of the electromagnetic radiation are found outside of the thermal equilibrium. Therefore, a population inversion is needed, which means that more particles are in the excited state E_2 than in ground state E_1 ($N_1 < N_2$). This can also be described by the Boltzmann distribution in Formula 3-1, but with negative temperature T. The population inversion is achieved by introducing a so-called pump energy from an external source. A second condition is the domination of stimulated emission over spontaneous emission. Additionally to a feedback, the selection of a narrow frequency band is needed. Both is achieved by introducing an optical resonator into the system [Kneubuehl1999, Eichler2002]. The result is light amplification by stimulated emission of radiation (laser).

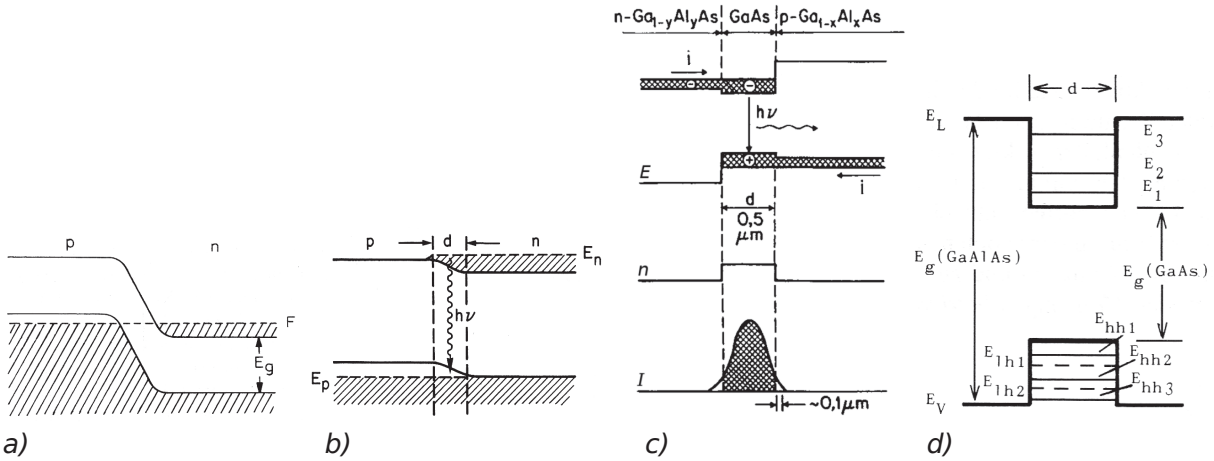

a) *b)* *c)* *d)*

Figure 3-1: p-n junction a) without voltage and b) with voltage applied. c) p-n-junction in a double heterostructure, showing energy bands, refractive index and light intensity. d) p-n junction of a quantum well (QW) laser diode with distinct energy levels in a thin active region. All according to [Kneubuehl1999].

Semiconductor lasers have already a long history of over 50 years. Their main advantages are the direct conversion of electric current into light at a high efficiency of typically 50 % and the small size in the order of 0.1 mm³. A p-n diode is the basic element, comprising heavily n-doped and p-doped semiconductors. Without an applied voltage the Fermi level F is constant within the p-n junction as depicted in Figure 3-1 a). Because of the heavy doping it extends into the valence band of the p-doped region and into the conducting band of the n-doped region. If a voltage in the range of the band gap E_g is applied ($E_g/e \approx 3.4$ V for GaN), carriers are injected into the p-n junction. Electrons from the n-

doped region and holes from the p-doped region move into it, which is shown in Figure 3-1 b). The Fermi energy E_n in the n-doped region is being shifted in respect to the Fermi energy E_p in the p-doped region. Thereby a region of population inversion with thickness d is generated. Electromagnetic radiation in this region will be amplified if the following relation is fulfilled [Kneubuehl1999]:

$$E_g < h \cdot \nu < E_n - E_p \quad (3\text{-}3).$$

This equation also shows that there are no definite energy levels for simple semiconductor lasers, but energy bands. The wavelength of the emitted and amplified light can be adjusted by choosing the correct compound (see Table 3-1). For example GaN is the material best suited for short-wavelength emission. Standard laser diodes use a planar Fabry-Perot resonator which encloses the active region on opposing parallel sides, mostly prepared by cleaving. These surfaces can be coated for additional or reduced reflection. The two other sides remain rough to suppress oscillations in that direction.

Table 3-1: Semiconductor compounds of III-V type [Kneubuehl1999, Nagahama2005].

Active compound	**Wavelength range [nm]**
GaN	365 – 483
InGaAlP	630 – 680
GaAlAs	670 – 890
InGaAs	880 – 1080
InGaAsP	1300 – 1650
GaInAsSb	~ 1900

The very first laser diodes had homojunction structures, which means that n- and p-doped regions were of the same compound. These types needed to be cooled to about 10 K because of a very high threshold current at room temperature. Better usability and lasing properties could be obtained by the development of heterostructures, especially double heterostructures which use a double sandwich of two different compounds, for example n-GaAs/n-GaAlAs/p-GaAs/p-GaAlAs as shown in Figure 3-1 c). The larger band-gap of GaAlAs forms a potential barrier around the active region, which suppresses the diffusion of carriers out of the active region. An additional improvement is provided by different refractive indices of the compounds, which confines the light in the active region perpendic-

ular to the p-n junction. A confinement of the laser modes parallel to the p-n junction was achieved either by narrowing the electrical contact to the p-doped region (gain-guided) or by burying the heterostructure inside a diode with reverse direction. The latter process results in an active region similar to a waveguide, which is why this structure is also called index-guided, and can therefore suppress higher oscillating modes. All these measures reduce the threshold current and facilitate single-mode operation of the laser diodes [Kneubuehl1999]. Using modern epitaxial methods periodic layers of differently composed compounds can be grown on substrates. These periods are so-called quantum wells and reduce the thickness *d* of the active region to below 30 nm. The electrons experience quantum effects in this thin layer and the energy bands are resolved to distinct states like in Figure 3-1 d). This reduces the threshold current as well as its dependence on temperature further. An additional result is a longer laser diode lifetime [Kneubuehl1999].

The laser light emitted from the junctions of the above described diodes is elliptical in the near field at the facet. Due to diffraction the divergence angle of the minor axis, perpendicular to the p-n junction, is larger than that of the major axis. In the far field the ellipticity is turned by 90° as a result of the difference in divergence angle. Gain-guided diodes have a higher ratio of major to minor axis than index-guided diodes, which can also be designed to have no astigmatism. But the astigmatism of gain-guided diodes can be corrected with use of appropriate cylindrical lenses, simultaneously collimating the laser beam [Mansuripur2002]. One effect determining the polarisation direction of emitted light is that the guided mode perpendicular to the junction has less overlap with the active region and does not start to lase. On the other hand, if the electromagnetic field is confined to thin layers of quantum wells the mode parallel to these layers can stimulate light more efficiently. Both effects combined result in the observation of linear polarised light parallel to the p-n junction [Mansuripur2002].

The first laser diode deployed for the violet region of the light spectrum was an InGaN multiple quantum well diode [Nakamura2000]. It allowed pulsed and continuous wave (CW) operation in the wavelength range of 390 to 440 nm. The periodic layers consisted of 2.5 nm $In_{0.2}Ga_{0.8}N$ and 5 nm $In_{0.05}Ga_{0.95}N$ sandwiched between p- and n-doped GaN layers (see Figure 3-2). The lateral mode formation is constraint by gain-guidance through a 2 µm wide metallic p-electrode and the 600 µm long resonator is coated on one side for improved reflectance. A stable transverse fundamental mode was observed in the active layer. The earliest InGaN laser diodes had single-mode output powers of 40 mW at 405 nm, but 300 mW single-mode are commercially available now and over 1 W in multimode operation are achieved at this wavelength [Nagahama2003, Skierbiszewski2005].

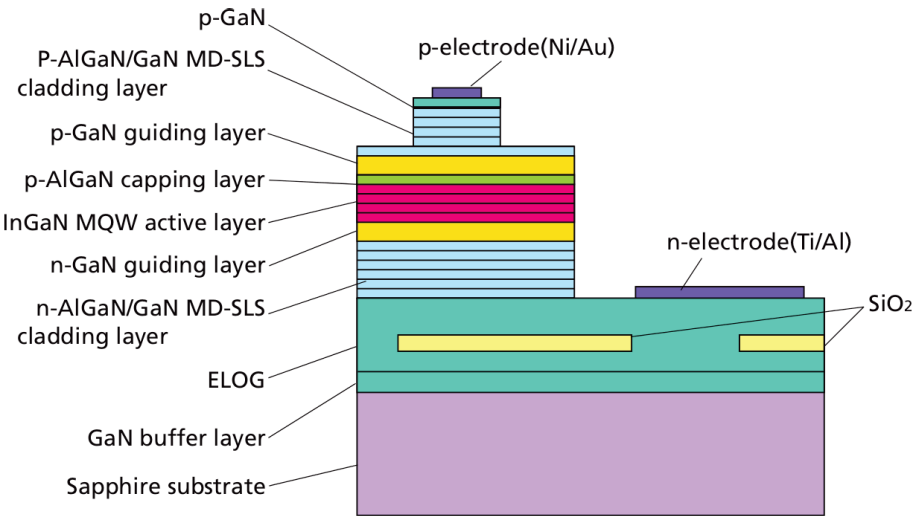

Figure 3-2: Cross sectional structure of GaN laser diode with gain-guidance through striped p-electrode and multiple quantum wells [Nakamura2000].
MQW: multiple quantum wells, ELOG: epitaxially laterally overgrown GaN ,
MD-SLS: modulation-doped strained-layer superlattices .

3.3 Bulk effects of irradiation

3.3.1 Defect-centre formation and transformation

Most fibre-optic systems available for the UV region use multi-mode fibres (MMF) comprising a core of pure synthetic silica and a fluorine-doped cladding. These systems typically use broadband light sources, for example deuterium lamps, or high-power lasers, for example excimer lasers (193 nm, 248 nm, 308 nm) or third and fourth harmonic of Nd:YAG lasers (355 nm, 266 nm). For DUV (170 – 280 nm) applications with these light sources, the existence and transformation of different UV defect centres have been studied in detail [Friebele1976, Friebele1979, Griscom1985, Khalilov1994]. The most prominent defect centres in silica fibres are related to an oxygen vacancy and are shown in Figure 3-3 [Skuja1998]. They can be distinguished as the oxygen deficiency centre ODC(I) at 7.6 eV (163 nm), the E'_{γ} centre at 5.8 eV (215 nm, see Figure 3-4 b)), the E'_{β} centre at 5.7 eV (229 nm), and the oxygen deficiency centre ODC(II) at 4.9-5.2 eV (243 – 254 nm, see Figure 3-4 c)). The E'_{β} centre is an E' centre with a hole/proton trapped in the vacancy. Other defects are oxygen excess related, such as the non-bridging oxygen hole centre (NBOHC) or peroxy radical (POR), both at 4.8 eV (260 nm) and the peroxy linkage (POL) at 3.8 eV (330 nm). Additionally bound hydroxyl groups (-OH), interstitial oxygen (O_2) or ozone (O_3), and interstitial or bound chlorine (Cl_2, -Cl) can exist in the material or occur during irradiation. Especially interstitial chlorine (Cl_2) has a large absorption band at 3.8 eV (330 nm).

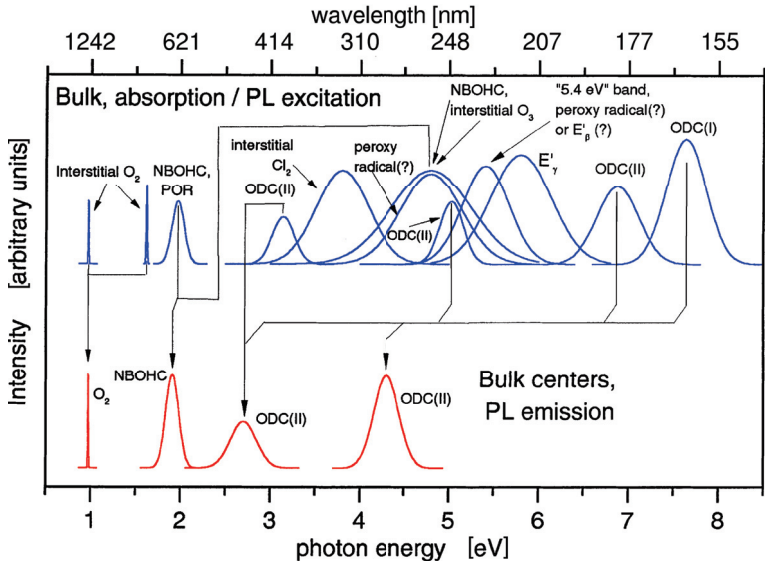

Figure 3-3: Spectral overview of known defect centres and their photo-luminescent emission bands [Skuja1998]. Centres marked with (?) are controversially discussed in literature.

The exact nature of some defect centres is still controversially discussed in literature. Those centres are marked with a question mark in Figure 3-3. The 250 nm band was assigned to the ODC(II) and the POR, but the POR is not confirmed, yet. Similarly the 330 nm band in pure silica is assigned to the Cl_2 band and the POL. Due to the improved modern fibre preform production process the peroxy defects are seen rarely and can be excluded for this work. The nature of the ODC(II) is also not definite. On one hand it is explained as an unrelaxed silicone dangling bond, on the other hand as a two-fold coordinated silicone atom [Skuja1998]. The oxygen deficient centres also have several absorption bands, mainly for the electronic singlet or triplet excitation of the defect. Both are important and included in the overview in Table 3-2.

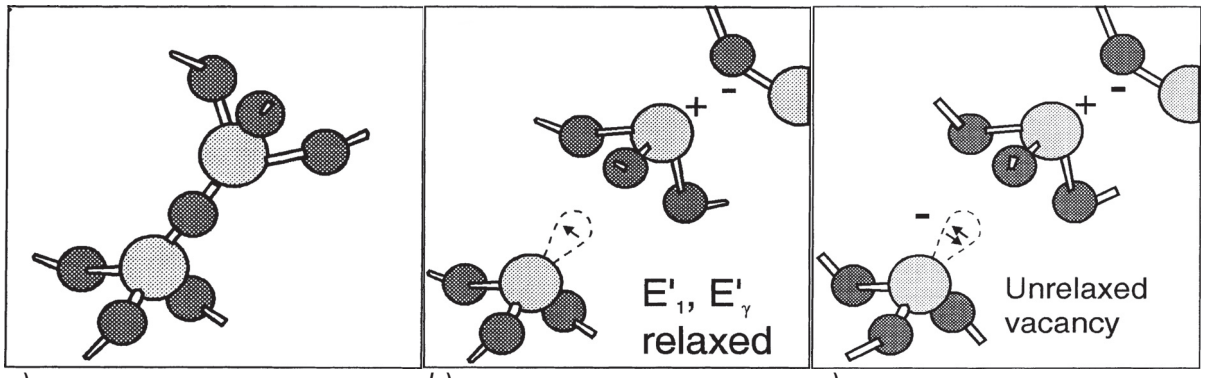

a) b) c)

Figure 3-4: a) Extract from a perfect SiO_2 network. b) Current model for E'$_\gamma$ centre with an unpaired electron on a single silicone atom. c) Unrelaxed oxygen deficiency suggested as one model for ODC(II). The dark spheres represent oxygen atoms and the light spheres silicone atoms. The arrows represent electrons with a corresponding spin. According to [Skuja1998].

Table 3-2: Characteristics of the defect centres used for explanations in this work. According to [Skuja1998]. The "≡" represents the bond to three oxygen atoms.

Defect name	Structural model	Peak position [nm]	FWHM [nm]
ODC(I)	≡Si-Si≡	163	10.7
E'$_\gamma$	≡Si• (…Si≡)	215	29.5
E'$_\beta$	≡Si• (…Si≡)	229	29.5
ODC(II) ($S_0 \rightarrow S_1$) ODC(II) ($S_0 \rightarrow T_1$)	≡Si…Si≡, -O-Ṣi-O-	243 – 254 394	14.9 42.5
NBOHC	≡Si-O•	260	56.6
POR	≡Si-O-O•	260	43.3
Interstitial Cl_2, Peroxy linkage	Cl-Cl ≡Si-O-O-Si≡	330	60
GeODC ($S_0 \rightarrow S_1$) GeODC ($S_0 \rightarrow T_1$)	≡Ge…Ge≡, -O-Ġẹ-O-	230 – 243 336	20 36.3
Ge(I)	≡Ge• (…Si≡)	280	114

The production of the preform and the fibre drawing process have the largest influence on the presence and generation of defect centres in silica fibres. The atmosphere during

the production and collapsing of a preform determine whether oxygen deficiency or oxygen excess defects are formed. A high tension during fibre drawing and uncontrolled rapid cooling of the fibre can induce strained Si-O or Si-Si bonds or lead to the rupture of those, which directly generates NBOHC and E'_γ centres, respectively [Friebele1976]. If the strained bonds, also called precursors, did not rupture during the drawing process, they can be broken by excitation through UV irradiation and in turn induce NBOHC and E'_γ centres. A production in a wet environment or a high-temperature treatment of the preform with H_2 can generate further precursors in the form of hydroxyl groups (Si-O-H) or hydrogen atoms bound to silicone (Si-H). If chlorine was not carefully removed after preform production, something similar can happen. Chlorine atoms are bound to silicone (Si-Cl) [Kirchhof1998]. When the precursors are then exposed to UV light the bonds to hydrogen and chlorine are broken and molecular hydrogen and chlorine can form. In the latter case this leads to the generation of the Cl_2 band at 330 nm. If high concentrations of chlorine or hydroxyl are bound in the silica network, then the spectral attenuation below 200 nm is increased as well [Klein1996b]. The reactions by single photon absorption are as follows:

$$\text{Si-O-H} + h\cdot\nu \rightarrow \text{NBOHC} + \text{H} \tag{3-4}$$

$$\text{Si-H} + h\cdot\nu \rightarrow \text{E'} + \text{H} \tag{3-5}$$

$$\text{Si-Cl} + h\cdot\nu \rightarrow \text{E'} + \text{Cl} \tag{3-6}$$

The influence of broadband UV light on the transmission properties of silica fibres was mainly investigated with deuterium lamps. The generation of the defect centres is commonly called solarisation and is driven by single photon absorption of photons with a high energy of more than 5.5 eV (225 nm). Mainly NBOHC and E'_γ centres are generated in high-OH fibres, while in low-OH fibres the ODC(II) can be generated additionally. The generation of NBOHC and E'_γ centres can be prevented by high-pressure low-temperature H_2 loading of the fibre. The generated defects will be passivated directly by the hydrogen and not seen as an additional spectral loss. However, this is only useful for large diameter fibres with outer silica diameter greater than 400 µm, because of the quick diffusion of H_2 out of the silica material. The reduction of the additional loss due to the NBOHC was achieved by a modification of the fibre production process. The generation of the E'_γ centre was dramatically reduced by treating the raw material and the fibre preform [Vydra1999]. But the generation of the absorption bands cannot yet be fully prevented [Klein1997b, Klein2001, Khalilov2006].

For high-power excimer laser light delivery the generation and transformation of defect centres during operation is a limitation. The absorption bands of E'_γ centres and

ODC(II) are strongly influenced by the ArF and KrF wavelengths at 193 nm and 248 nm, respectively, and subsequently attenuate the laser light [Klein1996a]. When the existence of the two different kinds of oxygen deficiency centres (ODC(I) and ODCII)) was discovered, it was also found that an ODC(II) can be photobleached to an E'_γ centre by excimer laser irradiation [Imai1988, Imai1991].

The experimental observations can be expressed in the following set of equations, where *(SiO₂)** stands for an exciton, *P* for a strained precursor site and *Ev* for an ionising event of $x \cdot h\nu$ with *x* photons participating [Muehlig2005]:

$$(SiO_2) + Ev \rightarrow (SiO_2)^* \tag{3-7}$$

$$P + (SiO_2)^* \rightarrow E' \tag{3-8}$$

$$P + (SiO_2)^* \rightarrow NBOHC \tag{3-9}$$

$$Si\text{-}H + (SiO_2)^* \rightarrow E' + H \tag{3-10}$$

$$Si\text{-}O\text{-}H + (SiO_2)^* \rightarrow NBOHC + H \tag{3-11}$$

$$Si\text{-}Cl + (SiO_2)^* \rightarrow E' + Cl \tag{3-12}$$

$$ODC(II) + Ev \rightarrow E' \tag{3-13}$$

Photolysed states of Si-H can readily recombine thermally if the hydrogen atom stays in close proximity to the E'_γ centre:

$$Si\text{-}H + Ev \rightarrow E' + H \tag{3-14}$$

$$E' + H \rightarrow Si\text{-}H \tag{3-15}$$

3.3.2 Change of silica density

A change of the density of silica upon irradiation was found as early as 1968 [Primak1968]. Those early experiments were performed with neutron, ion, electron, x-ray or gamma-ray radiation and only the increase of the material density (compaction) was observed. The photon energy of these radiation sources is in the range of keV and MeV. In the 1990s several studies using pulsed excimer lasers of type KrF (248 nm, 5 eV) and ArF (193 nm, 6.4 eV) also found the compaction of silica when irradiated with high-fluence nano-second pulses in the mJ/cm² range [Allan1999, Piao2000, Ikuta2004]. In all studies, disregarding the radiation source, a power-law behaviour of compaction over dose $D = I^2t$ was found:

$$\frac{d\rho}{\rho} = a \cdot (I^2 \cdot t)^b \tag{3-16}$$

Here dρ/ρ is the change in density and parameter *a* and exponent *b* are adjustable values. For fused silica values in the range of $b = 0.5$ to 0.6 and *a* in the order of unity showed best results for fits to experimental data. These parameters do not have any physical correspondence and should be treated with care, especially when comparing them [Allan1999]. The power law is just a way to represent the behaviour of experimentally measured compaction curves.

The amount of density increase that is actually produced by excimer lasers is in the order of 10^{-6}. This change is mostly measured by investigating the change in refractive index with an interferometer (wavefront distortion) or by stress measurements (birefringence). Both techniques can be performed using the pristine sample as a reference to see the actual change and not the absolute values [Moll2002, Kuehn2003, Moll2004]. These measurements are normally not done with the damaging excimer laser in the DUV, but with a HeNe laser at 632.8 nm.

It was postulated that the introduction of ODCs by laser radiation leads directly to a density increase [Sulimov2002]. But this was shown to not be the case for laser-induced ODC, only for thermally induced ODC(I) [Ikuta2004]. The origin of the compaction is widely accepted to be a long-range restructuring of the Si-O-Si network upon relaxation due to defect generation [Piao2000], which means a rearrangement of SiO_4 tetrahedra. Since the tetrahedra sustain their shape, only the Si-O-Si bridging bond angle can change

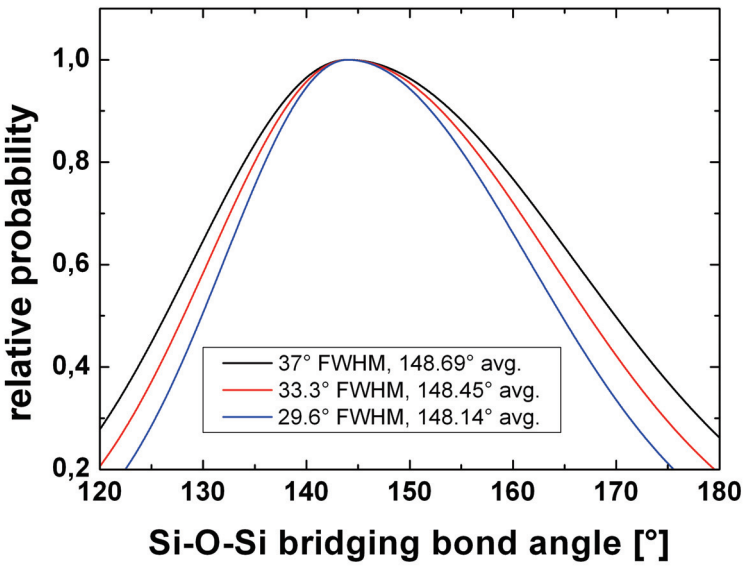

Figure 3-5: Approximation of non-symmetric probability distribution of Si-O-Si bridging bond angle in [Piao2000] using bi-Gaussian curves. For a narrower FWHM the average angle is reduced.

to a larger extent [Susman1991]. The distribution of this Si-O-Si bridging bond angle is

not symmetric (see Figure 3-5), with angles smaller than the most probable angle of $\beta = 144°$ being less likely than larger angles [Mozzi1969]. The FWHM of the distribution depends on the fictive temperature T_f at which the silica glass was quenched during the production. A broader distribution corresponds to a higher fictive temperature, indicating excess energy stored in the network as well. A relaxation of the silica network happens when atomic bonds are broken. This is explained by Piao and co-workers very graphically as a three-dimensional strained-spring network: “If one spring connection is broken, the system acquires additional freedom with the result that the whole network relaxes to a lower energy state” [Piao2000]. This in turn leads to a narrowing of the Si-O-Si bridging bond angle distribution. Since the distribution is non-symmetric a lower average angle is achieved. This is shown qualitatively and quantitatively in Figure 3-5 and the average angle is given for different angle distributions. A smaller distance between silicone atoms and an increased density is the result of the reduced average angle.

In long-term experiments with low-fluence excimer lasers in the range of µJ/cm² a rarefaction effect was observed [Peski2000]. The rarefaction, also called expansion, is a decrease in density. It occurs together with compaction and the type of silica and the irradiation conditions determine which of the two effectively changes the density [Smith2001, Moll2002, Algots2003, Kuehn2003, Allan2004]. It was also proposed in all the studies that the rarefaction depends linearly on the dose and that the pulse length has no influence:

$$\frac{d\rho}{\rho} = a \cdot I^b \cdot t \tag{3-17}$$

The parameters *a* and *b* are again fitting parameters. In the case of rarefaction the parameter *a* has to be negative in contrast to positive *a* for the case of compaction. The main influence for a decrease of the silica density was found to be the presence of H_2 [Smith2001] or a high OH content above 700 ppm [Kuehn2003]. It was proposed, in accordance with a gamma ray experiment [Shelby1979], that the incorporation of hydrogen into the silica network as Si-H and Si-O-H bonds leads to the rarefaction. Additionally to the decrease in density the generation of these bonds changes the chemical structure and increases the refractive index of the silica. This is known as the photorefractive effect and is the base for the production of fibre Bragg gratings (FBG). A kinetic model developed by Allan and co-workers predicts the change in optical path length based on a well-known set of equations for the generation of defect centres and bonded hydrogen, and photolytic processes (see end of Section 3.3.1) [Allan2004]. In this model the optical path length first increases with the number of pulses, but after a certain amount of pulses the path length decreases towards a saturated level, which is according to other experiments as well [Kuehn2003]. A similar behaviour was seen for the laser fluence. While the

rarefaction takes effect at lower laser fluences, it is masked by the compaction at higher fluences.

3.4 Surface effects of laser irradiation

3.4.1 Surface damage

Surface effects in silica optics due to high intensity laser light are well known using short-pulsed and high-power laser systems. Surfaces are quickly destroyed mechanically if not properly prepared and thoroughly cleaned. Linear and non-linear absorption of high intensity laser light in the bulk of the optics causes material modifications, like voids, cracks and UV defects. When MMF are used for high-power excimer laser light delivery [Dressel1991, Koehler2003], the surface damage threshold of synthetic silica is the primary limit. In the NUV severe optical damages were observed at power densities above 1 GW/cm² for pulsed 308 nm excimer lasers with 20 ns pulse width [Pini1987, Klein1996a]. A mechanically damaged fibre end is shown in Figure 3-6 after irradiation with a pulsed 355 nm third-harmonic generation (THG) Nd:YAG laser. A pulse energy of 6 µJ and a pulse width of 1.8 ns resulted in about 5 GW/cm² peak power density [Hillrichs2011].

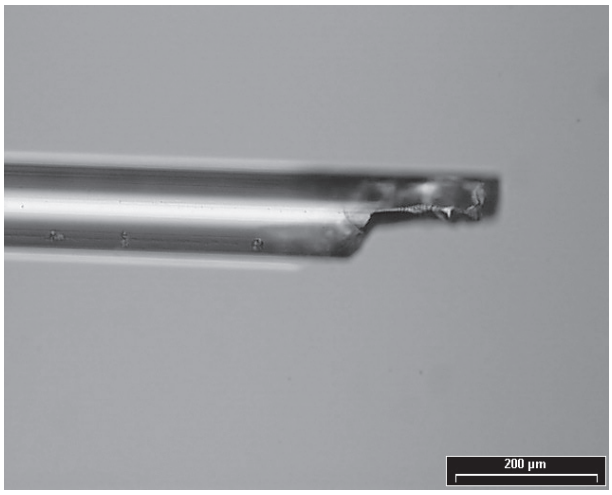

Figure 3-6: Fibre launching end damaged by a pulsed 355 nm THG Nd:YAG with 6 µJ pulse energy and 5 GW/cm² peak power density [Hillrichs2011].

3.4.2 Surface alteration

The first observation of a periodic surface structure was made in 1965 using a Ruby laser [Birnbaum1965]. In the following decades this phenomenon was observed more often with different kinds of lasers ranging from pulsed CO_2 lasers to femto-second lasers in the

visible region. Due to its structure of crests and valleys it was called ripples and later laser induced periodic surface structure (LIPSS). In the beginning different models were applied, including various interference models and models based on mechanical precursors like scratches [Soileau1984]. If the melting temperatures of a sufficiently conductive material, like metal or a semiconductor, was reached, a LIPSS might be formed by surface plasmon polariton interference [Keilmann1982]. A model of interference of the incident light wave with a surface-scattered wave was extended to a theory of radiation remnants. Until the 1990s, this so-called Sipe or efficacy factor theory was successfully used to describe an inhomogeneous energy deposition below a rough surface selvedge region [Driel1982, Sipe1983]. An electromagnetic wave is scattered in this region at statistical fluctuations smaller than the incident wavelength (Rayleigh scattering). The nature of the fluctuations can be miscellaneous, but surface roughness, electron density and refractive index are possible candidates. LIPSS were also created and seen at intensities well below the supposed damage threshold or melting point [Fauchet1983, Singh2003]. Some parts of the structures, like break-ups and bifurcations, are very unlikely only the result of an inhomogeneous energy input due to interference effects [Preston1989]. Nowadays it is still controversial, if the formation of these ripples is the result of an interference effect [Bonse2005] or of non-linear self-organisation from a strong material instability [Reif2010].

When irregular LIPSS were found in the ablation craters of femto-second laser irradiated semi-conductors and wide band-gap dielectrics in high vacuum, it was proposed that these LIPSS are formed by self-organisation [Henyk1999]. A visual comparison of an holographic interference pattern and an irregular LIPSS is given in Figure 3-7. The periodicity of the LIPSS, the spacing of valleys or crests, was always found to be in the order of the laser wavelength or smaller, but suggested to not be correlated to the wavelength and insensitive to the incident angle of the laser light [Keilmann1982, Varlamova2006, Varlamova2007]. Instead it was observed that the periodicity depends solely on the depth of the perturbed volume [Reif2004]. This means that it mainly depends on the local light intensity, which varies with the Gaussian beam profile. Different periodicities can be observed in the centre and at the edge of ablation spots, less intensity forming less developed and closer spaced ripples [Varlamova2006, Reif2010].

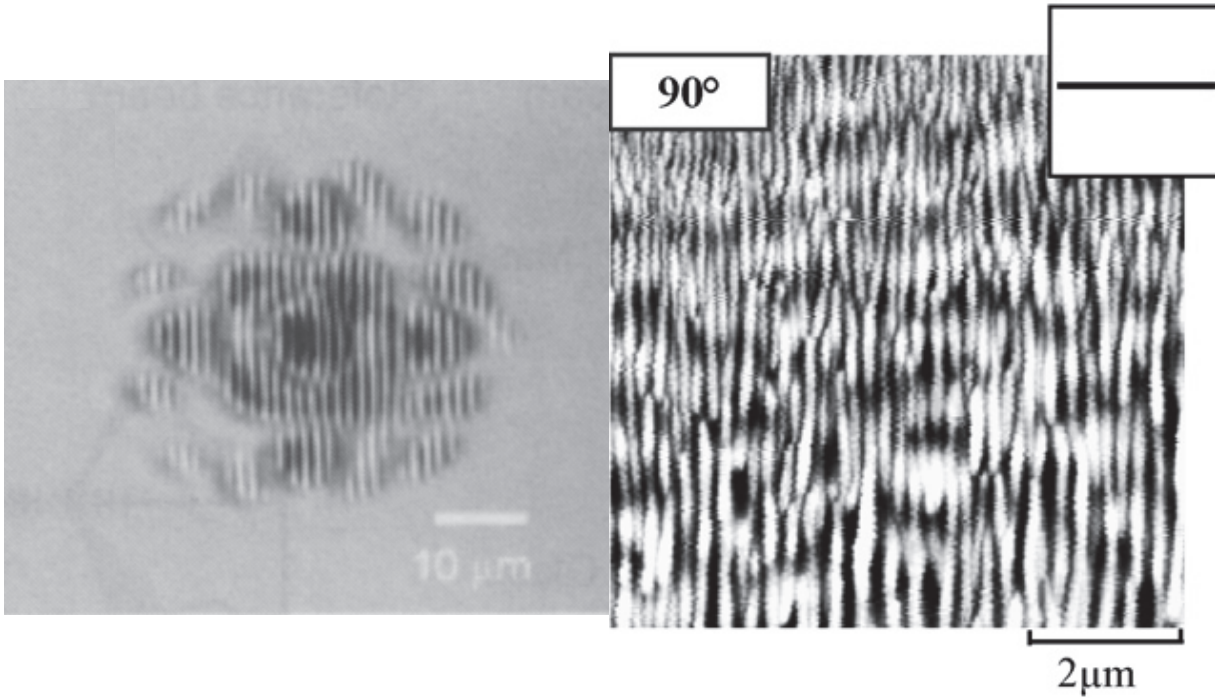

a) *b)*

Figure 3-7: a) Holographic interference written into fused silica [Watanabe2006]. b) Scanning electron microscope (SEM) image of ripples on CaF_2 surface [Varlamova2007].

In all pulsed laser experiments on semiconductors and transparent insulators the orientation of the ripples strongly correlated with polarisation direction [Keilmann1982, Varlamova2006]. For example on a CaF_2 surface a sub-wavelength periodicity of the ripples was found perpendicular and an about-wavelength periodicity parallel to the incident laser polarisation. Both periodicities can coexist and are then superimposed [Henyk1999, Reif2004, Varlamova2007]. The length of the ripples depends on the polarisation as well. A linear polarisation forms long ripples in contrast to a circular polarisation which forms very short ripples in the form of cones [Reif2006, Varlamova2007].

In one study focused ion beam (FIB) prepared lamellae of a silicone wafer damaged by a femto-second laser were examined in a transmission electron microscope (TEM). While the crests in the centre of the ablation spot were formed of crystalline silicone, amorphous silicone was found in the corresponding valleys. But outside the main damaged area, where the irradiation dose was smaller, a mixture of crystalline and amorphous silicone was found. This is shown in Figure 3-8 from [Reif2010].

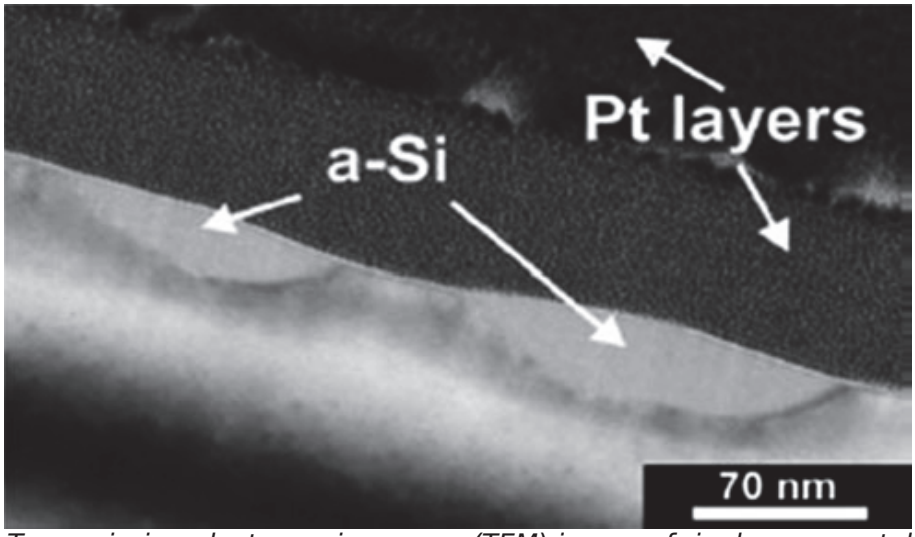

Figure 3-8: Transmission electron microscope (TEM) image of ripples on crystalline silicone surface outside of an ablation spot [Reif2010]. (a-Si: amorphous silicone, Pt: sputter specimen platinum)

The main effect driving the destabilisation of the molecular lattice on the surface of wide band-gap insulators is ionisation by multi-photon absorption. A strong surface ionisation in femto-second laser ablation leads to coulomb explosion and further to phase explosion [Henyk1999, Varlamova2006]. A thin unstable surface layer depleted of electrons is formed. The authors describe the thickness as in the range of the electron escape depth. Its thickness depends on local intensity, surface roughness and electronic defects [Reif1989, Varlamova2006]. For insulators and semiconductors the destabilisation of the lattice can happen within less than a pico-second [Varlamova2006]. This rapid, non-equilibrium destabilisation promotes the self-organisation of the thin surface layer [Reif2004].

Self-organisation is known in sputtering and thin-film growing processes for some time [Reif2006, Peled2000]. Simulations of such a sputtering process, like in Figure 3-9, show a large resemblance to the LIPSS generated by femto-second lasers. In an unstable surface layer the self-organisation is a competition between surface roughening, due to desorption, and surface smoothening, by atomic self diffusion [Henyk1999, Varlamova2006, Varlamova2007]. First, long ordered chains of nanoparticles are formed with an additional coarser overstructure, then ripples develop from coalescing smaller nanoparticles. A self-organised LIPSS is created and curvatures, breaks and bifurcations are formed in this process [Reif2004, Varlamova2006]. In addition a positive feedback was observed for multiple pulses below the materials damage threshold. So, incident pulses do not act individually and independently, but add to the effect of the previous pulses [Keilmann1982, Fauchet1983, Reif2004, Varlamova2006, Reif2010].

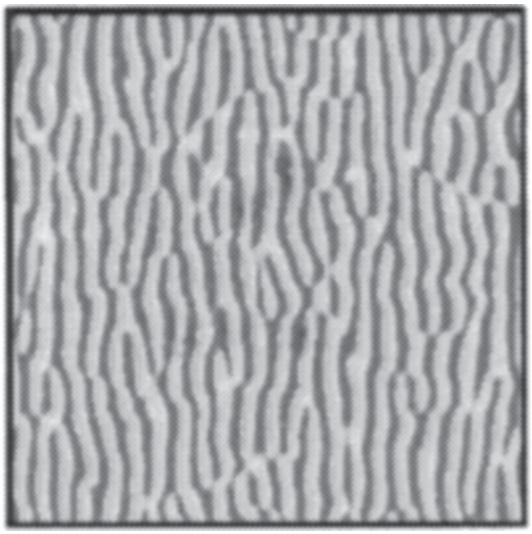

Figure 3-9: Simulation of self-organised pattern formation at an unstable surface [Reif2004].

The Sipe theory was successfully combined with the Drude model by Bonse and co-workers to explain most of the LIPSS effects seen after femto-second laser irradiation of different materials outside of a phenomenological framework [Hoehm2012]. The Drude model describes the transient changes of the optical properties of materials in dependence on the free-electron density in the conduction band. Since the surface-scattering in the Sipe theory largely depends on the optical properties of the surface, this combination improved the correlation of theoretical simulation and experimental results. Bonse et. al. distinguish between classic low spatial frequency LIPSS (LSFL) with a periodicity in the order of the laser wavelength ($\Lambda \approx \lambda_0$) and high spatial frequency LIPSS (HSFL) with a periodicity significantly smaller than the laser wavelength ($\Lambda < \lambda_0/2$). The periodicity and orientation of LSFL further depend on the irradiated material. On metals and semiconductors the ripples are oriented perpendicular to the polarisation of the incident beam and have $\Lambda \approx \lambda_0$. Both is attributed to the additional influence of surface plasmon polariton excitation [Dufft2009, Hoehm2012]. For wide band-gap dielectrics on the other hand the orientation of the ripples was mostly found to be parallel to the laser polarisation and the periodicity reduced by the refractive index of the irradiated material to $\Lambda \approx \lambda_0/n$ [Rohloff2011]. HSFL are mainly observed after femto-second laser irradiation in the region of intensity close to the ablation threshold.

Only few studies focused on the generation of LIPSS on amorphous silica in air environment or vacuum. Those studies were performed with Ti:sapphire femto-second lasers in the NIR (700 – 800 nm) on bulk material at normal laser incidence [Wagner2006, Rohloff2011, Hoehm2012]. Similar to Figure 3-10, the LSFL was found parallel to the orientation of the linearly polarised laser beam with periodicities in the range of 500 to

800 nm and HSFL were found perpendicular to the laser polarisation with periodicities in the range of 170 to 400 nm. Hoehm and co-workers were especially trying to explain the parallel orientation of the LSFL, and suggested that the formation of defect centres is one reason of the transition from perpendicular HSFL to parallel LSFL for an increased number of pulses [Hoehm2012]. A higher absorption due to the defect centres should result in a higher number of excited electrons in the conduction band. The combination of Sipe and Drude models predicts the formation and orientation of LSFL correctly and the inhomogeneous energy deposition is dictated by the optical properties in non- or weakly excited silica. The model also showed that for a low degree of excitation the periodicities are in order of $\Lambda \approx \lambda_0/n$ (dielectric behaviour) and for higher degrees of excitation increase towards $\Lambda \approx \lambda_0$ (metal-like behaviour).

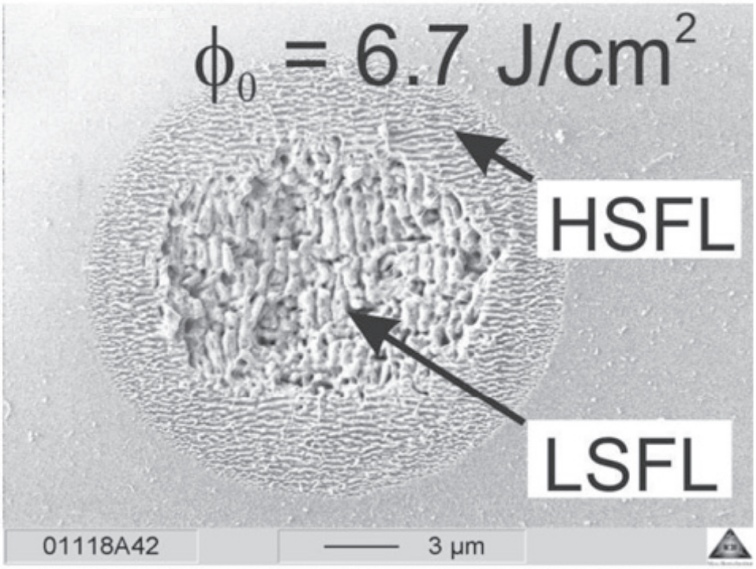

Figure 3-10: Scanning electron microscope (SEM) image of femto-second ablation spot, irradiated with Ti:sapphire laser (700 – 800 nm wavelength). The laser beam had a spot radius of ~18 µm and a peak energy density of 6.7 J/cm² in air environment under normal incidence [Hoehm2012].

3.5 Summary

A brief introduction to laser light generation was given and the technology of the laser diodes used in this work was presented. Furthermore, the interaction of laser light with material, especially silica, was discussed. Different defects due to irradiation in the bulk or on the surface of silica can be observed. The key-roles for the work presented in the coming chapters play the generation of defect centres in the bulk, the decrease of the density of silica and the formation of laser-induced periodic surface structures.

4 Surface effects by 405 nm laser irradiation of silica fibres

4.1 Abstract

In this chapter damage brought about on different silica-based fibre types with different violet laser light sources and the corresponding results are presented and discussed. After the consequences of the damage were recorded spectrally and at the laser wavelength, the surface damage was investigated by different microscopic methods. The damage of the launching fibre end surface was reconstructed with simulations using the finite-difference time-domain method. These show the influences of the structure on the light-guiding properties of the fibre. Finally, the effects found in the investigations are compared to results of short-pulsed laser ablation experiments on wide band-gap insulators.

4.2 Experimental setups

4.2.1 Previous work and experimental approach

Most fibre-optic systems available for the UV region use multi-mode fibres (MMF). The fibre comprises a core of high-OH (> 800 ppm) pure synthetic silica and a Fluorine doped cladding. These systems typically use broadband light sources, e.g. deuterium lamps, or high-power lasers, for example excimer lasers (193 nm, 248 nm, 308 nm) or third and fourth harmonic of Nd:YAG lasers (355 nm, 266 nm). For deep ultraviolet (DUV) applications (170 – 280 nm) with these light sources, the existence and transformation of different UV defect centres have been studied in detail [Griscom1985, Friebele1979, Friebele1976, Khalilov1994]. The most prominent defect centres in silica fibres are related to an oxygen vacancy [Skuja1998]. They can be distinguished as the oxygen deficiency centre ODC(I) at 7.6 eV (163 nm), the E'_γ centre at 5.8 eV (214 nm), and the oxygen deficiency centre ODC(II) at 4.9-5.2 eV (240 – 255 nm). Other defects are oxygen excess related, such as the non-bridging oxygen hole centre (NBOHC) at 4.67 eV (266 nm), or due to interstitial occurences of elements like Chlorine (Cl_2) at 3.76 eV (330 nm). Improvements in the manufacturing process have lead to UV fibres with significantly lower solarisation, that is less generated defect centres during operation, in the DUV region [Klein2001, Khalilov2006].

When MMF are used for high-power excimer laser light delivery [Dressel1991, Koehler2003], the surface damage threshold of synthetic silica is the primary limit. Severe optical damage is observed at power densities above 1 GW/cm² for pulsed lasers [Pini1987]. The generation and transformation of defect centres during operation is a

second limit. The absorption bands of E'_γ centres and ODC(II) strongly influence the ArF and KrF wavelengths at 193 nm and 248 nm, respectively [Klein1996a]. When the existence of two different kinds of oxygen deficiency centres was discovered, it was also found that an ODC(II) can be photobleached to an E'_γ centre by excimer laser irradiation [Imai1988, Imai1991].

Recent applications of fibre-optic systems in the near ultraviolet (NUV) require smaller spot sizes or better beam qualities that are not achievable with MMF [Kirshenbaum2011]. High-OH synthetic silica single-mode fibres (SMF) with mode-field diameters from 2 to 3 µm for delivery of UV light fulfil these requirements. They are commercially available for the NUV region (300 – 400 nm) and can be combined with light from continuous-wave (CW) single-mode diode lasers (375 nm, 395 nm, 405 nm). These single-mode lasers (SML) are under constant development and achieve high output powers in the range of 100 to 300 mW. If this high-power laser light is focused to beam waist diameters of about 2.5 µm for coupling to a SMF, power densities in the range of 2 to 6 MW/cm² are reached.

An effect, unexplained until now, causes the NUV SMF to degrade over time during operation with 405 nm lasers. In light of information obtained from users and manufacturers of fibre-coupled 405 nm diode laser systems, the time for an output power loss of 3 dB or more to be reached varies from a few days to a few weeks. It is important to notice that the photon energy at this wavelength is much lower than the energy of the DUV absorption bands and the power density that is achieved is three orders of magnitude lower than the optical damage threshold. A setup was built-up and improved to damage fibre samples and record the output power from the fibre. The loss at the laser wavelength was readily calculated and a damage rate could be assigned to the sample. Taking into consideration the results from previous work, not only the loss at the laser wavelength was measured, but also the spectral behaviour of the fibre samples down to 200 nm was investigated.

The approach in this work has combined the use of light microscopy, which was undertaken immediately after irradiation, with further examination of the fibre end surfaces using both, atomic force microscopy (AFM) and scanning electron microscopy (SEM) [Oura2003]. In addition, under circumstances where samples were particularly interesting, energy dispersive x-ray spectroscopy (EDX) was performed. Further, for two particular samples, high resolution transmission electron microscopy (HR-TEM) was used for analysing a focused ion beam (FIB) prepared lamella.

4.2.2 Damage measurement setup

For the irradiation of the fibre samples, laser diode modules (LDM) provided by Omicron-Laserage, incorporating Nichia GaN laser diodes which offer high-power at 405 nm, were used. The parameters listed in Table 4-1 for the multi-mode (MML) and single-mode lasers (SML) used in this work are achieved with the beam shaping optics in the modules. The SML uses only a single diode, while the MML comprises two diodes. The beams of the two diodes are cross-combined inside the module, to achieve a higher power output. The radiating area of the broad area laser diodes is 1 µm by 7 µm.

The output power of the employed SML has a maximum of 120 mW for the old version and 150 mW in the new version. The laser beam is optically corrected for astigmatism and is collimated. The beam quality of $M^2 < 1.2$ is suitable for high coupling efficiencies into SMF. The MML with the cross-combined laser diodes has a maximum output power of 390 mW and a beam quality of $M^2 < 6$. The polarisation of a single laser diode is parallel to the p-n junction. This corresponds to the broader slow axis of the laser diode [Mansuripur2002]. According to the orientation of the laser diode in the SML the polarisation is vertical at the exit of the LDM.

Table 4-1: Summary of characteristics of the used laser diode modules MML (Omicron LDM405D.450.CWA.M) and SML (Omicron LDM405.120.CWA.L).

Parameter	MML	SML
Wavelength λ_0 [nm]	405	405
Number of laser diodes	2 (cross-polarised)	1
Output power P_{out} [mW]	390±5	150±3
Power stability ΔP_{out} [%/h]	<0.25	<0.4
Beam quality M^2	3	1.1
Calculated spot diameter $2 \cdot w_0$ [µm]	5.9	2.78
Calculated power density in spot I_{spot} [MW/cm²]	1.4	2.45
Calculated peak power density I_{peak} [MW/cm²]	N/A	4.9

The LDMs are appropriately current and temperature stabilised to achieve a consistent output power over a long time period. The collimated laser beam is focused on the fibre

end surfaces with an imaging and alignment system (IAS) for connectorised fibres. The focal length of the aspheric lenses of 4 mm and 6 mm used in the MML and SML, respectively, give the spot diameters shown in Table 4-1. The fibre end can be adjusted along the optical axis and tumbled around it. This allows for optimal coupling efficiency, also with small angular mismatches on the surface up to 4°. Because of the small spot diameter power densities in the range of MW/cm² are achieved for output powers of a few hundred milliwatts.

During the period of irradiation of SMF the IAS was readjusted from time to time to make sure that the system was not misaligned by mechanical or temperature changes. Even small changes of less then a micrometer can change the coupling conditions noticeably, which in turn would alter the power reading at the fibre output. For low-mode fibre (LMF) the IAS was not changed for readjustment purposes, because a new spot for launching more light into the fibre might be found. But it was recognized, when readjusting the SMF, that the IAS is very stable, also over longer periods of time.

The progress of the fibre damage during the irradiation period was monitored using the fibre output power $P_{out,fibre}$ from the fibre samples. The long-term experiments were undertaken over a period ranging from four days to two weeks, depending on the loss L in the fibre output power that was experienced. The goal for long-term damage was a power reduction in the range of 1 to 5 dB, depending on the particular study being undertaken. The loss over time was calculated using:

$$L(t) = -10 \cdot \log_{10}\left(\frac{P_{out,fibre}(t)}{P_{out,fibre}(0)}\right) \qquad (4\text{-}1).$$

For the power readings thermopile power meters were used. The measurements with the MML were performed with a Melles-Griot 13 PEM001/J (10 mm aperture) and the SML measurements with a Coherent PowerMax PS19Q (19 mm aperture). In Figure 4-1 the whole setup is shown on a straight axis, but the actual damaging was done with the fibre under test (FUT) bent in some way. The length of the FUT depended on the fibre material and the desired dynamic of the spectral measurements in the DUV. If not mentioned otherwise a length of 1 m can be assumed. To connect the FUT to the IAS all proximal ends

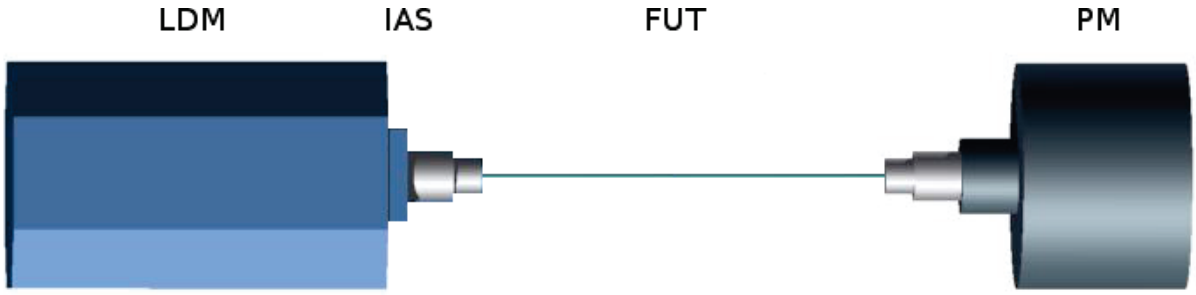

Figure 4-1: The damage setup consisting of stabilised laser diode module (LDM) with a wavelength of 405 nm, an imaging and alignment system (IAS) and a thermopile power meter (PM). The fibre under test (FUT) is aligned for maximal output power.

were connectorised with FC/PC connectors. The distal fibre end is aligned in front of the PM for free space irradiation and was appropriately connectorised for spectral measurements.

In all cases the proximal end was adjusted to maximum fibre output power using the IAS. During irradiation, the proximal fibre end is used inside the IAS, but not sealed or flushed with gas. The distal end is in free space and not protected from dust particles. All experiments are conducted in a standard laboratory environment at room temperature. To determine the error in the power reading, the standard deviation of a daily or semi-daily average is added to the uncertainties seen from the power meter and the laser diode module. For the error ΔL of the loss the non-linear propagation of error is used [Muehl2001]:

$$\Delta L = \sqrt{\left(\frac{\partial L}{\partial P_{out,fibre}(0)}\right)^2 \cdot \Delta P_{out,fibre}(0)^2 + \left(\frac{\partial L}{\partial P_{out,fibre}(t)}\right)^2 \cdot \Delta P_{out,fibre}(t)^2} \qquad (4\text{-}2).$$

4.2.3 Spectral measurement setup

In order to determine spectrally induced loss in small core fibres in the DUV, a newly developed spectrometer system was employed. As depicted in Figure 4-2, the whole setup consists of deuterium lamp (D_2) with an imaging system and the fibre-optic spectrometer (OceanOptics Maya2000Pro). Short pieces of MMF with low solarisation were used for coupling in and out of the FUTs through butt-coupling [Klein2001, Khalilov2006]. This procedure showed best reliability when changing between the laser and the broadband system. In spite of that, some of the measurement samples show white light interference due to misalignment at the coupling sites. The deuterium lamp provides broadband light starting at 180 nm. The spectrometer system uses a back-thinned CCD chip (charge-coupled device) for a higher sensitivity, than it is possible with older CCD chips or photo-diode arrays (PDA). The grating of the spectrometer covers the spectral range from 167 to 620 nm and for a good resolution Δλ a narrow slit of 5 µm width is utilised. The integration time starts at 13 ms and can be increased to several seconds. Despite the nar-

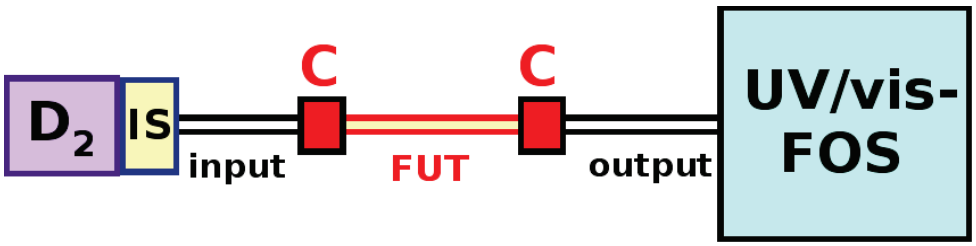

Figure 4-2: Spectral measurement setup; D_2: deuterium lamp, IS: imaging system, input/output: 100 µm input/output fibre, C: connector, FUT: fibre under test, FOS: fibre-optic spectrometer for UV and visible range.

row slit, the sensitivity is so high, that standard 100 µm core diameter step-index fibres cannot be measured, but drive the CCD chip into saturation.

The grating used in the spectrometer reflects the first higher order onto the CCD chip as well. This higher order needs to be taken into account for the spectral measurements. Unexpected signals with twice the wavelength of an expected signal, should be handled with care and could be an artefact. As an example Figure 4-3 shows the spectrum of a mercury lamp with a small peak at 508 nm, which is the first higher order reflection of the 254 nm mercury line attenuated by about 13 dB. Another artefact has to be expected at 486 nm, where the Balmer line D_β of deuterium can cause an oscillation in the calculated loss spectrum. The peak might shift in the spectrometer signal over time, due to warming up of the grating and chip. Therefore, this peak is also used in the analysis to adjust a drift in wavelength.

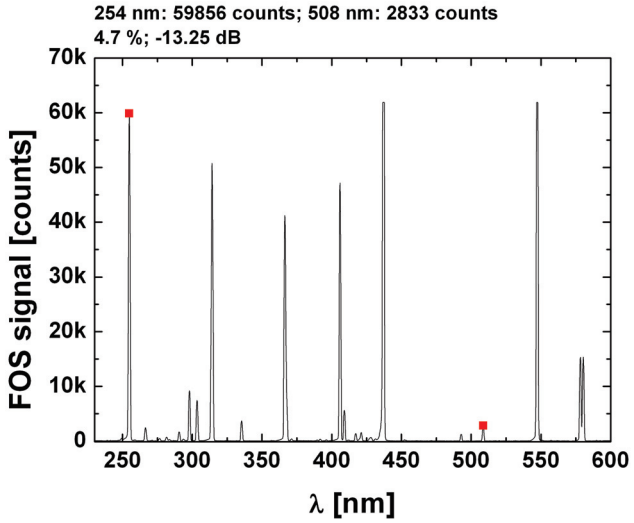

Figure 4-3: The spectrum of a mercury lamp measured with the spectrometer shows an unknown peak at 508 nm. Its origin is a higher order reflection of the well known mercury line at 254 nm at the spectrometers grating.

To demonstrate the capabilities of the new setup, several spectra of a 1 m long sample of 2.2 µm core diameter SMF were taken. Three different integration times were chosen. As can be seen in Figure 4-4 a) a short integration time of 100 ms gives the same shape as 800 ms and 2 s, but the signal is not as strong and has some noise. The difference between 800 ms and 2 s is only in the peak value of the signal, the noise is comparably low. Thus a reasonable integration time of 500 ms should allow for simple handling and enough dynamic range. It is worth mentioning that there is a signal below 200 nm and for the longer integration times it is in the range of a few kilocounts. This tail can be used for DUV loss measurement in SMF.

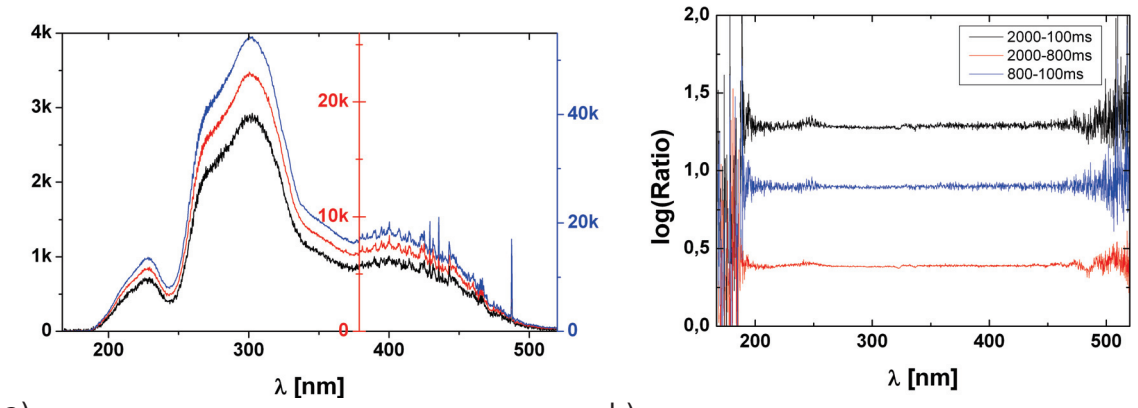

a) b)

Figure 4-4: a) 1 m 2.2 µm SMF in described spectral measurement setup. Spectra for three different integration times are shown. Left y-axis for 100 ms (black curve), centre y-axis for 800 ms (red curve) and right y-axis for 2 s integration time (blue curve). The unit of the y-axes is counts. b) The logarithmic ratio between the spectra is shown for better comparison.

The logarithmic ratio of the spectra is shown in Figure 4-4 b) to see the actual difference between the different integration times. All three curves are relatively flat. The comparison between highest and lowest integration time has the most noise, while it is reduced for the other comparisons. At both ends of the spectral range the low signal levels result in high oscillations, but this is a problem of the systems dynamic. These comparisons prove again that medium integration times can give good results, if some noise is accepted.

Spectral measurements of the FUTs were taken before and after exposures. The dark current reading was subtracted from the recorded spectra. To obtain the spectral loss induced by 405 nm irradiation the spectra were processed using the relationship:

$$L_{ind}(\lambda) = -10 \cdot \log_{10}\left(\frac{I_{after}(\lambda)}{I_{before}(\lambda)}\right) \qquad (4\text{-}3).$$

The spectral measurement system was also used to determine the attenuation profile α(λ) of the fibres by using the cut-back method. The fibres were cut back if possible from the length on the spool to 1 m and then to 0.5 m. The attenuation profile was calculated by using the relationship:

$$\alpha(\lambda) = \frac{-10}{\Delta l} \cdot \log_{10}\left(\frac{I_{long}(\lambda)}{I_{short}(\lambda)}\right) \quad \text{with} \quad \Delta l = l_{long} - l_{short} \qquad (4\text{-}4).$$

In the spectral measurements, a lamp signal error ΔI of ±3 % at 200 nm, ±2 % at 300 nm and ±1 % at 400 nm is taken into consideration. The noise in the spectrometer is much

lower than this error and not taken into account. For the error of the spectral loss ΔL_{ind} the non-linear propagation of error is used [Muehl2001]:

$$\Delta L_{ind} = \sqrt{\left(\frac{\partial L_{ind}}{\partial I_{before}}\right)^2 \cdot \Delta I_{before}^2 + \left(\frac{\partial L_{ind}}{\partial I_{after}}\right)^2 \cdot \Delta I_{after}^2} \quad (4\text{-}5).$$

4.3 Basic characterisation of fibre specimens

4.3.1 Fibre types

In this work mainly two fibre types with small core diameters were investigated:

- Single-mode fibre (SMF) for a wavelength range from 350 to 450 nm and
- Low-mode-fibre (LMF) with a core diameter of 15 µm.

The SMF can be further divided into three categories:

- Standard fibre with normal mode-field diameter,
- Polarisation-maintaining fibre (PM) with normal mode-field diameter and
- Large mode area fibres (LMA) with larger mode-field diameter.

While the standard fibre provides ease of use, the PM fibre is requested by most users due to the importance of the polarisation state in many applications. Fibres with larger mode field have a reduced power density in the fibre core and thereby an improved long-term stability. These three fibre types can be manufactured as common all-silica step-index fibres (AS) or as microstructured photonic crystal fibres (PCF). SMF samples were provided by *Fiberware*, Germany, and *Fibercore*, UK, PM-SMF samples by *Nufern*, USA, and LMA-PCF samples by *NKT Photonics*, Denmark. The LMF was provided by *IPHT* and *j-fiber*, both from Germany, and were produced using the same protocol. A pure synthetic silica preform with a low OH content of less than 1 ppm, is tempered with a Hydrogen flame and then drawn into fibre. This fibre type was engineered by *IPHT* as type *6u* and is commercially available from *j-fiber* as type *IG-15*. It was specially developed for blue pulsed high-power lasers at 446 nm.

All fibres have pure synthetic silica cores and F doped claddings. Only the Ge doped fibre *SM 450* from *Fibercore* has a doped core and a pure silica cladding. The Ge concentration profile and thus the refractive index profile of such a fibre is not a perfect step index profile, but rather a slight gradient index profile with a narrow dip in the centre [Mitschke2005]. All the fibres used were stored for several months before irradiation. Table 4-2 gives an overview of the properties of the different fibres investigated.

Table 4-2: Properties of the fibre types investigated in this work.

Fibre	Supplier	Type	Core / MFD [µm]	Material	NA
6u	IPHT	AS LM	15	Tempered with H_2 flame	0.1
IG-15/125/250	j-fiber	AS LM	15	Tempered with H_2 flame	0.1
LMA-10-UV	NKT Photonics	PCF LMA SM	7.5	low-OH	0.08
SM 350/125	Fiberware	AS SM	2.2@355 nm	low-OH	0.1
SM 400/125	Fiberware	AS SM	2.7@405 nm	low-OH	0.1
PM-S350-HP	Nufern	AS PM SM	2.3@350 nm	low-OH	0.12
PM-S405-HP	Nufern	AS PM SM	3.2@405 nm	low-OH	0.12
SM 400-SC	Fibercore	AS SM	2.5@405 nm	low-OH	0.12
SM 450	Fibercore	AS SM	3	low-OH	0.1

A theoretic coupling efficiency of η = 90 % from the SML to the SMF can be calculated using [Nemoto1979]:

$$\eta = \left(\frac{2 \cdot w_{0,1} \cdot w_{0,2}}{w_{0,1}^2 + w_{0,2}^2} \right)^2 \quad (4\text{-}6).$$

The actual coupling efficiency at 405 nm is in the order of 50 to 70 %. Although the effective mode areas are quite equal there are differences in modal shape and errors in angular and lateral alignment. The latter have a much higher influence for the small mode-field diameters used here, than for fibre-coupled laser systems in the near-IR. For the MML a coupling efficiency of about 20 % to the SMF and 55 to 70 % to the LMF was obtained.

For the influence of the 405 nm laser radiation on the fibre material the power density I_{core} in the fibre core needs to be taken into account.

$$I_{core} = \frac{P_{out,fibre}}{A_{eff}} = \frac{P_{out,fibre}}{\pi \cdot w_0^2} \quad (4\text{-}7)$$

The power density is averaged over the effective mode area A_{eff} of the fibre core. The peak power density I_{peak} of a gaussian beam in a SMF is twice as high as I_{core} [Pas-

chotta2008]. Typical values are given in Table 4-3. The actual power density experienced by the proximal fibre surface is in the range defined by I_{spot}, as given in Table 4-1.

Table 4-3: Data for the power density I_{core} in the fibre core for various combinations of laser diode modules and fibre types.

	MML	**SML**
LMF	I_{core} = 100 – 130 kW/cm²	I_{core} = 40 – 50 kW/cm²
SMF	I_{core} = 0.9 – 1.3 MW/cm² I_{peak} = 1.8 – 2.6 MW/cm²	I_{core} = 1.6 – 2 MW/cm² I_{peak} = 3.2 – 4 MW/cm²

4.3.2 Results of attenuation measurement

The SMF samples were cut back from the length on the fibre spool to 1 or 0.5 m, to receive an exact value for the attenuation at 405 nm. Every SMF in Figure 4-5 and Table 4-4 shows a good attenuation ≤ 0.15 dB/m at 405 nm. Only the Ge doped SM 450 reaches a value of 0.2 dB/m, because the UV absorption band starts at longer wavelengths for Ge doped fibres. The increase in attenuation above 400 nm of the fibres provided by *Fiberware* suggests that these are more sensitive to bending as a consequence of the fibre design. Therefore, the transmission window for these fibres is narrower than for the *SM 400-SC* or *PM-S350-HP*. For the *PM-S405-HP* a similar attenuation profile as for the *PM-S350-HP* can be assumed.

The visible peaks in the attenuation profile are not absorption bands. At these wavelengths lower than the design wavelength a second mode guided in the SMF core is cut off. This mode is highly bend sensitive and a differently bend or illuminated fibre before and after cut-back shows this artefact in the attenuation profile. But it is also used to determine the cut-off wavelength of the SMF.

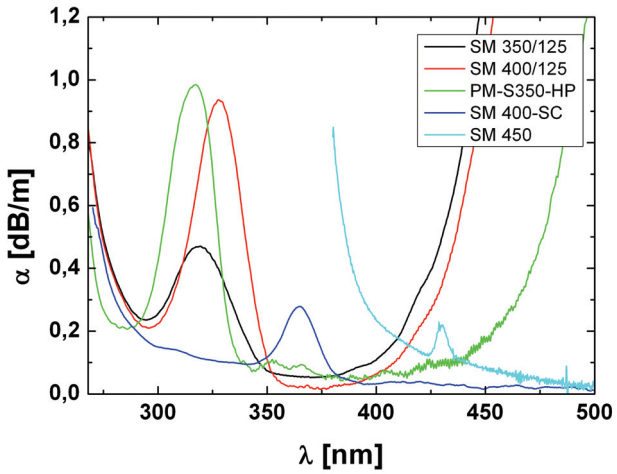

Figure 4-5: Measured attenuation profiles of SMF.

Table 4-4: Measured attenuation values of SMF.

Fibre type	Attenuation at 405 nm [dB/m]
SM 350/125	0.14
SM 400/125	0.08
PM-S350-HP	0.07
SM 400-SC	0.04
SM 450	0.2

For the LMF the attenuation profile was measured for the UV only. Therefore the cut-back length of the fibres could be chosen shorter than for the SMF. The results are shown in Figure 4-6. In these two cases there is an actual absorption band at 245 nm, which coincides with the ODC(II). Only the short final length of 0.1 m for the *IG-15* sample can resolve the absorption peak with more than 60 dB/m. Both fibres exhibit the same profile up to the absorption band, but show differences in the window of lower attenuation below it. Since both fibres are manufactured using the same protocol, this difference can only be explained by slight variations in the base material and the manufacturing process.

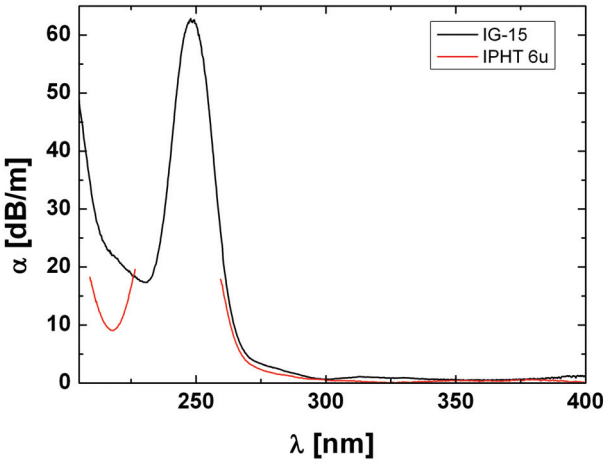

Figure 4-6: Measured attenuation profile of the LMF in the UV.

4.3.3 Results of cut-off wavelength measurement

A measurement of the cut-off wavelength λ_{CO} is important to determine that the SMF is actually operated in its single-mode regime at 405 nm. Therefore the measurement is performed according to [Cancellieri1993]. A piece of SMF is excited by broadband light and a spectral measurement is taken. Subsequently a loop with a diameter of 30 to 60 mm is formed in the piece of fibre and a second spectral measurement is taken. Finally the bending loss induced by the loop is calculated from the two spectra and observed from longer to shorter wavelength. The wavelength at which the loss increases by 0.1 dB is the cut-off wavelength λ_{CO}. As an example the bending loss of a 45 mm loop in the *SM 400-SC* sample is shown in Figure 4-7.

A summary of all cut-off wavelengths in Table 4-5 shows that all fibre types are within their specifications. Every SMF with a pure silica core is suitable for single-mode transmission at 405 nm. Except for the fibre type *SM 450* with a Ge doped core, which is not single-mode at 405 nm, because it is designed for the visible wavelength range starting at 450 nm. The excitation of a few modes has to be expected when operating this fibre type.

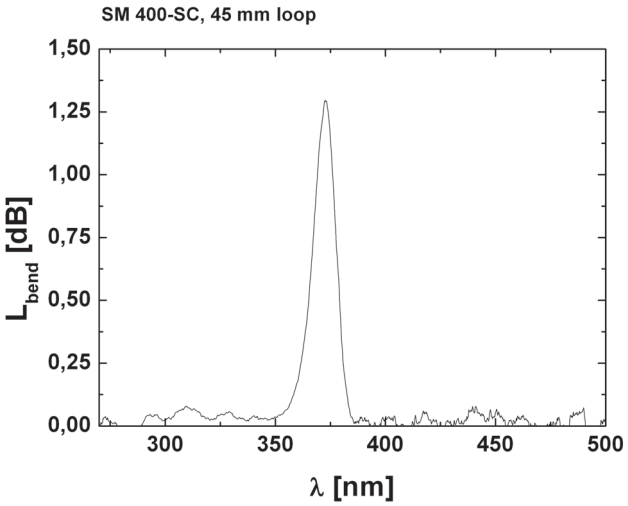

Figure 4-7: Bending loss of SM 400-SC with a 45 mm loop.

Table 4-5: Summary of measured cut-off wavelengths for the SMF.

Fibre type	Cut-off wavelength λ_{co} [nm]
SM 350/125	340
SM 400/125	350
PM-S350-HP	332
PM-S405-HP	372
LMA-10-UV	375
SM 400-SC	385
SM 450	430

4.3.4 Fibre end surface preparation

The FUTs were prepared and assembled with connectors shortly before being used in each experiment. Additionally to the standard way of gluing-and-polishing (GP), samples were also prepared in improved ways with lower end surface contamination and lower surface roughness. Those are clamping-and-polishing (CP), cleaving-and-clamping (CC) and cleaving-flame-polishing-and-clamping (CFC). The actual influence of these prepara-

tion methods on the surface quality was investigated with an atomic force microscope (AFM). The roughness and waviness were determined and eventually correlated with the results from the damaging experiments.

For the standard preparation GP, the samples were glued into the metal or ceramic ferrules of the connectors using two-component adhesive, which was then left to harden for 24 h. The ferrules with the fibres were polished using consecutively smaller polishing lap and finished with 0.5 µm grain size. These GP samples showed a very good polishing end surface.

In the next step, to a less contaminating way of preparation, the glue was left out. The fibre end was stripped, put into the connector and held in place with a clamping mechanism attached to the connector. Then the fibre and ferrule were polished in the same way as described for GP, until the end surface quality of the CP samples was very good.

To clear the end surface further from contaminations before irradiation, the cleaving method was used to prepare high quality fibre end surfaces. The fibres were stripped off their acrylate coating and cleaved using a standard telecommunications fibre cleaver (York cleaver or Fujikura CT 20). The fibre was then placed in the connector and held in place with the clamping mechanism attached to the connector. Using a microscope, the fibre end surface was then aligned to protrude just a little bit out of the ferrule, to allow for cleaning purposes of the CC samples.

To improve the surface roughness a fusion arc treatment was applied. In this case it means flame-polishing with the fusion arc. After cleaving as described above, the fibre was put into a telecommunications splicer (Fujikura FSM-30S or FSM-100MP) and treated with the fusion arc for one to two seconds. The fusion arc power and period was chosen in a way that the fibre end surface was not malformed or spherical. It is sufficient when the edges of the end surface are a little bit rounded and the fibre still fits into the connector. After that the CFC samples were aligned and clamped in the connector like the CC samples.

To evaluate the surface quality of the differently treated end surfaces, the surface roughness was measured using AFM. The AFM was used in force modulation mode with a probe tip diameter of 5 to 10 nm to measure topographies in the fibre core region. The actual roughness measurements were ten lines of 10 µm length (primary profiles) in the centre of the topography images [DIN4287, DIN4288, DIN3274]. The cut-off factor for the measurement was chosen to 0.02 [DIN11562] to make a good distinction between roughness and waviness.

In Figure 4-8 each topography image is scaled to a certain z-range for a most detailed view of the surface. The polished surfaces of *SM 400/125* show a typical grinding profile without a trend into one direction. These samples show the highest variation in surface

roughness, indicated by the z-range of 18 nm. *PM-S405-HP* on the other hand exhibits the grinding profile as well, but not with such a high roughness. A certain waviness due to the polishing remains however. This difference is probably subject to changes in the polishing process and differences in materials.

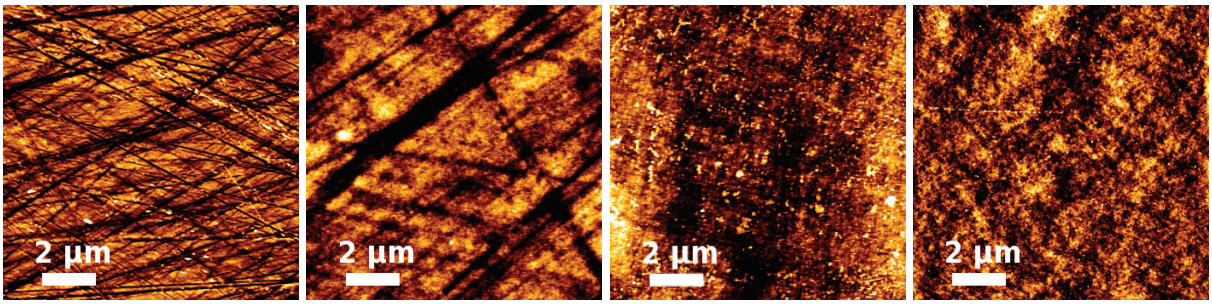

Figure 4-8: AFM topographies (LTR): SM 400/125 GP (z-range 18 nm); PM-S405-HP GP (z-range 2.9 nm); SM 400/125 CC (z-range 5.4 nm); SM 400/125 CFC (z-range 1.1 nm)

The CC samples of *SM 400/125* also show a structure of grooves, but very fine and into one direction, probably the direction of the cleave. The roughness is low, but the waviness of the surface is noticeable. The best visual end surface quality was achieved with the CFC samples, indicated by the lowest z-range of 1.1 nm. The height variation is almost in atomic scale and roughness and waviness are reduced to a minimum.

For a direct qualitative comparison Figure 4-9 shows GP, CC and CFC samples at the same z-range scaling. The reduction of rough structures to finer structures and from high roughness to lower roughness and little waviness is obvious.

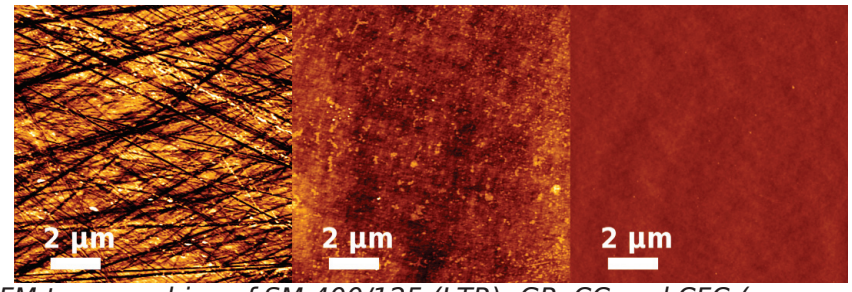

Figure 4-9: AFM topographies of SM 400/125 (LTR): GP, CC and CFC (z-range 15 nm for all).

From the primary profiles, taken from the measurements, values of average roughness and waviness can be deduced. The values shown in Table 4-6 are from ten primary profiles for each fibre end surface. For the GP samples of standard fibre (*SM 350/125* and *SM 400/125*) four samples were averaged, for the GP samples of PM fibre (*PM-S350-HP* and *PM-S405-HP*), CC and CFC samples of standard fibre (SM 400/125) each three samples were averaged.

In terms of average and RMS roughness, R_a and R_q, standard GP samples have the highest values. PM GP samples are comparable and standard CC and CFC samples have much lower values by a factor of five to ten. This stays true for peak-to-valley values R_t, which are the absolute maxima from highest peak to lowest valley, and for the average maximum values R_{z3ISO}, which are the average of the third highest peak to third lowest valley for all primary profiles. The PM GP samples have a high standard deviation due to one very well polished sample. This sample was an outlier and had values as good as CC samples, but could not be reproduced.

Almost all surfaces show an average waviness of 1 to 2 nm, except for the CFC samples. Those have a waviness which is lower by a factor of ten, almost not detectable by the system and therefore with a standard deviation of zero. This substantiates the perception that the treatment with the fusion arc enhances the mechanical surface quality beyond what is possible with cleaved fibre end surfaces.

Table 4-6: Surface roughness and waviness, average values from ten primary profiles. Analysis according to [DIN4287, DIN4288, DIN3274]; length of primary profile l_n=10 µm; cut-off factor 0.02.

Parameter	Standard GP	PM GP	Standard CC	Standard CFC
Average roughness R_a [nm]	1.8 ±0.37	1.37 ±1.26	0.37 ±0.06	0.13 ±0.01
RMS roughness R_q [nm]	2.45 ±0.64	1.81 ±1.69	0.5 ±0.1	0.17 ±0.01
Peak to valley R_t [nm]	18.53 ±6.45	13.3 ±11.9	3.13 ±0.67	0.93 ±0.12
Average maximum of roughness profile R_{z3ISO} [nm]	6.15 ±1.38	4.53 ±4.06	1.27 ±0.32	0.7 ±0.35
Average waviness W_a [nm]	1.58 ±0.29	1.53 ±0.76	1.07 ±0.47	0.1 ±0
RMS waviness W_q [nm]	2.0 ±0.37	1.87 ±1.0	1.23 ±0.49	0.13 ±0.06

4.4 Damage of fibres with larger core diameter with 405 nm diode lasers

4.4.1 Samples damaged with 405 nm single-mode laser

In the first tests a *6u* GP samples was irradiated. The old SML with 120 mW at 405 nm was used. A coupling efficiency of about 69 % resulted in 76.1 mW at the fibre output in the damage setup. This value corresponds to 0 dB in Figure 4-10. The resulting power

density in the fibre core is about 43 kW/cm². The coupling was readjusted after 14 days. Before the readjustment the output power dropped by about 10 mW, which is a loss of 0.6 dB. After readjusting the output power was as high as 74 mW. The recording of the output power was interrupted for about a week. After it was resumed the degradation was still increasing. The experiment was discontinued after 38 days when the output power was at 65.1 mW. Which is a loss of less than 1 dB.

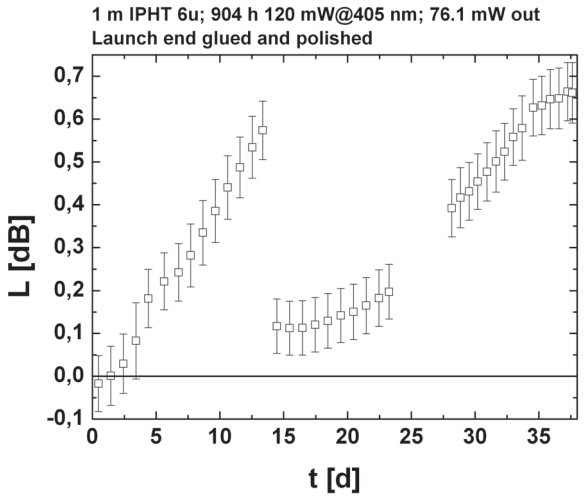

Figure 4-10: Loss over time of a 1 m long GP sample of 6u (15 µm core LMF) with 120 mW at 405 nm. The given power is the fibre output power at the beginning of the measurement and the power density in the core was 43 kW/cm².

4.4.2 Samples damaged with 405 nm multi-mode laser

The experiments with the 390 mW MML at 405 nm were performed on LMF and LMA samples, the first of them being GP samples. The larger spot diameter of the MML corresponds better to the 15 µm core of the LMF and the 7.5 µm MFD of the *LMA-10-UV*. The LMF *IG-15* and *6u* were damaged repeatedly.

The first damage test with a *IG-15* GP sample had only 62 mW fibre output power, giving a coupling efficiency of 17 %. This is the starting value for 0 dB in Figure 4-11. For the second irradiation of an *IG-15* GP sample the coupling was improved by a different imaging system with coated lenses and a shorter focal length of $f = 4$ mm. Now a fibre output power of 178 mW was measured, an efficiency of about 50 %, gaining the starting value for this curve for 0 dB in Figure 4-11. The output power degrades quickly and very linear on a logarithmic scale. Despite the different output powers almost the same slope was measured for both damaging cases. In the first case the damage rate was

0.98 dB/day and in the second case with the better coupling it was 1.02 dB/day. The loss reached over 13 dB for the first test, which continued for two weeks.

The GP sample of *LMA-10-UV* transmitted 75.8 mW of single-mode light from the MML. This coupling efficiency of 21 % resulted in a linear degradation with a rate of 1.02 dB/day over three days, in this case as well. Thus the damage rate for all irradiated GP samples with a larger core is in the range of 1 dB/day, despite different coupling efficiencies and fibre output powers.

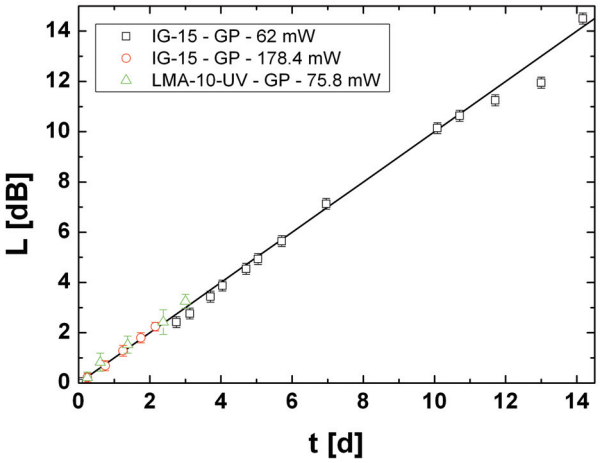

Figure 4-11: Loss over time in 1 m long GP samples of IG-15 and LMA-10-UV with 390 mW at 405 nm. Additionally a straight with a slope of 1 dB/day is plotted. The given power is the fibre output power at the beginning of the measurement.

As the loss curves in Figure 4-12 indicate there is no induced loss above 280 nm, especially not around 400 nm. Only some white light interference and the higher order of the change in the DUV is seen in this range. The most interesting part is below 280 nm. The

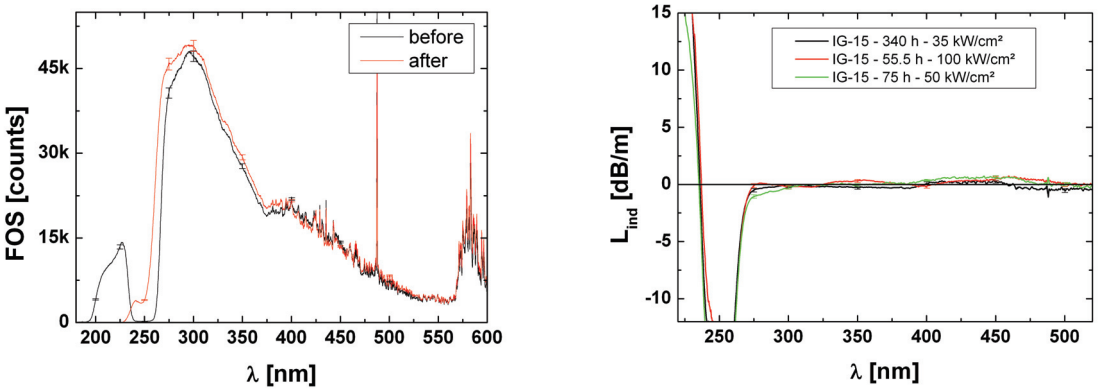

Figure 4-12: Spectra and induced loss for samples of IG-15 irradiated for 2.3 days up to 14 days. The respective power densities in the core are 35 kW/cm², 100 kW/cm² and 50 kW/cm². The two spectra on the left were taken before and after irradiation and belong to the black curve on the right.

ODC(II) absorption band at 245 nm was reduced and a gain is obvious in the loss curve. A large absorption band was formed below 230 nm, introducing a loss. The spectral behaviour did not differ for different periods and power densities of irradiation, almost the same curve is seen for 2 days or 4 weeks.

The damaging setup with the MML proved to be very efficient and delivered reproducible results with the GP samples. Those results are the references for improvements and the setup was used to damage several CC samples of the *6u* LMF. In addition, a CP sample was made for comparison with the CC samples. In its first irradiation this CP sample (black symbols in Figure 4-13) shows a similar behaviour to the GP samples. A better coupling efficiency of 61 % enabled a fibre output power of almost 220 mW. The coupling was readjusted after four days of irradiation. The new launching spot had a worse coupling efficiency than the first and a power of 215 mW was measured (red symbols in Figure 4-13). The damage followed the preceding spot and another adjustment after one day resulted in 211 mW fibre output power. This launching spot was finally irradiated for seven days. The trend of this curve (green symbols in Figure 4-13) resembles the other two curves and has a damage rate of 0.32 dB/day.

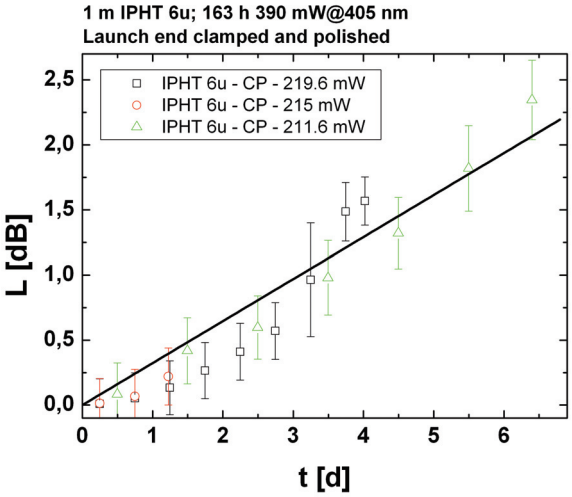

Figure 4-13: Loss over time of three launching spots on a CP sample of 6u with 390 mW at 405 nm. Additionally a linear fit of the data points at the third spot with a slope of 0.32 dB/day and $r^2 = 0.9884$ is plotted. The given power is the fibre output power at the beginning of the measurement.

In the experiments with the CC samples the behaviour of the power loss is very similar to the CP sample. The first irradiation of the first sample, with a fibre output power of 224 mW, showed a damage rate of 0.27 dB/day. This was so far the best coupling efficiency from MML to LMF with over 62 % and over two weeks of constant exposure the loss was 4 dB at 405 nm (black symbols and linear fit in Figure 4-14). The proximal end was cleaved off after the first experiment and again a fibre output power of 224 mW was

achieved (red symbols in Figure 4-14). After a short exposure of two days, one of the two laser diodes in the MML was switched off and the fibre adjusted. Now, with a coupling efficiency of 63.5 %, a power of 114 mW was measured at the fibre end. In this case of reduced power density on the fibre surface a damage rate of 0.25 dB/day was received.

A last experiment with CC samples of LMF was performed on a short 0.2 m long piece of *6u*. This should show, if the length of the fibre has an influence on the damage. Again a coupling efficiency of 62 % was achieved and the damage rate was 0.26 dB/day. The data points are shown as yellow triangles in Figure 4-15 together with a summary of all experiments with LMF CP and CC samples. On average a damage rate of 0.27 dB/day was found for irradiation periods from 2 up to 14 days. Only the CP sample shows a slightly higher damage rate of 0.32 dB/day over four days. If only one laser diode is turned on, then the damage rate is also in the range of 0.25 dB/day.

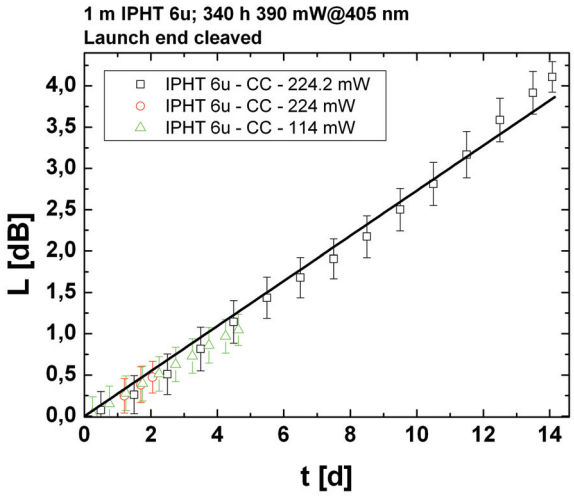

Figure 4-14: Loss over time of two cleaved launching ends of a CC sample of 6u with 390 mW at 405 nm. Additionally a linear fit of the data points of the first cleave with a slope of 0.27 dB/day and $r^2 = 0.9965$ is plotted. The second cleave was irradiated twice, first with 224 mW and then with 114 mW. The given power is the fibre output power at the beginning of the measurement.

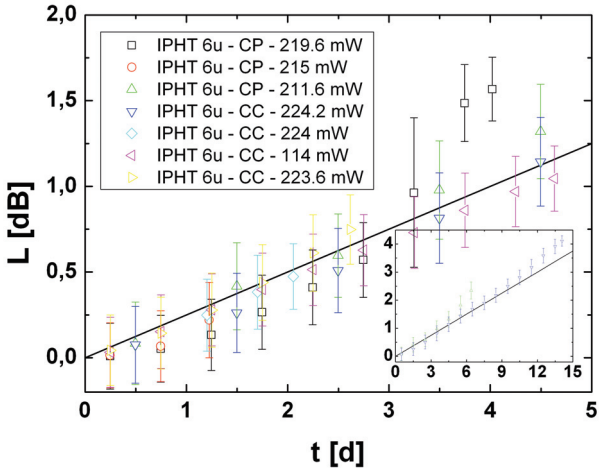

Figure 4-15: Loss over time of CP and CC samples of 6u irradiated with the MML. Additionally a straight with a slope of 0.25 dB/day is plotted. The given power is the fibre output power at the beginning of the measurement.

4.5 Damage of single-mode fibres with 405 nm diode lasers

4.5.1 Samples damaged with 405 nm multi-mode laser

The first experiments with SMF were performed with the MML to investigate the impact of surface roughness. GP, CC and CFC samples of *SM 400/125* and *PM-S405-HP* were prepared and irradiated. The summary of the resulting graphs is shown in Figure 4-16. Within the first days of irradiation no conclusive trend can be seen. Changes less than 1 dB can probably be more attributed to mechanical settling or variations of the IAS then to damage. Thus only the CC sample of *PM-S405-HP* showed a constant damage of 0.3 dB/day over six days (green triangle). This sample also had the highest coupling efficiency of 22 % and a fibre output power of 80.5 mW at the beginning. The CC sample of *SM 400/125* (black rectangle) started with a low damage rate of 0.1 dB/day and after seven days increased to 0.4 dB/day. The CFC samples performed differently from the CC samples. The CFC sample of *PM-S405-HP* had the worst coupling efficiency with only 68 mW fibre output power (blue triangle) and started with a sudden increase of 0.5 dB, which might be accounted to an environmental or alignment change in the measurement setup. But after that the fibre output power stays almost stable for nine days. For *SM 400/125* the CFC sample (red circle) shows no damage for four days and then gets damaged with a rate of 0.45 dB/day. Its loss increases parallel to the loss of the CC sample. For the other GP and CC samples, which were irradiated for spectral and surface

investigations, the periods of irradiation were too short to separate alignment and damage effects.

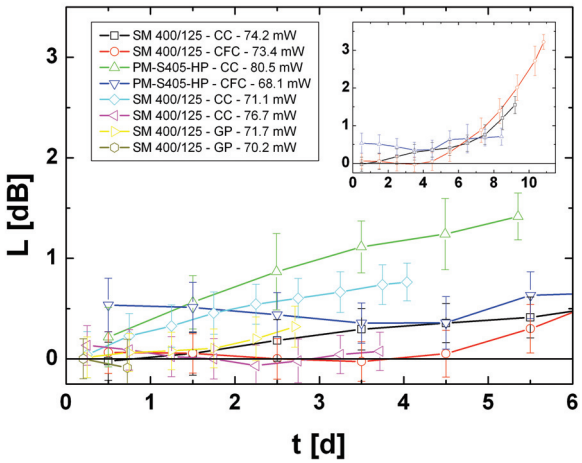

Figure 4-16: Loss over time of SMF GP, CC and CFC samples irradiated with the MML. The samples show no conclusive degradation behaviour with in the first days. The given power is the fibre output power at the beginning of the measurement.

A spectral behaviour similar to that of the LMF samples was found for the SMF samples. Two CC samples of *SM 400/125* were irradiated for four days (cyan rectangle and magenta triangle in Figure 4-16), one GP sample for three days (yellow triangle) and one GP sample for little more than one day (brown hexagon). The collection of induced loss spectra in Figure 4-17 shows the higher order of the DUV changes above 400 nm. Additionally, some samples exhibit white light interference due to different coupling conditions before and after irradiation. From the spectra taken before and after irradiation and also shown in Figure 4-17, the good transmission of this fibre type in the DUV has to be

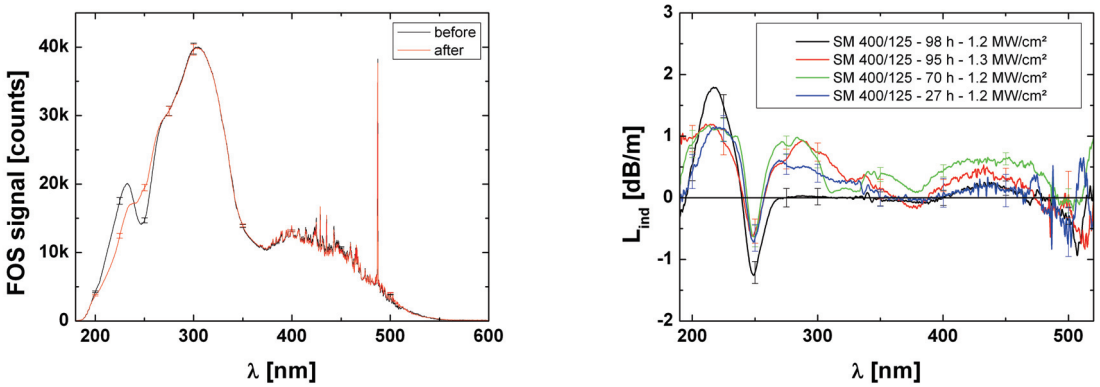

Figure 4-17: Spectra and induced loss for 1 m long samples of SM 400/125 for different periods of irradiation for similar power densities of 1.2 MW/cm² in the fibre core. The two spectra on the left were taken before and after irradiation and belong to the black curve on the right.

recognised. Because of that the change in the absorption bands at 215 and 250 nm is clearly visible. Whilst the first sample only shows changes of these two bands, the other samples show an additional loss in the range of 250 to 300 nm.

For Ge doped SMF experiments were performed on CC samples with the MML as well. In one case the fibre was irradiated for 16 days and in a second case for 7 days. In both cases high fibre output powers of 94.6 mW and 89.7 mW were achieved. Figure 4-18 shows the time-dependent loss on the left. After a quick increase right at the start, which is not shown here, the loss increased linearly with a rate of about 0.1 dB/day for the rest of the irradiation period. Finally losses of 1.65 dB and 0.92 dB were reached after 16 and 7 days of exposure, respectively. The spectral loss measurements that were performed on both samples show the formation of an absorption band. Only the tail of this absorption band was observed in the measurement. From Figure 4-18 it can be seen, that this tail increases the loss well into the visible range by about 2 dB/m. A drop in the induced loss can be recognised close to the cut-off wavelength when going from longer to shorter wavelengths. Below the cut-off wavelength the induced loss increases parallel to an imagined extrapolation of the induced loss above the drop. Nevertheless, the induced loss of 6.7 dB and 5.7 dB measured spectrally at 405 nm is considerably higher than the final loss after the irradiation periods.

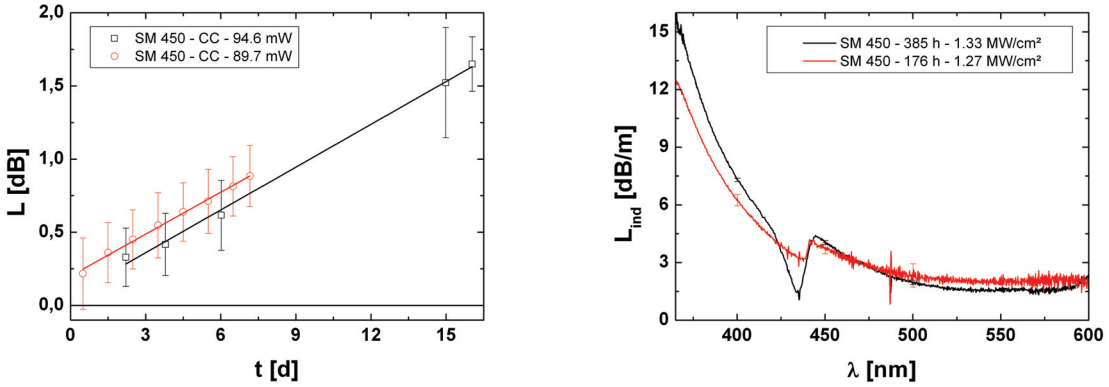

Figure 4-18: Loss over time of SM 450 CC samples irradiated with the MML on the left. The given power is the fibre output power at the beginning of the measurement. Induced loss for the 1 m long samples of SM 450 for different periods of irradiation for similar power densities of 1.3 MW/cm² in the fibre core.

4.5.2 Samples damaged with 405 nm single-mode laser

Finally SMF samples were also tested with the new SML with 150 mW output power. Two CC samples of *SM 400-SC* were constantly irradiated for ten days. The first sample had a

fibre output power of 73.6 mW and a coupling efficiency of 53 %. The coupling into the second sample was more efficient and values of 92.5 mW and 67 % were achieved. Both damage curves in Figure 4-19 show an exponential behaviour with similar slopes. The first sample (black rectangle) can be exponentially fitted to: $L=\exp(0.14\cdot t)-1$ with L in dB and t in days. The correlation coefficient of this fit is $r^2 = 0.9954$. The sample with the higher coupling efficiency showed a steeper slope following an adjustment after two days: $L=\exp(0.22\cdot t)-1$; $r^2 = 0.9996$. If the damage is seen in a linear fashion a damage rate of about 0.26 dB/day for the first and a higher rate of 0.45 dB/day for the second sample can be calculated. The CFC sample of the SM 400-SC starts with a fibre output power of 94.5 mW, a 68.5 % coupling efficiency. This samples loss also increases exponentially, but much stronger than for the CC samples: $L=\exp(0.27\cdot t)-1$; $r^2 = 0.9961$. Thus, a loss of 10 dB is reached after ten days of irradiation.

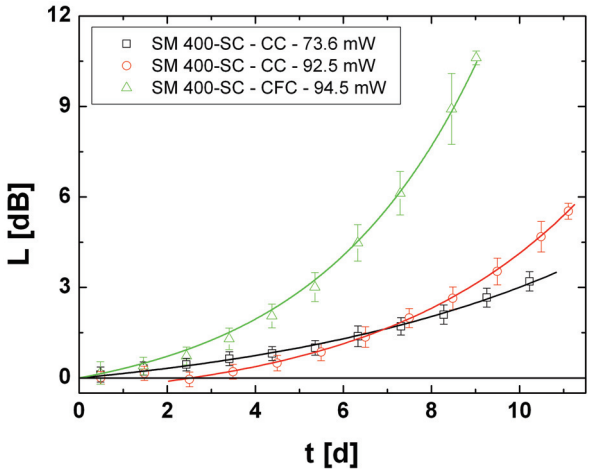

Figure 4-19: Loss over time of CC and CFC samples of SM 400-SC irradiated with the SML. The second sample was realigned after two days and an adjustment with higher coupling efficiency was found. The given power is the fibre output power at the beginning of the measurement.

4.5.3 Measurements of fibre surface temperature

To investigate the heating of the launching fibre surface one measurement with a thermographic camera and one measurement with a fibre Bragg grating (FBG) were performed. In case of the temperature measurement with the camera a SMF was irradiated in an open damage setup, which was not stable enough for the long-term irradiation experiments. But this setup allowed for reasonable room to place the camera near to the fibre end surface. Unfortunately, the resolution of the camera system was not high enough to have a detailed image of the surface. The temperature was averaged over a

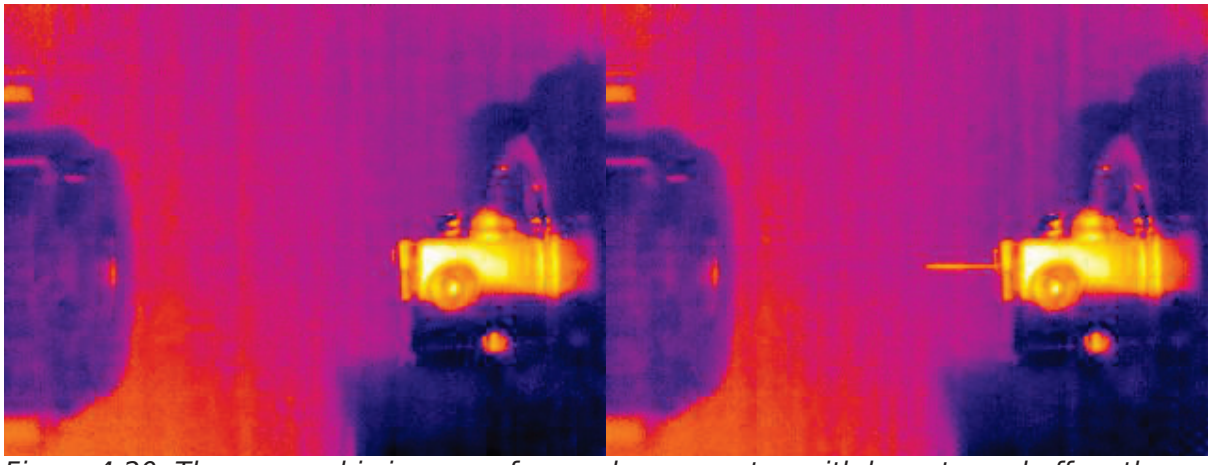

Figure 4-20: Thermographic images of open damage setup with laser turned off on the left and laser turned on on the right hand side.

larger area and shows an increase in temperature of about 1 K of the fibre tip when the laser is turned on (see Figure 4-20).

For the measurement with the FBG a 2 km long sample of standard Ge doped SMF from telecommunications was used in the long-term damage setup. At the launching end the FBG was positioned within the first 10 mm of the fibre by precision cleaving. At the other end of the 2 km fibre an amplified spontaneous emission (ASE) light source and an optical spectrum analyser (OSA) were attached using a 3 dB coupler according to Figure 4-21. In this manner the reflection of the FBG could be monitored. From the change of this reflection, shown in Figure 4-22, a temperature change of 1 K integrated over the length of the FBG was calculated, when the laser was turned on. The ridges seen in the graph are very interesting. There seems to be a Fabry-Pérot interference between the FBG and the fibre end surface. It also changes over the irradiation period. The FBG seems to be altered by the 405 nm irradiation.

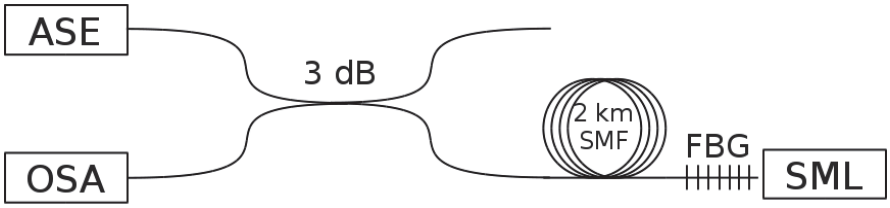

Figure 4-21: Setup for temperature measurement in a SMF fibre tip with fibre Bragg grating (FBG), amplified spontaneous emission light source (ASE), optical spectrum analyser (OSA), and 3dB coupler.

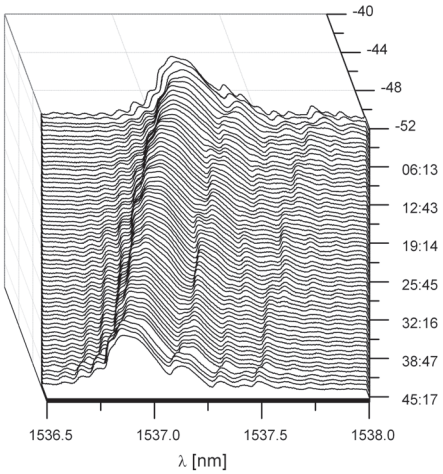

Figure 4-22: Birds view of the waterfall diagram of spectrally reflected light over time. After the laser is switched on the reflection wavelength increases slightly, then decreases slowly over 44 h. After the laser is switched off the wavelength decreases slightly, but abruptly.

4.6 Investigation of fibre surface damage

4.6.1 Overview of examination methods

In all long-term experiments with MML or SML, a modification of the launching end surface of the fibre samples could be observed and a series of different analyses was started. With an optical microscope with 200x magnification the broad outline of the damage is visible. For images with a higher magnification and for characterising the structure the damage was investigated with a confocal microscope. By use of this method the thickness of the projections could be determined. A much more detailed picture could be taken with atomic force (AFM) and scanning electron microscopy (SEM). The investigation with the SEM allowed for energy dispersive x-ray spectroscopy (EDX) as well, which is a chemical element detection method. To determine the distribution of elements on the fibre surface, two samples were examined with a time-of-flight secondary ion mass spec-

trometer (ToF-SIMS). The preparation of two samples for an high resolution transmission electron microscope (HR-TEM) allowed the examination of the cross section of the damage.

4.6.2 Microscopic surface examination

A cross could be seen on the surfaces of the launching ends of MML damaged samples. The shape of the cross is formed by the two cross-combined multi-mode laser diodes, if only one laser diode in the MML was turned on, then a line was formed. For SML damaged samples only a spot was observed. The marks were produced within the irradiation periods of a few days up to two weeks. The focusing is very important to obtain distinctive and clear shapes.

The launching surface of the first LMF GP sample damaged with the SML is shown in Figure 4-23 a). A modification was visible on the core of the fibre. The modification was

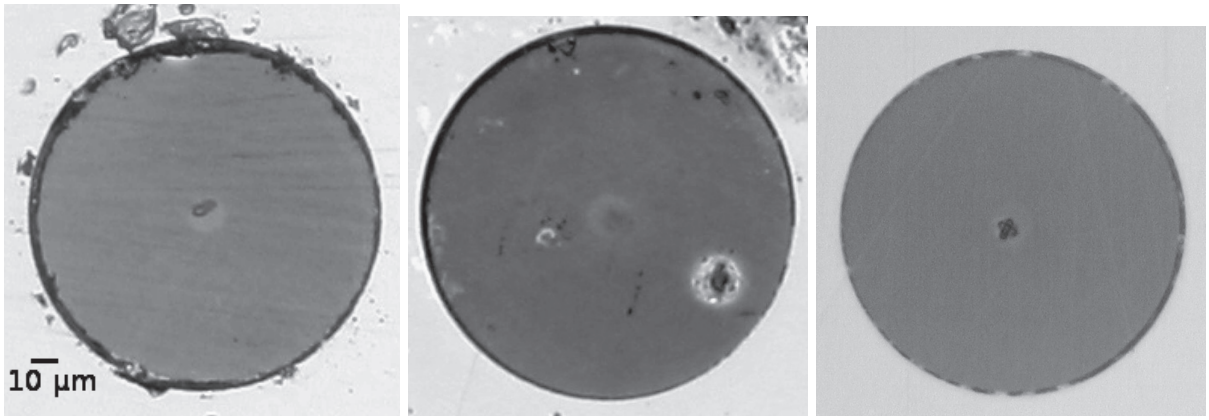

a) *b)* *c)*

Figure 4-23: Light microscope images of LMF GP samples: a) damaged with SML at two launching spots. b) damaged with MML. The modification covers about half the core. The white spots are no damage but dirt on the surface. c) damaged with MML. In this case the spot is much more distinct and the cross-combined laser diode beams can be seen.

not circular, but elliptical and about 10 µm long and 6 µm wide. This elliptical shape was formed by the adjustment, a superposition of the modifications by the first and second launching spot was seen. Unfortunately, no conclusive SEM analysis could be performed on this interesting sample.

The examination of the LMF GP samples damaged with MML in Figure 4-23 b) and c) showed a modification similar to the damage with the SML. In the first experiment, when the focusing was not adjusted, the modification was circular and blurry. The modification on the second irradiated fibre had a very distinctive shape. In both cases the modification

covers the core only partly, in a way that the spectral measurements of the fibre material were possible.

a) b) c)

Figure 4-24: a) CC sample after 160 h of irradiation with MML. No loss was seen during the irradiation, but the surface modification is clearly visible. The damage procedure was discontinued too early. b) Same surface with lit-up core. c) Lit-up core of CC sample with cross and line shaped damage.

The damaged CC samples exhibited the cross shape on the launching surface of the fibres, too, as it is shown in Figure 4-24 a) and b). If only one laser diode of the MML was operating, then only a line was formed. Figure 4-24 c) shows the CC sample which was first irradiated with two diodes and subsequently with only one and adjusted. On one side of the core the cross shape is visible and on the other side the line shape.

An interesting result was achieved with the CP sample. This particular sample was irradiated at three launching spots, which was visible with the light microscope as well, see

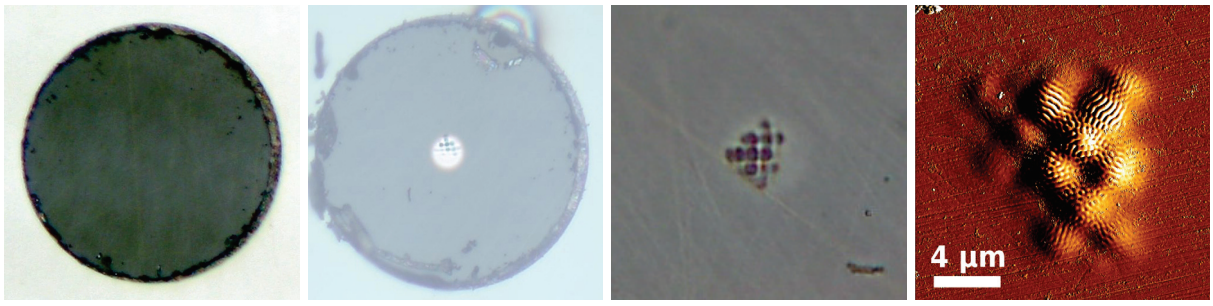

a) b) c) d)

Figure 4-25: CP sample a) before and b) after 241 h of irradiation with MML at three launching spots. c) Confocal microscope image of the same sample. d) AFM topography gradient of the modification on the fibre core.

Figure 4-25 b). It was further examined using the confocal microscope and AFM. In Figure 4-25 c) the structures are clearly recognisable. The cross shape had a diameter of about 6 µm and the modification was a projection of 800 nm height. With the AFM another finer ripple structure was found on the cross shapes (see Figure 4-25 d)). This ripple had a peri-

odicity of about 350 to 400 nm and the ripples were oriented along the slow axis of the single laser diodes. Along this axis the laser diodes are also polarised. In the centre, where the laser beams cross, a quasi-circular polarisation can be assumed and the ripples change shape into cones. The cross shape was not randomly oriented, but had the same orientation in every launching spot. This also indicates that the origin of the cross shape is the cross-combination of the multi-mode laser diodes.

For all irradiated LMF samples alike, the distal end surfaces did not show damages comparable to the launching surfaces. In Figure 4-26 the distal end of the CP sample can be examined. An aggregation of particles on the core was visible. The slight modification along the core-cladding interface could also be attributed to the refractive index difference highlighted by the confocal measurement.

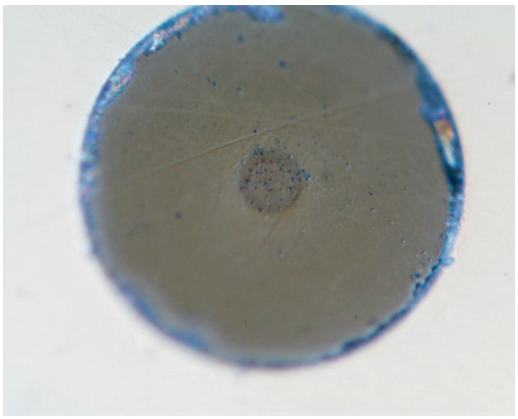

Figure 4-26: Distal end surface of CP sample from Figure 4-25 with confocal microscope.

In an experiment with a CC sample of *6u* fibre it was shown, that the structure cannot only grow on the core, but also on the cladding of the fibre. The launching end was adjusted to maximum fibre output power and then translated within the focusing plane in a way that the cladding and not the core was irradiated. After the irradiation over several days the cross shape was found in the F doped cladding region as well. Figure 4-27 shows light microscopy and AFM images. The AFM topography again highlights the fine ripple structure. In addition, a smoothing and cleaning of the surface in the surrounding area was found.

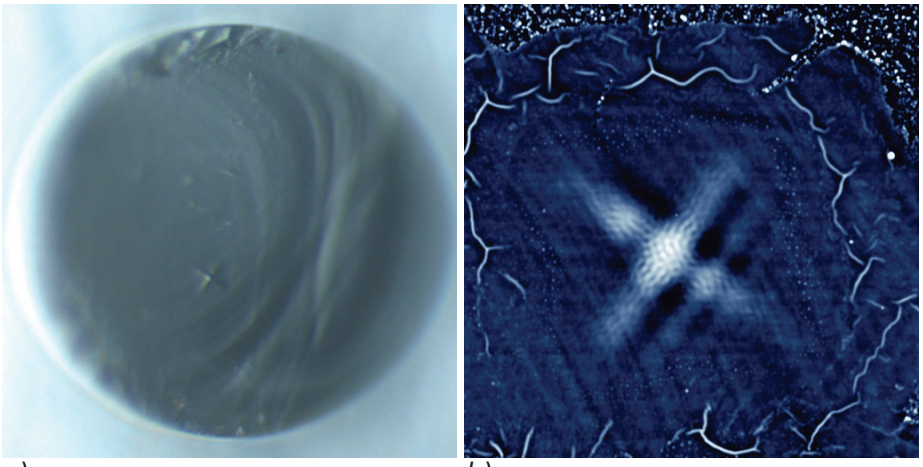

a) b)

Figure 4-27: a) Light microscope image of LMF CC sample irradiated in the cladding region with the MML. The structure of the not optimal cleave is recognisable. b) AFM topography of the damage in the cladding. The fine ripple and a smoothing effect are obvious.

In order to be able to determine the different influences of irradiation time, coupling efficiency or power density, and surface treatment of the fibre on the height and form of the structures, examinations of SMF CC and CFC samples were performed (first four samples in Figure 4-16). The samples were irradiated with the MML and the results of the AFM topography measurements are shown in Figure 4-28. The CC and CFC samples of *SM 400/125* were irradiated at comparable coupling efficiencies and for similar time periods. Despite that, the CC sample showed a stronger formation of the ripples, while the structure of the CFC sample was more than twice as high. Growth rates of about 48 nm/day and 110 nm/day, respectively, were calculated. The CC sample of *PM-S405-HP* had a much better coupling efficiency than the CFC sample, but a shorter irradiation time. Still, this was enough for the structure to grow higher and form more distinct ripples. For

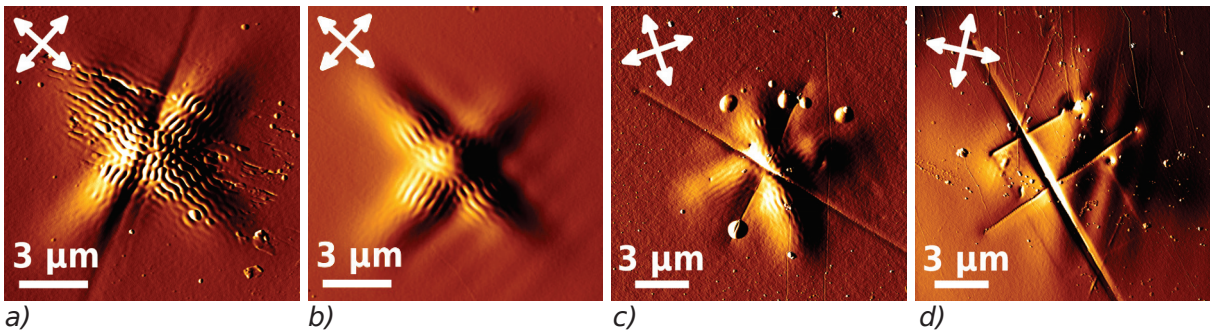

a) b) c) d)

Figure 4-28: AFM topography gradients of launching SMF ends after irradiation with MML: SM 400/125 CC (250 h, 500 nm high), SM 400/125 CFC (260 h, 1200 nm high), PM-S405-HP CC (137 h, 350 nm high) and PM-S405-HP CFC (212 h, 250 nm high). The polarisation of the laser diodes is denoted by the arrows. The grooves in the images are erosion from SEM EDX line scans.

these samples the calculated growth rates are about 61 nm/day and 28 nm/day, respectively (see also Table 4-7). Similar values are found for the CC samples, but due to different coupling efficiencies the growth rates of the CFC samples are quite different. Unfortunately, the samples were altered before the AFM by EDX line scans in the SEM. The erosion from that is clearly visible as straight grooves.

The structure did not only appear on pure silica core fibres, but also on the end surfaces of the Ge doped *SM 450* fibre samples. Figure 4-29 a) shows the proximal end of the sample irradiated for 7 days and the cross shape is clearly visible on the cleaved end surface. The distal end, which is shown in Figure 4-29 b), exhibits a large accumulation of particles. These could cover a possible modification of the core on the distal end.

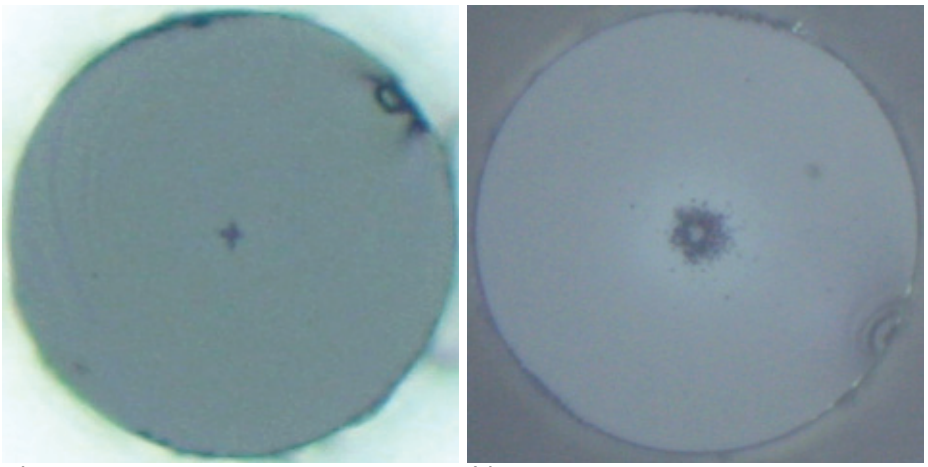

a) *b)*

Figure 4-29: a) Light microscope image of proximal end of SM 450 CC sample irradiated with the MML for 7 days. b) Distal end surface of same fibre sample.

A ripple structure was also observed on the cores of the launching ends of SML damaged SM 400-SC CC samples. From Figure 4-30 a) the diameter of the altered area can be estimated to 2.5 µm. Thus, the core was fully covered by the surface structure. The ripple periodicity was also in the order of 300 to 400 nm and the ripples were oriented parallel to the laser polarisation, just as for the MML. For the second sample with a higher coupling efficiency the structure grew much higher over a similar irradiation period. The growth rates in these cases of 37 nm/day and 57 nm/day are close to the values of the CC samples irradiated with the MML (comparison in Table 4-7). The area around the exposed material shows some smoothing in Figure 4-30 b).

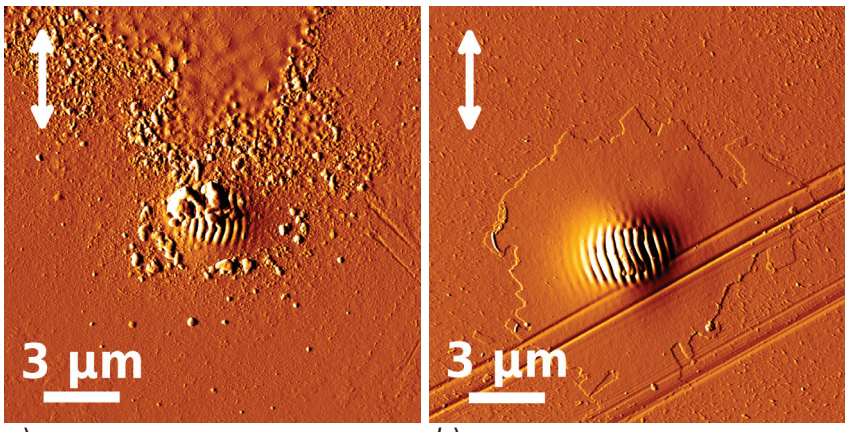

a) *b)*

Figure 4-30: AFM topography gradients of launching SMF ends after irradiation with SML: SM 400-SC CC (260 h, 400 nm high, some dirt can be seen) and SM 400-SC CC (295 h, 700 nm high). The polarisation of the laser diode is denoted by the arrow.

Table 4-7: Summary of measurement values for CC and CFC samples of SMF types SM 400/125, SM 400-SC and PM-S405-HP.

	CC MML	**CC MML**	**CC SML**	**CC SML**	**CFC MML**	**CFC MML**
Height [nm]	500	350	400	700	1200	250
Irradiation time [h]	250	137	260	295	260	212
Growth rate [nm/day]	48	61,3	36,9	56,9	110,9	28,3
$P_{out,fibre}$ [mW]	74.2	80.5	73.6	92.5	73.4	61.3

4.6.3 Spectroscopic surface examination

Some interesting samples were taken to a SEM for a detailed element analysis using EDX. In the SEM the structures could be seen clearly and the ripple on top of it as well. Several element analyses showed no extra elements for CC samples of LMF or SMF besides silicon, oxygen, carbon and metals, like platinum, gold or aluminium from preparation or the sputtering process. A study of the cross shape in the cladding (see Figure 4-31) was performed without sputtering the surface. For an acceleration voltage of 5 kV secondary electrons from as deep as 400 nm in SiO_2 were received. But the spectra of the structure and a reference area were almost identical. With a higher acceleration voltage of 10 kV

material as deep as 1200 nm was interrogated. The observation remained the same for this case, only that the amount of detected metals and carbon is reduced in comparison to silicon and oxygen. This signifies that these elements are scarcely distributed over the fibre surface, the fixture and also inside the chamber. EDX line scans on several samples showed no significant differences in elemental composition concerning carbon, oxygen or silicon in exposed and non-exposed areas. As an example the line scans on the CC sample from Figure 4-28 a) are shown in Figure 4-32 a) for 5 kV and b) for 10 kV.

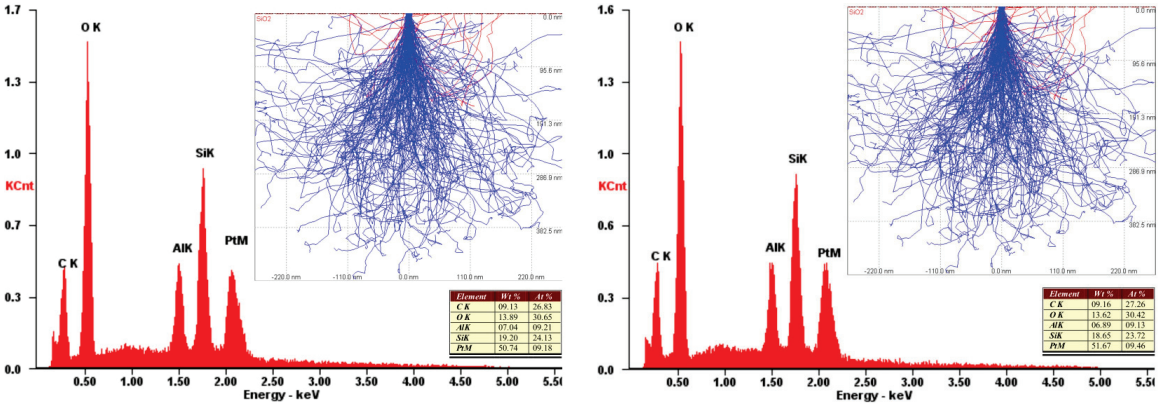

a) *b)*

Figure 4-31: EDX energy spectra of the structure in the cladding formed with MML at an acceleration voltage of 5 kV: a) damaged area or structure and b) undamaged reference area. The insets show a Monte-Carlo simulation of the escape depth of electrons (red: backscattered, blue: secondary) for SiO_2.

To verify the EDX analyses or maybe find small traces of contamination on the core, time-of-flight secondary ion mass spectroscopy (ToF-SIMS) was performed on damaged *SM 400/125 CC* and GP samples. Examples for the distribution of carbon, silicon and aluminium in the core area of a CC sample are shown in Figure 4-33. The carbon was evenly distributed over the surface and all other possible contaminants, mainly metals, that were found, were not concentrated in the core, but in the outer regions of the fibre surface. This, in turn, is a sign for impure overcladding tubes during fibre production and not for contamination during sample irradiation.

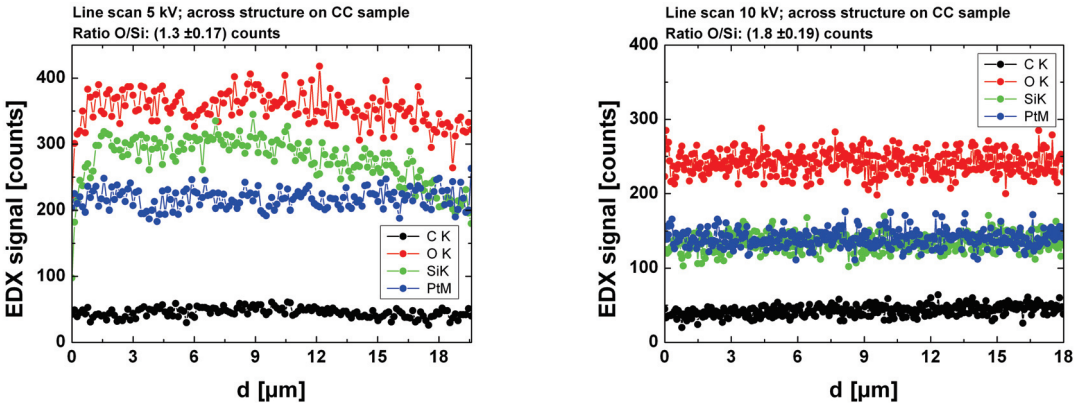

a) *b)*

Figure 4-32: EDX line scans on a SMF CC sample across the structure: a) for 5 kV and b) for 10 kV acceleration voltage.

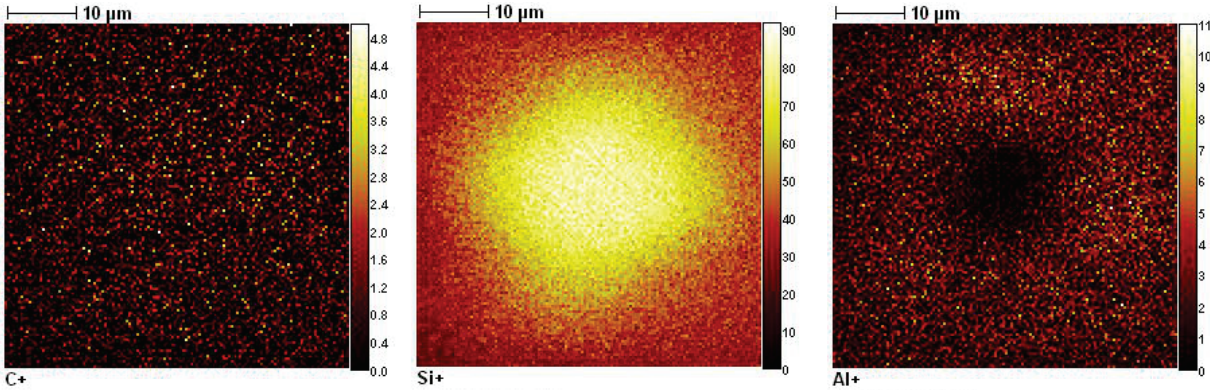

Figure 4-33: ToF-SIMS maps of core area of CC sample irradiated with MML for four days. The maps of carbon, silicon and aluminium are presented.

4.6.4 Microscopic cross section examination

In order to investigate the cross section of the damage, two 150 nm thick focused ion beam (FIB) prepared lamellae of MML damage spots were examined in a high resolution transmission electron microscopy (HR-TEM). The procedure was performed for GP and CC samples of *SM 400/125*. To be able to examine the cross sections, lamellae of the damaged area had to be prepared. Figure 4-34 shows the steps of the procedure for the CC sample. The lamellae had a thickness of 150 nm and were cut out in a way that, additionally to the damaged area, an undamaged reference area was preserved.

The lamellae were then transferred to the HR-TEM and examined up to a magnification of 50 000. The results for the GP and CC sample are shown in Figure 4-35 and 4-37, respectively. Within the images the black line on top was the remainder of the platinum bar and sputtering specimen. Below that a light stripe of material can be seen and then a

darker area which was the actual fibre core material. The light stripe was the altered core material and the projection we found with the AFM. The lighter colour indicates less electron scattering and thus a lower material density. No diffraction patterns indicating crystalline structures were observed in the TEM, hence the layer is an amorphous compound. The GP sample had a stronger barrier between higher and lower density material in comparison to the CC sample, no other apparent difference was observed. An even closer look in Figure 4-36 shows a porous structure with craters on the interface to the platinum. The craters are the cross sections of the ripple structure. Neither the light stripe nor the porous craters were observed in the reference areas of the lamellae. Some finer porosity can be observed in the reference area as well. But this reference area is very close to the damage and was probably also exposed to some laser light. The thickness of the layer of lower density was estimated to be 130 nm for the CC sample irradiated for four days and 100 nm for the GP sample with three days of irradiation. These values give growth rates of about 33 nm/day which is close to the growth rates calculated from the AFM measurements.

EDX analyses were also performed in the TEM. Again, no significant differences in chemical composition could be found between the layer of lower and higher density silica material. No other chemicals besides silicon, oxygen, carbon, and metals from the preparation were found.

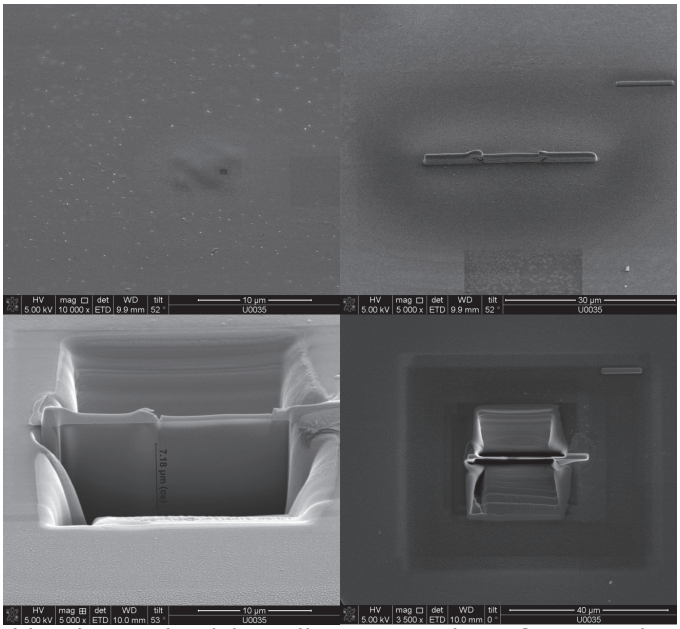

Figure 4-34: Focused ion beam (FIB) lamella preparation of a MML damaged CC sample. A 150 nm thick lamella, with the damaged area on the right hand side, was screened from the ion beam using a platinum bar. Then the lamella was cut out and placed in the TEM.

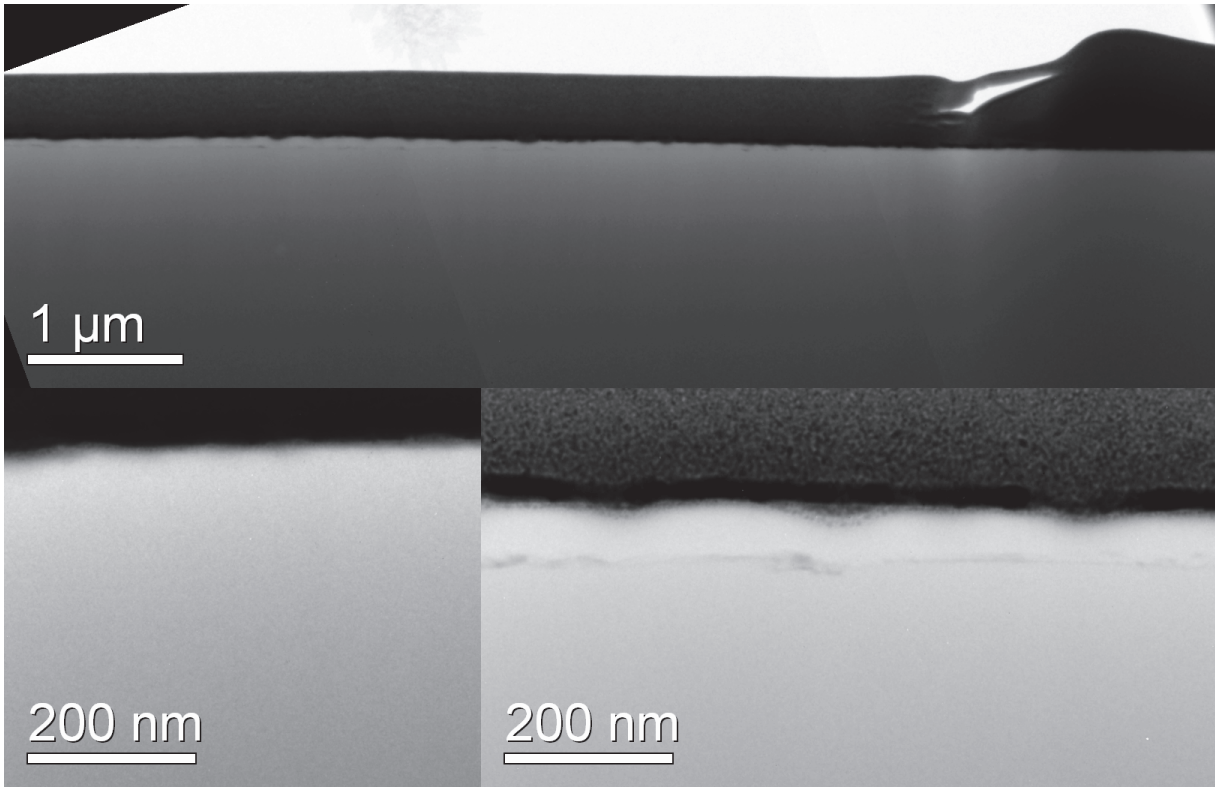

Figure 4-35: HR-TEM image of a 150 nm thick lamella of a GP sample irradiated with MML for three days. The compilation shows an overview on top, reference area on the lower left hand side and damaged area on the lower right hand side. The damaged area can be described with the sputter specimen platinum on top (black), below a porous, lower density silica material (lighter grey), and further below unchanged fibre material (darker grey) with a darker barrier material in between.

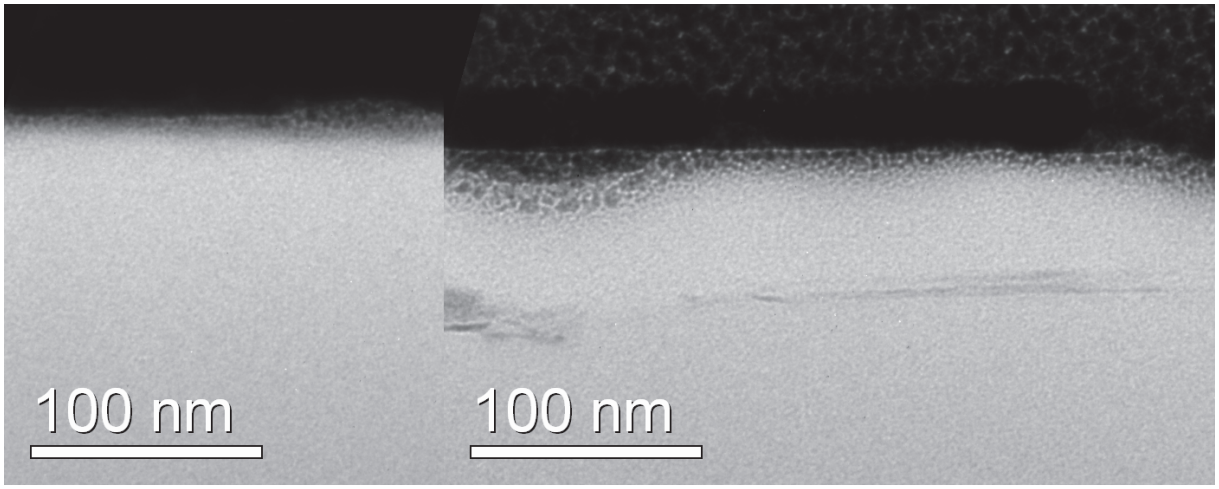

Figure 4-36: HR-TEM image with higher magnification of a 150 nm thick lamella of a GP sample irradiated with MML for three days. The compilation shows a reference area on the left hand side and damaged area on the right hand side.

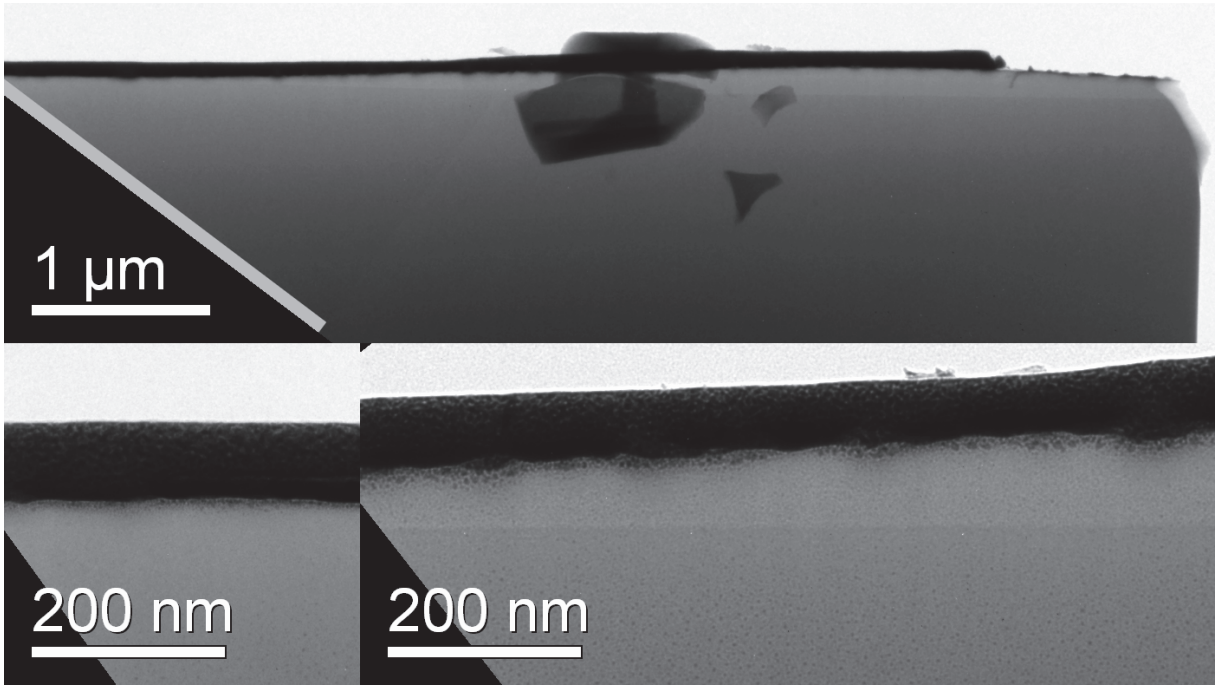

Figure 4-37: HR-TEM image of a 150 nm thick lamella of a CC sample irradiated with MML for four days. The compilation shows an overview on top, reference area on the lower left hand side and damaged area on the lower right hand side. The damaged area can be described with the sputter specimen platinum on top (black), below a porous, lower density silica material (lighter grey), and further below unchanged fibre material (darker grey).

4.7 Influence of the surface effects on the fibre-optic transmission system

4.7.1 Spectral influences of surface structure

The structural modifications, that were observed on the launching end surfaces of the fibres, mainly influence the coupling of light into the fibre core. Especially, for SMF, where the structure covers the whole core, the coupling losses are inevitable. Taking a look at a height line scan of a SML damage spot, for example Figure 4-38 shows a height scan across 4-30 b), the ripple structure is obvious. It had a periodicity of 250 to 400 nm in all cases, which did not vary with irradiation time. This ripple structure did not only form a scattering centre, but the projection also formed a convex lens. In the example, a lens of diameter c = 2.5 to 3.5 µm and a thickness of h = 450 to 600 nm would have a very short focal length of f = 3 to 6 µm, using the lensmaker's equation for thin lenses.

$$\frac{1}{f} = (n-1)\cdot\left(\frac{1}{R_1}-\frac{1}{R_2}\right) \approx \frac{n-1}{R_1} \quad ; \text{with} \quad R_1 = \frac{h}{2}+\frac{c^2}{8\cdot h} \tag{4-8}$$

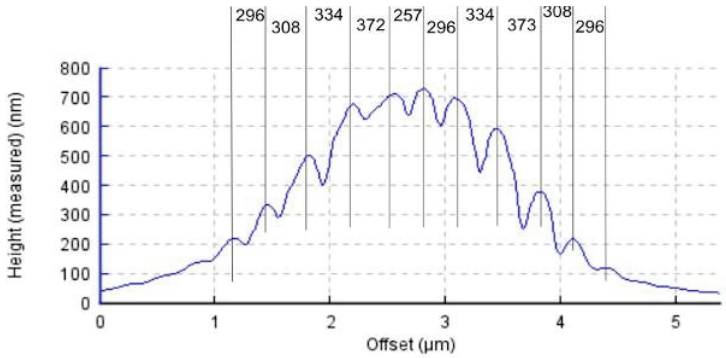

Figure 4-38: Diagonal line scan across AFM image from Figure 4-30 b) (SM 400-SC CC sample). Peaks of the crests are marked and labelled with the spacing to the next peak.

The losses due to the scattering centre and the convex lens are broadband, but only show their influence during the operation of the transmission system at the laser wavelength. They can be measured spectrally with a SMF when the structure covers the core completely. Figure 4-39 shows the difference for a fibre with a damaged end and with the end cleaved off. An increase of induced loss with decreasing wavelength was observed and the loss of about 3 dB at 400 nm corresponded well with the final loss of this sample (black curve in Figure 4-19). If the end with the surface structure was cleaved off, then the fibre output power returned to its initial value, too.

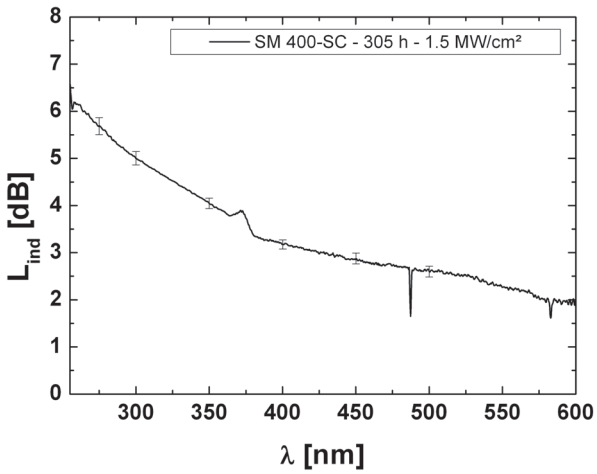

Figure 4-39: Spectral loss over wavelength by a SML damage spot on a CC sample of SM 400-SC. The artefact at 486 nm is an oscillation due to the hydrogen Balmer line D_β. The peak at 375 nm is the second mode cut-off of this fibre.

4.7.2 Simulation of launching end surface damage

The influence of a growing surface structure on the fibre transmission was reconstructed using simulations. The software that was employed uses the finite-difference time-domain method and is called FDTD Solutions by Lumerical Solutions, Inc.. A SMF with a core diameter of a = 1.2 µm, a refractive index of n_{co} = 1.45441 (SiO_2 glass, [Palik1997]) in the core and of n_{cl} = 1.44956 (F doped SiO_2) in the cladding was designed, giving a numerical aperture NA = 0.12 and a V number of V = 2.2 at λ_0 = 405 nm wavelength. The cut-off wavelength λ_{CO} for this SMF is 376 nm.

$$V = k_0 \cdot a \cdot \mathrm{NA} \quad ; \quad k_0 = \frac{2 \cdot \pi}{\lambda_0} \quad ; \quad \mathrm{NA} = \sqrt{n_{\mathrm{co}}^2 - n_{\mathrm{cl}}^2} \tag{4-9}$$

The surface structure was also modelled out of SiO_2 glass with a diameter of 3 µm and an approximated structural equation of $w = \sin^2(u \cdot 11 + 3 \cdot v^3 - 3 \cdot v)$. This equation results in eleven ripples across 3 µm, a periodicity of about 273 nm. Additional parameters for the growth of the structure, like height in the centre, the radius of curvature, and the amplitude of the ripple, are given in Table 4-8. The periodic structure in Figure 4-40 was designed to fit the surface structure measured with AFM in Figure 4-30 b). The smaller periodic structures are down scaled designs of the 700 nm high structure. Additional simulations for a periodic structure without the properties of a lens and heights of 0 and 700 nm were performed.

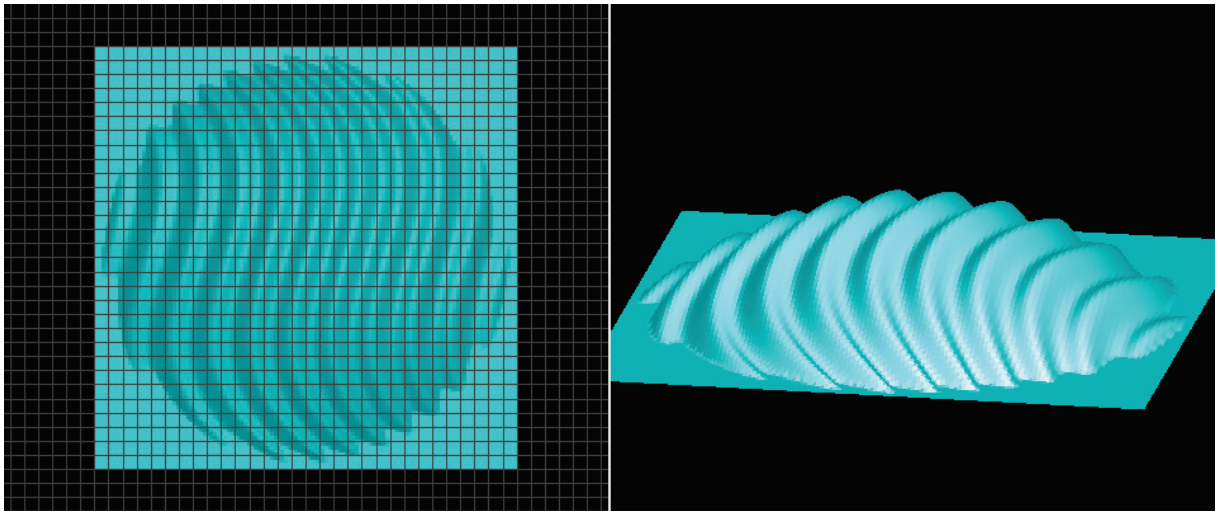

Figure 4-40: Model of 700 nm high periodic surface structure, adapted to Figure 4-30 b).

Table 4-8: Parameters of simulated surface structures.

Height [nm]	Radius of curvature [µm]	Ripple amplitude [nm]
100	11	15
300	3.6	40
500	2.2	70
700	1.5	100

The laser source with a wavelength of 405 nm was focused on the fibre end surface using a thin lens with a numerical aperture NA = 0.12 and a focal length of f = 7 µm. The polarisation of the laser source can be set parallel or perpendicular to the ripples. Both cases were studied here. The output power of the source was set in proportion to the output power at the end of a 120 µm long piece of SMF. These powers are measured by monitors that are inserted in the simulation at the particular positions. An example for the setup is shown in Figure 4-41 a) with the laser source, monitors, structure and SMF. A coupling efficiency of 87 % was achieved for the case without periodic surface structure in Figure 4-41 b). The growth of the structure was assumed to 60 nm/day, which is at the upper end of the perceived growth from AFM measurements on MML and SML damage spots. From heights of 100, 300, 500 and 700 nm time periods of 1.7, 5, 8.3 and 11.7 days were calculated. The loss was calculated from the ratio of the coupling efficiencies with and without structure.

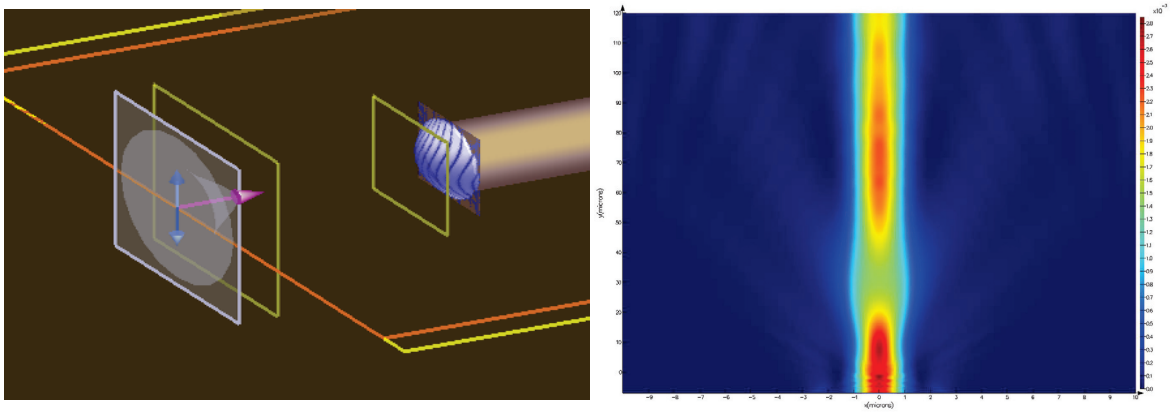

a) *b)*

Figure 4-41: a) Example of a simulation setup with a damaged fibre surface. The vertically polarised 405 nm laser source (violet and blue arrows), monitors (yellow frames), the surface structure (blue) and the fibre core (light brown) can be recognised. b) Power distribution of coupling from laser source into SMF with an efficiency of 87 %.

In the simulation perfectly matched layers (PML) are used as boundary conditions (BC). They are designed to absorb incident light with minimal reflections, but in the results, some reflections are seen and these result in interference patterns.

4.7.3 Results for damage on launching fibre end

The results of the simulations are presented as a distribution of the power in longitudinal and lateral direction. The laser source is located at y = -7 µm and the fibre starts at y = 0 µm The coupling efficiencies were directly calculated from the values provided by the monitor elements in front and at the end of the fibre. In Figures 4-42 and 4-43 the results of the simulations with the laser polarisation parallel to the ripples are shown. The results with polarisation perpendicular to the ripples look very similar to these and are not disclosed here.

The graphs show that the periodic surface structures focus the laser light right behind the fibre launching end. The numerical aperture in the fibre and focal length of the structures were calculated from the refractive index, diameter and radius of curvature according to Formula 4-8 and are given in Table 4-9. Higher surface structures focus the light stronger due to shorter focal lengths. These additional focusing elements interfere with the coupling by increasing the divergence angle of the light. This in turn does not allow the guiding of the light in the SMF since the numerical apertures are increased to values up to 0.66.

Table 4-9: Calculated properties of simulated surface structures and losses.

Height [nm]	Calculated focal length [µm]	Numerical aperture	Loss [dB]
100	24	0.09	∥ 0.08 (⊥ 0.07)
300	7.9	0.28	∥ 0.69 (⊥ 0.62)
500	4.8	0.45	∥ 1.8 (⊥ 1.6)
700	3.3	0.66	∥ 3.2 (⊥ 2.9)

The calculated losses for different heights of the structure were arranged in the same way as the loss curves from the damage measurements. If the polarisation was perpendicular to the ripples, then the loss was slightly lower than for parallel polarisation as can be seen in Figure 4-44. The curves were also exponentially fitted and resulted in $L=\exp(0.116\cdot t)-1$ for perpendicular and $L=\exp(0.122\cdot t)-1$ for parallel polarisation;

with L in dB and t in days. The correlation coefficient of both fits is $r^2 > 0.991$. The rates of these two exponential fits are close to the rates of 0.14 and 0.22 for SML damaged CC samples of SMF.

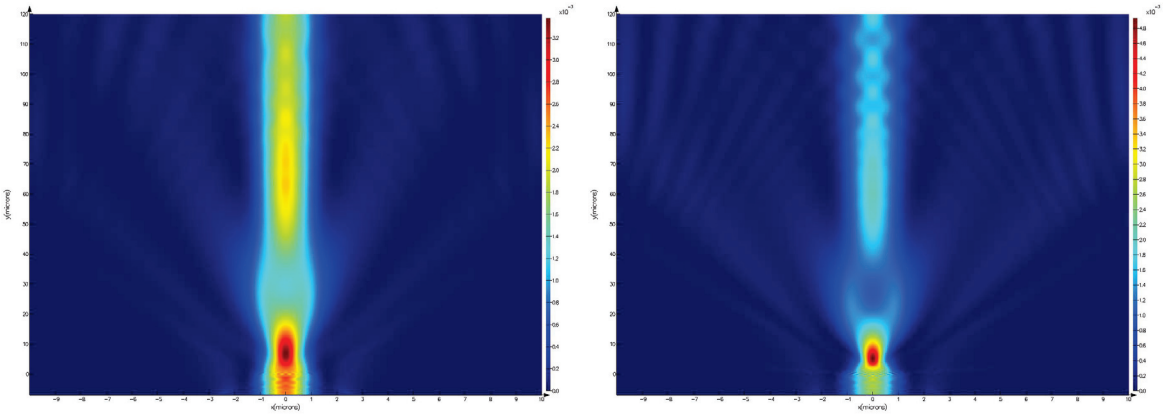

a) *b)*

Figure 4-42: Power distributions of coupling from laser source into SMF through a) 100 nm and b) 300 nm periodic surface structures. The graphs exhibit some interferences from reflections at the boundary conditions.

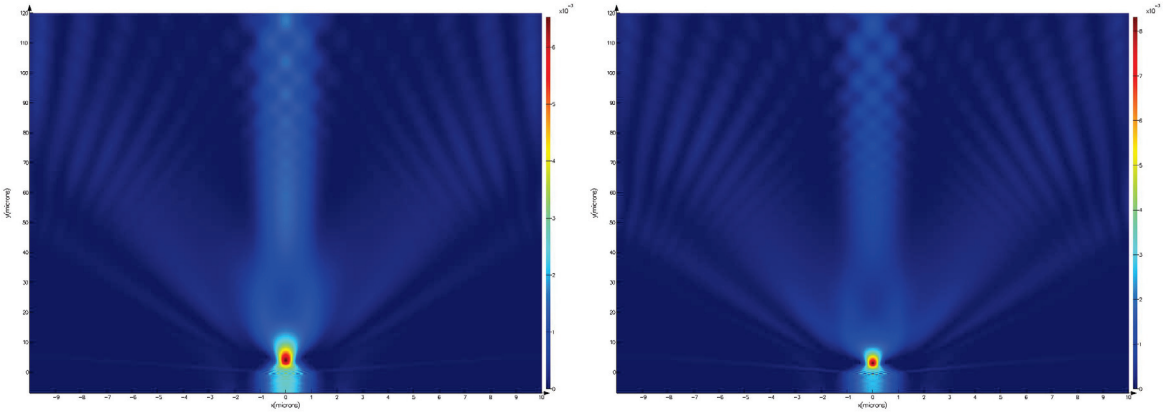

a) *b)*

Figure 4-43: Power distributions of coupling from laser source into SMF through a) 500 nm and b) 700 nm periodic surface structures. The graphs exhibit some interferences from reflections at the boundary conditions.

The simulations of periodic structures without the lens properties showed that the periodic structure itself results in a high loss of over 2 dB for parallel polarisation. This was a little less for perpendicular polarisation, but only if the amplitude of the ripples is as high as the structure, which was not seen in the AFM measurements.

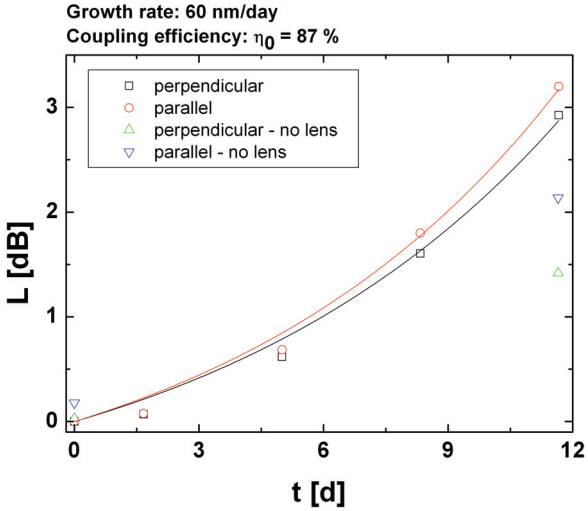

Figure 4-44: Simulated increase of loss over time in a SMF by increasing height of a periodic surface structure. The black curve shows polarisation perpendicular and the red curve parallel to the ripples. The initial coupling efficiency was 87 % and a growth rate of 60 nm/day was assumed. Green and blue symbols are results for structures without the lens properties.

4.7.4 Impact on spectral fibre transmission

A first simulation of the spectral influence of the 700 nm periodic structure with lens properties is shown in Figure 4-45. A white light source from 200 to 800 nm with a Gaussian distribution was used and the transmissions without and with periodic structure are compared. For wavelengths below 550 nm, which is not shown here, the loss is actually negative. This is due to enhanced coupling of longer wavelengths into the fibre by the structure. But these wavelengths are weakly guided and should be stripped out in a simulation with a bend fibre. The trend of the curve is similar to the one measured in Figure 4-39. Generally the loss is lower in the simulation than in the experiment. Nevertheless the simulation also shows the discontinuity below the cut-off wavelength of the SMF.

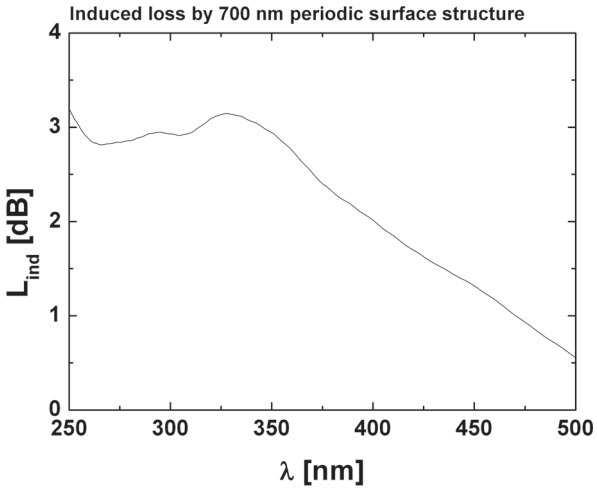

Figure 4-45: Simulated induced loss of a 700 nm high periodic surface structure on a 120 µm long SMF.

4.8 Discussion

In the experiments carried out at a wavelength of 405 nm, the CW power density in the laser beam waist was at least in the range of 0.5 to 1 MW/cm². Maximum values of 2.5 MW/cm² were obtained when the laser and fibre were operating in the single-mode regime. A loss was induced in transmission systems of LMF or SMF and MML or SML at the laser wavelength. A correlation of the loss measurements with the fibre surface quality indicates that cleaved surfaces have a damage rate lower than glued-and-polished surfaces by a factor of four.

With the new spectral measurement setup it was possible to measure the fibres with core diameters of less than 2.5 µm below 200 nm. An absorption change could be seen only in the LMF samples and short-term irradiated SMF samples. The damaged area of 6 µm in diameter on the 15 µm core LMF is over-illuminated by the deuterium lamp. Thus, the damage spot at the launching surface cannot interfere with the loss measurement. No change of the fibre absorption occurred at the laser wavelength, but in the DUV at the oxygen deficient centre ODC(II) at 245 nm and the E'_γ centre at 214 nm. The ODC(II) is an unrelaxed oxygen vacancy or a divalent silicon bond, which in our case might be precursors for defect centres [Skuja1998]. A transformation of the ODC(II) centres (5 eV) into E'_γ centres (5.8 eV), with an unpaired sp^3 electron, can be explained in several ways. A transformation through coherent two-photon absorption of 405 nm (3 eV) photons seems unlikely in a low power experiment of this type, but the probability of this increases with the

extremely long exposure. A two-step process is also possible [Messina2008] – if an exciton is generated when two consecutive photons are absorbed incoherently, then a non-radiative decay of the exciton can induce an E'_γ centre close to the absorption site. On the other hand, E'_γ centres can be generated directly at the absorption site by a two-step ionization of ODC(II) centres.

Nevertheless, this transformation reduces the number of ODC(II) centres and increases the number of E'_γ centres. As reported in the introduction, this bleaching of ODC(II) is also known from excimer laser experiments [Imai1991]. Since the fibres were stored for a long time before irradiation, all molecular H_2 remaining from their production should be reduced to atmospheric concentrations within the 125 µm fibres. In this case a passivation of defects from molecular H_2 is neglectable.

The increased loss of the Ge doped fibre samples in the visible range is due to the generation of defect centres at Ge sites, similar to those at Si sites. This effect is strong especially in oxygen deficient Ge doped material [Poyntz-Wright1989]. The broad half width of the Ge defects absorption extends into the visible range and affects the wavelength of 405 nm considerably. The disagreement of the spectral loss measurement and the loss calculated from the fibre output power monitoring is due to the few-mode nature of this fibre type at 405 nm. The transmitted power is split into the fundamental mode (FM) and a few higher-order modes (HOM). The total attenuation α_{tot} for this case follows the equation:

$$\alpha_{tot}(\lambda) = \frac{\alpha_{FM}(\lambda) \cdot P_{FM}(\lambda) + \alpha_{HOM}(\lambda) \cdot P_{HOM}(\lambda)}{P_{tot}} \qquad (4\text{-}10).$$

The FM is guided in the centre, while the HOM are guided in the periphery. The Ge concentration is higher in the centre than in the periphery and therefore the FM is more affected by the induced loss than the HOM. For wavelengths much shorter than the cut-off wavelength the HOM propagate closer to the centre and experience a higher attenuation. Since the Ge fibre samples were not forced into single-mode operation, for example by a small loop, the power could be mostly transmitted in HOM during irradiation. The spectral measurement on the other hand might probe the centre of the core more than the periphery resulting in a higher measured loss. Owing to the splitting of the transmitted power into FM and HOM below the cut-off wavelength, a drop in the induced loss was received.

Periodic surface structures have been observed on the end surfaces of all synthetic silica fibres when they were exposed to long-term irradiation with light from a 405 nm CW diode laser. The surface structures are generated when the laser power is at a level which is three magnitudes of order lower than that of the optical damage threshold. The latter is

higher than 1 GW/cm² for pulsed lasers in the NUV. Nevertheless, a deformation of the synthetic silica surface over a duration of several days was observed.

Similar periodic surface structures with ripples, called laser-induced periodic surface structures (LIPSS), were seen in short-pulsed laser experiments on mostly crystalline wide band-gap materials [Birnbaum1965, Keilmann1982, Driel1982]. Those structures also exhibit bifurcations, bends and break-ups, as it was seen in the case here. One of the currently accepted models explains these structures by self-organisation of an unstable surface layer by duelling processes of desorption and self-diffusion [Reif2006]. In the past, an interference model was used to describe these effects, but in the last decades new results and simulations have been presented to contradict this model [Preston1989, Reif2004, Reif2010].

It is suggested in this work that the fibre surface is destabilised by a multi-step surface ionisation leading to Coulomb explosion, that is desorption. The surface ionisation starts with the generation of unpaired electrons on or close to the surface through multi-step absorption of photons. This process is enhanced by the presence of electronic defects in the form of colour centres, mainly the E'_γ centre. The existence and generation of E'_γ centres in the fibre bulk material was shown and should happen on the surface as well. The E'_γ centres are generated either from ODC(II) as in the bulk of the fibre or from silan-

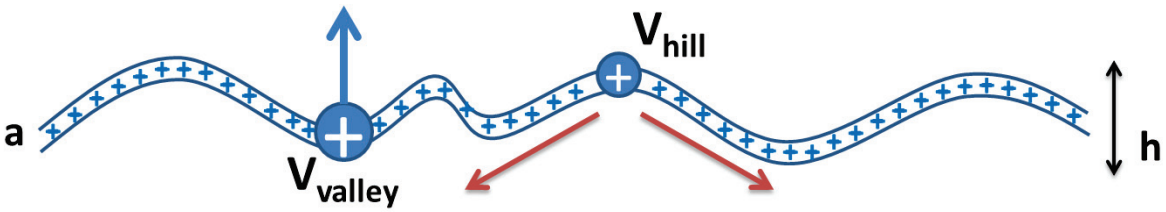

Figure 4-46: Model used to describe the self-organisation of an unstable surface layer. The layer has a modulation or roughness of h *and a thickness of* a*. Charged particles in the valleys* V_{valley} *are especially subject to Coulomb repulsion (blue arrow), while particles on the crests* V_{hill} *are primarily subject to self-diffusion (red arrows). According to [Reif2006].*

one and dioxasilirane surface centres [Skuja1998]. The unpaired electrons can be excited further and above a certain threshold escape from the surface leaving a positively charged surface behind, as shown in Figure 4-46. On this ionised surface coulomb repulsions can build up and lead to coulomb explosion, meaning desorption of material. Further on, duelling processes of material desorption and surface smoothing by atomic self-diffusion lead to self-organizing ripple structures.

The laser and material parameters contributing to the generation of periodic surface structures with short-pulsed laser experiments correspond to the important parameters

that were found [Reif2006, Henyk1999, Reif1989]. The detailed investigation undertaken in this work has concluded that the key parameters that contribute to the generation of the surface structures are polarisation direction, power density, surface roughness, and the presence or generation of ultraviolet defect centres. The thickness *a* of the unstable layer was seen to increase with the last three of these parameters. The dependence of the ripple periodicity on the thickness of the unstable layer could not be demonstrated in this work, yet. Only a slight difference in the mean periodicity between CC and CFC samples is seen and in comparison the ripples are clearer on CC samples for similar irradiation time and induced loss. No obvious periodicity difference between centre and edge of the damage is seen, probably due to the small influenced area and size of the ripples.

A reduction of the surface roughness by flame-polishing did not improve the performance of the fibre samples. To the contrary, the growth of the structure on flame-polished surfaces was higher than for cleaved surfaces. Additionally, the flame-polished samples performed worse than cleaved samples in SML damage experiments on SMF. While the fusion arc treatment reduces the roughness of the surface it might induce precursors for defect centres. During the irradiation the precursors are transformed into surface centres and enhance the destabilisation of the surface layer.

The form and orientation of the ripples depend strongly on the laser polarisation. In the work reported here on silica fibres, the structural orientation of the ripples correlates with the polarisation direction of the laser light. In case of the cross-polarised laser light short ripples and cones are observed, just as for elliptical and circular polarised light in the work of Varlamova and co-workers [Varlamova2007]. Over time the LIPSS grows higher and clearer, which indicates a process with positive feedback.

The formation of the periodic surface structure is a modification of the silica on the surface. It was found that there was no difference in the chemical composition between the core region and the area around or underneath it in the EDX analyses. The examination with the Tof-SIMS showed no contamination of the core area, too. The HR-TEM images showed that there is a surface layer in the area of irradiation with a lower density than the silica material around it. This layer of lower density has a porous structure in its outermost part. Since no diffraction patterns were observed in the TEM, it can be concluded that it is not crystalline but is rather an amorphous layer of lower density silica.

In this research, the fibre end surfaces were not explicitly protected from the environment. Thus, dust particles attracted by an ionized surface and water absorbed by the silica should not be ruled out as triggers of the modification effects seen. However, no other elements beside silicon, oxygen and the sputter specimen were found in significant quantities in the fibre core area by EDX analyses, carried out so far. Additionally, the heating of absorbed water in the fibre core is not likely at the short wavelength of 405 nm

used. Measurements concerning the heating of the launching fibre end detected a temperature increase of only 1 K.

The discovered surface structure consists of a projection and ripples on top of it. The periodicity of the ripples is just below the laser wavelength and ranges from 250 to 400 nm. If the surface structure is very distinct and covers the whole core, e.g. of the SMF, then the structure interferes with the light coupling into the fibre and only a broadband loss can be observed. This broadband power loss is the result of focusing and scattering by the periodic surface structure on the launching fibre end, impairing the coupling efficiency. The growing structure introduces another focusing element into the laser beam, which was also reconstructed using FDTD simulations. The simulations for SMF demonstrated a good accordance with the loss measurement results. This additional focusing element can also explain the different behaviour of LMF and SMF. Since the LMF has a larger core and higher numerical aperture the loss was induced in a more linear fashion and was for example rather low in a case of SMF damaged with SML.

To mitigate the growth of a laser-induced periodic surface structure three parameters need to be adjusted. The first is the power density on the fibre surface, which needs to be reduced. The surface roughness should also be reduced, but not at the cost of increased precursors for defect centres. The best preparation method is probably cleaving. This technique can be combined with the use of an end-cap on the fibre to reduce the power density. Further, an investigation on different fibre materials can perhaps determine a material with a low number of generated defect centres. But it should also be possible to draw this material into a small core fibre with single-mode behaviour at 405 nm.

4.9 Summary

Periodic surface structures have been observed on the launching end surfaces arising from prolonged irradiation with light from 405 nm CW diode lasers. In these cases, the laser power is at a level which is three orders of magnitude lower than that of the damage threshold. The structures exhibit multiple bends, break-ups and bifurcations, unlike interference patterns. They can be explained by a model used for femto-second irradiation of materials. It was concluded that the key parameters that contribute to the generation of the surface structures are power density, surface roughness, polarisation direction and the presence of ultraviolet defect centres. It was shown that the reduction of surface roughness by cleaving instead of glueing-and-polishing improves the lifetime of the system by a factor of four. This is a simple and low-cost fibre preparation method to enhance the lifetime of high power NUV fibre-coupled laser systems.

5 DUV bulk effects by 405 nm irradiation in low-mode fibres

5.1 Abstract

After the spectral and surface damages on standard single-mode fibres with low OH content were found, the influence of different preform manufacturing processes on the spectral damage will be discussed in this chapter. For the characterisation of the low-mode fibre samples the same 405 nm laser system and extremely sensitive spectrometer system were used. The induced losses were measured down to 210 nm wavelength, depending on the attenuation and length of the samples, and recorded time-dependently. Modifications of the fibre preform resulted in fibres with a surplus of hydrogen or with an oxygen deficiency. Additionally, fibres with Germanium, Phosphorous or Fluorine doped core were examined. All fibres exhibited a generation of UV defect centres after irradiation with 405 nm CW laser light. In the discussion the effects are explained and compared to earlier work on these fibre samples.

5.2 Introduction and earlier work

For fibre-optic applications in the UV region from 170 to 280 nm with different light sources, the existence and transformation of different UV defect centres have been studied in detail and an extract is shown in Figure 5-1 [Friebele1976, Friebele1979, Griscom1985, Khalilov1994]. The most prominent defect centres in silica fibres are related to an oxygen vacancy [Skuja1998]. They can be distinguished as the oxygen deficiency centre ODC(I) at 7.6 eV (163 nm), the E'$_\gamma$ centre at 5.8 eV (215 nm), the E'$_\beta$ centre

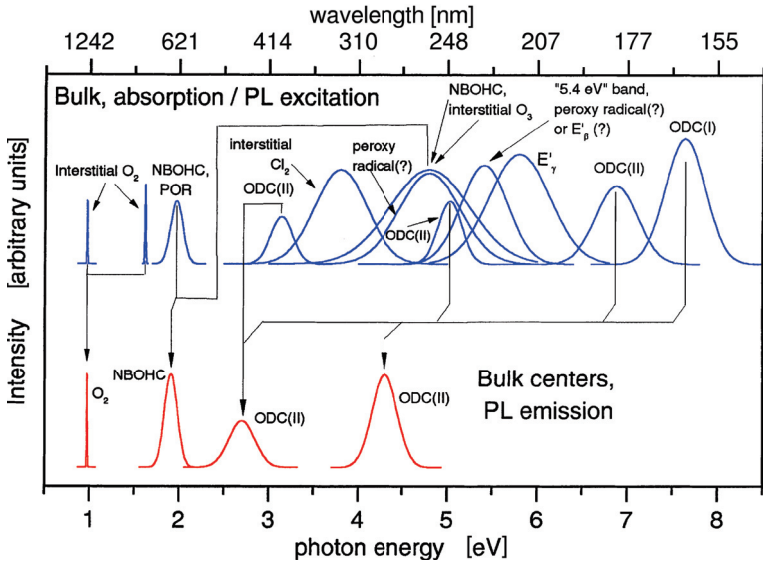

Figure 5-1: Spectral overview of known defect centres and their photo-luminescent emission bands [Skuja1998]. Centres marked with (?) are controversially discussed in literature.

at 5.7 eV (229 nm), and the oxygen deficiency centre ODC(II) at 4.9-5.2 eV (243 – 254 nm). Other defects are oxygen excess related, such as the non-bridging oxygen hole centre (NBOHC) or peroxy radical, both at 4.8 eV (260 nm) and the peroxy linkage at 3.8 eV (330 nm). Additionally bound hydroxyl groups (-OH), interstitial oxygen (O_2) or ozone (O_3), and interstitial or bound chlorine (Cl_2, -Cl) can exist in the material or occur during irradiation. Especially interstitial chlorine (Cl_2) has a large absorption band at 3.76 eV (330 nm).

The exact nature of some defect centres is still controversially discussed in literature. Those centres are marked with a question mark in Figure 5-1. The 250 nm band was assigned to the ODC(II) and the POR, but the POR is not confirmed, yet. Similarly the 330 nm band in pure silica is assigned to the Cl_2 band and the peroxy linkage. Due to the improved modern fibre preform production process the peroxy defects are seen rarely and can be excluded for this work. The nature of the ODC(II) is also not definite. On one hand it is explained as an unrelaxed silicone dangling bond, on the other hand as a two-fold coordinated silicone atom [Skuja1998]. The oxygen deficient centres also have several absorption bands, mainly for the electronic singlet or triplet excitation of the defect. Both are important and included in the overview in Table 5-1.

Table 5-1: Characteristics of the defect centres used for explanations in this work. According to [Skuja1998].

Defect name	Structural model	Peak position [nm]	FWHM [nm]
ODC(I)	≡Si-Si≡	163	10.7
E'_γ	≡Si• (…Si≡)	215	29.5
E'_β	≡Si• (…Si≡)	229	29.5
ODC(II) ($S_0 \rightarrow S_1$) ODC(II) ($S_0 \rightarrow T_1$)	≡Si…Si≡, -O-Ṡi-O-	243 – 254 394	14.9 42.5
NBOHC	≡Si-O•	260	56.6
POR	≡Si-O-O•	260	43.3
Interstitial Cl_2, Peroxy linkage	Cl-Cl ≡Si-O-O-Si≡	330	60
GeODC ($S_0 \rightarrow S_1$) GeODC ($S_0 \rightarrow T_1$)	≡Ge…Ge≡, -O-Ġe-O-	230 – 243 336	20 36.3

Defect name	Structural model	Peak position [nm]	FWHM [nm]
Ge(I)	≡Ge• (…Si≡)	280	114

The production of the preform and the fibre drawing process have the largest influence on the presence and generation of defect centres in silica fibres. The atmosphere during the deposition and collapsing of a preform determine whether oxygen deficiency or oxygen excess defects are formed. A high tension during fibre drawing and uncontrolled rapid cooling of the fibre can induce strained Si-O or Si-Si bonds or lead to the rupture of those, which directly generates NBOHC and E'_γ centres, respectively [Friebele1976]. If the strained bonds, also called precursors, did not rupture during the drawing process, then they can be broken by excitation through UV irradiation and in turn induce NBOHC and E'_γ centres. A production in a wet environment or a high-temperature treatment of the preform with H_2 can generate further precursors in the form of hydroxyl groups (Si-O-H) or hydrogen atoms bound to silicone (Si-H). This can also happen if the chlorine was not carefully removed after preform production, chlorine atoms are then bound to silicone (Si-Cl) [Kirchhof1998]. When the precursors are then exposed to UV light the bonds to hydrogen and chlorine are broken and molecular hydrogen and chlorine can form. In the latter case this leads to the generation of the Cl_2 band at 330 nm. If high concentrations of chlorine or hydroxyl are bound in the silica network, then the spectral attenuation below 200 nm is increased as well.

The influence of broadband UV light on the transmission properties of silica fibres was mainly investigated with deuterium lamps. The generation of the defect centres is commonly called solarisation and is driven by single photon absorption of photons with a high energy of more than 5.5 eV (225 nm). Mainly NBOHC and E'_γ centres are generated in high-OH fibres, while in low-OH fibres the ODC(II) can be generated additionally. The generation of NBOHC and E'_γ centres can be prevented by high-pressure low-temperature H_2 loading of the fibre. The generated defects will be passivated directly by the hydrogen and not seen as an additional spectral loss. However, this is only useful for large diameter fibres with outer silica diameter greater than 400 µm, because of the quick diffusion of H_2 out of the silica material. The reduction of the additional loss due to the NBOHC was achieved by a modification of the fibre production process. The generation of the E'_γ centre was dramatically reduced by treating the raw material and the fibre preform. But the generation of the absorption bands cannot yet be fully prevented [Klein1997b, Khalilov2006].

In the early 2000s a fibre development project was started at the *Institute of Photonic Technologies* (IPHT) in Jena, Germany. Its goal was the improvement of fibre material for

the visible range of the light spectrum (VIS) after it was observed that pulsed blue lasers brought a time-dependent damage to fibres with high and low OH content. The laser system worked at 446 nm with 9 ps pulses and 80 MHz repetition rate [Frost2001]. Pulse energies of about 12 nJ resulted in 1 W average power and power densities of about 600 kW/cm² in a 15 µm core fibre.

Using the production of a low-OH preform by modified chemical vapour deposition (MCVD) as a starting point, different production processes and preform modifications were performed [Kirchhof2001]. The main goal was the reduction of the absorption peaks in the VIS and of the tail of the interstitial Cl_2 band at 330 nm extending into the VIS. The influence of collapsing in different atmospheres, hydrogen diffusion by preform tempering as well as weakly doping the fibre core were investigated [Unger2002]. Almost all treatments improved the transmission behaviour in the VIS towards the theoretical Rayleigh limit. On the other hand, the ODC(II) absorption band at 240 to 250 nm was extremely enhanced simultaneously to values of 20 to 70 dB/m. The interchange between the ODC(II) and the Cl_2 band were explained by an incorporation of nuclear chlorine into the oxygen deficient site during production [Kirchhof2001]. If the number of ODC(II) is small, then the chlorine molecules are stable in the silica network. A narrower absorption band at 330 nm was seen in Ge doped fibres, which in this case was attributed to a singlet-triplet transition of the oxygen deficiency GeODC in Germanium doped silica [Gallagher1992].

In long-term experiments with the 446 nm laser lasting up to 160 h it was shown, that collapsing in a He atmosphere improved the lifetime of the fibre only marginally. The H_2 diffusion fibre as well as the Ge and P doped fibres exhibited a significantly increased lifetime. Spectral loss measurements showed that the Ge doped fibre had an increased absorption in the UV with the tail now extending stronger into the VIS. The H_2 diffusion fibre had an overall increased loss in the VIS. The doping with Fluorine resulted in no distinct differences to the standard fibre. It is very interesting to note, that this research also found “geometrical alterations of the input and output end faces … of the fibres with long lifetimes”. After thorough discussion with the group at the *IPHT*, old atomic force microscope (AFM) images revealed that laser-induced periodic surface structures (LIPSS) had been found on the end surfaces, but were not further investigated [Schwuchow2012].

For the investigations in this work some reference fibres and the most promising modified fibres were provided by the *IPHT*. Besides the standard fibre, H_2 diffusion and He collapsed fibres were examined as well as fibres weakly doped with Ge, P and F.

5.3 Experimental setups

5.3.1 Damage measurement setup

For the irradiation of the low-mode fibre (LMF) samples, a laser diode module (LDM) provided by Omicron-Laserage, was used. The module Omicron LDM405D.450.CWA.M incorporates Nichia GaN laser diodes which offer high power at 405 nm. This multi-mode laser (MML) comprises two diodes with their beams cross-combined inside the module. The MML has a maximum output power of P_{out} = (390±5) mW and a beam quality of $M^2 \approx 3$. The laser beam, optically corrected for astigmatism, is collimated and additionally focused on the fibre end surfaces with an imaging and alignment system (IAS) for fibres assembled with FSMA connectors. The focal length of the aspheric lens f = 16 mm gives a focus diameter $2 \cdot w_0$ = 20.6 µm (according to Formula 6-8) and a mean power density I_{spot} = 117 kW/cm² in the focus (according to Formula 6-3). The fibre end can be adjusted along the optical axis and tumbled around it.

The fibre output power $P_{out,fibre}$ from the fibre samples was noted once for every irradiation period. For the power readings a thermopile power meter Coherent PowerMax PS19Q was used. In Figure 5-2 the whole setup is shown on a straight axis, but the actual damaging was done with the fibre under test (FUT) bent in some way, which was maintained for every irradiation period. The length of the FUT depended on the fibre material and the desired dynamic of the spectral measurements in the deep ultraviolet (DUV). To attach the FUT to the IAS and the spectral measurement setup all fibre ends were connectorised with FSMA connectors. The distal fibre end is aligned in front of the power meter for free space irradiation and the proximal end was adjusted to maximum $P_{out,fibre}$ using the IAS. All experiments are conducted in a standard laboratory environment at room temperature. The samples were irradiated for short periods between 30 seconds and one hour. UV spectra were taken before, in between and after irradiation with the spectral measurement setup described in the section below.

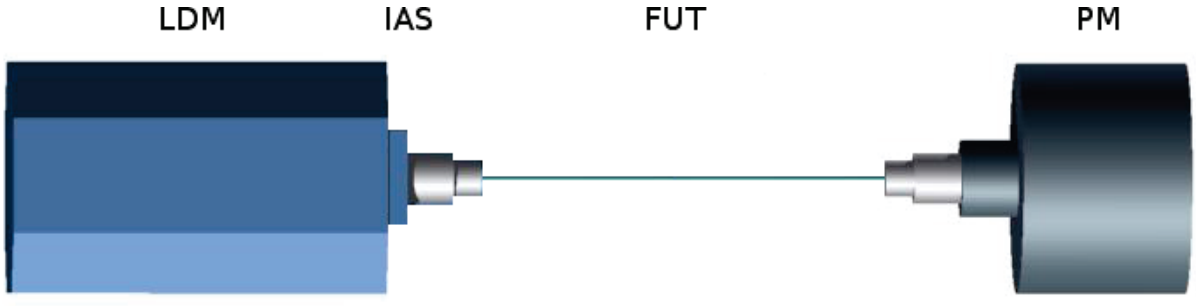

Figure 5-2: The damage setup consisting of stabilised laser diode module (LDM) with a wavelength of 405 nm, an imaging and alignment system (IAS) and a thermopile power meter (PM). The fibre under test (FUT) is aligned for maximal output power.

5.3.2 Spectral measurement setup

In order to determine spectrally induced losses, a spectrometer system as depicted in Figure 5-3 was employed. The whole setup consisted of a deuterium lamp (D_2) with an optimised imaging system and the fibre-optic spectrometer (OceanOptics Maya2000Pro). The deuterium lamp provides broadband spectrum starting below 180 nm. However, an optical signal can only be detected above 180 nm due to increasing silica and gas (e. g. oxygen) absorption with decreasing wavelength. The spectrometer uses a back-thinned CCD chip (charge-coupled device) for a significantly higher quantum efficiency below 200 nm. Therefore, the sensitivity is higher in comparison to older standard CCD chips

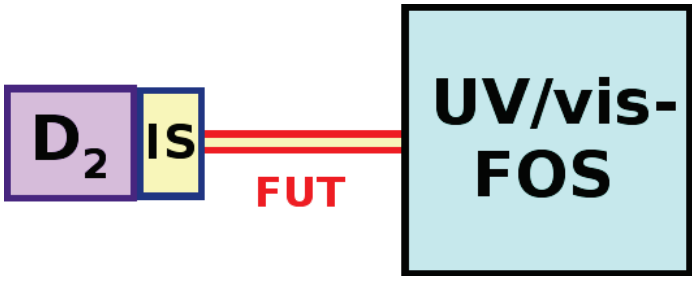

Figure 5-3: Spectral measurement setup; D_2: deuterium lamp, IS: imaging system, FUT: fibre under test, FOS: fibre-optic spectrometer for UV and visible range.

with light-converting layers or photo-diode arrays (PDA). The selected grating of the used spectrometer covers the spectral range from 167 to 620 nm. For a good spectral resolution Δλ a narrow slit of 5 µm width is utilised. The integration time starts at 13 ms and can be increased to several seconds.

The grating reflects the higher, second order onto the CCD chip as well. This higher order needs to be suppressed for the spectral measurements. Because of stray-light and spectral transmission, unexpected signals with twice the wavelength of an expected high-intensity signal should be handled with care and could be an artefact (see section 4.2 for details). Another artefact has to be expected at 486 nm, where the Balmer line D_β of deuterium can cause an oscillation in the calculated loss spectrum. The peak might shift in the spectrometer signal over time, due to warming up of the grating and chip. Therefore, this peak is also very helpful in the analysis to adjust a drift in wavelength.

Spectral measurements of the FUTs were taken before, in between, and after laser exposures. Measurements during exposure were taken for example after 5, 15 and 30 minutes, while the total irradiation time was 60 or 120 minutes in this chapter. The dark current signal was subtracted from the recorded spectra for every new measurement, leading to $I_{before}(\lambda)$ or $I_{after}(\lambda)$. To obtain the spectral loss $L_{ind}(\lambda)$ induced by 405 nm irradiation the spectra were processed using the following relationship:

$$L_{ind}(\lambda) = -10 \cdot \log_{10}\left(\frac{I_{after}(\lambda)}{I_{before}(\lambda)}\right) \quad (5\text{-}1).$$

In addition, the spectral measurement system was also used to determine the spectral attenuation α(λ) of the fibres by using the cut-back method. The fibres were cut back from 1 m to 0.5 m, then to 0.25 m and 0.11 m. The spectral attenuation α(λ) was calculated by using the relationship:

$$\alpha(\lambda) = \frac{-10}{\Delta l} \cdot \log_{10}\left(\frac{I_{long}(\lambda)}{I_{short}(\lambda)}\right) \quad \text{with} \quad \Delta l = l_{long} - l_{short} \quad (5\text{-}2).$$

If a specimen is exposed to a deuterium lamp for too long, an unintentional, additional loss can be induced. Therefore, the damage by deuterium lamp irradiation and annealing at room temperature of one sample of LMF was investigated. Spectral measurements were taken with a different spectrometer (OceanOptics USB4000) during the irradiations and annealing.

In the spectral measurements, a lamp signal error ΔI of ±3 % at 200 nm, ±2 % at 300 nm and ±1 % at 400 nm is taken into consideration. The noise in the spectrometer is much lower than this error and not taken into account. For the error of the spectral loss ΔL_{ind} the non-linear propagation of error is used [Muehl2001]:

$$\Delta L_{ind} = \sqrt{\left(\frac{\partial L_{ind}}{\partial I_{before}}\right)^2 \cdot \Delta I_{before}^2 + \left(\frac{\partial L_{ind}}{\partial I_{after}}\right)^2 \cdot \Delta I_{after}^2} \quad (5\text{-}3).$$

5.3.3 Fibre specimens

The investigated LMF was all-silica step-index fibre. The experimental samples of LMF for laser treatment were supplied by the *IPHT* in Jena, Germany. The seven fibre types had a core diameter 2·*a* of 10 or 15 µm, a cladding diameter of 50 µm and a standard outer diameter of 125 µm. The cladding was 3 mol% Fluorine doped to achieve the difference in refractive index and a numerical aperture NA = 0.11 in all cases. An overview of the differences in the fabrication process is given in Table 5-2. The standard fibre *1u* had a pure synthetic silica preform, with a low OH content of less than 1 ppm. For types *6u* and *23u* this preform was heat-treated with a H_2O_2 flame with hydrogen excess, for H_2 diffusion into the preform, and then drawn into fibres with 15 and 10 µm core diameter, respectively. The preform of fibre type *18u* was collapsed in a helium (He) atmosphere to achieve an oxygen deficit. The difference for the three other types is a weak doping of the fibre core material. Type *22u* was doped with Germanium (Ge, $GeCl_4$ admixed to MCVD process), type *26u* with phosphorus (P, $POCl_3$ admixed to MCVD process) and type

42u with Fluorine (F, $C_2F_3Cl_3$ admixed to MCVD process). A chlorine concentration of 0.14 mol% was measured in the core and cladding region of the collapsed preforms [Kirchhof2001]. Additionally, a commercial LMF sample was provided by *j-fiber* from Jena, Germany. This fibre type *IG-15* was manufactured using the protocol engineered by *IPHT* for type *6u*. Despite this fact, differences in the machinery and drawing conditions can lead to slightly different outcomes in spectral attenuation and induced loss.

Table 5-2: Properties and fabrication process of the LMF types investigated in this work.

Fibre type	Core diameter 2·*a* [µm]	Core material
1u	15	Standard low-OH (< 1 ppm)
6u	15	Like *1u*, but treated with H_2O_2 flame (H_2 excess)
18u	15	Like *1u*, but collapsed in He atmosphere
22u	15	0.3 mol% GeO_2 doped
23u	10	Like *1u*, but treated with H_2O_2 flame (H_2 excess)
26u	15	0.6 mol% P_2O_5 doped
42u	15	0.25 mol% SiF_4 doped
IG-15	15	Low-OH preform treated with H_2O_2 flame (H_2 excess)

For the influence of the 405 nm laser radiation on the fibre material, the power density I_{core} in the fibre core needs to be taken into account.

$$I_{core} = \frac{P_{out,fibre}}{A} = \frac{P_{out,fibre}}{\pi \cdot a^2} \tag{5-4}$$

The power density is averaged over the core area A of the fibre core. Typical values for the LMF with 15 µm core diameter are 100 to 160 kW/cm², depending on the particular coupling efficiency and attenuation at 405 nm. For a rough estimation of the coupling efficiency the formula for the transmission of a Gaussian beam through an aperture can be used [Paschotta2008]:

$$P = P_{out} \cdot \left(1 - e^{\frac{-2 \cdot a^2}{w_0^2}}\right) \tag{5-5}.$$

For a LMF with 15 µm core diameter the coupled power P is 256 mW and for $2 \cdot a$ = 10 µm P = 147 mW. This in turn would result in power densities of I_{core} = 144 kW/cm² and 187 kW/cm², respectively. The internal attenuation of the fibre samples at 405 nm was not explicitly measured, but values below 1 dB/m can be considered. Kirchhof and co-workers found values of 0.7 dB/m for *1u*, 0.04 dB/m for *6u* and *18u*, 0.05 dB/m for *26u* and *42u*, and 0.075 dB/m for *22u* at 400 nm wavelength [Kirchhof2001, Unger2002]. Taking Fresnel losses into account, the total loss for a 1 m long sample will be less than 1.1 dB.

The spectral attenuation of all samples was measured before irradiation. Since the pre-existing absorption bands in the DUV were most interesting, the LMF samples were cut back to short length of 0.25 m or even 0.11 m. A full resolution of strong absorption bands is thereby possible, too, as it is shown in Figure 5-4. The sample of type *6u* was only cut back from 1 m to 0.5 m and the dynamic of the absorption measurement was restricted to 20 dB/m. The same fibre type *IG-15* was cut back to 0.11 m, thus a complete measurement of the absorption band at 245 nm was possible with a maximal value of 62 dB/m. All other samples were cut back to 0.25 m, yielding in a complete resolution of the absorption bands. The singlet-singlet transition of the GeODC of *22u* could not be resolved and was estimated to be in the order of 10^4 dB/m [Kirchhof2001].

The overlay shows that almost every sample had a pre-existing absorption band around 245 nm, which can be correlated to the ODC(II) band. A reinterpretation of the work by Kirchhof, especially using the VIS and NIR part of their spectral loss measurements, allows the conclusion that the *1u* exhibited a NBOHC band at 260 nm and an additional band at 330 nm which coincides with the Cl_2 band. In the original work the 630 nm band had not been correlated to the NBOHC and the peak at 250 m was interpreted as ODC(II). A shift of the ODC(II) to 265 nm resulted in the absorption peak of the P doped sample *26u*. In the wavelength region below 225 nm the absorption of all fibre samples increases strongly and the profile could not be resolved any further. This edge is located at a longer wavelength of 300 nm for the Ge doped sample *22u*, which in addition also exhibited an absorption band at 330 nm. In that case it is not the interstitial Cl_2 band but an oxygen deficiency at a Ge site (singlet-triplet transition of GeODC, 3.8 eV) [Gallagher1992, Skuja1998]. Table 5-3 provides an overview of the found absorption peaks and their association in this work.

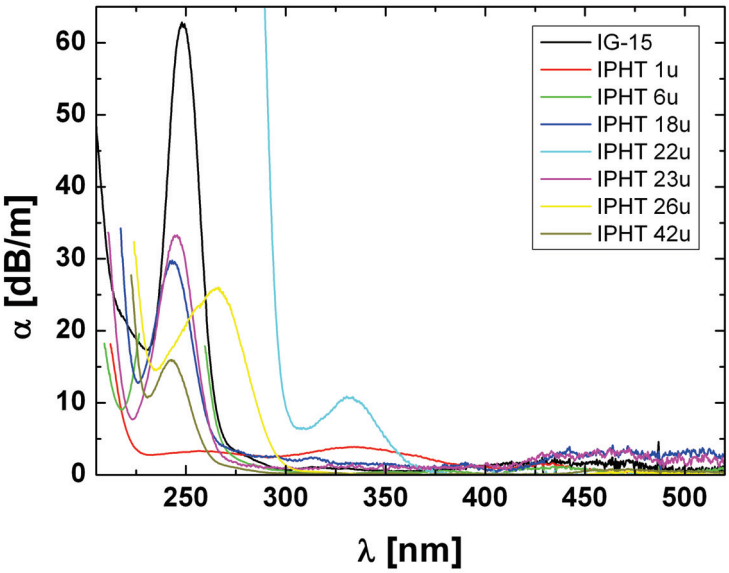

Figure 5-4: Measured spectral attenuation of the LMF samples in the DUV.

Table 5-3: Overview of absorption peaks found in this work with their associated defect centre, centre wavelength and attenuation.

Fibre type	Lower peak	Upper peak
1u	NBOHC, 260 nm, 3.3 dB/m	Cl_2 band, 334 nm, 3.9 dB/m
18u	ODC(II), 243 nm, 29.6 dB/m	N/A
22u	GeODC, 240 nm, 10^4 dB/m	GeODC, 333 nm, 10.7 dB/m
23u	ODC(II), 245 nm, 33.2 dB/m	N/A
26u	ODC(II), 265 nm, 25.8 dB/m	N/A
42u	ODC(II), 243 nm, 15.75 dB/m	N/A
IG-15	ODC(II), 248 nm, 62.3 dB/m	N/A

5.4 Modification of UV defect centres by 405 nm laser irradiation

5.4.1 Damage by deuterium lamp radiation

A characterisation of the damage by the deuterium lamp was performed on the LMF type *IG-15*. After a 4 h irradiation period the 0.2 m long sample was left to anneal for 20 h and was then irradiated additionally for 1 h. This is a standard procedure to characterise the generation of UV defect centres in MMF samples [Klein2009]. Figure 5-5 a) shows the measurement spectra before and after the complete procedure and in Figure 5-5 b) the resulting induced loss. The latter shows a reduction of the ODC(II) absorption band at 245 nm of 2.3 dB and an increase of the E'_{γ} centre at 214 nm of about 2 dB, both in the 0.2 m long sample. Besides these two changes nothing else could be observed in the overall spectral measurements.

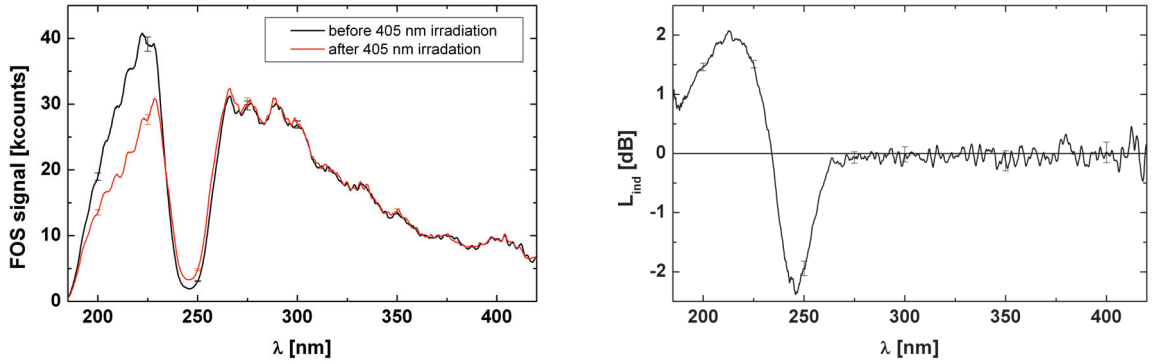

a) *b)*

Figure 5-5: Example of a 0.2 m long IG-15 sample: a) Spectra taken before and after deuterium lamp irradiation. b) Induced loss after 25 h of deuterium lamp irradiation and annealing procedure.

The loss at known defect centres (see Figure 5-1) was calculated from the recorded spectra and traced over time. Those defect centres are the E'_{γ} centre (214 nm), the E'_{β} centre (229 nm), the ODC(II) (244–254 nm), the NBOHC (266 nm) and the interstitial Cl_2 band (330 nm). However, three of these were actually not observed (E'_{β}, NBOHC, Cl_2), but they can guide the eye concerning overall spectral changes. The strong noise and fluctuations of the 245 nm loss trace in Figure 5-6 a) is due to the low reference value at the beginning of the measurement. The same changes are seen on the other traces, but with a much smaller value. Directly after the start of the exposure the E'_{γ} centre starts to increase, which is also seen in the 229 nm trace on the tail of the absorption band. During the annealing phase the E'_{γ} centre was stable and recommenced to increase when the permanent irradiation started again.

The reduction of the ODC(II) band traced at 244 nm and 254 nm started only after about half an hour, but then had a steeper progression than the E'_{γ} centre. The gain at 244 nm after four hours was higher than the loss at 214 nm. In the beginning of the annealing the reduction of ODC(II) proceeded and then stabilised. When the permanent irradiation started again the ODC(II) abruptly increased by about 0.5 dB, afterwards the band was again reduced for the remaining hour of irradiation. The traces at 266 nm and 330 nm behave similar to the ODC(II) at a smaller scale, since these traces are on the tail of the absorption band. The evaluation of the induced loss at specific times is shown in Figure 5-6 b). At the start of the damage an absorption band at 245 nm appeared simultaneously to the E'_{γ} centre. After thirty minutes it started to be reduced and during the annealing phase it stabilised. When damaging commenced the 245 nm band increased abruptly, as seen in Figure 5-6 a).

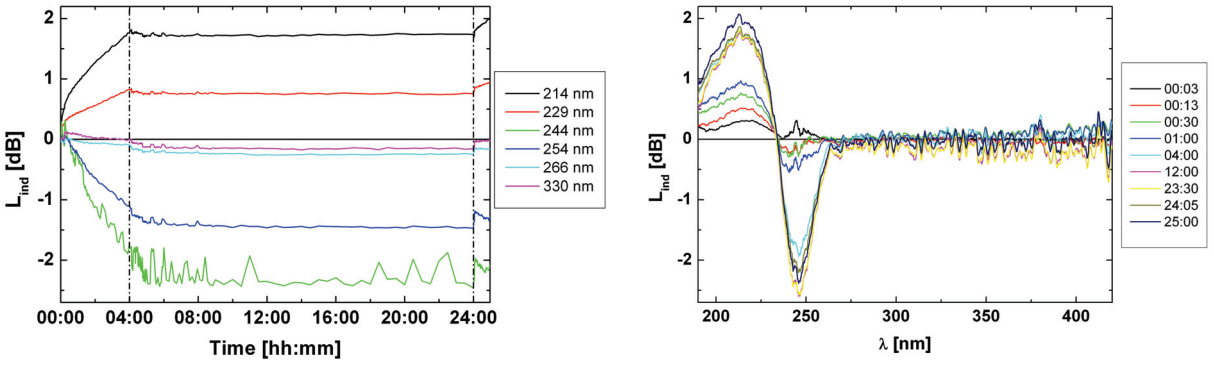

a) *b)*

Figure 5-6: a) Trace of induced loss over time at specific wavelengths during irradiation with a deuterium lamp and annealing of a 0.2 m long IG-15 sample. The dashed-dotted line marks the time stamps when the permanent irradiation with the deuterium lamp was terminated and commenced. b) Induced loss at specific time stamps during deuterium lamp irradiation and annealing of a 0.2 m long IG-15 sample.

5.4.2 Length distribution of damage by 405 nm radiation

The length distribution of the damage, that was found in 405 nm laser irradiated samples, was examined by irradiating a 1.5 m long sample of *IG-15*. After exposure to the 405 nm MML for one hour with a fibre output power of 240 mW, the sample was cut into three equally long pieces. Part 1 was the piece at the launching end, Part 2 the centre piece and Part 3 the piece at the distal end. Figure 5-7 a) shows the spectra before and after ir-

radiation. The transmission window between 200 and 230 nm was completely removed and the edge of the larger transmission window moved to shorter wavelength by 25 nm. From the induced loss shown in Figure 5-7 b) the actual improvement and loss cannot be determined for this long sample. The inset in Figure 5-7 b) shows the region around 450 nm with the second order reflection of the DUV change at the spectrometer grating, which was seen in other measurements as well, but will not be further discussed here. The extent of this effect mainly depends on the strength of the signals in the DUV and is no issue for a small signal absorption.

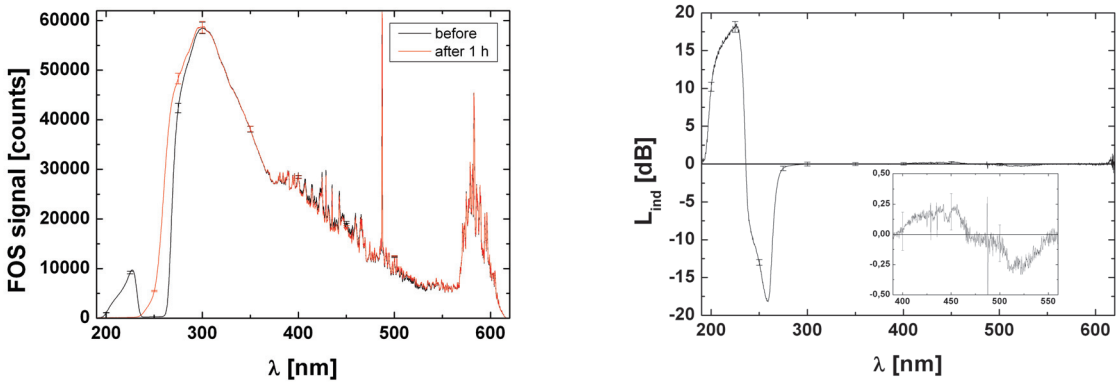

a) *b)*

Figure 5-7: A 1.5 m long IG-15 sample (H_2 treated preform) after 1 h of 405 nm MML irradiation: a) Spectra taken before and after irradiation. b) Induced loss after irradiation. The intensity in the fibre core was I_{core} = 135 kW/cm². The inset shows magnified the region around 450 nm with the second order reflection of the DUV change at the spectrometer grating.

The spectra for the individual pieces are shown in Figure 5-8 a). Only slight differences between the 0.46 m long pieces were observed, this is why a relative comparison is shown in Figure 5-8 b). The differences between the individual pieces at 215 nm and 250 nm are not so large compared to the drastic spectral changes in the whole sample. The comparisons show that the ODC(II) was more reduced in the front of the sample and that the E'_γ centre was generated stronger in the rear of the sample. Since there is an attenuation of about 0.04 dB/m at 405 nm a power difference of 3 mW between proximal and distal end can be estimated. Nevertheless, an almost evenly distributed damage could be observed.

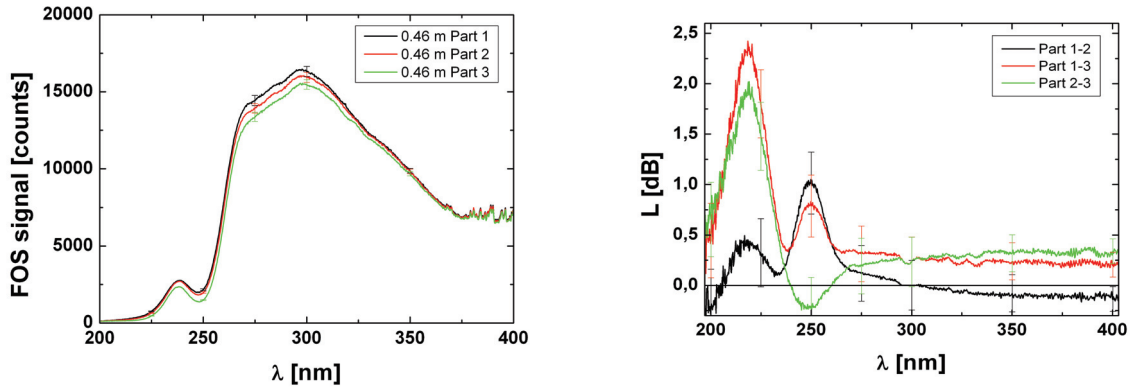

a) *b)*

Figure 5-8: a) Spectra taken for three equally long parts of the 1.5 m IG-15 sample (H_2 treated preform). b) Comparison expressed in loss between front (1) and centre (2) part, front (1) and rear (3) part, and centre (2) and rear part (3).

5.4.3 Damage of low-mode fibre samples with different dopants

The three H_2 flame treated LMF types *IG-15*, *6u* and *23u* are discussed first, one after the other. A very short sample of *IG-15* with 0.114 m length was irradiated for an optimal resolution of the modification of the absorption bands. Figure 5-9 shows that the absorption band at 250 nm was removed within the 5 minutes of the first irradiation period with $P_{out,fibre}$ = 230 mW. The E'_γ centre on the other hand increased with irradiation time. The traces weighted by the length of the sample in Figure 5-10 show that the ODC(II) is completely healed with -62 dB/m and the E'_γ increases up to 40 dB/m. This can be stated because it was shown that the loss distribution is not length dependent. Besides the second order reflection of the mentioned DUV changes in the wavelength range from 380 to 550 nm no further modifications of defect centres were found.

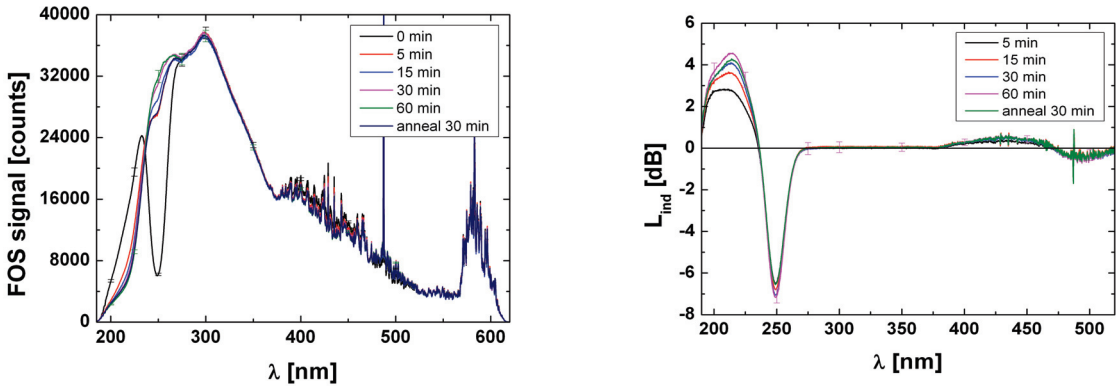

a) *b)*

Figure 5-9: Example of a 0.114 m long IG-15 sample (H_2 treated preform): a) Spectra taken before, during and after 405 nm MML irradiation. b) Induced loss during and after 405 nm MML irradiation. The intensity in the fibre core was I_{core} = 130 kW/cm².

The only sample of *6u* had a length of 1 m and $P_{out,fibre}$ = 218 mW. Due to the long length only a small transmission window at 218 nm and the beginning of a large transmission window above the ODC(II) absorption band were observed (see Figure 5-11 a)). The peak of the small window was attenuated to about 18 dB/m within 45 minutes in Figure 5-11 b). Comparable to the *IG-15* sample this E'$_\gamma$ centre increased with irradiation time, but could not be observed significantly beyond 30 minutes due to the dynamic restriction of the system. A reduction of the ODC(II) could be seen by a 2 nm shift of the edge of the large window to shorter wavelength. The gain in the tail of the ODC(II) at 260 nm was 3.4 dB/m and constant after the first irradiation period (see Figure 5-13). In contrast to the *IG-15* sample an additional reduced absorption band was observed between 260 and 300 nm with -1.2 dB/m. For comparison both wavelengths of 260 nm and 273 nm were traced in Figures 5-10 and 5-13 for *IG-15* and *23u*, respectively. The absorption band at 273 nm behaved simultaneously to the ODC(II) and could be attributed to the NBOHC, but it was not seen for the *IG-15*.

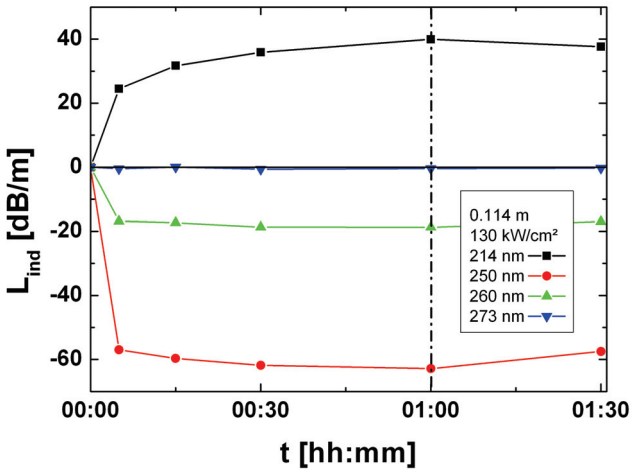

Figure 5-10: Trace of induced loss over time at specific wavelengths during irradiation with 405 nm MML and annealing of a 0.114 m long IG-15 sample (H_2 treated preform). The dashed-dotted line marks the time stamp when the permanent irradiation with the 405 nm MML was terminated. The intensity in the fibre core was I_{core} = 130 kW/cm².

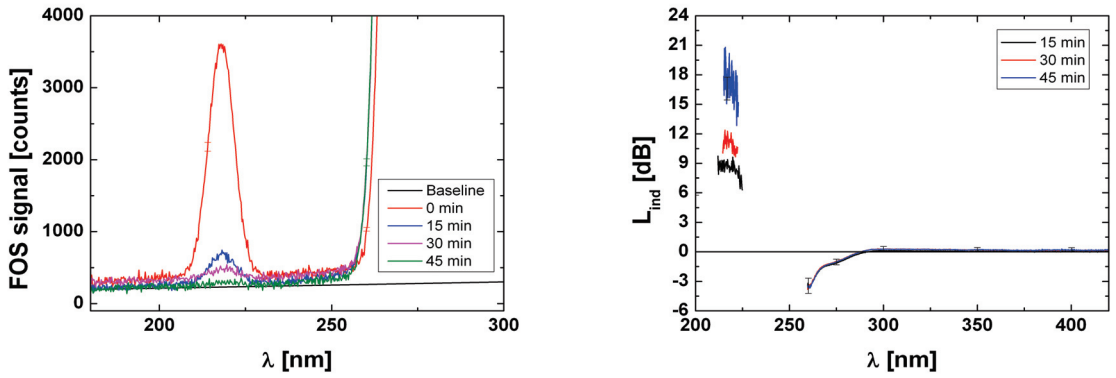

a) *b)*

Figure 5-11: Example of a 1 m long 6u sample (H_2 treated preform): a) Spectra taken before, during and after 405 nm MML irradiation. b) Induced loss during and after 405 nm MML irradiation. The intensity in the fibre core was I_{core} = 123 kW/cm².

A 0.254 m long *23u* sample with $P_{out,fibre}$ = 256 mW exhibited the same changes as the *6u* sample, because it is the same material. However, the fibre core diameter was different. In Figure 5-12 a) the small transmission window is reduced over time and the edge of the large window also shifted to shorter wavelength. For the induced loss in Figure 5-12 b) this resulted in an increasing E'_{γ} centre and an abruptly reduced ODC(II). The *23u* also shows the improvement between 250 and 300 nm, just like the *6u*. Surprisingly another small absorption band around 230 nm was created during the first irradiation period, but did not seem to increase afterwards. The band could be attributed to the E'_{β} centre. This

was not seen for the *6u* due to the worse dynamic below 250 nm. The traces for three *23u* samples are shown, together with the only *6u* sample, in Figure 5-13 for length of 0.25 and 0.5 m and power densities between 222 and 324 kW/cm². For the third sample no significant trace was measured at 215 nm. All samples showed a quick improvement in the ODC(II) within the first 5 minutes to about -10 dB/m. The trace at 273 nm, which could be attributed to the NBOHC, behaved accordingly and improved to about -1.4 dB/m. After the irradiation these two defect centres increased slowly. The E'_γ centre again was generated more slowly over time to reach 17 dB/m or 24 dB/m before the annealing phase. During the annealing this absorption band was slightly reduced. Despite the different core diameters the modifications of defect centres during irradiation of *6u* and *23u* were the same after being weighted by the length of the samples.

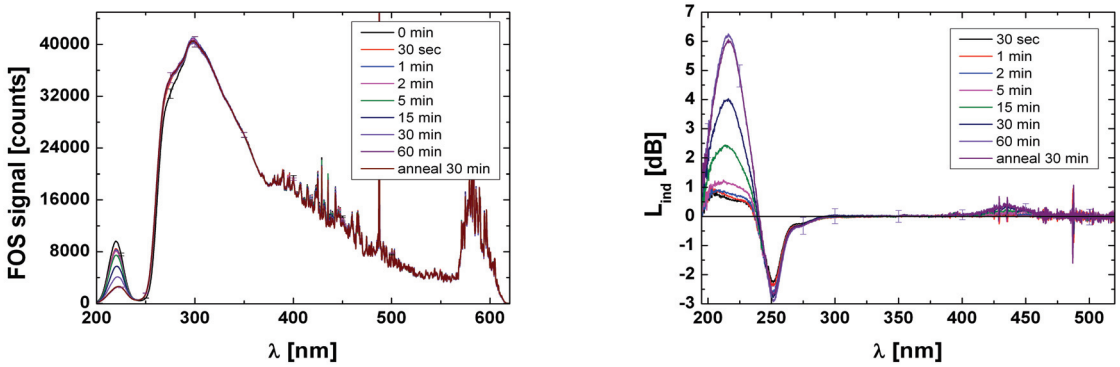

a) *b)*

Figure 5-12: Example of a 0.254 m long 23u sample (H_2 treated preform, 10 µm core): a) Spectra taken before, during and after 405 nm MML irradiation. b) Induced loss during and after 405 nm MML irradiation. The intensity in the fibre core was I_{core} = 324 kW/cm².

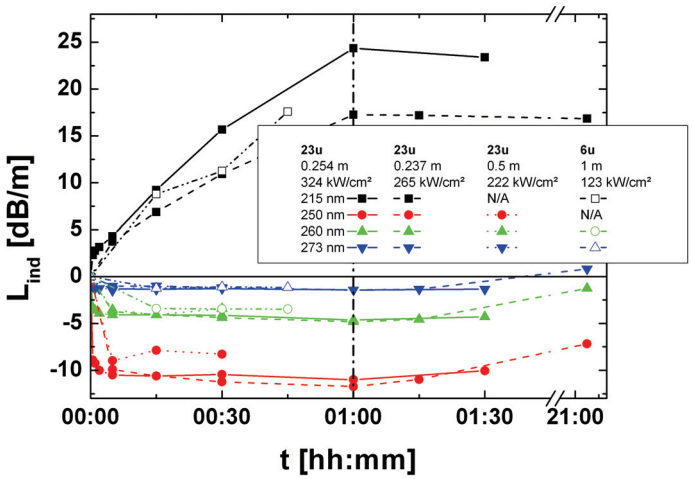

Figure 5-13: Traces of induced loss over time at specific wavelengths during irradiation with 405 nm MML of three 23u samples and one 6u sample (both H_2 treated preform, but 10 µm and 15 µm core). The dashed-dotted line marks the time stamp when the permanent irradiation with the 405 nm MML was terminated.

One sample of standard LMF *1u* was irradiated for a total of one hour and then left to anneal for two hours. The fibre output power was 230 mW to 240 mW and a mean power density in the core of 135 kW/cm² was assigned to this sample. The spectra and the calculated induced loss L_{ind} in Figure 5-14 show several changes below 400 nm wavelength. The defect centres E'_γ at 215 nm, ODC(II) at 245 nm and NBOHC at 260 nm were generated or increased simultaneously, but the NBOHC had the strongest progression. The defect centres stayed almost stable during the annealing phase and were only slightly reduced. An abrupt and broad improvement can be seen in the wavelength range around 355 nm after 5 minutes. This improvement was reversed over the course of irradiation.

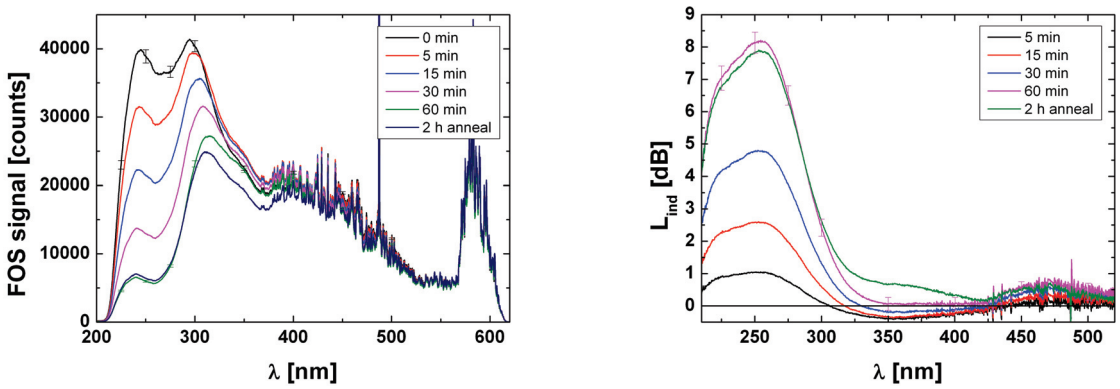

a) *b)*

Figure 5-14: Example of a 0.56 m long 1u sample (standard low-OH): a) Spectra taken before, during and after 405 nm MML irradiation. b) Induced loss during and after 405 nm MML irradiation. The intensity in the fibre core was I_{core} = 135 kW/cm².

During the annealing this band seems to have increased further. In Figure 5-15 the changes at the mentioned wavelengths are traced over time and weighted by the length of the LMF sample. The trace of ODC(II) and NBOHC is combined at 250 nm, because a separation of the two is not possible. The loss at 250 nm and 215 nm increased almost linearly to over 14 and 10 dB/m, respectively. The band at 355 nm improved to about -0.7 dB/m and then the loss increased to about 1.2 dB/m.

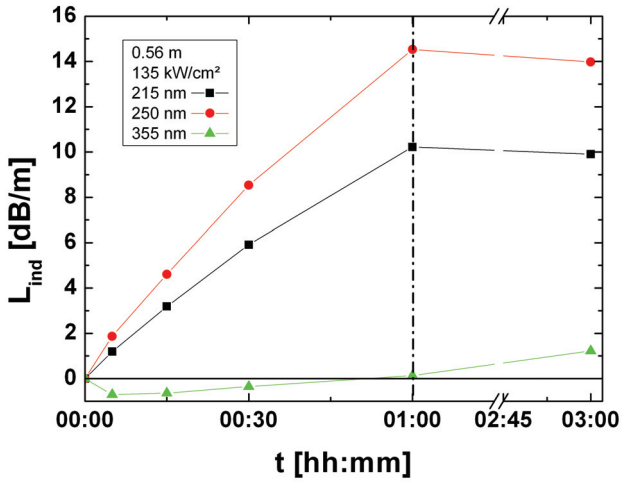

Figure 5-15: Trace of induced loss over time at specific wavelengths during irradiation with 405 nm MML and annealing of a 0.56 m long 1u sample (standard low-OH). The dashed-dotted line marks the time stamp when the permanent irradiation with the 405 nm MML was terminated. The intensity in the fibre core was I_{core} = 135 kW/cm².

The Fluorine doped samples *42u* behaved similar to the untreated standard LMF *1u*. The results presented in Figure 5-16 are for a 0.131 m long sample which transmitted $P_{out,fibre}$ = 210 mW. The attenuation below 230 nm is much higher than for the *1u*, therefore the E'$_\gamma$ centre could not be measured directly. Instead the tail up to 230 nm was used as an indicator. It increases over irradiation time together with the NBOHC at 260 nm. A very slight depression of the overlaid curves at 250 nm could indicate a reduced ODC(II), but this is not very significant. For the annealing phase slight changes were seen below 280 nm, but a broad absorption band built up around 315 nm. The traces in Figure 5-17 show a maximum of about 18 dB/m for the NBOHC and of about 36 dB/m for the tail of the E'$_\gamma$ centre after one hour. While the E'$_\gamma$ centre was reduced during annealing, the NBOHC increased. The slow increase at a wavelength of 330 nm during irradiation can be accounted to the position on the NBOHC tail. After the permanent irradiation was terminated, the loss around 330 nm increased to over 4 dB/m and became stable.

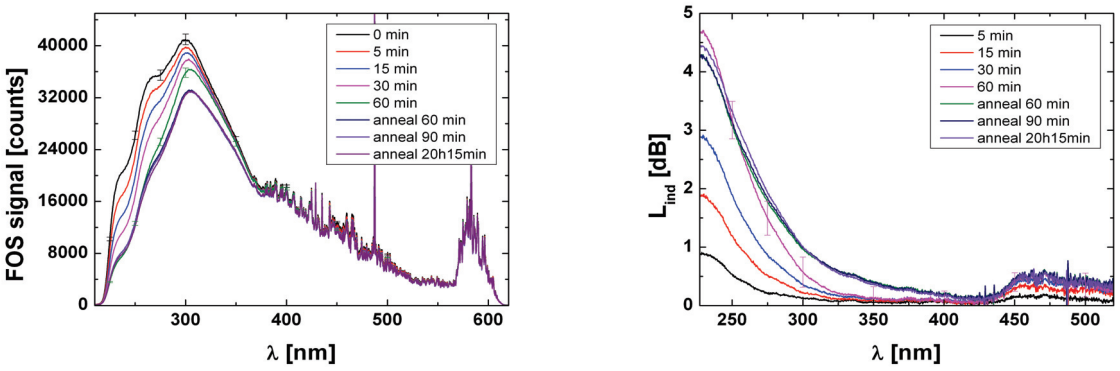

a) *b)*

Figure 5-16: Example of a 0.131 m long 42u sample (F doped core): a) Spectra taken before, during and after 405 nm MML irradiation. b) Induced loss during and after 405 nm MML irradiation. The intensity in the fibre core was I_{core} = 119 kW/cm².

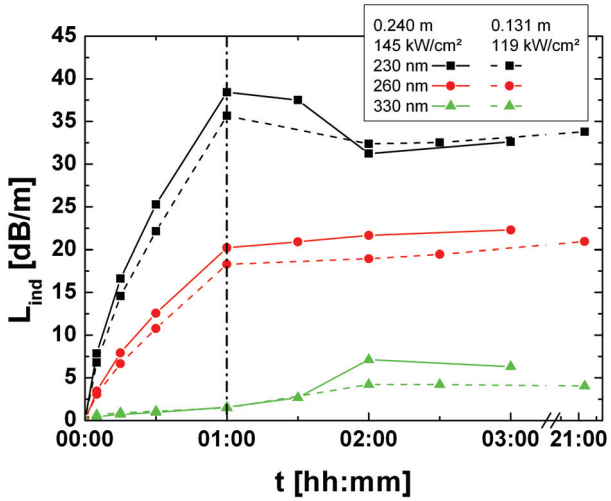

Figure 5-17: Traces of induced loss over time at specific wavelengths during irradiation with 405 nm MML of two 42u samples (F doped core). The dashed-dotted line marks the time stamp when the permanent irradiation with the 405 nm MML was terminated.

The sample of *18u* presented in Figure 5-18 had a length of 0.255 m and $P_{out,fibre}$ = 250 mW. A slight improvement in the ODC(II) was almost covered by a strong generation of the E'$_\gamma$ centre and the NBOHC. Additional absorption bands at 235 nm and 285 nm were observed, but did not have a particularly strong absorption or increase. The first could be again attributed to the E'$_\beta$ centre, but the latter is unknown and might be a metal ion contamination, perhaps chromium or copper. The annealing curve in Figure 5-18 b) shows no significant change for the E'$_\gamma$ centre after 18 hours, but the ODC(II) and the NBOHC increased by about 0.2 dB in this sample. In Figure 5-19 the traces of the one sample irradiated for one hour with annealing for 18 hours and one sample irradiated for two hours are presented. They had fibre output powers of 250 mW and 260 mW, respectively. Both samples exhibited the delayed increased loss at 250 nm, pointing to an improvement of the ODC(II) at the beginning. Afterwards a steady increase of the E'$_\gamma$ centre towards values above 15 dB/m and of the NBOHC to above 5 dB/m were observed after one hour. The final values of the two hour sample were 27.2 dB/m and 11.9 dB/m, respectively.

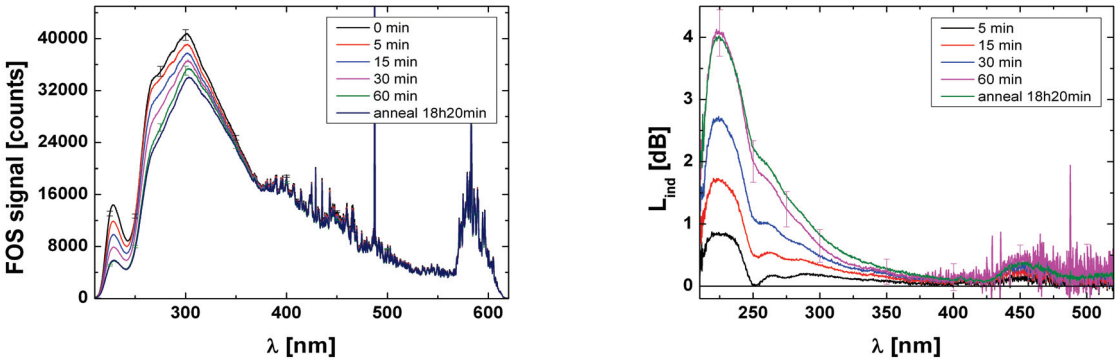

a) *b)*

Figure 5-18: Example of a 0.255 m long 18u sample (He atmosphere): a) Spectra taken before, during and after 405 nm MML irradiation. b) Induced loss during and after 405 nm MML irradiation. The intensity in the fibre core was I_{core} = 141 kW/cm².

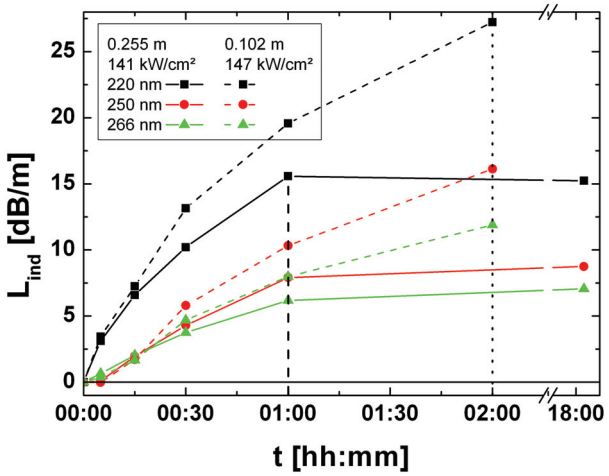

Figure 5-19: Traces of induced loss over time at specific wavelengths during irradiation with 405 nm MML of two 18u samples (He atmosphere). The dashed and the dotted lines mark the time stamp when the permanent irradiation with the 405 nm MML of the first and second sample was terminated, respectively.

The results of the 0.25 m long P doped sample *26u* in Figure 5-20 looks very similar to the results of the *18u*, but slightly shifted to longer wavelength. Again the E'$_\gamma$ centre, traced in the tail at 226 nm in Figure 5-21, increases over time, just like the ODC(II) at 265 nm, for a fibre output power of 272 mW. A small reduction at 255 nm could be observed, which is attributed to the spectral gap between ODC(II) and E'$_\gamma$ centre. After one hour of irradiation values above 20 dB/m and 12 dB/m were reached at the E'$_\gamma$ centre and the ODC(II), respectively. During the annealing phase the E'$_\gamma$ centre reduced very slightly and the ODC(II) increased.

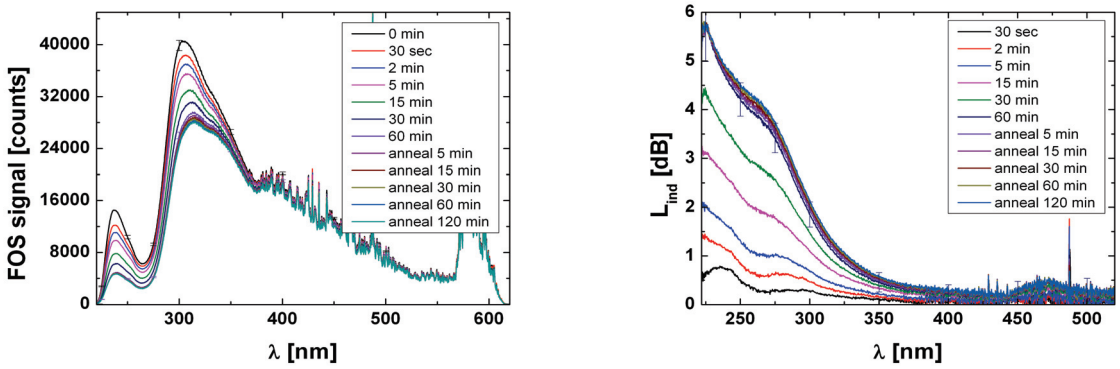

a) *b)*

Figure 5-20: Example of a 0.25 m long 26u sample (P doped core): a) Spectra taken before, during and after 405 nm MML irradiation. b) Induced loss during and after 405 nm MML irradiation. The intensity in the fibre core was I_{core} = 154 kW/cm².

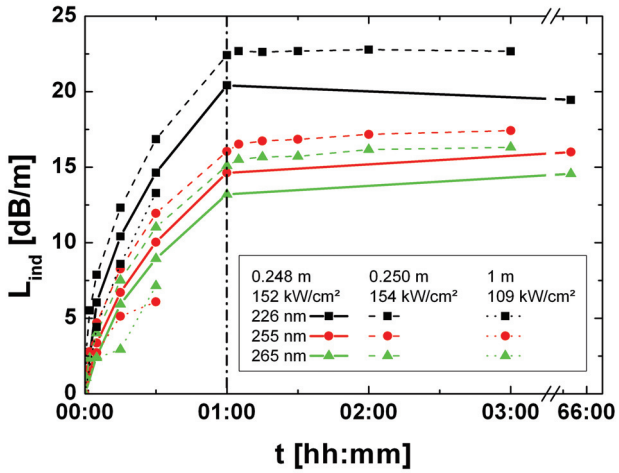

Figure 5-21: Traces of induced loss over time at specific wavelengths during irradiation with 405 nm MML of three 26u samples (P doped core). The dashed-dotted line marks the time stamp when the permanent irradiation with the 405 nm MML was terminated.

The Ge doped samples *22u* showed a completely different behaviour. The discussed sample in Figure 5-22 had a length of 0.151 m and $P_{out,fibre}$ = 280 mW. As a consequence of the longer UV absorption wavelength of this material no signal could be measured below 280 nm (see Figure 5-22 a)). Nevertheless, an improved loss was calculated between 280 and 300 nm in Figure 5-22 b) due to a shift of the absorption edge, which happened quickly within the first five minutes long irradiation period. On the other hand, the tail of an absorption band was measured between 300 and 350 nm. Figure 5-23 shows the quick improvement at 285 nm to -100 dB/m and -150 dB/m, followed by a slow increase. This was probably caused by the increase of a tail, which was traced at 305 nm and 330 nm

and showed a slow increase over time. Both trends continued after the permanent irradiation was terminated, stressing the major influence of the tail in this region for longer irradiation. This interesting behaviour between 280 and 300 nm was approximated using Gaussian distributions at the GeODC singlet excitation, at the 330 nm band and at the NBOHC. The result for a NBOHC at 265 nm with 4.9 dB, a GeODC singlet excitation at 240 nm with $-8.3 \cdot 10^6$ dB and a 330 nm band with 0.3 dB of induced loss is included in Figure 5-22 b) as a green dashed line. This line approximates the 30 minutes irradiation curve well and should fit better if a GeODC wider than the value from literature is assumed. The loss for the GeODC at 240 nm is extremely high, but a value in the range of 10^4 dB was estimated in the first place and only by these means the crossing of L_{ind} =0 at λ = 295 nm was achieved.

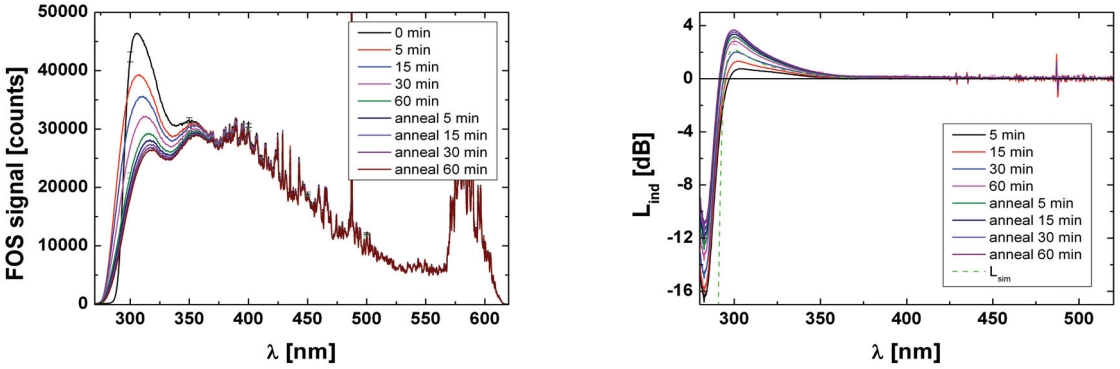

a) *b)*

Figure 5-22: Example of a 0.151 m long 22u sample (Ge doped core): a) Spectra taken before, during and after 405 nm MML irradiation. b) Induced loss during and after 405 nm MML irradiation. The intensity in the fibre core was I_{core} = 158 kW/cm².

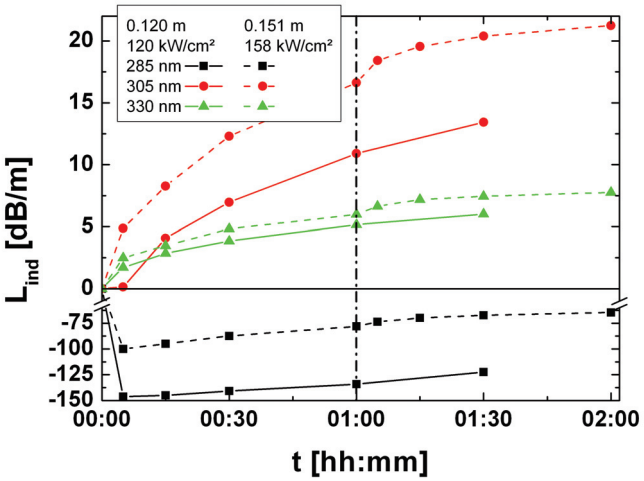

Figure 5-23: Traces of induced loss over time at specific wavelengths during irradiation with 405 nm MML of two 22u samples (Ge doped core). The dashed-dotted line marks the time stamp when the permanent irradiation with the 405 nm MML was terminated.

5.5 Discussion

The damage with the deuterium lamp demonstrated that defect centres at the wavelengths of 215 nm and 250 nm can be altered in the *IG-15* LMF. The E'_γ centre and the ODC(II) at these wavelengths were generated and reduced slowly within the irradiation time with no obvious saturation. After an annealing phase the changes recommenced. Interestingly, the ODC(II) increased at the beginning of the irradiation and started to reduce only after about 30 minutes. It seems that there are two processes of ODC(II) modification, one quickly induces defect centres while the other anneals this defect centre over time. In the first minutes these two processes duelled each other, but when one of them reached saturation the other increased its effect.

Surprisingly, all the differently prepared LMF samples showed modifications to their defect centres in the DUV. With the comparably low photon energy of 3.07 eV at 405 nm wavelength almost all varieties of DUV bulk defect centres were altered in some way. This happened even if the ODC(II) was not strongly pronounced in the pristine samples, like for the *1u* (standard preform), or the ODC(II) was not bleached or transformed completely as for the *IG-15* (H_2 treated preform). In general, it was observed that a reduction of ODC(II) happened abruptly within the first five minutes of irradiation with the 405 nm MML. On the contrary, if an increase of the ODC(II) was observed it happened over a longer period. The E'_γ centre also increased slowly over the course of irradiation, just like

the NBOHC when it was observed. In case of the *6u* (H_2 treated preform, 15 µm core fibre) and the *23u* samples (H_2 treated preform, 10 µm core fibre) the abrupt reduction of an absorption band was seen, simultaneously to the ODC(II), which could be attributed to the NBOHC. In addition to these normally seen defect centres the E'_β centre seemed to occur in some samples, like *1u* and *23u*. However, this defect showed only a quick small increase, maybe followed by a masking through the ODC(II) and E'_γ centres with higher damage values in respect to 229 nm.

During the annealing phases the E'_γ centre was never seen to increase. Either it was stable or it reduced slightly without the 405 nm irradiation. The ODC(II) and the NBOHC on the other hand increased during annealing. In the case of *1u* and *42u* (F doped core) an absorption band between 300 and 350 nm was observed to build up, with peaks at 350 nm and 313 nm, respectively. This band might be the interstitial Cl_2 absorption. A similar behaviour of *1u* and *42u* was already seen in the work of Unger [Unger2002]. The interesting behaviour of the Ge doped samples *22u* was approximated using Gaussian distributions. A model of a quickly and strongly reduced GeODC and a slowly increasing NBOHC is consistent with the observations on the other LMF samples. In general, the ODCs are reduced, the NBOHC is increased and during the annealing phase the ODCs and the NBOHC increase slowly.

The changes in the *IG-15* material by deuterium lamp and 405 nm laser are essentially the same, but much more expressed for the laser irradiation. From earlier work on multimode fibres [Klein1998, Huebner2000] it was deduced that about 2 nW/nm of deuterium light are coupled into the LMF, which results in 30 nW in the absorption band of the ODC(II) at 5 eV (250 nm). This has to be set in contrast to 240 mW at 3 eV (400 nm). However, the process by which the longer-wavelength light manipulates the DUV defect centres is still not clear and not described in literature, so far.

From my side, a real coherent two-photon absorption of 3 eV photons seems unlikely in a low power experiment of this type, but the probability of this might increase with the extremely long exposure. More likely is a two-step process as proposed by Messina and co-workers [Messina2008]. In this process an exciton is generated when two consecutive photons are absorbed incoherently. A non-radiative decay of the exciton can induce a defect centre at a precursor close to the absorption site. On the other hand, E'_γ centres can be generated directly at the absorption site by a two-step ionization of ODC(II) centres. While the work of Messina used the transition of the GeODC as an intermediate step for the two-step absorption of 5.1 eV laser light, the long-lived (~ 10 ms) singlet-triplet excitation ($S_0 \rightarrow T_1$) of the ODC(II) at 3.15 eV (394 nm) with a width of 42.5 nm is the only possible absorption in this case [Skuja1994]. As it can be seen from Figure 5-24 an absorption of a second photon at this transition can be treated like a $S_0 \rightarrow S_1$ excitation. The os-

cillator strength of the triplet excitation is rather low, but since we are very close to this wavelength with our laser a consequence should be seen from this excitation.

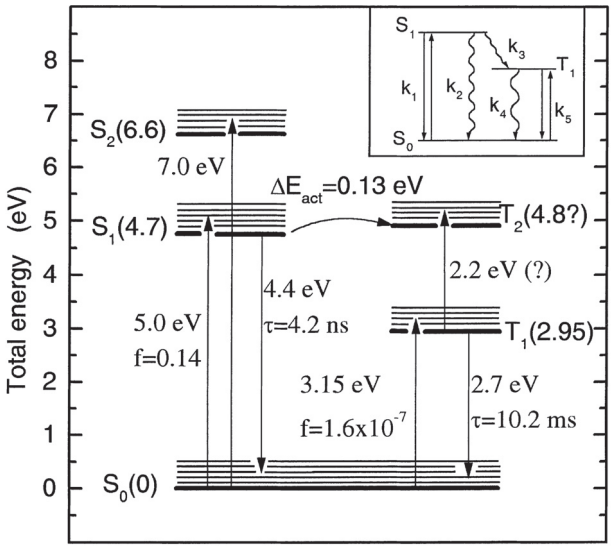

Figure 5-24: Energy term schematic of the ODC(II) with singlet ground state S_0 and singlet as well as triplet excited states [Skuja1998].

The quick reduction of ODC(II) within the first minutes of 405 nm irradiation is interpreted as a direct influence on the ODC(II) by an excitation through the triplet transition. In the *IG-15* the ODC(II) were completely transformed, probably into E'_γ centres by two-step ionisation. The *6u* and *23u*, which were also H_2 treated like the *IG-15*, did not show a complete transformation of the 250 nm absorption band. Either the band was not fully resolved by the spectral measurement or two different species of defect centres were observed at 250 nm. Candidates are the description of the ODC(II) as a silicone dangling bond and as two-fold coordinated silicone as well as the peroxy radical, which is controversially discussed in literature. All the other defects that were generated, were very likely due to decays of excitons *(SiO_2)** at strained precursor sites *P* or where hydrogen and chlorine were bound into the silica network [Friebele1979, Skuja1998, Muehlig2005].

$$(SiO_2) + 2\cdot h\nu \rightarrow (SiO_2)^* \quad (5\text{-}6)$$

$$P + (SiO_2)^* \rightarrow E' \quad (5\text{-}7)$$

$$Si\text{-}H + (SiO_2)^* \rightarrow E' + H \quad (5\text{-}8)$$

$$Si\text{-}O\text{-}H + (SiO_2)^* \rightarrow NBOHC + H \quad (5\text{-}9)$$

$$Si\text{-}Cl + (SiO_2)^* \rightarrow E' + Cl \quad (5\text{-}10)$$

Formula 5-10 would also explain the generation of the 330 nm band in *1u* and *42u* samples. The strong increase of the ODC(II) in the *1u* when irradiated with 405 nm laser

light would render the Cl_2 molecules unstable and incorporate some of them into defect centres [Kirchhof2001], leading to the reduced 330 nm band for *1u*. The bond of a chlorine to a silicone atom, also from production (0.14 mol% Cl content in core and cladding), would later be broken by a decaying exciton, then the chlorine could dimerise and form the interstitial Cl_2 band again.

The explanation of the laser-induced periodic surface structures on the fibre end surfaces for long-term irradiation bases on the surface ionisation of the silica material (see Section 4.8). The main contribution to the surface ionisation would come from positively charged E' centres close to or on the surface. If a modified silica fibre with a small core diameter did not show the generation of the E' centre band during 405 nm irradiation, it would be perfectly suited for this application. Unfortunately, all the LMF samples examined here showed a strong generation of E' centres and other defect centres. On one hand, the improved materials for 446 nm laser applications did not exhibit a large loss in the visible range due to an extended UV absorption tail, except for the Ge doped sample. On the other hand, the increased resistance against the so-called photo-darkening in the visible revealed the strong influence of the surface effects on fibre transmission in the long term [Kirchhof2001, Unger2002]. Further tests with low-temperature high-pressure hydrogen loaded fibre samples could show the reduced generation of E' centres. A positive influence along the fibre could probably be observed, but the molecular H_2 would not be stable at the fibre surfaces and diffuse out of the material.

5.6 Summary

The spectral damage behaviour of different low-mode fibre types was investigated by 405 nm laser irradiation. Fibres drawn from modified preforms were examined at known UV defect centres for induced losses and those recorded time-dependently. The preforms were either standard low-OH material, prepared with H_2 diffusion or collapsed in a He atmosphere for an oxygen deficit. Fibres with cores weakly doped with Ge, P or F were examined as well. All fibres showed a strong defect centre generation and transformation after 405 nm irradiation. Thus, non of the investigated samples is well suited for long-term stability concerning the previously found surface damage. No significant length dependence of the loss distribution was found and a comparison to standard deuterium lamp damage revealed a very efficient process of defect generation for the 405 nm laser irradiation. This leads to the conclusion that a multi-photon process is responsible for the induced defect centres. A two step absorption at the singlet-triplet transition of the ODC(II) is proposed and consistent with models from literature [Skuja1994, Messina2008]. This absorption could generate excitons which in turn transform precursors into defect

centres. An efficient transformation or bleaching of ODC(II) into E'_{γ} centres supports this proposal.

6 Evolution and mitigation of periodic structures on fibre end surfaces

6.1 Abstract

After the discovery of laser-induced periodic surface structures (LIPSS) on the launching end surfaces of single-mode fibre irradiated with 405 nm CW laser light, different measures were investigated to mitigate the effect and stabilise the fibre output power. Together with the transformation of defect centres, the power density and the surface roughness are the most influential parameters to the growth of the LIPSS. It will be shown that a spliced and cleaved short piece of launch-fibre stabilises the fibre output power. However, the growth of a LIPSS on the distal end was stimulated, due to a constantly high power density. This effect can also be mitigated by using launch-fibres or end-caps. In addition to the investigation of the distal end damage, step-wise simulations of the growth of the LIPSS on the distal fibre end were undertaken to see the impact on transmission properties and beam quality. Finally, these results will be compared to experimental data of output beam quality degradation.

6.2 Introduction

When the output power degradation of 405 nm fibre-coupled diode laser systems was investigated in detail, it became apparent that no photo-degradation or contamination absorbed or attenuated the laser light at this wavelength. The coupling and transmission loss of the laser light was associated to the growth of a laser-induced periodic surface structure (LIPSS, see Chapter 4). This LIPSS grows due to the irradiation of the fibre end surface with 405 nm CW laser light and forms a lens and a scattering centre on the launching surface. The additional optical element changes the coupling conditions into the low-mode (LMF) or single-mode fibre (SMF). As the structure grows in height, less power is coupled into the fibre core and the fibre output power decreases over time. The main factors contributing to the formation of the LIPSS are the power density, surface roughness, generation of UV defect-centres, and the polarisation direction of the laser light. The polarisation determines the orientation of the ripples, which in this work on silica were found to form parallel to it. This can be confirmed by results from femtosecond laser experiments on silica in literature [Hoehm2012]. On the other hand, it was concluded that the other three factors determine the thickness of an unstable ionised surface layer. As shown before, this layer self-organises into the LIPSS over the period of irradiation [Reif2006].

Different solutions which reduce the intensity on the fibre launching end were examined in this work. Different end surface preparation methods were compared in Chapter 4 and fibre cleaving turned out to be the most reliable one, concerning the surface damage. The application of glass windows is widespread in fibre-coupled high-power laser systems for the near-IR region, especially for fibre laser systems. These so-called end-caps are glass ferrules that are fused to the fibre end, preferably by using CO_2 lasers [Boehme2009]. The result of using an end-cap is the reduction of power density on the fibre end surface, to mainly prevent mechanical damage of the glass surface. Such a product with silica tubing is also offered by Polymicro Technologies [Acuna2010, US2011/0235973] and was provided for this work fused to different SMF and LMF samples with a CO_2 laser. Through this silica window the laser beam incides with a large spot, the light is then focused into the fibre within the silica material. Unfortunately, it was not possible to use these samples with silica end-caps in an existing, mechanically stable, damage setup for long-term irradiation. No connector or holder for these ferrules was available for the use on the launching fibre end.

During the search for an own solution a possibility was found to splice pieces of multimode fibre (MMF) to SMF and cleave the MMF at a precise distance from the splice. Thereby producing a short launch-fibre, like an end-cap, with a good surface quality that can be employed with the SMF inside a standard connector for 125 µm fibre. A patent application has been filed for a similar procedure by Coherent Inc. and been published at the beginning of 2010 [US20100027569]. In that application the splicing of a MMF and SMF and a subsequent polishing process are described, but not a preparation by cleaving. The likelihood of the application being granted is low, because a patent on the use of MMF as launch-fibre for small core fibres was already granted in 1987 to AT&T [US4701011]. It should be noted, that the duration of this particular patent was over in 2005.

In the future the output power of CW diode lasers at 405 nm will increase further and single-mode laser diode modules (LDM) with 300 mW output power are already commercially available. Therefore, more than just the reduction of power density should be considered for the production of a high performance launch-fibre. The other important parameters, which enhance the formation of a laser-induced periodic surface structure, that were found are the surface roughness and the generation of defect centres. If these are considered as well, then it should be avoided to polish the launch-fibre. Alternatively, a precise cleaving of the end surface is possible with common telecommunications fibre cleavers, thereby improving the surface roughness as shown in section 4.3.4. The MMF that is employed as a launch-fibre should exhibit a low solarisation to reduce the genera-

tion of UV defect centres. Therefore, a FDP type MMF, produced by Polymicro Technologies, was used that shows only a very low solarisation in the DUV [Khalilov2006].

In this chapter experiments and results obtained for improved fibre assemblies are presented. The calculation and production of an assembly with a high performance launch-fibre are described. All proximal fibre ends have a launch-fibre. For the investigation of the distal fibre end damage assemblies with and without silica end-cap were prepared. The assemblies were long-term irradiated with 405 nm CW laser diodes. Additionally, measurements of spectral loss and beam quality were performed at the fibre output. The results on the distal fibre end damage are compared with step-wise simulations of the growth of a LIPSS on the distal fibre end.

6.3 Experimental setup

6.3.1 Measurement setups

For the irradiation of the fibre assemblies, laser diode modules (LDM) for 405 nm were used. The single-mode laser (SML, Omicron LDM405.120.CWA.L) uses only a single diode, while the multi-mode laser (MML, Omicron LDM405D.450.CWA.M) comprises two cross-combined diodes. The output power of the employed SML has a maximum of P_{out} = 150 mW and the laser beam is collimated and optically corrected for astigmatism. The beam quality of M^2 = 1.1 is suitable for high coupling efficiencies into SMF. The MML has a maximum output power of P_{out} = 390 mW and a beam quality of M^2 = 3. The LDMs are current and temperature stabilised for long-term irradiation. The collimated laser beam is focused on the fibre end surfaces with an imaging and alignment system (IAS) for connectorised fibres. The focal length of the aspheric lens used in the SML is f = 6 mm and f = 4 mm in the MML. The fibre end can be adjusted along the optical axis and tumbled around it. Because of the small spot diameter power densities in the range of MW/cm² are achieved for output powers of a few hundred milliwatts.

The progress of the experiments was monitored using the fibre output power $P_{out,fibre}$ from the fibre assemblies. The assemblies were irradiated over a period ranging from eight days to over two months. The loss over time was calculated using the formula:

$$L(t) = -10 \cdot \log_{10}\left(\frac{P_{out,\,fibre}(t)}{P_{out,\,fibre}(0)}\right) \qquad (6\text{-}1).$$

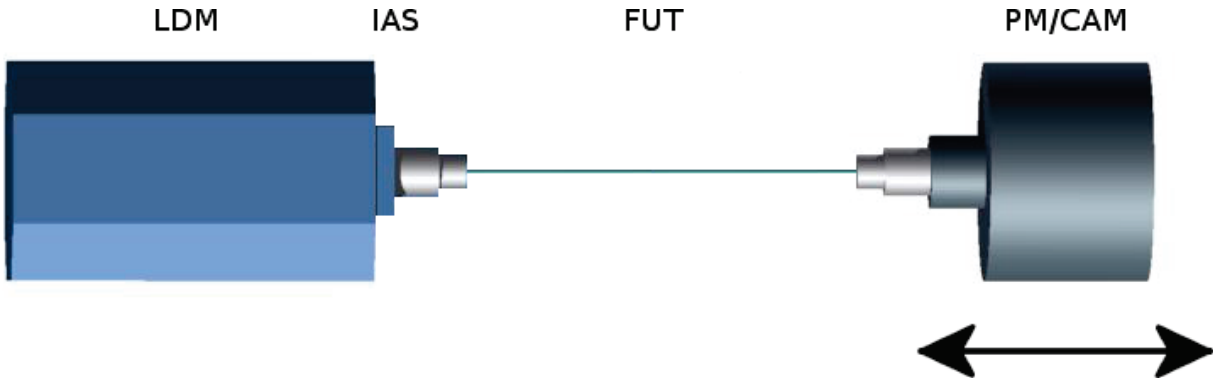

Figure 6-1: The damage setup consisting of stabilised laser diode module (LDM) with a wavelength of 405 nm, an imaging and alignment system (IAS) and a movable thermopile power meter (PM) or camera (CAM). The fibre under test (FUT) is aligned for maximal output power.

For the power readings a thermopile power meter (PM) of type Coherent PowerMax PS19Q (19 mm aperture) was used. In Figure 6-1 the whole setup is shown, where the fibre under test (FUT) is a fibre assembly with launch-fibre or end-cap and a length of 1 m in all cases. To connect the FUT to the IAS all proximal ends were connectorised. The FUTs were not glued in the connector, but rather held in place by a clamping mechanism attached to the connector. For the MML FSMA connectors were used and for the SML FC/PC connectors. The distal fibre end is aligned 10 mm in front of the PM for free space irradiation and was appropriately connectorised for spectral measurements. The distance between fibre end and PM can be accurately varied for divergence angle measurements.

In all cases the proximal end was adjusted to maximum fibre output power using the IAS. The polarisation of the SML was aligned to the slow axis of the polarisation-maintaining (PM) fibres. During irradiation, the proximal fibre end is used inside the IAS, but not sealed or flushed with gas, and readjusted from time to time to make sure that the system was not misaligned by mechanical or temperature changes. The distal end is in free space and not protected from dust particles. All experiments are conducted in a standard laboratory environment at room temperature. To determine the error in the power reading, the standard deviation of a daily or semi-daily average is added to the uncertainties seen from the power meter and the laser diode module. For the error ΔL of the loss the non-linear propagation of error is used [Muehl2001]:

$$\Delta L = \sqrt{\left(\frac{\partial L}{\partial P_{out,fibre}(0)}\right)^2 \cdot \Delta P_{out,fibre}(0)^2 + \left(\frac{\partial L}{\partial P_{out,fibre}(t)}\right)^2 \cdot \Delta P_{out,fibre}(t)^2} \qquad (6\text{-}2).$$

For the influence of the 405 nm laser radiation on the fibre material the power density I_{core} in the fibre core needs to be taken into account.

$$I_{core} = \frac{P_{out,fibre}}{A_{eff}} = \frac{P_{out,fibre}}{\pi \cdot w_0^2} \quad (6\text{-}3)$$

The power density is averaged over the effective mode area A_{eff} of the fibre core. The peak power density I_{peak} of a Gaussian beam in a SMF is twice as high as I_{core} [Paschotta2008].

M² measurements of the beam quality at the distal fibre end were performed on the light emitted from the fibre, which was collimated with a microscope objective. Behind the objective a lens with a focal length $f = 40$ mm and a sliding CCD camera (DataRay WinCamD-UV) were installed to take the measurements (CAM in Figure 6-1). For each measurement 20 data points were taken with a distance of 3 mm in between.

In order to determine the spectrally induced loss in one MMF and one SMF sample, a spectrometer system as depicted in Figure 6-2 was employed. The system consists of a deuterium lamp (D_2) with an imaging system and the fibre-optic spectrometer (OceanOptics Maya2000Pro). The FUT was connected with FSMA connectors to the spectrometer and the deuterium lamp. This lamp provides a broadband light spectrum starting at 180 nm while the spectrometer covers the spectral range from 167 to 620 nm.

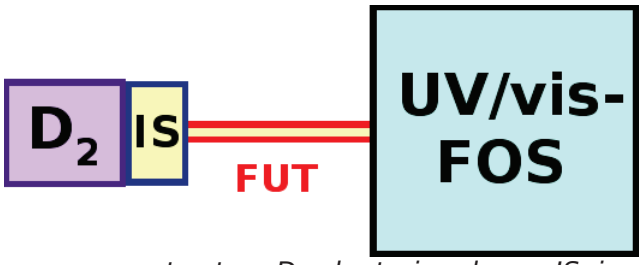

Figure 6-2: Spectral measurement setup; D_2: deuterium lamp, IS: imaging system, FUT: fibre under test, FOS: fibre-optic spectrometer for UV and visible range.

Spectral measurements were taken before and after exposure for the MMF. The damaged SMF on the other hand was compared to a pristine piece of this fibre of the same length, after the launch-fibre was removed to equalise the coupling conditions. The dark current reading was subtracted from the recorded spectra. To obtain the spectral loss induced by 405 nm irradiation the spectra were processed using the relationship:

$$L_{ind}(\lambda) = -10 \cdot \log_{10}\left(\frac{I_{after}(\lambda)}{I_{before}(\lambda)}\right) \quad (6\text{-}4).$$

In the spectral measurements, a lamp signal error ΔI of ±3 % at 200 nm, ±2 % at 300 nm and ±1 % at 400 nm is taken into consideration. The noise in the spectrometer is much lower than this error and not taken into account. For the error of the spectral loss ΔL_{ind} the non-linear propagation of error is used [Muehl2001]:

$$\Delta L_{ind} = \sqrt{\left(\frac{\partial L_{ind}}{\partial I_{before}}\right)^2 \cdot \Delta I_{before}^2 + \left(\frac{\partial L_{ind}}{\partial I_{after}}\right)^2 \cdot \Delta I_{after}^2} \quad (6\text{-}5).$$

The damaged distal fibre end surface of one assembly was repeatedly cleaved off. The cleaved off distal end was stored for investigation in a scanning electron microscope (SEM) with energy-dispersive x-ray spectrometer (EDX). Cleaved samples of the distal fibre end were taken for periods of 14, 8, 1, 2, 6, 4 and 12 days of irradiation at constant power densities of 1.3 MW/cm² at the fibre end. The order of the samples depended on the access to the experiment, for example on weekends, and therefore is not from shorter to longer periods. For other assemblies the damaged distal fibre end was cleaved off only once for the SEM examination. Photographs of the far-field on a screen were also taken for pristine and damaged distal fibre ends.

6.3.2 Length calculation of a launch-fibre or end-cap

If the beam spot size $w_{0,s}$ of a focused laser beam is assumed to be the same in air with a refractive index $n_1 \approx 1$ and a medium with $n_2 \neq 1$, then the beam parameter product BPP is [Paschotta2008]:

$$BPP = \theta_{ff} \cdot w_{0,s} = \frac{\lambda_n}{\pi} \quad (6\text{-}6),$$

with $\lambda_n = \frac{\lambda_0}{n}$ and λ_0 the vacuum wavelength (6-7).

The BPP in a medium is divided by n, effectively reducing the wavelength λ_n for a higher refractive index. The far-field angle is then reduced due to refraction. This also means that the diffraction limit of the beam is lower in a medium with $n > 1$. If the laser beam is not a Gaussian beam, then the diffraction limit and beam parameter product are increased by the M^2 factor [Sun2012], which is 1.07 for a SMF. The actual beam spot size $w_{0,s}$ in the focus can then be calculated by far-field approximation:

$$w_{0,s} = \frac{\lambda_n \cdot f}{\pi \cdot w_{0,l}} \cdot M^2 \quad (6\text{-}8).$$

Here f is the focal length of the imaging system and $w_{0,l}$ the beam radius of the collimated laser beam at the input of the focusing lens. If the beam spot size $w_{0,s}$ in the laser focus is different from the spot size $w_{0,f}$ of the SMF, then the coupling efficiency η and loss L are given by Formula 6-9.

$$\eta = \left(\frac{2 \cdot w_{0,s} \cdot w_{0,f}}{w_{0,s}^2 + w_{0,f}^2}\right)^2 \quad ; \quad L = 20 \cdot \log_{10}\left(\frac{w_{0,s}^2 + w_{0,f}^2}{2 \cdot w_{0,s} \cdot w_{0,f}}\right) \quad (6\text{-}9)$$

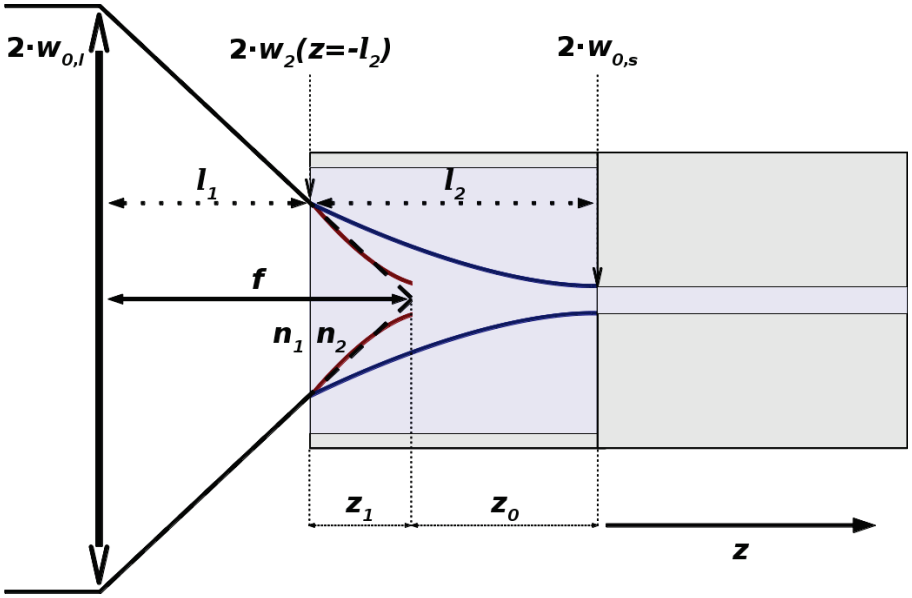

Figure 6-3: Sketch of launching setup with SMF and MMF launch-fibre of length l_2. A lens with focal length f is in a distance of l_1 from the end surface.

The setup for a launching system with launch-fibre is sketched in Figure 6-3. For launching light into the fibre end with an attached MMF launch-fibre, it is very important to avoid cutting off too much of the flanks of the Gaussian power distribution. The power P of a Gaussian-shaped beam that is transmitted through an aperture with radius r is given by [Marcuse1982, Neumann1988, Sun2012]:

$$P(w,z) = P_{out} \cdot \left(1 - e^{\frac{-2 \cdot r^2}{w_n(z)^2}}\right) \tag{6-10}.$$

$$w_n(z) = w_{0,s} \cdot \sqrt{\left(\frac{z}{z_{R,n}}\right)^2 + 1} \approx \frac{w_{0,s} \cdot z}{z_{R,n}} \tag{6-11}$$

(approximation only valid for $|z| \gg z_{R,n}$)

$$z_{R,n} = \frac{\pi \cdot w_{0,s}^2}{M^2 \cdot \lambda_n} \tag{6-12}$$

The beam radius w_n depends on the position z along the propagation axis of the beam, starting at the focus, and the Rayleigh length $z_{R,n}$, as shown by Formulae 6-11 and 6-12. The Rayleigh length $z_{R,n}$ is the distance from the focus at which the beam radius increases by factor $\sqrt{2}$. It is shorter for beams with larger M^2 factor.

For the calculation of the coupling conditions and properties of the imaging system the propagation needs to be viewed from the focus. First, the actual beam spot size $w_{0,s}$ is determined for the imaging system with focal length f using Formula 6-8. This is the focus

with $z = 0$ inside the silica launch-fibre. The propagation of the beam inside the launch-fibre towards the source with negative z is specified by:

$$w_2(z) = w_{0,s} \cdot \sqrt{\left(\frac{z}{z_{R,2}}\right)^2 + 1} \tag{6-13}$$

with $n_2 = 1.45$ for silica.

In contrast to a silica end-cap, a launch-fibre has a small core diameter. The beam radius $w_2(z=-l_2)$ at the entrance aperture of a launch-fibre with a core radius $r = 50$ µm and length l_2 for which 98 % of the power are retained is determined using a transposed form of Formula 6-10:

$$w_2(-l_2) = \sqrt{\frac{-2 \cdot r^2}{\ln(1-0.98)}} = \sqrt{\frac{-2 \cdot 50^2}{\ln(0.02)}}\ \mu m \approx \sqrt{\frac{5000}{3.9}}\ \mu m \approx 35.8\ \mu m \tag{6-14}.$$

Consequently, the length l_2 is:

$$l_2 = z_{R,2} \cdot \sqrt{\left(\frac{w_2(-l_2)}{w_{0,s}}\right)^2 - 1} \approx z_{R,2} \cdot \frac{w_2(-l_2)}{w_{0,s}} \tag{6-15}.$$

For a LDM at $\lambda_0 = 405$ nm with $w_{0,l} = 0.6$ mm, $M^2 = 1.2$ and $f = 6$ mm the following values are received with $\lambda_n \approx 279.3\ nm$:

$$w_{0,s} \approx 1.55\ \mu m \quad \text{and} \quad z_{R,2} \approx 22.4\ \mu m \tag{6-16}.$$

The maximum length l_2 is approximately:

$$l_2 \approx 22.4\ \mu m \cdot \frac{35.8\ \mu m}{1.55\ \mu m} \approx 517\ \mu m \tag{6-17}.$$

The beam propagation in the air towards the laser source has to be calculated only after $z = -l_2$. The two propagation schemes have to be stitched together at that point. Therefore, the position z_1 at which the beam in air has the same diameter $w_2(z=-l_2)$ as the beam in silica needs to be determined:

$$z_1 = z\left(w_2(z=-l_2)\right) = z_{R,1} \cdot \sqrt{\left(\frac{w_2(z=-l_2)}{w_{0,s}}\right)^2 - 1} = z_{R,1} \cdot \frac{l_2}{z_{R,2}} = l_2 \cdot \frac{n_1}{n_2} \tag{6-18}.$$

The offset z_0 of the beam in air on the propagation axis is:

$$z_0 = l_2 - z_1 = l_2 \cdot \left(1 - \frac{n_1}{n_2}\right) \tag{6-19}$$

and the relation of l_1, l_2 and z_0 according to Figure 6-3 is:

$$l_1 = f + z_0 - l_2 = f + l_2 - l_2 \cdot \frac{n_1}{n_2} - l_2 = f - l_2 \cdot \frac{n_1}{n_2} \quad \text{or} \quad \frac{f}{n_1} = \frac{l_1}{n_1} + \frac{l_2}{n_2} \tag{6-20}.$$

The distance between the focusing lens, where the beam radius is $w_{0,l}$, and the focus, with $w_{0,s}$, is approximately the focal length f in the far field (see also Formula 6-8):

$$f = z_{r,1} \cdot \sqrt{\left(\frac{w_{0,l}}{w_{0,s}}\right)^2 - 1} \approx \frac{\pi \cdot w_{0,s}^2}{M^2 \cdot \lambda_n} \cdot \frac{w_{0,l}}{w_{0,s}} = \frac{\pi \cdot w_{0,s} \cdot w_{0,l}}{M^2 \cdot \lambda_n} \qquad (6\text{-}21),$$

with $w_{0,l} \gg w_{0,s}$.

Therefore, the major change in the imaging system is not in the lens, but rather in the distance l_1 between the lens and the end surface. This depends on the length of the launch-fibre and its refractive index. The distance l_1 will be linearly reduced by z_1, which depends on the length l_2 of the launch-fibre, as shown in Figure 6-4. This adjustment is possible with most alignment systems, either by z-axis alignment or by putting the lens closer to the end stop of the connector socket. The intensity $I(z=-l_2)$ at the air-silica interface is:

$$I(z=-l_2) = \frac{P_{out}}{\pi \cdot w_2^2(z=-l_2)} \qquad (6\text{-}22).$$

It is also shown in Figure 6-4 for the LDM with Formulae 6-16 and 6-17, and output power P_{out} = 150 mW. The power density can be reduced from about 2 MW/cm² in the focus to below 10 kW/cm² with l_2 > 320 µm.

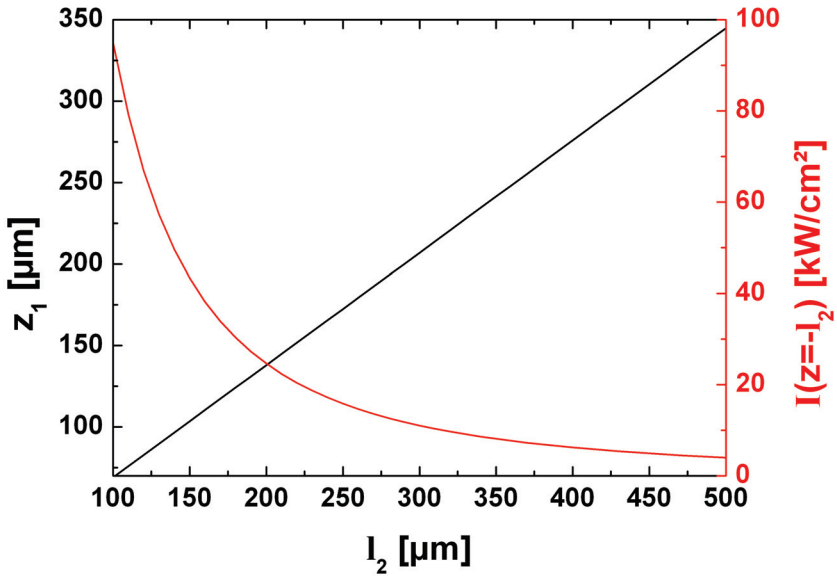

Figure 6-4: The distance z_1 (black), by which the launch-fibre end surface needs to be put closer to the lens, in dependence on the length l_2 of the launch-fibre. Values according to Formula 6-20 with f = 6 mm and n_2 = 1.45. Intensity $I(z=-l_2)$ (red) at the air-silica interface for the LDM with Formulae 6-16 and 6-17, and output power P_{out} = 150 mW.

The radius of curvature *R(z)* of the beam propagating into the launch-fibre increases abruptly at the air-silica interface due to refraction. Figure 6-5 shows this together with *w(z)* along the propagation axis into the launch-fibre. Using the approximation $|z| \gg z_{R,n}$ the radius of curvature is given by [Marcuse1982, Neumann1988, Sun2012]:

$$R(z) = z \cdot \left[\left(\frac{z_{R,n}}{z} \right)^2 + 1 \right] \approx z \quad ; \tag{6-23}$$

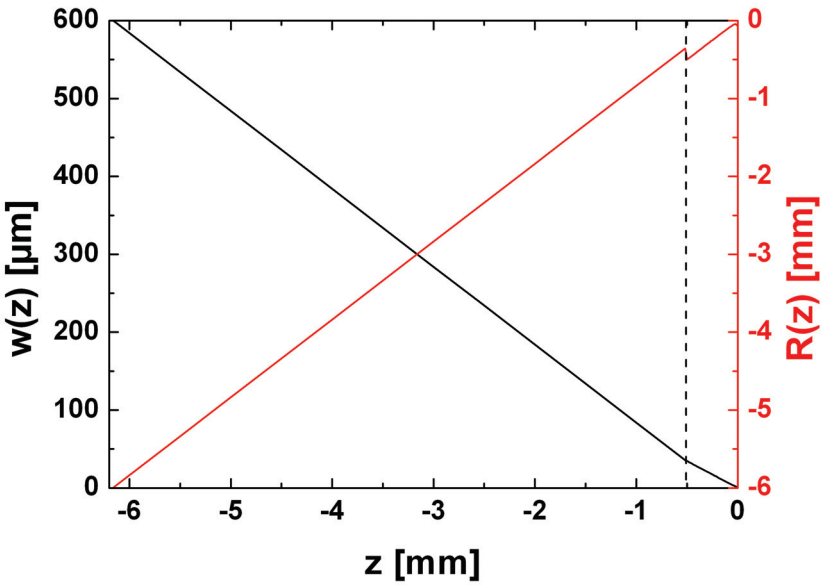

Figure 6-5: Beam radius w and radius of curvature R over position z for λ_0 = 405 nm, $w_{0,l}$ = 0.6 mm, M^2 =1.2 and f = 6 mm with l_2 = 517 µm. The dashed line marks the transition from $n_1 \approx 1$ to n_2 = 1.45.

6.3.3 Sample preparation

The high quality of the employed FDP MMF was confirmed by a damage test with a multimode LDM with 390 mW output power. A 1 m long piece of FDP100 was irradiated for 4 h and then additionally for 12 h. The induced loss L_{ind} in Figure 6-6 shows almost no change after 4 h and a very small E'_{γ} centre after 16 h of irradiation. Due to the large core diameter of 100 µm the power density I_{core} in the core was only 4.4 kW/cm² during the damage. Therefore, a quick degradation of a cleaved surface of a FDP100 launch-fibre is not likely.

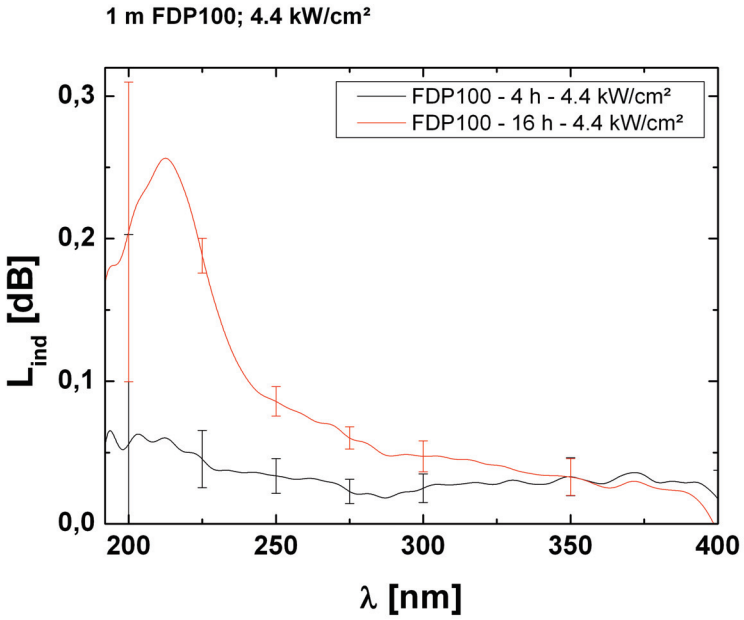

Figure 6-6: Induced loss for a 1 m long sample of fibre type FDP100. A power density of 4.4 kW/cm² was achieved for an irradiation period of 16 h.

A spliced and cleaved launch-fibre of FDP100 with an outer diameter (cladding) of 110 µm is shown in Figure 6-7. Standard telecommunications splicers (Fujikura FSM-30S or FSM-100MP) and a specialty fibre cleaver (Vytran LDC-400) were used. The production can easily be observed by using a small digital microscope connected to a computer by USB (universal serial bus), for example a Dino-Lite microscope. These microscopes also allow geometrical measurements in the stored or live transferred pictures, thereby simplifying the production process. Lengths of 420 to 530 µm of the launch-fibre were cleaved on the experimental assemblies and a length accuracy of ± 10 µm was achieved.

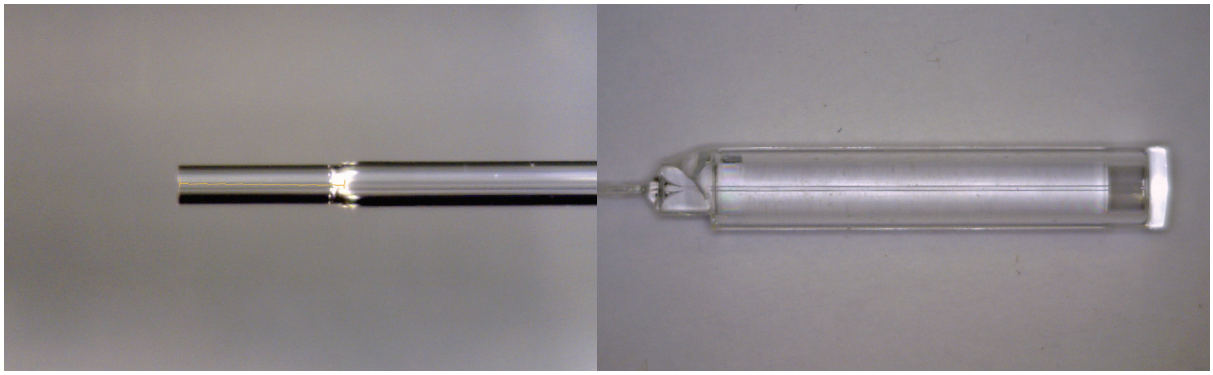

a) *b)*

Figure 6-7: a) A launch-fibre with a length of l_2 = 450 µm spliced to SM 400-SC. The splice is easily recognisable by the transition from 110 µm to 125 µm outer diameter. b) A end-cap fused to a fibre end by Polymicro.

The preparation of photonic crystal fibre (PCF) is facilitated by the means of splicing to a launch-fibre. Without a launch-fibre the holes of the PCF needed to be closed at the ends and the end surfaces had to be flattened by polishing. When splicing the MMF to the PCF the microstructure at the end is protected by the splice. Therefore, a PCF, especially engineered for this work, was one of the first samples with a launch-fibre. This particular PCF was designed and drawn by *Fiberware* and is called *PM-LMA-375*. It is a large mode area PCF with an elliptical mode field that maintains the polarisation. It was designed for the violet region with a high OH content of > 700 ppm in the core material.

The other SMF type that was prepared with launch-fibre was *SM 400-SC* from *Fibercore*, UK. While those assemblies only have launch-fibres on the proximal end, two other assemblies were protected on the distal end as well. For this purpose Polymicro Technologies fused silica end-caps to an experimental LMF type *6u* from *IPHT*, Germany, and to the commercial PM fibre *PM-S405-HP* from *Nufern*, USA. The end-caps have a diameter of 2.7 mm and a length of 15 mm. The distance between the fused region and the air-silica interface is in the range of 300 to 600 µm.

Even if it was not used on the samples presented, it is possible to create a specific angle on the launch-fibre end surface with a Vytran LDC-400. This is important for a final product to reduce back-reflection into the laser diode. After the fibre is fixed in the holding blocks of the cleaver, one of the blocks is rotated in a certain angle and then the fibre is cleaved [Neumann1988]. The specific angle on the end surface depends on the applied torsion or rotation angle, the distance between the holding blocks, and the fibre modulus of rigidity, which is in the order of 28 to 32 GPa for silica fibres. In the experiments the angle on the end surface was not an issue, but a final commercial product has to incorporate an angled fibre end surface. Especially for PM-SMF the orientation of the cleave angle in respect to the birefringent structure needs to be taken care of [Mende2002,

Caloz2004, Agrawal2007]. Only then, an assembly like FC/APC is possible. The first experiments for an 8° angle on SMF and PM-SMF resulted in an angle of (7.59±0.75)° on *SM 400-SC* and (6.87±0.91)° on *PM-S350-HP*. A correct alignment of the cleave and the PM axes was possible, but yet with a lot of effort to achieve this.

6.4 Results

6.4.1 Performance of fibre-coupled diode laser systems with launch fibre

The coupling efficiency from the laser into the SMF through the launch-fibre also depends on the quality of the splice, besides the spot sizes of laser focus and SMF [Neumann1988]. The light-guiding structure of the SMF could deform in the first few 10 µm due to the heat of the fusion arc. As a consequence the laser light is not guided or coupled with a low loss. Furthermore, the interface between MMF and SMF can get contaminated by burn-off from the electrodes of the fusion arc splicer. In Table 6-1 the achieved coupling efficiencies for the different investigated combinations of LMF, SMF and PM-SMF with launch-fibre of different lengths are reported. The PM-SMF and LMF assembly had a launch-fibre on the proximal end and a silica end-cap on the distal end. The second *SM 400-SC* sample with a single launch-fibre was also checked in reverse. With the launch-fibre on the distal end and a bare fibre end on the launching end. In this arrangement the assembly had a fibre output power of 90.7 mW. In comparison to the intended arrangement the coupling efficiency was better, with 65.7 % compared to 47.2 % and 65.1 mW. But with the launch-fibre on the distal end, interference rings were seen in the far field.

The fibre output power $P_{out,fibre}$ was stabilised to a large degree in the samples with launch-fibre. Figure 6-8 shows that the damage rate is below 0.03 dB/day for the protected samples. For comparison, the damage rate for SMF samples without protection irradiated with the SML was 0.2 to 1 dB/day, depending on the surface preparation (see section 4.3). On the surfaces of the launch-fibre no damage could be found after the irradiation. The first assemblies had a low coupling efficiency, nevertheless power densities I_{core} in the SMF cores of 800 kW/cm² to 1.3 MW/cm² were reached.

Table 6-1: Coupling efficiencies of transmission systems with different fibre types and launch-fibres of different lengths. (: assemblies with silica end-cap on distal end)*

Type	Mode-field diameter [µm]	Length [µm]	$P_{out,fibre}$ [mW]; Coupling efficiency
SM 400-SC	2.5	420	53.1 mW; 38.5 %
SM 400-SC	2.5	450	65.1 mW; 47.2 %
PM-LMA-375	2.6 / 4.3 (elliptical)	490	72.2 mW; 52.3 %
PM-S405-HP *	3.2	530	81.2 mW; 58.8 %
6u *	15 (core diameter)	490	268 mW; 74.7 %

When the second assembly with *SM 400-SC* (red circle in Figure 6-8) showed a higher loss of 0.38 dB after 14 days, the distal end was cleaved off. The loss was thereby reduced by 0.13 dB. It was noticed that the divergence angle of the beam coming from the fibre was smaller after the damaged distal end was cleaved off. Therefore it was assumed that the reduction in power that was measured was not due to a loss, but due to an increase in

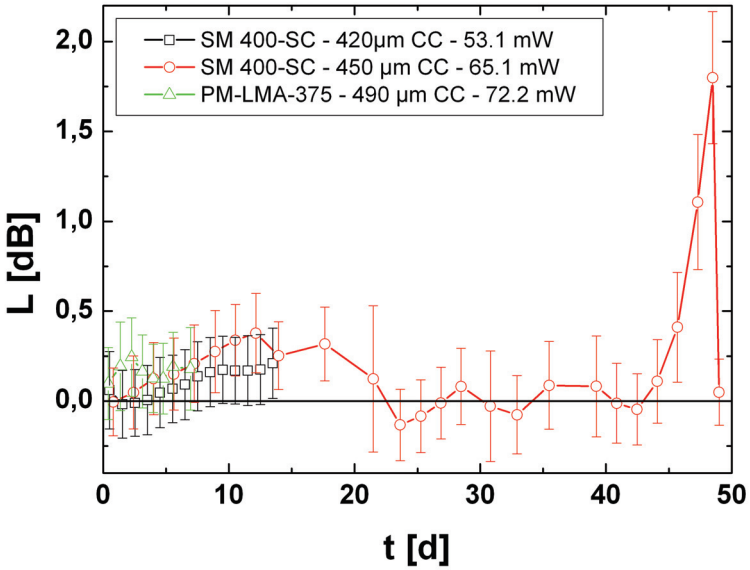

Figure 6-8: Loss over time of SMF samples with launch-fibre irradiated with the SML. The second sample (red circle) was adjusted several times during irradiation. The given power is the fibre output power at the beginning of the measurement.

far-field angle. The light spot was larger than the aperture of the power meter and could not be completely collected. The last of seven samples which were cleaved off after dif-

ferent periods showed the lowest measured power after 12 days of irradiation, but when it was cleaved off all the light could be collected again for the power measurement. For this last sample of damaged end surfaces an M^2 measurement was performed directly after cleaving and after the 12 days of irradiation. On one axis a degradation from $M^2 = 1.2 \pm 0.2$ to $M^2 = 5 \pm 0.5$ was measured and on the axis perpendicular to that a degradation from $M^2 = 1.6 \pm 0.2$ to $M^2 = 9 \pm 0.5$.

The increase in far-field angle of the light emitted from the fibre end was most notable for the assembly with *PM-LMA-375*. Before the irradiation the web around the PCF core

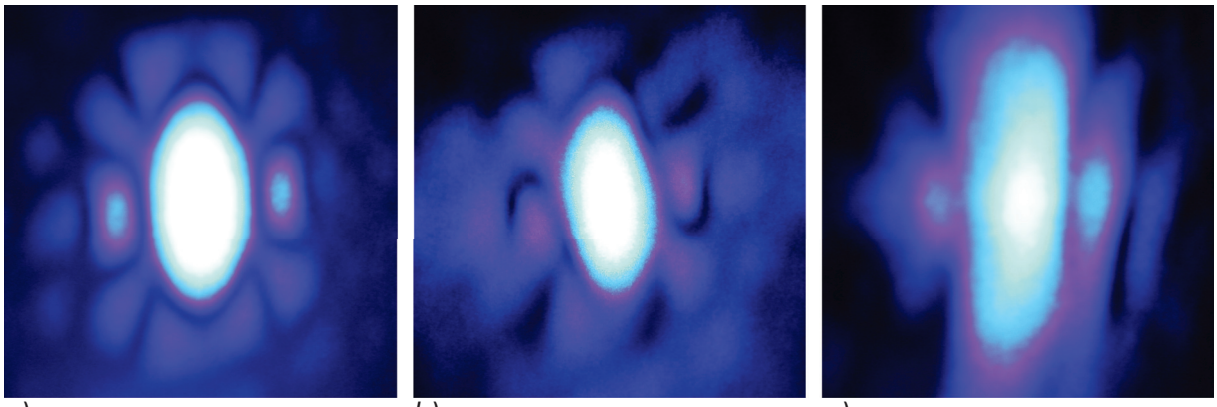

a) b) c)

Figure 6-9: Photographs of the far-field of the PM-LMA-375 assembly on a screen for a) the pristine end surface, b) irradiated for one day and c) irradiated for five days.

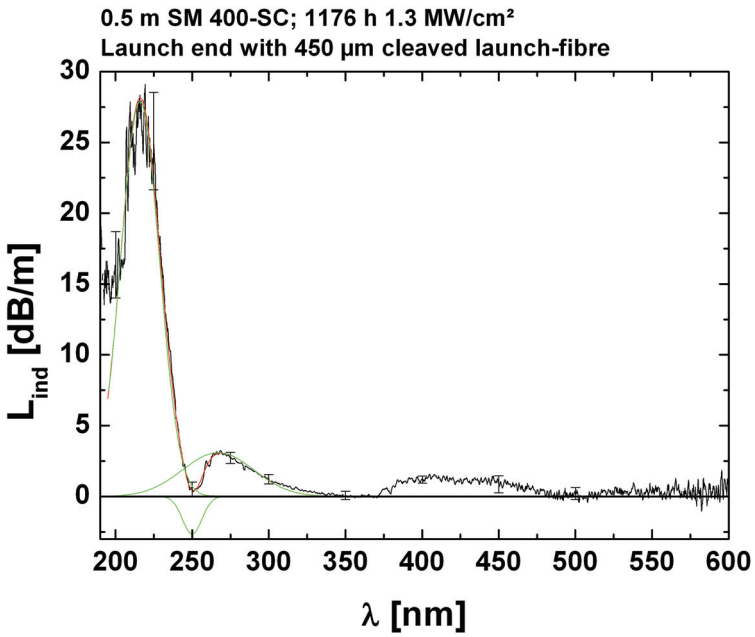

Figure 6-10: Induced loss for 0.5 m long sample of fibre type SM 400-SC. A power density of I_{core} = 1.3 MW/cm² was achieved for an irradiation period of 49 days (1176 h). The fibre assembly had a 450 µm long cleaved launch-fibre. An approximation of the damage by three Gaussian distributions at well-known UV defect centres (green colour) is drawn with red colour and had a $r^2 = 0.977$. In the wavelength range of 380 to 500 nm the higher order of the damage reflected by the spectrometer grating can be observed.

was also illuminated and projected onto the screen, shown in Figure 6-9 a). This projection of the web got more blurry over the course of irradiation, until after five days in Figure 6-9 c) mainly the core was projected onto the screen. At the same time the increase in divergence angle was obvious, but constrained to the vertical axis.

The stable long-term irradiation of the second *SM 400-SC* sample gave the possibility to investigate the generation and transformation of UV defect centres on a longer timescale. A constant power density I_{core} of 1.3 MW/cm² was achieved in the SMF. The result of an induced loss measurement after 49 days of exposure is shown in Figure 6-10. The curve shows an increased loss at around 215 nm and at 260 nm, with a window of low loss in between. In the wavelength range of 380 to 500 nm the higher order of the damage reflected by the spectrometer grating can be observed. This is not a photo-degradation effect. The loss behaviour in the DUV was approximated by adding up Gaussian distributions at known centre wavelengths of defect centres (green curves in Figure 6-10). The E'_γ centre at 215 nm with 29.6 nm spectral width (FWHM), the oxygen deficient centre ODC(II) at 250 nm with 14.9 nm spectral width and the non-bridging oxygen hole centre NBOHC at 266 nm with 54.7 nm spectral width were fitted to the curve [Skuja1998]. The E'_γ centre and NBOHC had a peak loss of 27.9 dB/m and 3.1 dB/m, respectively. The ODC(II) on the other hand had a gain of 2.65 dB/m. For this approximation a correlation coefficient $r^2 = 0.977$ was reached in the wavelength range from 195 to 370 nm (red curve Figure 6-10).

6.4.2 Investigation of distal fibre surface damage

When the impact on the distal fibre end was recognised, the damaged end surfaces were cleaved off and examined using a scanning electron microscope (SEM). It is important to see and point out, that the fibre ends were not contaminated after irradiation, except for particles in the region around the core as shown in Figure 6-11. Taking a closer look at the fibre core region reveals the existence of a periodic surface structure. Figure 6-12 a) shows the core of a pristine *SM 400-SC* distal end that had been exposed to a constant power density I_{core} = 1.3 MW/cm² in the core for 14 days. This value is calculated using the ratio of fibre output power and effective mode area. A periodic structure with a ripple was formed on the distal surface, which did not cover the whole core and had a diameter of about 1.5 µm. The ripple was most pronounced in an elliptical area. The structure was centred on the core at the intensity peak of the Gaussian light distribution, which is twice the mean value I_{core}. The periodicity of the ripples was Λ = 275 nm. In addition, spherical particles of sizes ranging from 150 to 900 nm and clusters of those aggregated in a ra-

dius of about 5 µm around the centre of the fibre. These particles were not seen on the freshly cleaved surface, which was observed to be ‘perfectly’ clean.

The experiment with the *PM-LMA-375* shows that the orientation of the ripples depends on the polarisation of the light. The PM fibre was aligned with its fast axis to the laser polarisation and the polarisation was maintained along the fibre. In Figure 6-12 b) it can be seen that the ripples of the periodic surface structure formed parallel to the polarisation direction of the light emitted from the fibre. This structure was also centred on the core and had the form of the elliptical mode field. Its diameters were 1.6 µm and 3.6 µm on the minor and major axis, respectively. The periodicity of this ripple is $\Lambda = 285$ nm. The aggregation of particles in the core area is not as distinct as for the *SM 400-SC*, only a few particles were seen.

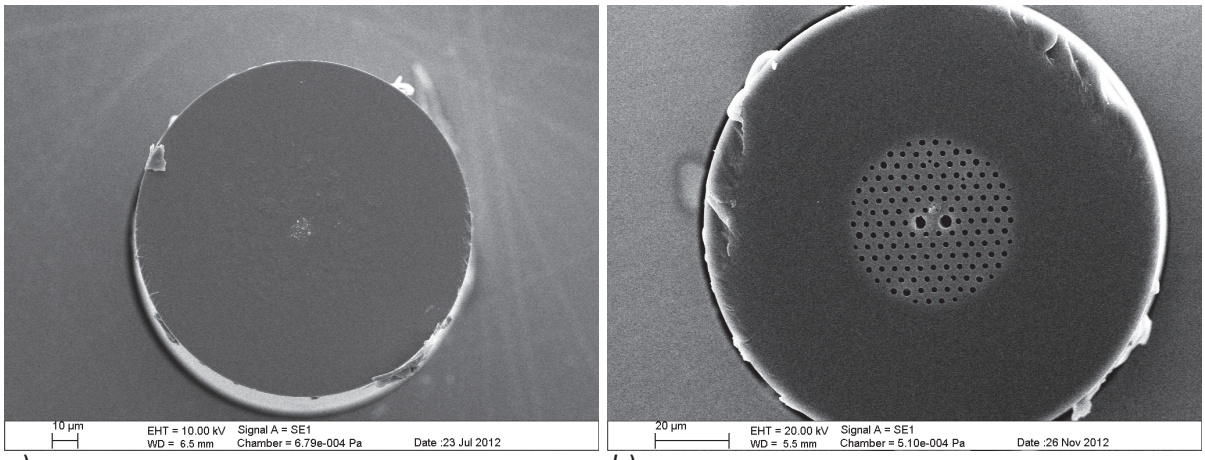

a) *b)*

Figure 6-11: SEM micrographs of cleaved SMF distal ends after irradiation with SML: a) SM 400-SC (I_{core} = 1.3 MW/cm² for 8 days) and b) PM-LMA-375 (I_{core} = 822 kW/cm² for 5 days). The polarisation in the PM-LMA-375 was horizontal, along the fast axis.

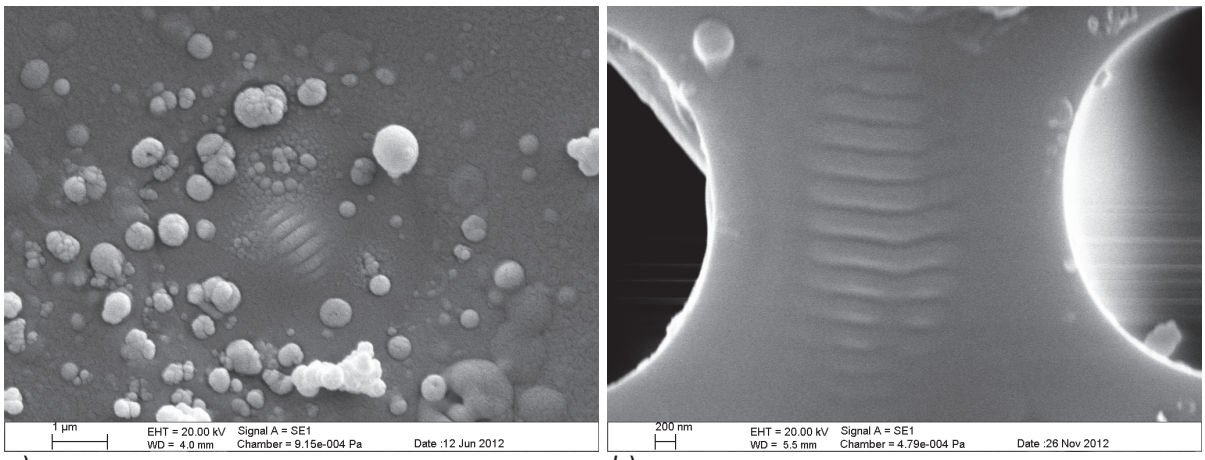

a) *b)*

Figure 6-12: SEM micrographs of the core regions of cleaved SMF distal ends after irradiation with SML: a) SM 400-SC (I_{core} = 1.3 MW/cm² for 14 days) and b) PM-LMA-375 (I_{core} = 822 kW/cm² for 5 days). The polarisation in the PM-LMA-375 was horizontal, along the fast axis.

The *SM 400-SC* assembly was then further irradiated. To show the growth of the damage, the distal ends were cleaved after well-defined times. The damage effects were visualised with the SEM as well. In addition the modification was examined with energy-dispersive x-ray spectroscopy (EDX). The samples are presented in chronological order. Since the fibre was not pristine and the core that was exposed had already been irradiated for some time, an influence of the pre-irradiation on the formation should be taken into account.

The second sample was cleaved off after 8 days of exposure and the structure (in Figure 6-13 a)) had a completely different morphology. It covered a larger area than the first sample with a diameter of about 2.2 µm. There was no spherical projection with the ripple on top, but the ripple itself rose high at the peak intensity in the core. The ripples were also not as orderly as for the first sample. Still, the periodicity was almost the same with Λ = 278 nm. Large particles with sizes up to 1.3 µm and different shapes aggregated in the core region. In addition to spherical particles and their clusters angular crystal-type particles were observed.

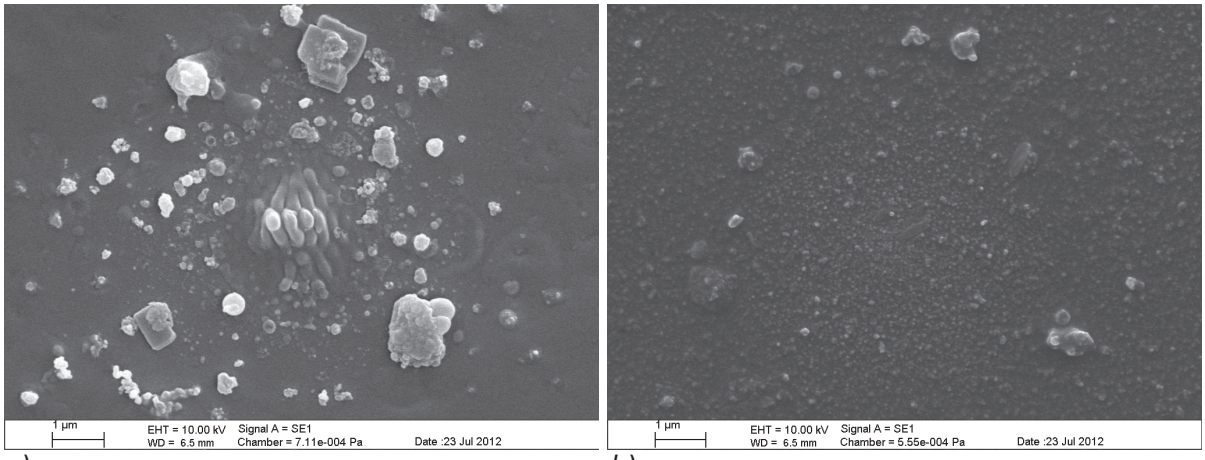

a) *b)*

Figure 6-13: SEM micrographs of the core regions of cleaved SM 400-SC distal ends after irradiation with SML and I_{core} = 1.3 MW/cm²: a) for 8 days and b) for 1 day.

For only one day of exposure no formation of a structure was seen in Figure 6-13 b). A lot of small and few medium sized (up to 800 nm) particles aggregated in the core region. If the irradiation was longer, then a smoothing in the centre of the small aggregated particles could be observed. Figure 6-14 a) shows the circular aggregation of particles, in a diameter of 4.7 µm, and the circular smoothing in its centre, with a diameter of 1.9 µm, for two days of exposure.

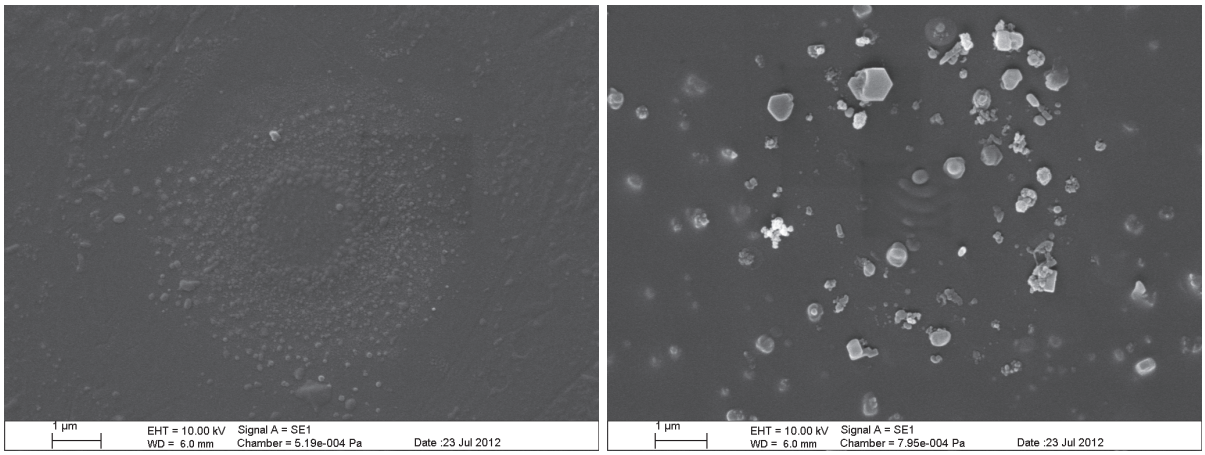

a) *b)*

Figure 6-14: SEM micrographs of the core regions of cleaved SM 400-SC distal ends after irradiation with SML and I_{core} = 1.3 MW/cm²: a) for 2 days and b) for 6 days.

Unfortunately, the sample for four days of irradiation was lost during preparation for the SEM. The sample for six days is shown in Figure 6-14 b) and had only medium sized particles of about 600 nm in the region around the core. I showed clusters of spheres and crystalline shapes. The beginning of the formation of a ripple structure could be seen on the fibre core. With a diameter of 1 µm the area is rather small. Three to four ripples with a periodicity of Λ = 294 nm were observed.

A very interesting morphology of the surface structure was received for the last sample surface. It was irradiated for 12 days and had shown the highest increase in divergence angle of the emitted light. As Figure 6-15 shows, the structure had a strong three-dimensional character. The ripple structure rose out of the surface as if it filled out the

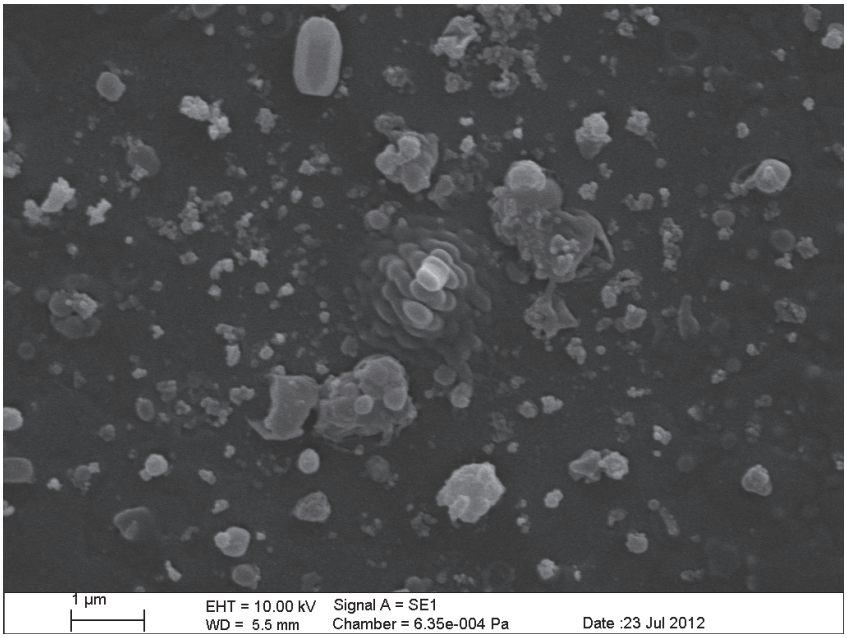

Figure 6-15: SEM micrograph of the core region of a cleaved SM 400-SC distal end after irradiation with SML and I_{core} = 1.3 MW/cm² for 12 days.

Gaussian shape of the beam. The three major ripples had periodicity of Λ = 296 nm and the whole structure formed within a circle of 2 µm in diameter. For this long-term exposure the aggregated spherical and angular particles are again medium to large sized as seen above. They are not on the structured area of the end surface, but cover the area around it. Mostly clusters of the particles were seen.

For several of the samples EDX analyses of the core-particle and a reference region were performed. An overlay of all spectra is shown in Figure 6-16. A major influence was seen from the thickness of the sputtering layer. With increased thickness of the gold layer, the oxygen and silicon signals were lower due to attenuation. Surprisingly, the carbon signal was not affected by the thickness of the gold layer. This is a very strong indication that the carbon signal did not come from the sample but from the surface of the mountings or contamination within the SEM chamber. Otherwise, the core-particle and reference region did not show any major differences. Oxygen and silicon signals are almost equal and no other specimens were found in those areas.

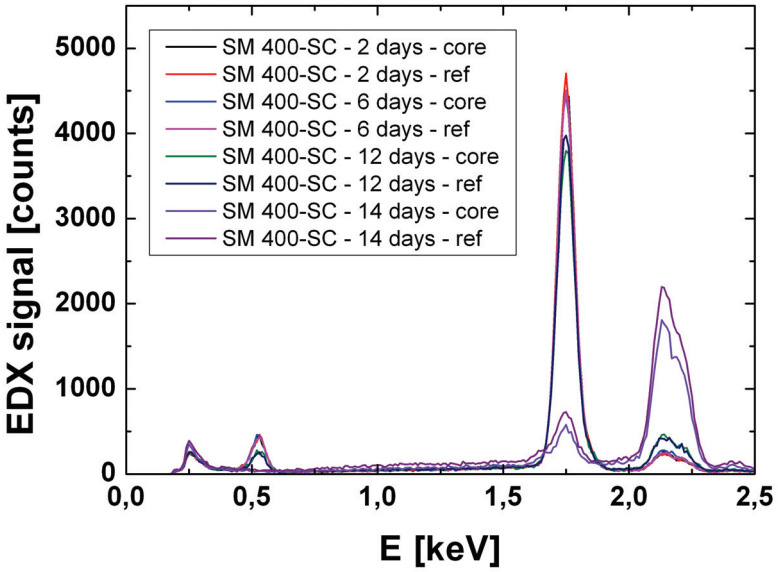

Figure 6-16: EDX spectra of different samples from the core and a reference area on the fibre. The peaks from left to right are carbon, oxygen, silicon, and gold. The samples had a different thickness of the sputtering specimen gold.

The results and measurements on the damaged fibre end surfaces are summarised in Table 6-2. Combining Formulae 6-10 and 6-3 gives the power P_{LIPSS} and the intensity I_{LIPSS} in the modified areas with radius r_{LIPSS}. A threshold intensity I_{th} at the onset of the LIPSS can be calculated by using:

$$I_{th} = I_{peak} \cdot e^{-2 \cdot \left(\frac{r_{LIPSS}}{w_{0,f}}\right)^2} \tag{6-24}$$

The squared value of r_{LIPSS} is adapted as the product of the minor and major radii of the elliptical LIPSS on *PM-LMA-375*. The periodicities of all samples are in the vicinity of λ_n, which is approximately 280 nm for silica at 405 nm. The periodicity increases slightly with the period of irradiation prior to exposing the core of the fibre when cleaving. Of course the calculated threshold intensity I_{th} decreases with increasing LIPSS diameter. It starts with high values of ~ 1 MW/cm² at the beginning and reduces to ~ 300 kW/cm² for longer irradiation. A comparison of pristine and pre-irradiated samples for similar irradiation periods shows a quicker formation on the pre-irradiated samples, when considering r_{LIPSS} over time.

Table 6-2: Summary of periodicities and radii of laser-induced periodic surface structures (LIPSS) on distal SMF surfaces. Calculated values of threshold intensity I_{th} at the onset r_{LIPSS} of the LIPSS, power P_{LIPSS} and power density I_{LIPSS} within this area. The first entry is for the elliptical LIPSS on the PM-LMA-375, the other entries are for the SM 400-SC. The days in parenthesis are the period of irradiation prior to exposing the fibre core by cleaving.

Period [d]	Λ [nm]	r_{LIPSS} [µm]	I_{th} [kW/cm²]	P_{LIPSS} [mW]	I_{LIPSS} [MW/cm²]
5	285	0.8x1.8	586	46.4	1
14	275	0.75	1266	31.7	1.8
8 (+14)	278	1.1	552	51.3	1.35
6 (+25)	294	0.5	1888	17.8	2.27
12 (+37)	296	1	722	47	1.5

6.4.3 Performance of fibre-coupled diode laser systems with launch fibre and silica end-cap

The longest irradiation experiments were performed on the fibre assemblies with launch-fibre on the proximal end and silica end-cap on the distal end. The first assembly is a PM-SMF *PM-S405-HP* and the second is a LMF *6u*. A very slow linear degradation of 0.01 dB/day is visible for both assemblies in Figure 6-17 for the first 35 days. After an inspection of the freely accessible end-caps with an optical microscope and with a white screen in the far field the issue could be resolved (see Figure 6-18). Over the long irradiation period dust particles had accumulated in the area where the beam passed through

the silica-air interface. The dust particles scattered the light which then could not be collected by the power meter completely. The end-cap could be easily cleaned by wiping off the dust. The far-field image showed a clean Gaussian distribution again and the power meter could collect more power. The output power of the LMF could be completely restored by cleaning (see Figure 6-19), while the loss of the SMF only improved by 0.35 dB. After the cleaning process the slow degradation commenced.

When the experiments were discontinued after 50 and 60 days, respectively, the surface of the launch-fibre was inspected, too. The launch-fibre on the LMF was completely clean. The launch-fibre on the SMF on the other hand showed an accumulation of contamination across the whole surface (see Figure 6-20 b)). This contamination was also easily removable by using optics cleaning wipes. Unfortunately, the improvement by cleaning the launch-fibre surface could not be demonstrated due to a failure in the LDM at that time. However, for both assemblies on both fibre ends no surface damage could be found.

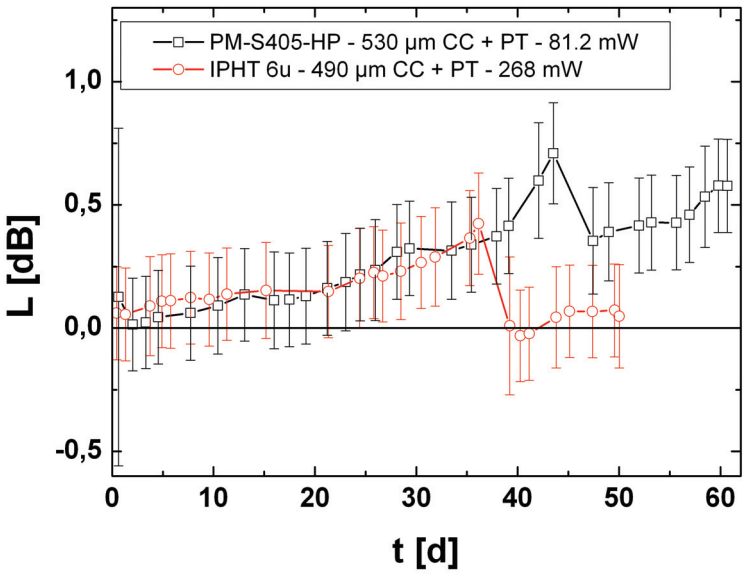

Figure 6-17: Loss over time of SMF and LMF samples with launch-fibre and end-cap irradiated with the SML and MML, respectively. Both samples were adjusted several times during irradiation. The given power is the fibre output power at the beginning of the measurement.

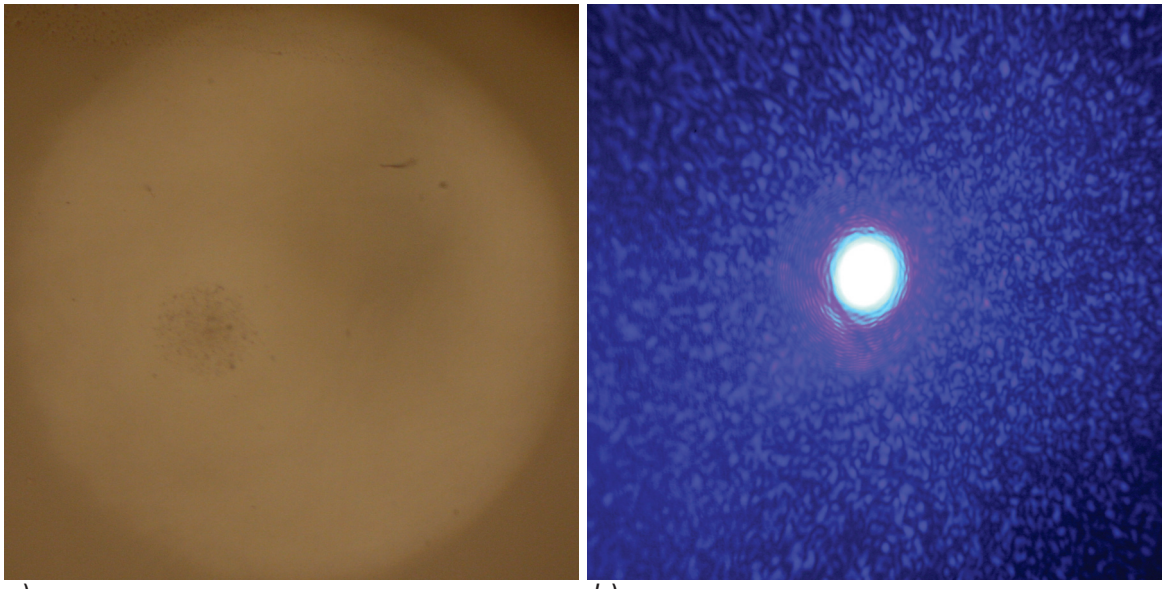

a) b)

Figure 6-18: a) Picture of silica end-cap on PM-S405-HP after 44 days of irradiation. b) Picture of far field emitted from contaminated silica end-cap on PM-S405-HP.

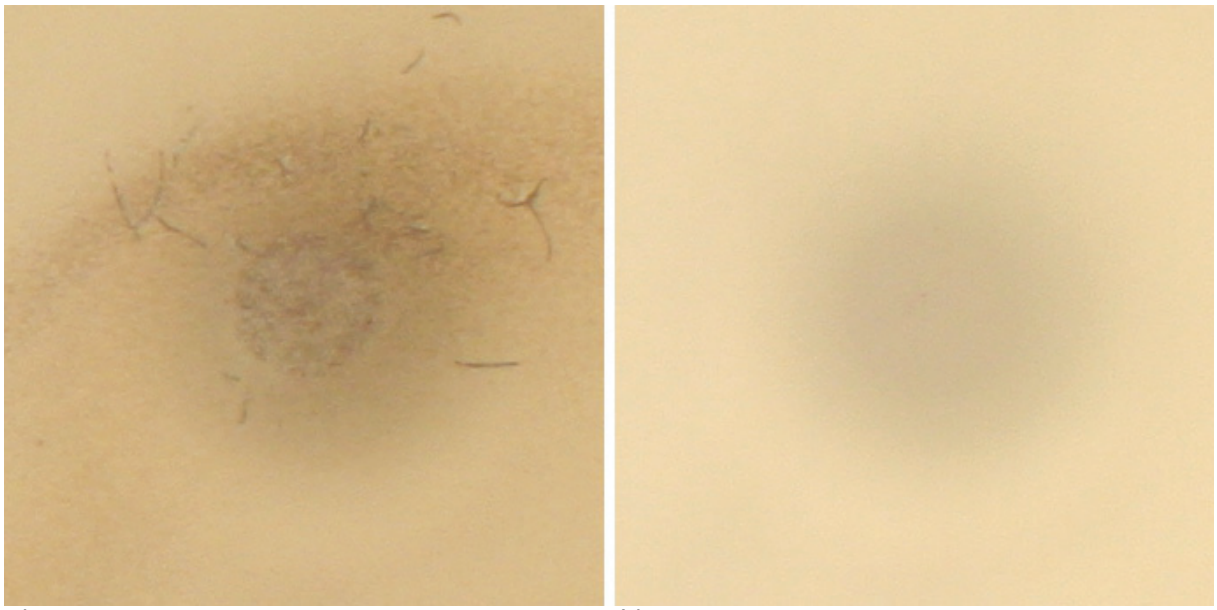

a) b)

Figure 6-19: Pictures of the silica end-cap surface of 6u: a) after 39 days of irradiation and b) after simple cleaning.

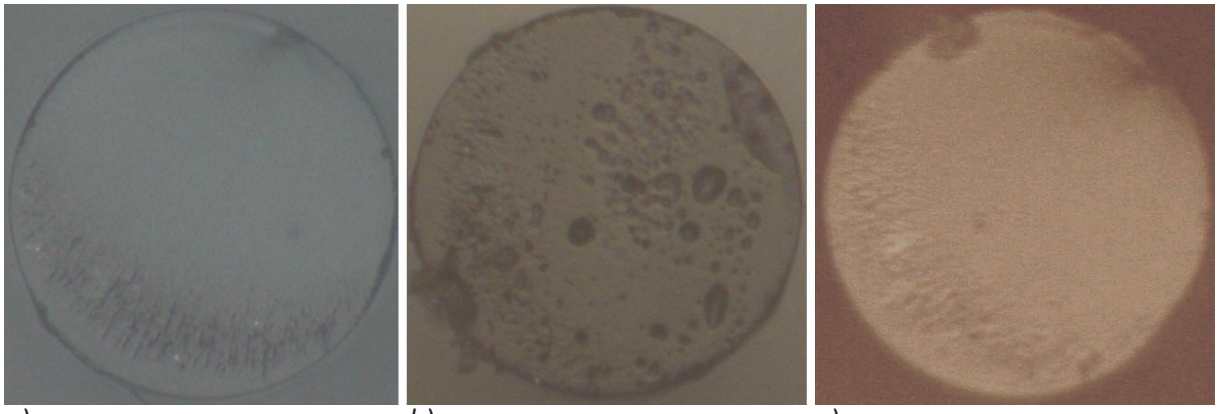

a) *b)* *c)*

Figure 6-20: Pictures of the launch-fibre surface of PM-S405-HP: a) before irradiation, b) after 60 days of irradiation and c) after simple cleaning.

6.5 Simulation of distal end surface damage

The influence of a growing surface structure on the beam quality at the distal end was re-constructed using simulations. The software that was employed uses the finite-difference time-domain method and is called FDTD Solutions by Lumerical Solutions, Inc.. A SMF with a core diameter of $a = 1.2$ µm, a refractive index of $n_{Co} = 1.45441$ (SiO_2 glass at 405 nm, [Palik1997]) in the core and of $n_{Cl} = 1.44956$ (F doped SiO_2) in the cladding was designed, giving a numerical aperture NA = 0.12 and a V number of V = 2.2 at $\lambda_0 = 405$ nm wavelength, according to Formula. The cut-off wavelength λ_{CO} for this SMF is 376 nm. These values are in good correspondence to the specifications of the *SM 400-SC*. As a light source the fundamental mode with $\lambda_0 = 405$ nm was generated in the fibre core, which is easily possible with the simulation tool.

Table 6-3: Parameters of simulated surface structures.

Height [nm]	Radius of curvature [µm]	Ripple amplitude [nm]
100	11	15
300	3.6	40
500	2.2	70
700	1.5	100
700 (no lens)	0.7	500

The surface structure was also modelled out of SiO_2 glass with a diameter of 3 µm and eleven ripples across, which is a periodicity of about $\Lambda = 273$ nm. Additional parameters for the growth of the structure, like height in the centre, the radius of curvature, and the amplitude of the ripple, are given in Table 6-3. The periodic structure in Figure 6-21 a) was designed to fit the surface structure measured with AFM on a launching surface of a SMF. The smaller periodic structures are down scaled designs of the 700 nm high structure. After the actual form of LIPSS on pre-irradiated cores were found with SEM analyses, an additional structure was modelled with a diameter of 2 µm and almost no lens property or more specifically with a high ripple amplitude. Seven ripples across the 2 µm result in $\Lambda = 285$ nm and the structure is shown in Figure 6-21 b).

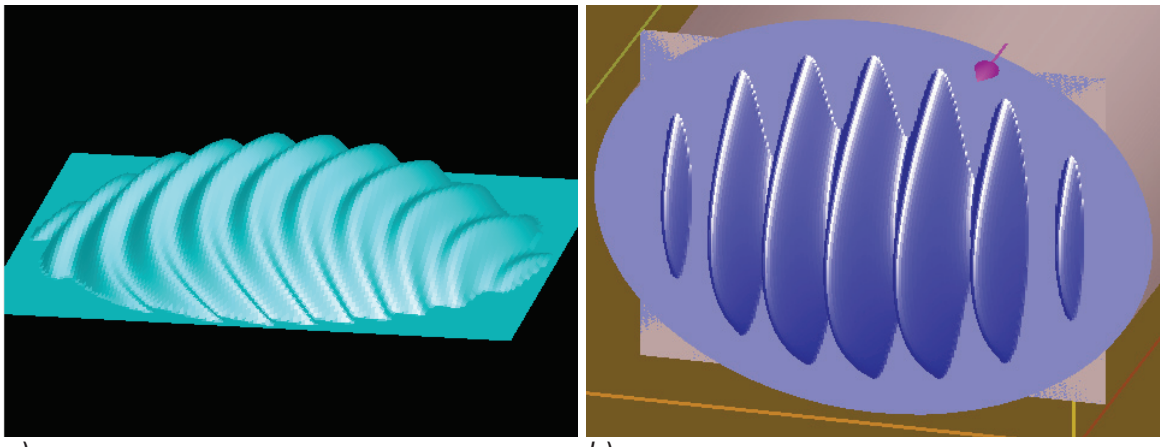

a) b)

Figure 6-21: Model of 700 nm high periodic surface structures adapted to a) the LIPSS measured with AFM on a launching surface of a SMF and b) the distal fibre end LIPSS on pre-irradiated cores.

Examples of the power distribution of light excited inside the SMF and transmitted through the LIPSS is shown in Figure 6-22. The SMF light source has a length of 3 µm after which the LIPSS is positioned. In the case without LIPSS the light propagation is according to the Gaussian beam equations. In the case of the 700 nm high LIPSS with lens property the light is strongly focused behind the end surface. The focal length f and spot size w_0 can be determined at the point of highest intensity. The result for the LIPSS without lens property and smaller diameter also exhibits the focusing effect. This is shown in Figure 6-23 for the power distribution parallel and perpendicular to the orientation of the ripples.

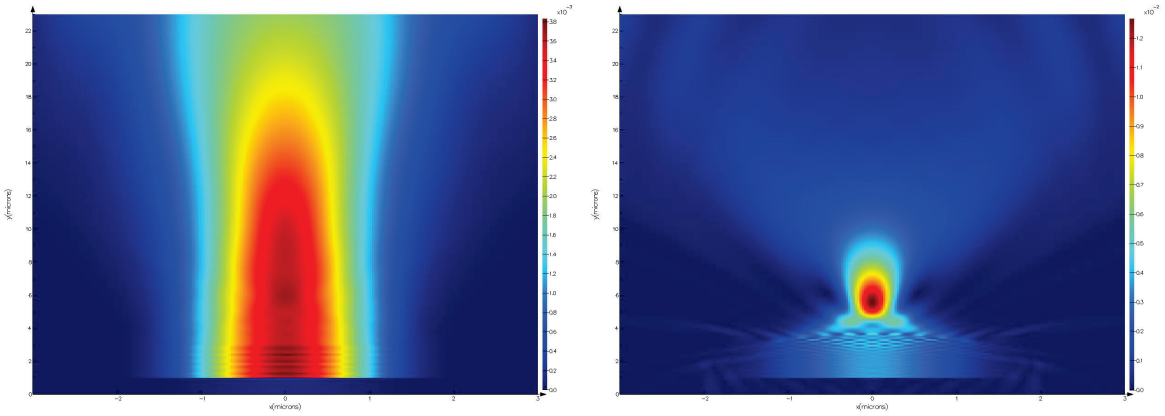

a) b)

Figure 6-22: Power distributions of light transmitted from SMF a) without LIPSS and b) through 700 nm high LIPSS. The graphs exhibit some interferences from reflections at the boundary conditions.

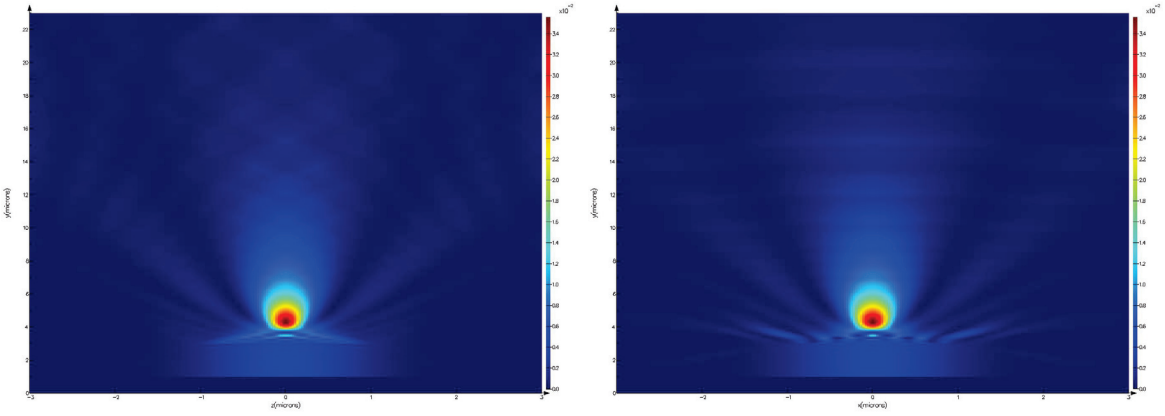

a) b)

Figure 6-23: Power distributions of light transmitted from SMF through 700 nm high LIPSS without lens property a) parallel and b) perpendicular to orientation of the ripples. The graphs exhibit some interferences from reflections at the boundary conditions.

If a LIPSS forms a lens and a scattering centre on the distal end of the fibre its major impact is on the divergence angle of the emitted light. If the light is collected with a detector with an aperture radius of r_{det}, then the detected power P_{det} is described by:

$$P_{det}(z) = P_{out,fibre} \cdot e^{\frac{-2 \cdot r_{det}^2}{w(z)^2}} \quad (6\text{-}25).$$

The beam radius $w(z)$ and the Rayleigh length z_R are calculated according to Formulae 6-11 and 6-12, with $n = 1$ and $M^2 = 1.07$. The beam spot size w_0 depends on the LIPSS that was simulated and was determined in the focus behind the fibre end. For a distal fibre end without a structure the spot size of the fibre was determined. The Rayleigh lengths and the spot sizes received from the experiments are shown in Table 6-4.

Table 6-4: Calculated properties of simulated surface structures and losses.

Height [nm]	Calculated focal length [µm]	w_0 [µm]	z_R [µm]
0	N/A	1.3	12.25
100	5.3	1.08	8.46
300	4.2	0.67	3.25
500	3.3	0.465	1.57
700	2.6	0.33	0.79
700 (no lens)	∥ 1.3; ⊥ 1.3	∥ 0.31; ⊥ 0.29	∥ 0,697; ⊥ 0,61

The increase in divergence angle was measured for the last exposed distal fibre surface of the second *SM 400-SC* sample. A simple aperture test, with the power detector as aperture (r_{det} = 9.5 mm), was performed before and immediately after cleaving off the damaged distal end in Figure *6-15*. The detector is located 17 mm inside the power meter housing. The power meter was being moved away from the fibre and measurements of P_{det} were taken at distances z of 17, 22, 27, 32, 37, 77 and 102 mm between fibre surface and detector plane. The loss $L_{det}(z)$ due to less detected power with a movable aperture in z direction is shown in Figure 6-24. For the case without a surface structure, simulation and measurement are in very good agreement. The distal end that was damaged for 12 days had an unknown height and a base diameter of 2 µm, which is smaller than the fibre mode-field diameter. The simulation of a LIPSS with 3 µm base diameter might not be very appropriate, but the measured loss curve after 12 days falls well in between the LIPSSs with heights of 500 and 700 nm. It also exhibits the same behaviour as the simulated curves. A comparison with the loss curves of the LIPSS with the smaller diameter of 2 µm shows a similar behaviour. Probably the height of the LIPSS was a little less than 700 nm. The loss at z = 27 mm (10 mm distance between power meter and fibre) is the same as the maximum in Figure 6-8, because this was the standard distance in the long-term experiments.

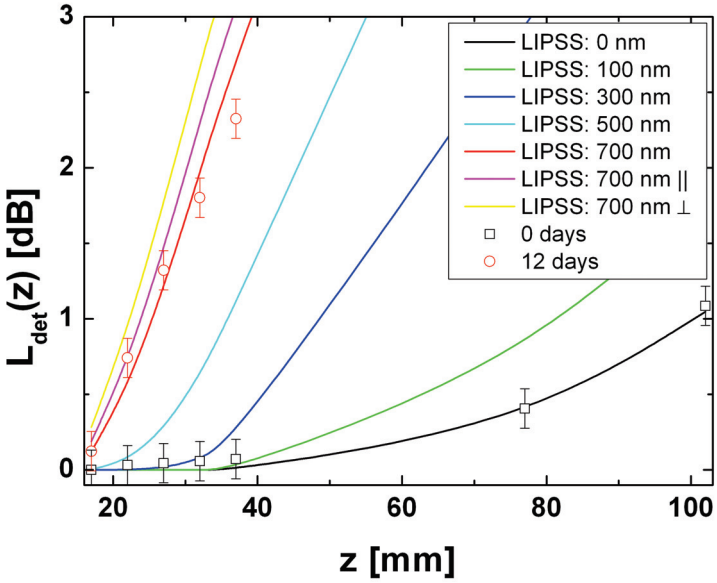

Figure 6-24: Loss due to less detected power along z, the distance from the fibre end surface, for a detector radius of 9.5 mm. The lines represent the simulation results for different heights of LIPSS. The symbols are the measurements at specific distances from the fibre end surface for an undamaged surface and a surface exposed for 12 days (see Figure 6-15).

6.6 Discussion

The propagation of a beam into a launch-fibre or silica end-cap can be completely described using Gaussian beam and far-field equations. The optimal length for a high performance concerning surface damage was found to be in the range of 400 to 500 µm for the laser system used in this work. The exact length is not too critical, as the power density on the air-silica interface is reduced to values below 10 kW/cm² for the whole range. The prepared samples had lengths of the launch-fibre between 420 µm and 530 µm. In all cases a fibre output power of 50 mW was achieved and for the best samples the coupling efficiency was above 50 %.

The use of a launch-fibre, as long as those used for this work (see Figure 6-7), on the distal fibre end cannot be recommended for applications which need a high beam quality. Due to reflections of the Gaussian beam flanks at the core-cladding interface of the MMF, interference rings were seen in the far field of the emitted light. For shorter lengths of launch-fibre this effect is reduced and might not be an issue. However, if a silica end-cap without a restricting aperture is used on the distal end there is no problem with a reflective aperture and the beam quality of the SMF is preserved.

The loss in fibre output power that was measured in some cases cannot be attributed to an actual transmission loss. When a laser-induced periodic surface structure (LIPSS) forms on the distal end surface, the light is scattered and focused with a very short focal length. This in turn degrades the beam quality and increases the far-field angle. Since the power P_{det} that was detected was just a section of the emitted power $P_{out,fibre}$ for higher far-field angles, this needs to be corrected and Formula 6-1 modified to:

$$L(t) = -10 \cdot \log_{10}\left(\frac{P_{det}(t)}{P_{det}(0)}\right) \quad (6\text{-}26).$$

This was also proven by the simulations of a LIPSS on a distal fibre end. The detected power decreases at a constant distance from the fibre surface due to an increasing far-field angle. Thereby, the transmitted power $P_{out,fibre}$ is proven to have been constant.

Again the transformation and generation of defect centres in the DUV was found. In earlier experiments the generation of E'_γ centres was observed, mostly accompanied by the reduction of the oxygen deficient centres ODC(II). In the case of the *SM 400-SC* for an irradiation period of almost 50 days the generation of E'_γ centres and non-bridging oxygen hole centres (NBOHC) were observed in high quantity at 215 nm and 266 nm, respectively. When an approximation of the loss by Gaussian distributions was performed, it was also found that the absorption band of ODC(II) was reduced. A transformation of ODC(II) and generation of E'_γ and NBOHC can be explained by a multi-step absorption of photons at the singlet-triplet transition of ODC(II) with a fluorescence lifetime of about 10 ms [Skuja1994, Messina2008]. The incoherent absorption of consecutive photons with 3.07 eV (405 nm) at the transition centred at 3.15 eV (394 nm) with a FWHM of 0.34 eV could on one hand directly ionise an ODC(II) into an E'_γ. On the other hand, an exciton $(SiO_2)^*$ could be generated (Formula 6-27) and decay non-radiatively close to the site. This non-radiative decay in turn can break a strained precursor P and induce an E'_γ centre (Formula 6-28) [Muehlig2005, Friebele1979].

$$(SiO_2) + x \cdot h\nu \rightarrow (SiO_2)^* \quad (6\text{-}27)$$

$$(SiO_2)^* + P \rightarrow E'_\gamma \quad (6\text{-}28)$$

The long-term irradiation lead to the generation of a LIPSS on unprotected distal fibre ends as well, which received a constant power density. These LIPSS had a ripple with periodicities in the range of $\Lambda = \lambda_n$, which is called a low spatial frequency LIPSS (LSFL) in literature [Rohloff2011]. As for most LSFL in experiments on wide band-gap dielectrics the orientation of the ripple was parallel to the polarisation of the laser light [Hoehm2012]. This could be proven in this work by using polarisation-maintaining PCF, where the LIPSS

formed on the distal end parallel to the polarisation direction that was launched into the fibre. In contrast to the damage on the launching fibre end, the LIPSS on the distal end did not cover the whole core. After irradiation periods of one to two weeks, an onset of the LIPSS was found for a position along the radius where the power density is in the range of 0.5 to 2 MW/cm². This is about three quarters of the mode-field radius. Additionally, the accumulation of spherical particles was observed around but not on the core.

The evolution of the LIPSS on the distal end over time showed that the damage started with a roughening of the surface in and around the core area. This roughening might be an explanation for an improved coupling efficiency before damage started on the launching ends of unprotected fibres: the rough surface acts as an anti-reflection coating. After two days the core area itself was smooth again. The roughening turned into an accumulation of small and medium sized particles with diameters up to 1.3 µm, while the LIPSS started to grow out of the smooth area on the core. After eight days the LIPSS is highly developed and surrounded by medium and large sized particles. The periodicity of the LIPSS slightly increases with the time that the fibre core was irradiated prior to exposure. It is known that the periodicity of the LIPSS increases with the carrier density in the conduction band, from $\Lambda = \lambda_n$ in a dielectric to $\Lambda = \lambda_0$ in a metal-like material [Hoehm2012]. If this is applied here, the direct influence of generated defect centres on the properties of the LIPSS is demonstrated. In addition, it was seen that the LIPSS grows quicker and with a more interesting morphology on pre-irradiated core material with more generated defect centres. This supports the above mentioned influence, too.

It is also important to mention, that no carbon or other contaminant was found on the damaged fibre cores of the distal end with EDX. The comparison between the core-particle and reference area showed no significant differences, which leads to the conclusion that the LIPSS is a modification of the silica material. The spherical particles that were found look very similar to the clusters of silica micro-spheres known from the chemical vapour deposition (CVD) process for fibre preform production [Kemeter2002, Li1985]. The angular particles have a shape not unlike silica crystals. It has to be assumed that both types of particles are actually comprised of silica.

A Sipe model [Sipe1983] cannot be directly applied in this case here. This model explains the LIPSS as the result of an uneven energy deposition during ablation due to the interference of the incident and a scattered surface wave. But the fibre end damage does not show an ablation, the LIPSS rather builds up in the irradiated area. A rarefaction or expansion of a surface layer of silica by incorporation of hydrogen atoms on the other hand seems possible [Allan2004]. Especially, when the reaction of molecular hydrogen with ODC(II) surface centres is considered. This reaction can only be photostimulated by the excitation of the triplet state T_1 of ODC(II) [Skuja1994]. An uneven energy deposition

during the rarefaction would then result in unevenly expanded material and the observed LIPSS. The orientation of the ripples could then be explained with the Sipe-Drude model of Bonse and co-workers [Hoehm2012]. Due to the finding of amorphous silica particles around the fibre core another process is proposed. The LIPSS formation might be started by the ionisation of the surface leading to Coulomb repulsion and material desorption. The desorbed silica material then condensates on the surface close to the site of desorption. Outside of the high power density silica micro-spheres and crystals are formed. In the area of high power density the silica self-organises as it was described by Reif and co-workers [Henyk1999, Reif2006]. An unstable surface layer can develop from duelling processes of material desorption and surface tension or atomic self-diffusion. Such an unstable layer then self-organises into the ripple structure known as LIPSS [Costache2004, Varlamova2006].

The most stable fibre system was found to have a launch-fibre on the proximal end, for ease of assembling with a connector, and a silica end-cap on the distal end. Thus, both fibre ends were protected from high power densities. The launch-fibre was prepared from a MMF with low solarisation and by using fibre cleaving for improved surface roughness. The low solarisation is usually verified by irradiation with a deuterium lamp, but was shown here for the case of 405 nm laser irradiation, too. These improvements should show their effect for extremely long-term irradiation or very high laser power. The two systems that were examined had a high output power with good coupling efficiencies of about 60 and 75 %. Due to the use of an end-cap on the distal end a good beam quality was achieved. The only thing that was found to deteriorate the measured power was an accumulation of dust particles on the silica-air interface. Those are attracted by the lightly ionised surface and can be easily wiped off. A high stability of the systems with a loss rate of only 0.01 dB/day and no damage on either end promises high performance for long-term use in high-power applications.

6.7 Summary

An improvement in the damage behaviour of SMF and LMF in fibre-coupled 405 nm diode laser systems was achieved by specifically implementing conditions which take the key influential parameters into account. The major advance has been the reduction of the power density on the fibre launching end. For that purpose a short cleaved launch-fibre was produced. As a preparation for future higher power laser diodes, the launch-fibre was made from a very low solarisation multi-mode fibre. Since cleaving had proven its positive influence on the damage behaviour in earlier experiments, it was also used for the end surface preparation of the launch-fibre. The damage on the distal fibre end due to

constant high power density was studied using a scanning electron microscope. The evolution of a laser-induced periodic surface structure (LIPSS) over the course of two weeks could be shown and discussed in detail. A new model for the formation of the surface damage was proposed. In order to prevent this damage, a silica end-cap was used on the distal end. This assembly performed with high stability over a period of two month of constant irradiation with the 405 nm single-mode laser.

7 Conclusions and future scope of this work

7.1 Conclusions of the work carried out

The objectives of the work were put forward in the first chapter, with the general aim to find the reasons for a strong degradation of near ultraviolet (NUV) single-mode fibres (SMF) when irradiated with 405 nm diode lasers and to mitigate these issues. The investigations undertaken in this work lead into several directions, where contributing effects and their influential parameters were found. The conclusions drawn from the results in the specific directions are addressed below.

- The investigation of the generation and transformation of UV defect centres in small core fibres was only possible after a new spectral measurement system was implemented. This system allowed for the first time the resolution of E', ODC(II) and NBOHC absorption bands between 200 and 300 m wavelength in fibres with core diameters as small as 2.2 µm. Additionally, the spectral attenuation and cut-off wavelengths of single-mode (SMF) or low-mode fibre (LMF) samples could be determined. In a separate setup 405 nm diode laser modules with imaging systems were combined with a power meter to damage individual SMF and LMF samples.
- Different fibre types and end surface preparation methods were studied under long-term irradiation with 405 nm laser light. The loss behaviour at laser wavelength over days and weeks showed a lower damage rate for cleaved fibres in comparison to glued and polished fibres. This was attributed to a reduced surface contamination and surface roughness of the cleaved samples. Furthermore, a change in the UV defect centres allowed the conclusion that 405 nm laser light can influence those absorption bands by a multi-photon process. Since coherent two-photon absorption can be excluded, a two step absorption at the singlet-triplet transition of the ODC(II) was suggested, as proposed in literature [Skuja1994, Messina2008].
- The study of surface modifications on proximal and distal fibre end surfaces was performed using different microscope techniques, like atomic force microscopy (AFM) and scanning electron microscopy (SEM). It was shown that a surface damage in form of an alteration grows at a power density of about 1 MW/cm². This is three orders of magnitude below the damage threshold of pulsed lasers in this wavelength range. The alteration is a ripple structure projecting from the surface and is known from literature as laser-induced periodic surface structure (LIPSS).

These were first found on the proximal end and after using launch-fibres for mitigating this effect were also found on the distal end. The LIPSS form a lens and scattering centre on the fibre core and are therefore the main cause of power loss over time. On the proximal end the launching conditions are changed, light is tightly focused behind the front surface and cannot be guided by the fibre. At the distal end the LIPSS focuses and scatters the light as well, thereby increasing the divergence angle and degrading the beam quality. Both effects were reconstructed and confirmed by simulations of differently high LIPSS on SMF proximal and distal ends irradiated with 405 nm laser light.

- LIPSS found in this work exhibit the same characteristics as LIPSS generated with femto-second laser irradiation on silica in air [Hoehm2012]. The orientation of the ripples, with a periodicity between λ/n and λ, is parallel to the polarisation direction of the linearly polarised laser. They are formed of amorphous silica and no contaminating elements were found by energy dispersive x-ray analysis (EDX). The cause of LIPSS is still controversially discussed in literature and the two main theories could be applied here. The results for continuous-wave 405 nm irradiation show, that self-organisation of an unstable ionised surface layer is possible. The main parameters for this effect are the surface roughness, power density and generation of defect centres [Reif2006]. On the other hand, a decreased density was found for the damaged surface layer, which could be explained by the incorporation of hydrogen into the irradiated region of the silica material. An inhomogeneous energy deposition, due to interference of the incident beam with a scattered surface wave, could then form the LIPSS in the expanding material.
- To learn if the core composition or fibre preform treatment had an influence on the modification of UV defect centres by 405 nm irradiation, studies on experimental LMF were performed. The fibre preforms were either treated by H_2 diffusion or collapsed in a He atmosphere. Fibre cores were weakly doped with Ge, P or F. All fibre types showed a variety of generated UV defect centres. Those defects were found to be almost equally distributed along the fibre length, again indicating a multi-photon process. It was suggested that the variety of defect centres is generated by non-radiative decay of excitons. Those excitons themselves are generated at the singlet-triplet transition of the ODC(II) defect centre by a two step excitation process.
- From the parameters determined, and influential to the growth of the LIPSS, an improved fibre system was derived. Since the power density is the major factor, its reduction was a primary goal. This was achieved by using a spliced short piece of

launch-fibre with a length of ~0.5 mm, which can be used with the fibre inside a connector. To account for the other parameters, surface roughness and susceptibility for UV defect centres, the launch-fibre was cleaved and made of a low-solarisation multi-mode fibre (MMF). The experiments following these measures showed a high stability in power transmission. However, a LIPSS was generated on the distal fibre end and degraded the beam quality, as mentioned above. The use of a second piece of MMF on the distal end cannot be recommended. Rings in the far field of the emitted light were seen from interference with light reflected at the core-cladding interface of the MMF. Therefore, a large silica end-cap fused to the fibre with a CO_2 laser was used on the distal end for a stable beam quality. A polarisation-maintaining (PM) system with a launch-fibre and a silica end-cap showed a very high stability with a maximum loss of about 0.5 dB over 60 days.

- It was learned from private discussions with other researchers that LIPSS can also be generated by other laser sources in the blue region of the spectrum. In Appendix III structures observed after 446 nm pulsed irradiation are presented and look very similar to the LIPSS found in this work. Therefore the use of launch-fibres and end-caps is recommended for all NUV and visible range fibre-coupled high power lasers.
- The wavelength of 405 nm has various applications in medicine and biosensing [Guffey2006, Kirshenbaum2011]. During this work a possible lifetime improvement of the scanning fibre endoscope (SFE) was investigated together with the University of Washington, Seattle [Lee2010]. This wavelength is used in the extremely small endoscope with a SMF for fluorescence measurements on cancer tissue. In the future, 405 nm laser light should also be used for tissue ablation, which requires higher power densities. The possibility of incorporating a short launch-fibre into the SFE design enables the long-term use of this system.
- Recently manufacturers of printing presses have found increased interest in fibre-coupled laser diodes emitting around 400 nm. In addition to the short wavelength, smaller spot sizes are needed to achieve higher resolutions in the printed media, which means the introduction of low-mode fibre (LMF) and SMF for these systems. For the first generation of machines with 405 nm multi-mode laser diodes and LMF severe end surface damage was observed and is briefly reported in Appendix I. Future generations of printing machines will incorporate SMF for 405 nm operation. The experience gained in this work as well as the demonstrated highly stable fibre-coupled NUV laser systems are of great benefit to this industry.

7.2 Future directions

The main issues of SMF damage by 405 nm irradiation were found and first long-term stable fibre-coupled systems demonstrated. To improve upon these systems and to perhaps find further solutions to inhibit the damage effects the following future objectives are suggested.

- Standard connecting fibre assemblies for laser modules use FC/APC connectors (fibre connector with angled physical contact). An angled fibre end surface on both sides prevents the back reflection of laser light into the resonator or cavity and does not lead to output power variations. In addition, mainly PM-SMF is used in sensing and lithography applications. To develop the demonstrated highly stable system further towards a commercial product the use of angled fibre end surfaces is absolutely necessary. A reliable technique for applying an angled cleave on a launch-fibre, with the slope of the cleave perpendicular to the desired polarisation axis of the PM-SMF, is required.
- The influence of the environment on the generation of laser-induced periodic surface structures (LIPSS) by 405 nm laser light was not studied, yet. The expansion of the surface might be enhanced by the presence of molecular hydrogen or water vapour. From a different point of view a continuous flow of inert gas might reduce the ionisation of the surface. Therefore the damage on a distal SMF end surface in a sealed and flushed box should be investigated. Ideally the box is an integrating sphere to directly record the fibre output power. Submersing the distal fibre end in a purified liquid, preferably deionised water, can also be an option. The first results of angle polished fibre ends in sealed and nitrogen purged collimators are presented in Appendix II and show LIPSS with interesting features.
- A treatment of fibre end surfaces with a fusion arc for reduced surface roughness resulted in similar or worse damage rates than for cleaved surfaces. It is known that a fusion arc is not the cleanest way of heat-treating materials. Contaminations from electrode burn-off or the material itself can get impregnated into the surface. A much cleaner way, but requiring more expensive tools, is laser polishing with a CO_2 laser. Experiments on the damage rate of CO_2 laser polished SMF end surfaces should show a positive or negative impact. If a positive impact could be shown, then laser polishing launch-fibres would add a high quality finish for high-power laser applications.

- A more academic objective of such future work would be to gain a deeper insight into the defect generation by two-step absorption at the singlet-triplet transition of the ODC(II). Therefore, a setup has to be devised, which allows for time-resolved *in situ* spectral measurement during 405 nm laser irradiation of a LMF or SMF. For studies with higher power lasers in the DUV, fibres are radially irradiated with the laser and broadband light propagating in the fibre core is used for the spectral measurement.

References

[Acuna2010] Acuna R & Zhou J. Innovative patent-pending end cap for high power laser-fiber coupling (white paper). *Laser Focus World* (2010) **46**.

[Agrawal2007] Agrawal GP. Nonlinear fiber optics (fourth edition). Academic Press, 2007.

[Algots2003] Algots JM, Sandstrom R, Partlo WN, Maroevic P, Eva E, Gerhard M, Linder R & Stietz F. Compaction and rarefaction of fused silica with 193-nm excimer laser exposure. In *Proc. SPIE 5040-1639*. 2003.

[Allan1999] Allan DC, Smith CM & Borrelli NF. Measurement and analysis of compaction in fused silica. In *Proc. SPIE 3578-16*. 1999.

[Allan2004] Allan DC, Araujo RJ, Smith CM & Borrelli NF. Induced density changes in 193-nm excimer-laser-damaged silica glass: a kinetic model. In *Proc. SPIE 5377-827*. 2004.

[Baumann2008] Baumann S. Omicron Laserage GmbH. private communication.

[Birks1997] Birks TA, Knight JC & Russell PSJ. Endlessly single-mode photonic crystal fiber. *Opt. Lett.* (1997) **22**: pp. 961-963.

[Birnbaum1965] Birnbaum M. Semiconductor Surface Damage Produced by Ruby Lasers. *J. Appl. Phys.* (1965) **36**: p. 3688.

[Boehme2009] Boehme S, Beckert E, Eberhardt R & Tuennermann A. Laser splicing of end caps: process requirements in high power laser applications. In *Proc. SPIE 7202-05*. 2009.

[Bonse2005] Bonse J, Munz M & Sturm H. Structure formation on the surface of indium phosphide irradiated by femtosecond laser pulses. *Journal of Applied Physics* (2005) **97**: p. 013538.

[Brimacombe1989] Brimacombe RK, Taylor RS & Leopold KE. Dependence of the nonlinear transmission properties of fused silica fibers on excimer laser wavelength. *J. Appl. Phys.* (1989) **66**: p. 4035.

[Brinkmeyer2002a] Brinkmeyer E. **Optische Fasern: Grundlagen**. In *Optische Kommunikationstechnik: Handbuch für Wissenschaft und Industrie*. Petermann K & Voges E (Eds.). 2002.

[Caloz2004] Caloz F & Rossini P. Montage- und Messtechnologie für faseroptische polarisationshaltende Komponenten. *Test Kompendium* (2004): pp. 106-108.

[Cancellieri1993] Cancellieri G. Single-mode optical fiber measurement: characterization and sensing. Artech House, 1993.

[Cregan1999] Cregan RF, Mangan BJ, Knight JC, Birks TA, Russell PSJ, Roberts PJ & Allan DC. Single-Mode Photonic Band Gap Guidance of Light in Air. *Science* (1999) **285**: pp. 1537-1539.

[DIN11562] DIN EN ISO 11562:1996, Geometrical Product Specifications (GPS) - Surface texture: Profile method - Metrological characteristics of phase correct filters.

[DIN3274] DIN EN ISO 3274:1998, Geometrical Product Specifications (GPS) - Surface texture: Profile method - Nominal characteristics of contact (stylus) instruments.

[DIN4287] DIN EN ISO 4287:2010, Geometrical Product Specifications (GPS) - Surface texture: Profile method - Terms, definitions and surface texture parameters.

[DIN4288] DIN EN ISO 4288:1998, Geometrical Product Specifications (GPS) - Surface texture: Profile method - Rules and procedures for the assessment of surface texture.

[Dressel1991] Dressel M, Jahn R, Neu W & Jungbluth K. Studies in fiber guided excimer laser surgery for cutting and drilling bone and meniscus. *Lasers in Surgery and Medicine* (1991) **11**: pp. 569-579.

[Driel1982] van Driel HM, Sipe JE & Young JF. Laser-Induced Periodic Surface Structure on Solids: A Universal Phenomenon. *Phys. Rev. Lett.* (1982) **49**: pp. 1955-1958.

[Dufft2009] Dufft D, Rosenfeld A, Das SK, Grunwald R & Bonse J. Femtosecond laser-induced periodic surface structures revisited: A comparative study on ZnO. *Journal of Applied Physics* (2009) **105**: p. 034908.

[Eichler2002] Eichler J & Eichler HJ. Laser: Bauformen, Strahlführung, Anwendungen. Springer, 2002.

[Emslie2007] Emslie C. **Polarization Maintaining Fibers**. In *Specialty optical fibers handbook*. Mendez A & Morse TF (Eds.). 2007. pp. 243-277.

[Fabian1993] Fabian H, Grzesik U, Hillrichs G & Neu W. Optical fibers with enhanced performance for excimer laser power transmission at 308 nm. In *Proc. SPIE 1893-24*. 1993.

[Fauchet1983] Fauchet PM & Siegman AE. Observations of higher-order laser-induced surface ripples on ⟨111⟩ germanium. *Applied Physics A: Materials Science & Processing* (1983) **32**: pp. 135-140.

[Friebele1976] Friebele EJ, Sigel GH & Griscom DL. Drawing-induced defect centers in a fused silica core fiber. *Applied Physics Letters* (1976) **28**: pp. 516-518.

[Friebele1979] Friebele EJ & Griscom DL. **Radiation Effects in Glass**. In *Treatise on materials science and technology: Glass II*. Tomozawa M & Doremus RH (Eds.). 1979. pp. 257-351.

[Frost2001] Frost H, Deter C, Kirchhof J, Unger S, Schroeter S & Schwuchow A. Laser TV - High power in optical fibers. *GMM Fachbericht* (2001) **34**: pp. 41-45.

[Gallagher1992] Gallagher MD & Osterberg UL. Ultraviolet absorption measurements in single-mode optical glass fibers. *Applied Physics Letters* (1992) **60**: pp. 1791-1793.

[Gambling1978] Gambling WA, Matsumura H & Cowley AG. Jointing loss in single-mode fibres. *Electronics Letters* (1978) **14**: pp. 54-55.

[Gloge1971] Gloge D. Weakly Guiding Fibers. *Appl. Opt.* (1971) **10**: pp. 2252-2258.

[Griscom1985] Griscom DL. Defect structure of glasses: Some outstanding questions in regard to vitreous silica. *Journal of Non-Crystalline Solids* (1985) **73**: pp. 51-77.

[Guffey2006] Guffey JS & Wilborn J. Effects of Combined 405-nm and 880-nm Light on Staphylococcus aureus and Pseudomonas aeruginosa in Vitro. *Photomedicine and Laser Surgery* (2006) **24**: pp. 680-683.

[Heitmann2004] Heitmann W & Klein K. Infrared Absorption of Silica Fibers. *Journal of Optical Communications* (2004) **25**: pp. 106-109.

[Henyk1999] Henyk M, Vogel N, Wolfframm D, Tempel A & Reif J. Femtosecond laser ablation from dielectric materials: Comparison to arc discharge erosion. *Applied Physics A: Materials Science & Processing* (1999) **69**: pp. S355-S358.

[Hillrichs2011] Hillrichs G, Gonschior CP, Klein K & Wandschneider R. Performance of low mode and single mode optical fibers for high peak power 355 nm laser radiation. In *Proc. SPIE 7894-0Z*. 2011.

[Hoehm2012] Höhm S, Rosenfeld A, Krüger J & Bonse J. Femtosecond laser-induced periodic surface structures on silica. *Journal of Applied Physics* (2012) **112**: p. 014901.

[Huebner2000] Hübner M, Meyer H, Klein K, Hillrichs G, Ruetting M, Veidemanis M, Spangenberg B, Clarkin JP & Nelson GW. Fiber optic systems in the UV region. In *Proc. SPIE 3911-303*. 2000.

[Ikuta2004] Ikuta Y, Kajihara K, Hirano M & Hosono H. Correlation between Oxygen-Deficient Center Formation and Volume Compaction in Synthetic SiO2 Glass Upon ArF or F2 Excimer-Laser Irradiation. *Appl. Opt.* (2004) **43**: pp. 2332-2336.

[Imai1988] Imai H, Arai K, Imagawa H, Hosono H & Abe Y. Two types of oxygen-deficient centers in synthetic silica glass. *Phys. Rev. B* (1988) **38**: pp. 12772-12775.

[Imai1991] Imai H, Arai K, Hosono H, Abe Y, Arai T & Imagawa H. Dependence of defects induced by excimer laser on intrinsic structural defects in synthetic silica glasses. *Phys. Rev. B* (1991) **44**: pp. 4812-4818.

[Karlitschek1995] Karlitschek P, Hillrichs G & Klein K. Photodegradation and nonlinear effects in optical fibers induced by pulsed uv-laser radiation. *Optics Communications* (1995) **116**: pp. 219-230.

[Kato2008] Kato J, Hatayama H, Miyazaki H, Akashi G, Moriya K, Inoue A & Hirai Y. Surgical performance of a 405-nm diode laser in treatment of soft tissue. *Laser Physics Letters* (2008) **5**: pp. 316-320.

[Keilmann1982] Keilmann F & Bai YH. Periodic surface structures frozen into CO2 laser-melted quartz. *Applied Physics A: Materials Science & Processing* (1982) **29**: pp. 9-18.

[Kemeter2002] Kemeter K. **Herstellungsverfahren von Lichtwellenleitern**. In *Optische Kommunikationstechnik: Handbuch für Wissenschaft und Industrie*. Petermann K & Voges E (Eds.). 2002.

[Khalilov1994] Khalilov VK, Dorfman GA, Danilov EB, Guskov MI & Ermakov VE. Character, mechanism of formation and transformation of point defects in type IV silica glass. *Journal of Non-Crystalline Solids* (1994) **169**: pp. 15-28.

[Khalilov2006] Khalilov VK, Klein K, Belmahdi J, Timmerman R & Nelson GW. High-OH fibers with higher stability in the UV-region. In *Proc. SPIE 6083-08*. 2006.

[Kirchhof1998] Kirchhof J, Unger S, Knappe B, Pissler H, Ruppert K & Koppler R. Chlorine incorporation into silica lightguide materials. In *Optical fiber communication conference and exhibit, 1998. OFC '98., technical digest*. 1998.

[Kirchhof2001] Kirchhof J, Unger S, Schroeter S, Schwuchow A, Frost H & Deter C. High-power stability of optical fibers for the visible wavelength region. In *Proc. SPIE 4579-322*. 2001.

[Kirchhof2004] Kirchhof J, Kobelke J, Schuster K, Bartelt H, Iliew R, Etrich C & Lederer F. **Photonic crystal fibers**. In *Photonic crystals advances in design, fabrication, and characterization*. Busch K, Lölkes S, Wehrspohn RB & Föll H (Eds.). 2004. pp. 266-288.

[Kirshenbaum2011] Kirshenbaum MR & Seibel EJ. Delivery of single-mode and multi-mode therapeutic laser light using a single and dual cladding optical fiber for a scanning fiber endoscope. In *Proc. SPIE 7894-13*. 2011.

[Klein1996a] Klein K, Bauer A, Hacker M, Hillrichs G & Smolka E. UV-stabile Quarzglasfasern für Anwendungen bei 200 nm Wellenlänge. *VDI-Berichte* (1996) **1255**: pp. 453-458.

[Klein1996b] Klein K, Rode H, Belz M, Boyle WJO & Grattan KTV. Water-quality measurement using fiber optics at wavelengths below 230 nm. In *Proc. SPIE 2836-186*. 1996.

[Klein1997] Klein K, Schließmann P, Smolka E, Hillrichs G, Belz M, Boyle WJO & Grattan KTV. UV-stabilized silica-based fibre for applications around 200 nm wavelength. *Sensors and Actuators B: Chemical* (1997) **39**: pp. 305-309.

[Klein1998] Klein K, Huettel S, Kaminski R, Kirchhof J, Grimm S & Nelson GW. Stability and lifetime improvements of UV fibers for new applications. In *Proc. SPIE 3262-150*. 1998.

[Klein2001] Klein K, Arndt R, Hillrichs G, Ruetting M, Veidemanis M, Dreiskemper R, Clarkin JP & Nelson GW. UV fibers for applications below 200 nm. In *Proc. SPIE 4253-42*. 2001.

[Klein2009] Klein K, Mannhardt J, Belz M, Gonschior CP & Eckhardt HS. Optical fibers in instrumental UV-analytics (Invited Paper). In *Proc. SPIE 7173-02*. 2009.

[Kneubuehl1999] Kneubühl FK & Sigrist MW. Laser. Springer, 1999.

[Knight1996] Knight JC, Birks TA, Russell PSJ & Atkin DM. All-silica single-mode optical fiber with photonic crystal cladding. *Opt. Lett.* (1996) **21**: pp. 1547-1549.

[Knight1998] Knight JC, Birks TA, Cregan RF, Russell PSJ & de Sandro PD. Large mode area photonic crystal fibre. *Electronics Letters* (1998) **34**: pp. 1347-1348.

[Koehler2003] Köhler M, Dietz H, Matsuura Y, Miyagi M, Klein K & Hillrichs G. Status and improvements of UV laser scalpel. In *Proc. SPIE 4957-92*. 2003.

[Kuehn2003] Kühn B, Uebbing B, Stamminger M, Radosevic I & Kaiser S. Compaction versus expansion behavior related to the OH-content of synthetic fused silica under prolonged UV-laser irradiation. *Journal of Non-Crystalline Solids* (2003) **330**: pp. 23 - 32.

[Lee2010] Lee CM, Engelbrecht CJ, Soper TD, Helmchen F & Seibel EJ. Scanning fiber endoscopy with highly flexible, 1 mm catheterscopes for wide-field, full-color imaging. *Journal of Biophotonics* (2010) **3**: pp. 385-407.

[Li1985] Li T. Optical fiber communications: Volume 1 Fiber Fabrication. Academic Press, 1985.

[Mansuripur2002] Mansuripur M & Wright EM. The Optics of Semiconductor Diode Lasers. *Optics & Photonics News* (2002) **13**: pp. 57-61.

[Marcuse1977] Marcuse D. Loss Analysis of Single-Mode Fiber Splices. *Bell System Technical Journal* (1977) **56**: pp. 703-718.

[Marcuse1982] Marcuse D. Light transmission optics. Van Nostrand Reinhold, 1982.

[Mende2002] Mende B & Behm K. **Faseroptische Verbindungen**. In *Optische Kommunikationstechnik: Handbuch für Wissenschaft und Industrie*. Petermann K & Voges E (Eds.). 2002.

[Messina2008] Messina F, Cannas M & Boscaino R. Generation of defects in amorphous SiO 2 assisted by two-step absorption on impurity sites. *Journal of Physics: Condensed Matter* (2008) **20**: p. 275210.

[Mitschke2005] Mitschke F. Glasfasern: Physik und Technologie. Rüdinger A (Ed.). Elsevier, 2005.

[Moll2002] Moll J & Dewa PG. Laser resistance of fused silica for microlithography: experiments and models. In *Proc. SPIE 4691-1734*. 2002.

[Moll2004] Moll J, Allan DC & Neukirch U. Advances in the use of birefringence to measure laser-induced density changes in fused silica. In *Proc. SPIE 5377-1721*. 2004.

[Mozzi1969] Mozzi RL & Warren BE. The structure of vitreous silica. *Journal of Applied Crystallography* (1969) **2**: pp. 164-172.

[Muehl2001] Mühl T. Einführung in die elektrische Messtechnik. Teubner, 2001.

[Muehlig2005] Mühlig C. **Zur Absorption gepulster ArF-Laserstrahlung in hochtransparenten optischen Materialien**. PhD thesis. Friedrich-Schiller-University Jena.2005.

[Nagahama2003] Nagahama S, Sano M, Yanamoto T, Morita D, Miki O, Sakamoto K, Yamamoto M, Matsuyama Y, Kawata Y, Murayama T & Mukai T. GaN-based laser diodes emitting from ultraviolet to blue-green. In *Proc. SPIE 4995-108*. 2003.

[Nagahama2005] Nagahama S, Sugimoto Y, Kozaki T & Mukai T. Recent progress of AlInGaN laser diodes. In *Proc. SPIE 5738-57*. 2005.

[Nakamura2000] Nakamura S. Current status and future prospects of InGaN-based laser diodes. *JSAP International* (2000) **1**: pp. 5-17.

[Nemoto1979] Nemoto S & Makimoto T. Analysis of splice loss in single-mode fibres using a Gaussian field approximation. *Optical and Quantum Electronics* (1979) **11**: pp. 447-457.

[Neumann1988] Neumann E. Single-mode fibers: Fundamentals. Tamir T (Ed.). Springer, 1988.

[Oura2003] Oura K, Lifshits VG, Saranin AA, Zotov AV & Katayama M. Surface Science: An Introduction. Springer, 2003.

[Palik1997] Palik ED. Handbook of Optical Constants of Solids. Elsevier, 1997.

[Paschotta2008] Paschotta R. Encyclopedia of Laser Physics and Technology. Wiley-VCH, 2008.

[Peled2000] Peled A, Mirchin N, Zacharia Z & Peled CR. Simulation of thin film growth visualization in photodeposition. *Applied Surface Science* (2000) **154–155**: pp. 324-330.

[Peski2000] Peski CKV, Morton R & Bor Z. Behavior of fused silica irradiated by low level 193 nm excimer laser for tens of billions of pulses. *Journal of Non-Crystalline Solids* (2000) **265**: pp. 285-289.

[Piao2000] Piao F, Oldham WG & Haller EE. Ultraviolet-induced densification of fused silica. *J. Appl. Phys.* (2000) **87**: pp. 3287-3293.

[Pini1987] Pini R, Salimbeni R & Vannini M. Optical fiber transmission of high power excimer laser radiation. *Appl. Opt.* (1987) **26**: pp. 4185-4189.

[Polymicro2011] **The Book on the technologies of Polymicro**. Polymicro Technologies, Phoenix, AZ, 2011.

[Poyntz-Wright1989] Poyntz-Wright LJ & Russell PSJ. Spontaneous relaxation processes in irradiated germanosilicate optical fibres. *Electronics Letters* (1989) **25**: pp. 478-480.

[Preston1989] Preston JS, van Driel HM & Sipe JE. Pattern formation during laser melting of silicon. *Phys. Rev. B* (1989) **40**: pp. 3942-3954.

[Primak1968] Primak W & Kampwirth R. The Radiation Compaction of Vitreous Silica. *Journal of Applied Physics* (1968) **39**: pp. 5651-5658.

[Reif1989] Reif J. High power laser interaction with the surface of wide bandgap materials. *Optical Engineering* (1989) **28**: pp. 1122-1132.

[Reif2004] Reif J, Costache FA, Eckert S, Kouteva-Arguirova S, Bestehorn M, Georgescu I, Semerok AF, Martin P, Gobert O & Seifert W. Formation of self-organized regular nanostructures upon femtosecond laser ablation. In *Proc. SPIE 5662-737*. 2004.

[Reif2006] Reif J, Costache F & Bestehorn M. **Self-Organized Surface Nanostructuring by Femtosecond Laser Processing**. In *Recent advances in laser processing of materials*. Perrière J, Millon E & Fogarassy E (Eds.). 2006. pp. 275-290.

[Reif2010] Reif J, Varlamova O, Ratzke M, Schade M, Leipner H & Arguirov T. Multipulse feedback in self-organized ripples formation upon femtosecond laser ablation from silicon. *Applied Physics A: Materials Science & Processing* (2010) **101**: pp. 361-365.

[Rohloff2011] Rohloff M, Das SK, Höhm S, Grunwald R, Rosenfeld A, Krüger J & Bonse J. Formation of laser-induced periodic surface structures on fused silica upon multiple cross-polarized double-femtosecond-laser-pulse irradiation sequences. *Journal of Applied Physics* (2011) **110**: p. 014910.

[Scharnweber2011] Scharnweber T, Truckenmüller R, Schneider AM, Welle A, Reinhardt M & Giselbrecht S. Rapid prototyping of microstructures in polydimethylsiloxane (PDMS) by direct UV-lithography. *Lab Chip* (2011) **11**: pp. 1368-1371.

[Schwuchow2012] Schwuchow A. IPHT, Jena. private communication.

[Senior1992] Senior JM. Optical fiber communications: Principles and practice (second edition). Prentice Hall, 1992.

[Shelby1979] Shelby JE. Radiation effects in hydrogen-impregnated vitreous silica. *Journal of Applied Physics* (1979) **50**: pp. 3702-3706.

[Singh2003] Singh AP, Kapoor A & Tripathi KN. Recrystallization of germanium surfaces by femtosecond laser pulses. *Optics & Laser Technology* (2003) **35**: pp. 87-97.

[Sipe1983] Sipe JE, Young JF, Preston JS & van Driel HM. Laser-induced periodic surface structure. I. Theory. *Phys. Rev. B* (1983) **27**: pp. 1141-1154.

[Skierbiszewski2005] Skierbiszewski C. From High Electron Mobility GaN/AlGaN Heterostructures to Blue-Violet InGaN Laser Diodes . *Acta Physica Polonica A* (2005) **108**: pp. 635-651.

[Skuja1994] Skuja L. Direct singlet-to-triplet optical absorption and luminescence excitation band of the twofold-coordinated silicon center in oxygen-deficient glassy SiO2. *Journal of Non-Crystalline Solids* (1994) **167**: pp. 229-238.

[Skuja1998] Skuja L. Optically active oxygen-deficiency-related centers in amorphous silicon dioxide. *Journal of Non-Crystalline Solids* (1998) **239**: pp. 16-48.

[Smith2001] Smith CM, Borrelli NF, Price JJ & Allan DC. Excimer laser-induced expansion in hydrogen-loaded silica. *Applied Physics Letters* (2001) **78**: pp. 2452-2454.

[Soileau1984] Soileau M. Ripple structures associated with ordered surface defects in dielectrics. *Quantum Electronics, IEEE Journal of* (1984) **20**: pp. 464-467.

[Sulimov2002] Sulimov VB, Sushko PV, Edwards AH, Shluger AL & Stoneham AM. Asymmetry and long-range character of lattice deformation by neutral oxygen vacancy in a-quartz. *Phys. Rev. B* (2002) **66**: p. 024108.

[Sun2012] Sun H. **Laser Diode Beam Propagation Basics**. In *Laser diode beam basics, manipulations and characterizations*. 2012.

[Susman1991] Susman S, Volin KJ, Price DL, Grimsditch M, Rino JP, Kalia RK, Vashishta P, Gwanmesia G, Wang Y & Liebermann RC. Intermediate-range order in permanently densified vitreous SiO2: A neutron-diffraction and molecular-dynamics study. *Phys. Rev. B* (1991) **43**: pp. 1194-1197.

[Taylor1988] Taylor RS, Leopold KE, Brimacombe RK & Mihailov S. Dependence of the damage and transmission properties of fused silica fibers on the excimer laser wavelength. *Appl. Opt.* (1988) **27**: pp. 3124-3134.

[Unger2002] Unger S, Kirchhof J, Schroeter S, Schwuchow A & Frost H. Transmission behavior of silica core: fluorine-doped cladding fibers in the visible and ultraviolet region. In *Proc. SPIE 4616-161*. 2002.

[US2010/0027569] UV diode-laser module with optical fiber delivery.

[US2011/0235973] Optical element with mechanical alignment and method of making same.

[US4701011] Multimode fiber-lens optical coupler.

[Varlamova2006] Varlamova O, Costache F, Reif J & Bestehorn M. Self-organized pattern formation upon femtosecond laser ablation by circularly polarized light. *Applied Surface Science* (2006) **252**: pp. 4702-4706.

[Varlamova2007] Varlamova O, Costache F, Ratzke M & Reif J. Control parameters in pattern formation upon femtosecond laser ablation. *Applied Surface Science* (2007) **253**: pp. 7932-7936.

[Vydra1999] Vydra J & Schoetz GF. Improved all-silica fibers for deep-UV applications. In *Proc. SPIE 3596-165*. 1999.

[Wagner2006] Wagner R, Gottmann J, Horn A & Kreutz EW. Subwavelength ripple formation induced by tightly focused femtosecond laser radiation. *Applied Surface Science* (2006) **252**: pp. 8576-8579.

[Watanabe2006] Watanabe W & Itoh K. **Three-Dimensional Micromachining with Femtosecond Laser Pulses**. In *Recent advances in laser processing of materials*. Perrière J, Millon E & Fogarassy E (Eds.). 2006. pp. 291-315.

Appendix I: Surface effects on fibres for printing

Damaged fibre samples were provided by a printing machine manufacturer. The alteration on the launching surface of the conventionally assembled multi-mode fibres looks similar to the laser-induced periodic surface structures (LIPSS) found in this work. The fibres were irradiated with 375 nm or 405 nm multi-mode laser diodes with upto 175 mW output power. In these modules the laser diode was exactly focused onto the fibre surface. However, the position of the lens along the optical axis was different between particular modules. Thus, the focus with highest power density was in a different spot for every module, as it can be seen from Figure I-1. The maximum longitudinal offset was determined to 300 µm. The severity of the damage varied from module to module, because higher and lower power densities were obtained on the fibre surfaces at the end stop.

An example of a damaged fibre surface is shown in Figure I-2. The damage had a size of 3 µm by 21 µm and is a magnified image of the laser diode facet, which has a size of 1 µm by 7 µm. For this damage area a mean power density of 350 kW/cm² was calculated for 405 nm, which is close to the mean power densities seen from experiments in this work. However, there are no ripples on this damage spot, it is only a projection. An EDX analysis of damage and reference areas in Figure I-3 showed no differences in elemental concentrations. By varying the position of the end stop inside the module the laser spot on the fibre surface was enlarged in a controlled manner within the boundaries of the fibre core. Thereby significantly reducing the loss in long-term operation.

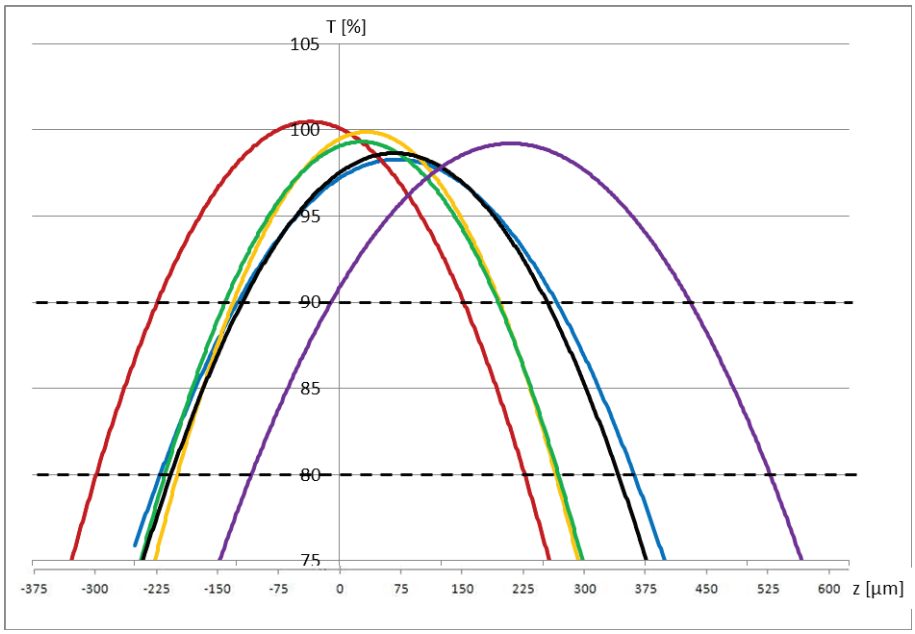

Figure I-1: Measurement of focus position in different laser diode modules of the same manufacturer.

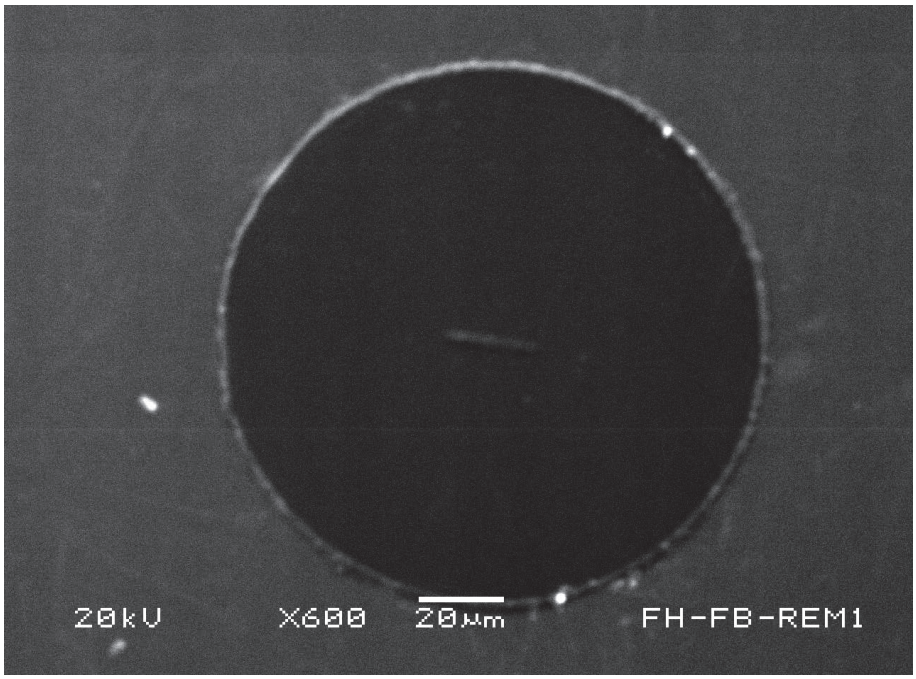

Figure I-2: SEM image of the surface damage due to exactly focused diode laser on a fibre launching surface.

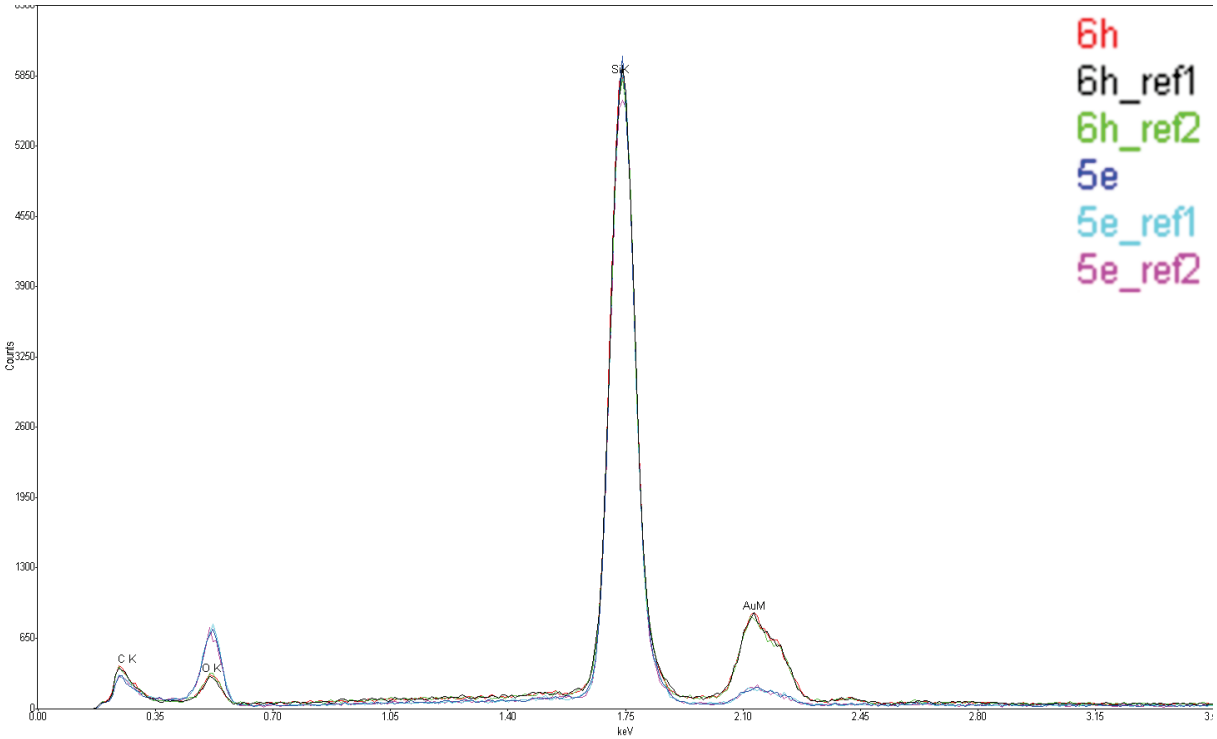

Figure I-3: Energy dispersive x-ray analysis (EDX) of two damage areas and according reference areas. The peaks from left to right: C, O, Si, Au.

Appendix II: Surface effects on single-mode fibres in sealed collimators

Long-term experiments were performed at Omicron-Laserage GmbH, Rodgau, Germany, with sealed fibre collimators purged with nitrogen at both ends of a polarisation-maintaining single-mode fibre (PM-SMF). Over an irradiation period of 50 days the assembly was irradiated with a 250 mW single-mode laser at 405 nm wavelength and a moderate loss of 1 dB was observed, while the collimator windows were cleaned regularly. After the experiment was terminated, both fibre ends were examined at the Technische Hochschule Mittelhessen, Gießen, Germany, using scanning electron microscopy (SEM). The images in Figure II-1 and II-2 show clearly that a periodic surface structure with cones and not ripples was formed.

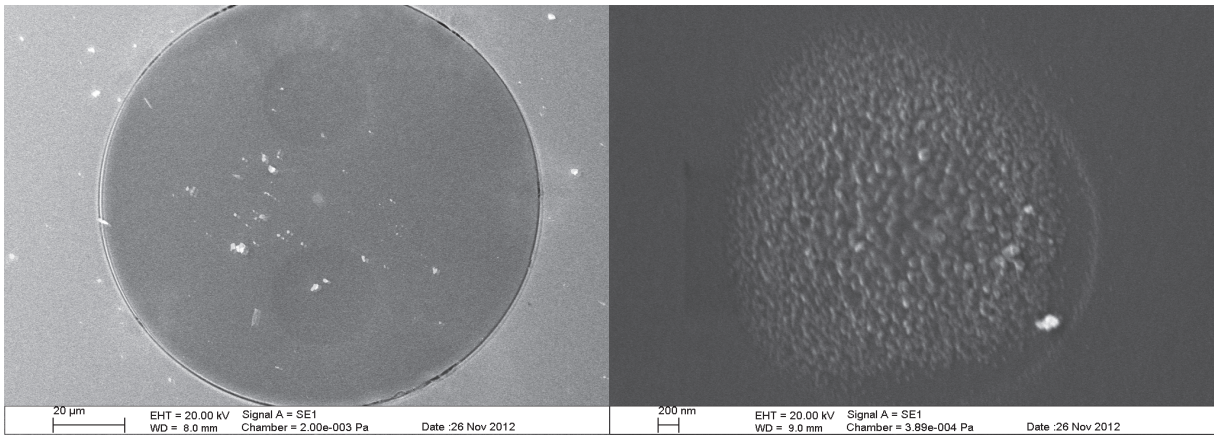

a) *b)*

Figure II-1: SEM images of PM-SMF launching surface after 50 days of 250 mW at 405 nm. a) The whole fibre surface is shown and the core as well as the stress members are clearly visible. b) The core area with the damage with a diameter of about 2.5 µm.

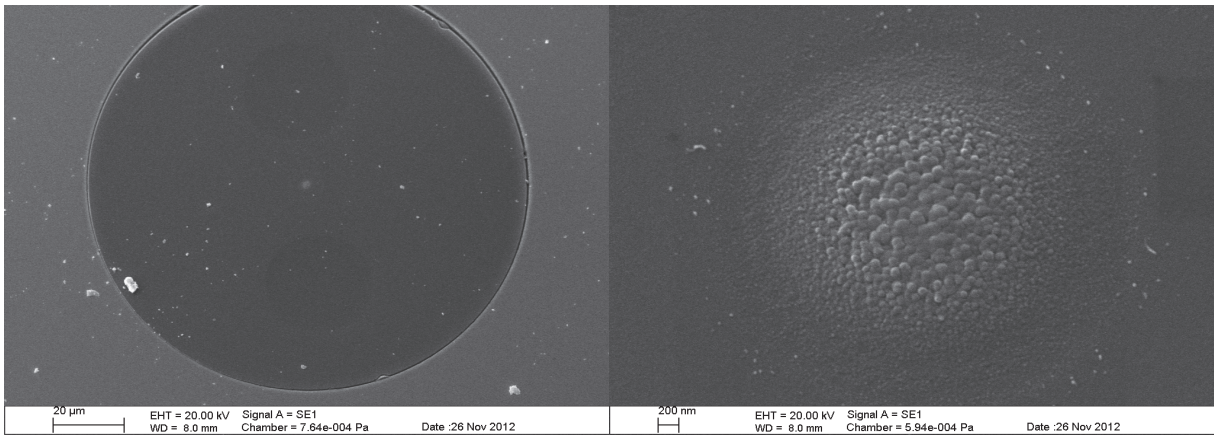

a) *b)*

Figure II-2: SEM images of PM-SMF distal surface after 50 days of 250 mW at 405 nm. a) The whole fibre surface is shown and the core as well as the stress members are clearly visible. b) The core area with the damage with a diameter of about 2 µm.

Appendix III: Surface effects by 446 nm laser irradiation

In experiments for [Frost2001, Kirchhof2001, Unger2002] low-mode fibre (LMF) was being damaged with pulsed 446 nm single-mode laser diodes. The pulse width was 9 ps and at a repetition rate of 80 MHz an average power of 1 W was achieved, which means a pulse energy of about 12.5 nJ. The LMF samples were irradiated for 150 to 180 hours. Besides the generation of UV defect centres, this research also found “geometrical alterations of the input and output end faces ... of the fibres with long lifetimes” [Kirchhof2001]. After thorough discussion with the group at the IPHT, Jena, old atomic force microscope (AFM) images revealed that laser-induced periodic surface structures (LIPSS) with periodicities in the range of 250 to 280 nm had been found on the end surfaces, but were not further investigated [Schwuchow2012]. The AFM images of the launching and distal fibre ends are shown in Figures III-1 and III-2.

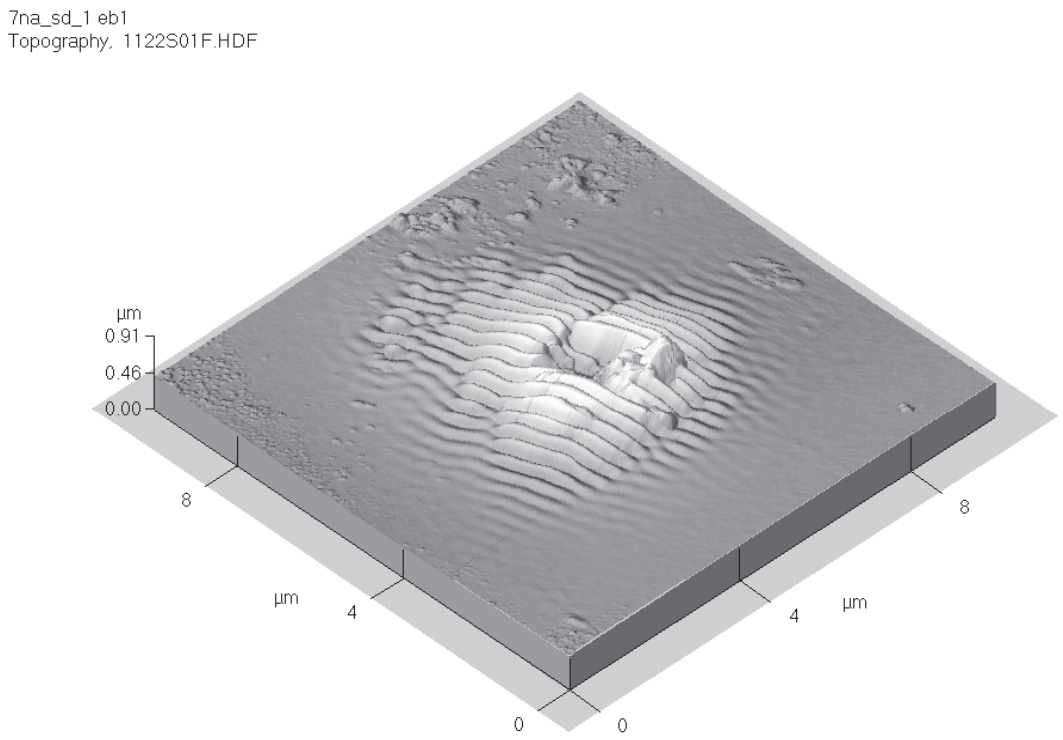

Figure III-1: Damage probably found on the launching end of a LMF after pulsed 446 nm irradiation with an average power of 1 W.

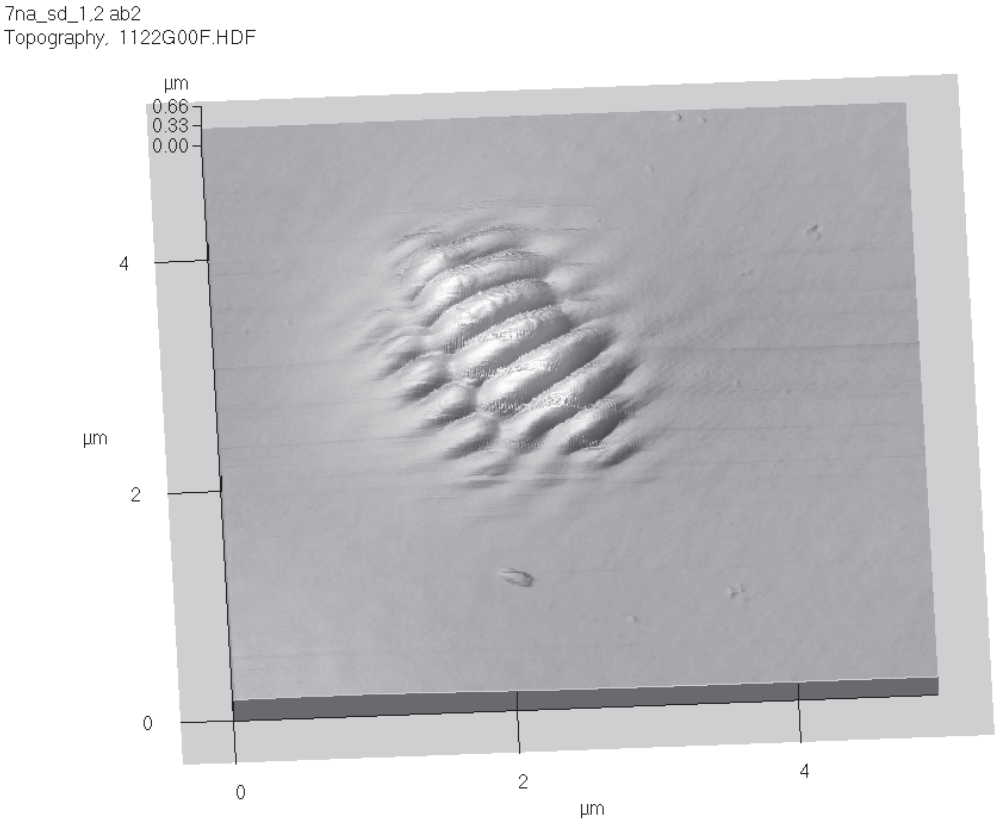

Figure III-2: Damage probably found on the distal end of a LMF after pulsed 446 nm irradiation with an average power of 1 W.

List of publications by the author relevant to this thesis

Journals

1. **Gonschior CP**, Klein K, Sun T & Grattan KTV. Generation of periodic surface structures on silica fibre surfaces with 405 nm CW diode lasers. *Journal of Non-Crystalline Solids* (2013) **361**: pp. 106-110.
2. Heimann JC, **Gonschior CP**, Klein K, Hillrichs G & Takala E. Spectral UV losses in 355 nm pulsed laser delivery system at low temperatures. Accepted for publication in *Journal of Non-Crystalline Solids*.

Conferences

1. Klein K, Mannhardt J, Belz M, **Gonschior CP** & Eckhardt HS. Optical fibers in instrumental UV-analytics (Invited Paper). In *Proc. SPIE 7173-02*. 2009.
2. **Gonschior CP**, Eimer D, Klein K, Sun T & Grattan KTV. Characterization of UV single-mode and low-mode fibers. In *Proc. SPIE 7559-0X*. 2010.
3. **Gonschior CP**, Klein K, Sun T, Grattan KTV, Kirshenbaum MR & Seibel EJ. Lifetime prediction for 405-nm single-mode delivery systems for therapeutic laser applications. In *Proc. SPIE 8218-0A*. 2012.
4. **Gonschior CP**, Klein K, Sun T & Grattan KTV. Influence of high power 405-nm multi-mode and single-mode diode laser light on the long-term stability of fused silica fibers. In *Proc. SPIE 8426-0P*. 2012.
5. **Gonschior CP**, Klein K, Sun T & Grattan KTV. Generation of periodic surface structures on silica fibre surfaces with 405 nm CW diode lasers. Presented at the 9th Symposium "SiO_2, Advanced Dielectrics and Related Devices". Hyères, France. June 2012.
6. **Gonschior CP**, Klein K, Sun T & Grattan KTV. Surface and bulk effects in silica fibers caused by 405 nm CW diode laser irradiation and means for mitigation. In *Proc. SPIE 8530-0A*. 2012
7. **Gonschior CP**, Klein K, Heyse D, Baumann S, Sun T & Grattan KTV. High power 405 nm diode laser fiber-coupled single-mode system with high long-term stability. In *Proc. SPIE 8605-24*. 2013.

Reports

1. Klein K & **Gonschior CP**. *Entwicklung von faseroptischen Übertragungssystemen mit UV-Diodenlasern und einmodigen Lichtwellenleitern mit hoher UV-Beständigkeit (UV-SMS)* (ISBN: 978-3-00-040891-5). Selbstverlag Klaus Schmidt, Friedberg, 2013.